

# Calibrated Numerical models for masonry buildings subjected to subsidence-related ground settlements

---

**Javier Fuertes Guadarrama**

**a Master Thesis**

submitted in partial fulfilment of  
the requirements for the Degree of  
Master of Science in Civil Engineering

**Feb-Oct  
2024**

In collaboration with

**TNO** innovation  
for life

# Calibrated Numerical models for masonry buildings subjected to subsidence-related ground settlements

A study into the capabilities and development of assessment methods for predicting damage to masonry structures undergoing subsidence-related settlements.

## Javier Fuertes Guadarrama

In fulfilment of the requirements to obtain the degree of Master of Science in Civil Engineering at the Faculty of Civil Engineering and Geosciences, Delft University of Technology. To be defended on the 24<sup>th</sup> of October 2024

Student number: 5832918

Project Duration: Feb 2024 – Oct 2024

Graduation committee:	Prof.dr.ir J.G. (Jan) Rots	Committee Chair
	Ir. C. (Cor) Kasbergen	Committee Vice-chair
	A. (Alfonso) Prospero, Msc	Daily Supervisor
	Ir. D. (Davide) Moretti	Daily and Company
	G. (Giovanna) Cera, Msc	Supervisors

An electronic version of this thesis is available at <https://repository.tudelft.nl/>. Any data and code written for this project is also available at <https://github.com/JavFuertes>. A Special thanks to the collaboration from the Data in the Built Environment research group at TNO and the Department of Applied Mechanics of Structures at Delft University of Technology.



## Abstract

Due to the Netherlands' topography and geology, many regions have weak soil resistance, causing numerous buildings to experience settlements from subsidence processes, with masonry structures being the most commonly affected. In these buildings, damage typically appears as cracks and deformations, indicating the foundation's inability to support the structure. To enhance decision-making and the engineering of effective countermeasures in these scenarios, accurate and reliable building assessments are needed to predict the expected damage based on the amount of soil deformations. This thesis, therefore, aims to evaluate the capabilities of a set of state-of-the-art damage assessment methods. These methods have been applied to a case study, with their results benchmarked against evidence from a Building Foundation Assessment report, where recorded damage features were used to evaluate the accuracy and characteristics of each assessment method.

The study began with a Visual Assessment using a Decision Diagnostic Support Tool to analyze damage features and hypothesize the causes of the building's behavior. This was followed by an Empirical Assessment, applying empirical limits to relate expected damage to Subsidence-Related Intensity (SRI) parameters. Next, an Analytical Assessment used the Limit Tensile Strain Method (LTSM) to approximate building deformations, treating it as a linear-elastic isotropic masonry beam and correlating strain estimates to damage levels. Finally, a 2D Finite Element Analysis (FEA) using a continuum crack-modelling approach was conducted on the most damaged wall to more accurately reproduce the crack widths, crack locations and the behaviour of the wall.

The results show that while the building's damage state can be approximated with reasonable accuracy, challenges remain in predicting specific damage features. The visual assessment successfully identified the building's underlying mechanism. Empirical and analytical methods accurately predicted damage levels in 5 out of 6 walls, proving to be efficient assessment techniques. The 2D Finite Element Analysis (FEA) successfully simulated the crack pattern on Wall 2 with a Root Mean Square Error (RMSE) of  $+1 \Psi$  or  $+4.7\text{mm}$  against the maximum mean crack widths and reproduced 5 out of 7 cracks with similar characteristics. Additionally, FEA results showed that mesh sizes of 200, 100, and 50 mm made results deviate by  $\sigma = 0.33 \Psi$  and  $\sigma_{\text{CWmax}} = 2.3\text{mm}$ , with observable changes in crack shapes in EMM models.

To address the slight deviations in the less accurate analysis of the outer leaf, primarily driven by conservative crack width estimates, a Bayesian Optimization procedure was used on the outer leaf models to identify the optimal set of material parameters that minimized the discrepancy between the damage state of the results and the target damage level in the case study.

The implementation of the approach demonstrated sufficient efficiency in identifying the optimal set of parameters, despite the computational expense of the Finite Element models. The procedure's effectiveness varied across models with it significantly reducing damage levels in the Engineering Masonry Model (EMM) variations but showed more limited improvements in the Total Strain Crack Model (TSCM). Additionally, the approach allowed for an investigation into the influence of material properties, revealing that Young's Modulus and tensile strength were the most influential parameters across both models. Furthermore, the results indicated that the influence of material parameters is highly non-linear, meaning changes in material properties do not always lead to predictable outcomes. Instead, specific combinations of parameters had a greater impact on reducing damage, demonstrating the complex interplay between material properties particularly in the EMM model variant.

# Acknowledgements

This thesis marks the end of my master's studies. Not long ago, I wouldn't have expected to reach this point or develop such a deep interest in Structural Engineering and the many topics it encompasses. Nevertheless, this project reflects the skills and knowledge I've gained through exploring this field, which I hope, when applied to this thesis, will make for an engaging read.

Nonetheless, producing this thesis would not have been possible without the support of all my committee members throughout this project and previous studies. I would therefore like to extend my sincere thanks to my chairs, Prof. dr. ir. Jan Rots and Ir. Cor Kasbergen, for your feedback, dedicated involvement, and exemplary approach to teaching. I also wish to express my gratitude to my supervisors, Alfonso Prospero, MSc, Ir. Davide Moretti, and Giovanna Cera, MSc, who provided me the opportunity to undertake this project and have been exceptional mentors. Your guidance, patience, and understanding throughout my many challenges have been fundamental in improving my work and approach, thank you.

Most importantly, I would like to thank my family. Your unwavering love and support have enabled me to pursue both my passions and education over the last years. I hope that my graduation brings you happiness. Finally, I would like to thank my friends, whose support throughout my education has allowed me to truly enjoy this significant chapter of my life. Your support during this time has been invaluable and I thank you for all the good times we've spent together.

# Table of Contents

<b>1. Introduction.....</b>	<b>12</b>
1.1 Background and motivation.....	13
1.2 Research aim and research questions.....	14
1.3 Research scope .....	15
1.4 Methodology .....	15
<b>2. Literature review .....</b>	<b>18</b>
2.1 Land subsidence .....	19
2.2 Masonry Structures .....	23
2.2.1 Masonry's material properties.....	23
2.2.2 Characterization of masonry's material properties .....	25
2.3 The response of masonry structures to settlements .....	28
2.3.1 Superstructural behaviour .....	28
2.3.2 Substructural behaviour.....	31
2.3.3 Definition of damage & assessment indicators .....	32
2.4 Damage assessment procedures for Masonry Structures subjected to settlements...34	
2.4.1 Empirical methods: Empirical based literature thresholds.....	35
2.4.2 Analytical methods: Limit Tensile Strain Method and Load Path Method.....	37
2.4.3 Numerical Methods: Masonry Finite Element Analysis .....	40
2.4.5 Modelling approaches specific for settlement-induced Masonry Structures .....	46
2.5 Calibration of Finite Element Models .....	48
2.5.1 Successful calibration instances of Finite Element Models .....	48
2.5.2 Bayesian optimisation: a possible solution.....	49
2.5.3 Detailed Insights into Bayesian Optimisation algorithms.....	52
2.6 Conclusions .....	54
<b>3. Case study selected for the damage assessment.....</b>	<b>56</b>
3.1 The building's superstructure .....	58
3.2 The building's substructure .....	59
3.3 The buildings' damage state .....	60
3.3.1 Evaluation of the foundation assessment report's completeness and robustness.....	65
<b>4. Damage assessment through empirical and analytical procedures ...</b>	<b>67</b>
4.1 Visual investigation .....	68

4.2 Empirical assessment .....	71
4.2.1 Results from the empirical assessment .....	71
4.3 Analytical assessment.....	75
4.3.1 Approach 1: Direct use of the building displacements.....	77
4.3.2 Approach 2: Extrapolating the greenfield profile from the wall measurements .....	80
4.4 Conclusions .....	80
<b>5. 2D Finite Element Analysis damage assessment .....</b>	<b>84</b>
5.1 Methodology .....	85
5.2 Finite Element models.....	86
5.2.1 Geometry, discretization & loads .....	86
5.2.2 Analysis and problem limitations .....	87
5.2.3 Model 1: Analysis through the Total Strain based Rotating Crack-Model (TSCM) .....	88
5.2.4 Model 2: Analysis through The Engineering masonry model (EMM).....	88
5.3 Model 1: TSCM results.....	91
5.3.1 Model precision: Damage severity and similarity .....	91
5.3.2 Convergence and mesh sensitivity .....	91
5.4 Model 2: EMM results .....	94
5.4.1 Model precision: Damage severity and similarity .....	94
5.4.2 Convergence and mesh sensitivity .....	95
5.5 Conclusions .....	97
5.5.1 Key Factor 1: Evaluating the influence of the lintels by Comparing Inner Leaf and Outer Leaf Models .....	97
5.5.2 Key Factor 2: Model's mesh objectivity.....	98
5.5.3 Key Factor 3: The influence and behaviour of the constitutive laws.....	98
<b>6. Material parameter identification for light settlement-induced masonry damage .....</b>	<b>102</b>
6.1 Introduction .....	103
6.2 Optimisation problem formulation .....	104
6.2.1 Choosing target features and optimisation parameters for continuum crack models.....	104
6.3 Optimisation algorithm .....	107
6.3.1 Hyperparameter selection for a continuum crack model .....	108
6.3.2 Limitations .....	109
6.3.3 Implementing the automatic calibration procedure.....	110
6.4 Material parameter identification results.....	111
6.4.1 Damage assessment results .....	111
6.4.2 Discussion on the optimisation Procedure .....	112

6.5 Observations about the material model behaviour .....	116
6.5.1 General Observations.....	116
6.5.2 Total Strain based crack model observations .....	117
6.5.3 Engineering Masonry Model observations .....	118
6.6 Conclusions .....	120
<b>7. Conclusions .....</b>	<b>121</b>
7.1 Research contributions .....	122
7.2 Returning to the research questions .....	122
7.3 Recommendations for future research .....	125
<b>Appendix 1: FE Model parameters and results .....</b>	<b>127</b>
Appendix 1.1: Calculation of building element contributions .....	128
Appendix 1.2: Determination of the material parameters through Jafari, 2021 .....	131
Appendix 1.3: Total Strain based Crack Model (TSCM) analysis results .....	133
Appendix 1.4: Engineering Masonry Model (EMM) analysis results .....	146
Appendix 1.5: Influence on results by using different damage assessment indicators....	161
Appendix 1.5.1: Max-Mean influence on the Damage parameter $\Psi$ .....	162
Appendix 1.6: TSCM and EMM GP at the mean material properties .....	163
<b>Appendix 2: Model analysis algorithms.....</b>	<b>166</b>
Appendix 2.1: Crack detection algorithm .....	167
Appendix 2.2: Initial benchmarking of the parameter identification algorithm .....	169
Appendix 2.3: Parameter identification results .....	169
<b>Bibliography.....</b>	<b>176</b>

# Table of Figures

Figure 1: Research methodology .....	17
Figure 2: Global impact extent of land subsidence in worldwide investigated sites (Dinar, et al., 2021).....	19
Figure 3: Schematic overview of Holocene processes in the coastal deltaic plain (Koster, et al., 2018). .....	20
Figure 4: Overview of typical causes of structural damage in masonry in the Netherlands (de Vent, 2011)..	21
Figure 5: Use of Gaussian function to predict surface settlements (Marto, et al., 2015) and the mechanical response of sagging and hogging settlements (Ritter, et al., 2020).....	22
Figure 6: Most encountered displacement profile shapes in a Dutch buildings measurement survey (Prosperi, et al., 2023).....	22
Figure 7: Material response curves for masonry units under different stresses (Lourenço, 1996). .....	24
Figure 8: Factors influencing the response of the unit-mortar interface (Lourenço, 1996). .....	25
Figure 9: Experimental characterization of masonry at different scales (D'Altri, et al., 2020).....	26
Figure 10: A simplified literature workflow for understanding the behaviour of buildings under soil subsidence (Ozer & Geurts, 2021). .....	28
Figure 11: Distortion and cracking caused by a hogging subsidence profile (Chancery group, s.f.). .....	28
Figure 12: Classification of masonry structure assessment methods. ....	34
Figure 13: LTSM approach scheme (Netzel, 2003). .....	37
Figure 14: Different recommended E/G ratios for the LTSM.....	38
Figure 15: LPM on one ended settlement in a (State 1), b-c-d (State 2) (Palmisano & Elia, 2015).....	39
Figure 16: Block-based modelling strategies (Asteris, et al., 2015; DIANA FEA BV, 2024) .....	42
Figure 17: Continuum homogeneous modelling strategies (Asteris, et al., 2015; DIANA FEA BV, 2024) .....	43
Figure 18: Numerical modelling strategies for masonry structures an adaptation of D'Altri, et al., 2020.....	44
Figure 19: Failure mechanisms considered by the engineering masonry model, and estimation of crack angle (Lisanne, 2019).....	45
Figure 20: Subsoil modelling approaches for settlement-induced building damage. Coupled (Left), uncoupled (centre) and semi-coupled (right) (Giardina, 2013). .....	46
Figure 21: Sensitivity analysis on settlement experiencing FE Models (Prosperi, et al., 2023; Giardina, 2013). .....	47
Figure 22: RMSE for the calibration procedure through both surrogates (Ramancha, et al., 2022).....	49
Figure 23: Basic pseudo-code for the Bayesian optimisation procedure (Frazier, 2018). .....	50
Figure 24: Objective function evaluation on the severely non-convex Ackley benchmark problem (Ament, et al., 2023).....	53
Figure 25: Illustration of worsening discrepancies of traditional vs pseudo-random search techniques in low sample spaces (Baird, 2024).....	53
Figure 26: Adaptation sketch of the case study building .....	57
Figure 27: Archive architectural drawing of case study building .....	58
Figure 28: Approximated lithology at building foundation level and Borehole sample lithological graph.....	59
Figure 29: Open data CPT exploration around 1km east of the building. ....	60
Figure 30: Building skew measurements and building settlement surface approximation.....	64



Figure 31: Representation of damage hypothesis categories (de Vent, 2011). .....	68
Figure 32: Soil subsidence profile approximation.....	77
Figure 33: Model and mesh schemes for Wall 2 Outer-Inner.....	87
Figure 34: Observation of failures in the middle portion of the crack pattern in Wall 2 .....	89
Figure 35: Crack patterns at load factors where $\Psi_{\text{Analysis}} = \Psi_{\text{Model}}$ .....	92
Figure 36: Convergence behaviour of W2O – EMS .....	95
Figure 37: Best FEA results: Their crack patterns, damage parameters and percentage difference. ....	97
Figure 38: Damage parameter lowest value and values as a function of model iterations .....	111
Figure 39: Comparison of surrogate limitations, unable to capture true global minima (left) EMM (right). ...	112
Figure 40: Truss mechanical simplification.....	128
Figure 41: Scheme for estimation of first-floor supports.....	129
Figure 42: Approximated Wall 2's dimensions .....	130
Figure 43: TSCM 200mm mesh results final crack pattern .....	167
Figure 44: Processed Data frame for W2O - TS - 200mm .....	167
Figure 45: Identified integration point clusters for load step 750 of W2O – TS – 200mm.....	168
Figure 46: Best regret against number of objective function evaluations of different solvers against the Branin benchmark problem.....	169

## Table of Tables

TABLE 1: Classification of causes of building damage (Ozer & Geurts, 2021). .....	21
TABLE 2: Dutch masonry compressive material properties (Jafari, et al., 2017).....	27
TABLE 3: Dutch masonry bending material properties (Jafari, et al., 2017). .....	27
TABLE 4: Dutch masonry shear material parameters (Jafari, et al., 2017).....	27
TABLE 5: Recommended mean input parameters for masonry structures (Jafari, 2021) .....	27
TABLE 6: Comparison between parameters obtained by Jafari, 2021 and those from NEN-NPR 9998 .....	27
TABLE 7: Deformations and cracking from principal deformation shapes (de Vent, 2011). .....	29
TABLE 8: Masonry damage expressions to different processes (Korswagen, et al., 2017). .....	30
TABLE 9: Definition of settlement deformation mechanisms (Burland & Wroth, 1974). .....	30
TABLE 10: Damage classification criteria according to (CEN, 2022). .....	32
TABLE 11: Compiled Strain and SRI thresholds for different damage levels (Ozer & Geurts, 2021).....	36
TABLE 12: Building damage parameter $\Psi$ assessment as per Korswagen, et al., 2019. ....	61
TABLE 13: Schematic damage review of the case study building. ....	63
TABLE 14: Building rotational deformations.....	65
TABLE 15: Foundation assessment report confidence assessment.....	66
TABLE 16: Damage classification assessment and hypothesised rationale according to de Vent 2011. ....	70
TABLE 17: Building Rotation thresholds calibrated based on the damage levels of the different walls of the case study building.....	72

TABLE 18: SRI parameters for the case study building .....	73
TABLE 19: Building damage assessment according to a set of compiled empirical thresholds. ....	74
TABLE 20: Wall characteristics and E/G ratio estimations.....	75
TABLE 21: Obtained Gaussian parameters for different walls.....	76
TABLE 22: All approximated strain values according to the LTSM through approach 1 .....	77
TABLE 23: LTSM strain values according to approach 1.....	78
TABLE 24: Identified regions for the displacement profile .....	78
TABLE 25: Schematic breakdown of the LTSM results through direct application of skew measurements... ..	79
TABLE 26: All approximated strain values according to the LTSM through approach 2. ....	80
TABLE 27: LTSM strain values for approach 2 .....	82
TABLE 28: Parameters for fitted Gaussian shapes per wall .....	82
TABLE 29: Breakdown of the LTSM results through the reconstruction of greenfield profile .....	83
TABLE 30: Model evaluation criteria and studied model features. ....	85
TABLE 31: W2 – TS Model parameters breakdown. ....	90
TABLE 32: W2 – HJ, S model parameters breakdown. ....	90
TABLE 33: First principal crack width at last load step for all Total Strain based Crack Model models. ....	93
TABLE 34: First principal crack width at last load step for all Engineering Masonry Models models. ....	96
TABLE 35: Analysis benchmark scores for the different models. ....	100
TABLE 36: Cross-Model Evaluation of Damage Evolution, Crack Width Progression, Displacement, Numerical Stability, and Mesh Influence (200mm Models).....	101
TABLE 37: Breakdown of the Finite Element Model’s material parameters and optimisation bounds. ....	106
TABLE 38: Algorithm components and hyperparameters. ....	109
TABLE 39: Results comparison between identified against mean material parameters analysis results.....	113
TABLE 40: $\Psi$ Mean and variance for the TSCM at region close to the best solution. ....	114
TABLE 41: $\Psi$ Mean and variance for the EMM at region close to the best solution. ....	115
TABLE 42: Benchmarking of calibration gains and feature importance scores. ....	116
TABLE 43: Parameter covariance as understood by the GP’s Matern kernel for the calibration of the EMM and the TSCM .....	119
TABLE 44: Reference material parameters from Jafari, 2021 based on case study specifications .....	131
TABLE 45: Masonry shear material properties from tests on cores and triplets (Jafari, et al., 2022).....	131
TABLE 46: Analysis results for W2O – TSCM – 0.2m .....	135
TABLE 47: Analysis results for W2O – TSCM – 0.1m .....	137
TABLE 48: Analysis results for W2O – TSCM – 0.05m .....	139
TABLE 49: Analysis results for W2I – TSCM – 0.2m .....	141
TABLE 50: Analysis results for W2I – TSCM – 0.1m .....	143
TABLE 51: Analysis results for W2I TSCM - 0.05m .....	145
TABLE 52: Analysis results for W20 - EMHJ.....	148

TABLE 53: Analysis results for W2O – EMMS – 0.2m.....	150
TABLE 54: Analysis results for W2O – EMMS – 0.1m.....	152
TABLE 55: Analysis results for W2O – EMMS – 0.05m.....	154
TABLE 56: Analysis results for W2I – EMMS – 0.2m.....	156
TABLE 57: Analysis results for W2I – EMMS – 0.1m.....	158
TABLE 58: Analysis results for W2I – EMMS – 0.05m.....	160
TABLE 59: Analysis benchmark scores according to different damage assessment indicators.....	161
TABLE 60: $\Psi$ Mean and variance for the TSCM results at mean material parameters. ....	164
TABLE 61: $\Psi$ Mean and variance for the EMM results at the mean model parameters. ....	165
TABLE 62: Crack detection algorithm results for TSCM models.....	170
TABLE 63: Crack detection algorithm results for EMM models. ....	171

## Table of Extracts

EXTRACT 1: Rationale for the research. ....	13
EXTRACT 2: Thesis research aim .....	14
EXTRACT 3: Thesis research question.....	15
EXTRACT 4: Research scope.....	15
EXTRACT 5: Research Methodology.....	16
EXTRACT 6: Script to fit the subsidence measurements to Gaussian shapes.....	76
EXTRACT 7: Proposed Finite Element model BOPT calibration approach. ....	107
EXTRACT 8: Tabulated analysis main function “analyse_tabulated” .....	172
EXTRACT 9: Crack detection main “analyse_cracks”.....	173
EXTRACT 10: Principal crack component detection function “find_connected_components” .....	174
EXTRACT 11: Crack property processing function “calculate_crack_properties”.....	175

## Table of Equations

Equation 1: Damage parameter ( $\Psi$ ) formula and damage parameter categories (Korswagen, et al., 2019). 33	33
Equation 2: LTSM formulas by Burland and Wroth (1974) altered by Mair et al. (1996) (Korff, 2009). ....	37
Equation 3: Gaussian process formulation when employed for a regression task.....	50
Equation 4: Matern Kernel formulation and covariance matrix for a sinusoid function. ....	51
Equation 5: Exact Marginal Log Likelihood. ....	51
Equation 6: Log Expected Improvement (LEI) Acquisition function and its analytical formulation.....	52
Equation 7: Calibration objective function. ....	104
Equation 8: Huber Loss function under different Delta parameters .....	106
Equation 9: PSI formulation difference use in the benchmarking of models.....	162

# 1. Introduction

---

This section provides the context and outlines the scope, objectives, and methodology of the research. It establishes the relevance of subsidence-induced damage assessment of masonry structures and its broader significance.

## 1.1 Background and motivation

26% of the Netherlands's surface lies below sea level (van Alphen, et al., 2022), a fact which has constituted a longstanding challenge for the country's environment. As a result, the country has historically been affected by subsurface changes, due to naturally occurring and human-induced land subsidence. Subsidence, the change in land elevation relative to sea level (Kooi, et al., 1998; van Gils, et al., 2020), distorts not only the ground but also the structures resting on it. When these distortions are severe surface structures can be damaged when their structural equilibrium changes and deformations occur. This is particularly problematic in the Netherlands where construction has traditionally relied on masonry, a brittle and inflexible material, characteristically making masonry structures a focus of subsidence-induced building damage.

According to KCAF, one in eight homes—about 1 million—will experience foundation problems within the next 20 years. Ground subsidence has been identified as the primary cause of these foundation issues (Kok, et al., 2020; KCAF, 2022), which leads to various forms of building damage in distortions and cracking. The associated repair and maintenance costs were projected to reach €60 billion as of 2020 (KCAF, 2022). In response, research focussed on improving the structural analysis capabilities can improve damage prediction and allow for better engineering of countermeasures and mitigation strategies that reduce the effects caused by subsidence issues.

---

### *EXTRACT 1: Rationale for the research.*

Subsidence is a constantly ongoing process in the Netherlands, which occurs due to a combination of long-term differential subsidence or human-induced short-term settlements. Such processes, specifically urban settings, are common around the Netherlands' western coastal deltaic plain where the low bearing capacity of the underlying soil is greatest. This region is characterized by the presence of soft soils primarily, peats, organic materials, and clays. Soft soil layers often lie in the shallow subsurface (i.e., 20-30 meters), and are most prone to the shallow subsidence mechanisms of shrinkage, compression, and oxidation (Southamer, et al., 2020; Koster, et al., 2018). Yet, usually, the main driving factor behind subsidence processes has mainly been changing surface loading conditions, mining activities, changes to the water table and drainage history.

The best-documented instances of these processes have been in Groningen where subsidence is debated to occur as a combination of deep and shallow subsidence-related phenomena due to human-driven mechanisms in mining or gas extraction (Muntendam-Bos, et al., 2015), other relevant instances of subsidence processes occur across the heavily urbanised regions of Amsterdam, Rotterdam and Utrecht where intense phreatic groundwater lowering and surface human activity has accelerated the severity and speed of surface deformations (Koster, et al., 2018). Therefore, tackling ongoing subsidence-related issues has become a priority for the Dutch public from which many technical challenges remain, of which this piece's focus will be centred on the capabilities of structural vulnerability assessment to masonry buildings.

Masonry has been a ubiquitous construction material in the Netherlands since the 15th century, the combination of the materials' ease of construction and its durability makes it a suitable material for the Dutch climate. Widespread subsidence issues therefore can have widespread implications for masonry constructions in the Netherlands. Destructive actions in soil settlements in the best of cases cause

cracking or distortions, which affect a building's weather tightness, insulation ability and, architectural aesthetic (Masia, et al., 2004). Whilst in the worst of cases can lead to the possibility of partial or total collapse (Erturk Atmaca, et al., 2023; de Vent, 2011).

Currently, it is possible to estimate the amount and location of damage through a range of analytical, empirical and numerical possibilities, out of which the most capable is Non-Linear Finite Element Analysis (NLFEA), which has been shown to most closely resemble observed and experimental data (Tzamtzis & Asteris, 2003). Despite the accuracy provided by NLFEA its implementation and use can be a time-consuming and technically challenging feat therefore, other alternatives such as analytical or empirical formulations, in their most basic form, have the greatest potential for implementation and facilitate informed decision-making when studying the vulnerability of masonry structures or a preliminary step to full-fledged NLFEA.

Yet it is often the case that the simpler a method the more numerous its assumptions and the stronger its limitations as the simplification involved in semi-empirical evaluations strongly reduces the vast number of factors at play to the overall behaviour (Tzamtzis & Asteris, 2003). The opposite is also true in the case of Finite Element Analysis (FEA), which requires the definition of a large number of parameters for analyses to be made. This characteristic of FEA introduces uncertainty in its results, as the influencing factors are numerous and often interact in complex ways. Therefore, for both analysis forms, it is essential for engineers and researchers to thoroughly understand how different assessment methods behave under various conditions and how different parameters impact these assessments. The ultimate goal is to achieve the most accurate and reliable analysis possibilities for the assessment of masonry structures.

## 1.2 Research aim and research questions

The main objective of this thesis is to perform, validate and investigate popular as well as potentially suitable assessment methods. Thus, the main content of this thesis will consist of a varied mix of assessments which can allow the evaluation of masonry structures under most instances including cases of limited and asymmetric information. Therefore, this project's aim can be stated as follows:

To conduct and validate structural analyses of masonry buildings affected by ground settlements and evaluate the accuracy of various techniques and the influence parameters have on the assessments.

---

### *EXTRACT 2: Thesis research aim*

The work won't just limit itself to conducting and validating the assessments but it also aims to provide a comprehensive review and documentation of the knowledge required to perform such assessments, identify the key limitations and characteristics of various analysis methods, and explain the rationale behind each procedure. This will offer engineers and researchers clear, practical evidence of how assessments were carried out for a typical case study of a residential masonry home. Additionally, the thesis addresses how to mitigate the challenges posed by limited data from foundation investigations taken measurements while still achieving relatively accurate assessments. To support this, tools and algorithms will be developed to support the execution of these procedures and facilitate the analysis of results. Ultimately, this work believes that having achieved the above it will be able to answer the following research questions:

**RQ 1.** To what extent can current solution methods based on state-of-the-art approaches predict a masonry building's state when undergoing a subsidence process?

Given that, an approach has a level of success:

**RQ 2.** What are its characteristics and limitations when predicting the mechanical response of the structure? And under what circumstances should it be adopted?

**RQ 3.** What is the influence different parameters have on the assessment?

**RQ 4.** What improvements might be necessary to improve its precision and robustness?

*EXTRACT 3: Thesis research question*

## 1.3 Research scope

The possibilities for masonry structural analysis can vary drastically under different settlement types and drivers. Furthermore, building superstructure and substructure characteristics can have a profound impact on the necessary building components influencing the response and therefore, necessary to be modelled under an assessment approach modelling approach and scheme. The available information to determine the severity and characteristics of the subsidence. Therefore, this thesis will limit itself to:

- The scope of this research encompasses the evaluation of damage to Masonry buildings under shallow subsidence effects and clay masonry structures.
- This thesis mostly tackles masonry damage which does not pose a collapse risk. These damage states can be classified as “light damage” or early “Structural Damage”.
- Due to the characteristics of the available data from the foundation assessment study, the assessments will focus on reproducing the building's superstructure behaviour.
- Since only a single case study is available, the evaluations will pertain specifically to detached unreinforced red brick masonry structures.

*EXTRACT 4: Research scope*

## 1.4 Methodology

Aiming to present and investigate the possible ways to analyse a subsidence experiencing masonry structure several assessment methods were carried out. Nevertheless, these required benchmarking against in this instance a real-world case study. To allow for the evaluation of the assessment methods benchmarking through an accepted damage quantification measure was necessary and thus this allowed the possible forms and instances under which analysis can be made. For this purpose, this work's methodology took the following form:

1. A Literature review, based on investigating the mechanisms and characteristics of Subsidence

processes followed by the known superstructure responses to such effects and lastly, the possible ways in which building response to such effects can be approximated.

2. A case study review, to determine the key relevant structural characteristics of the building. An analysis of the documented damage forms, followed by a quantification of the damage state, damage forms and their location. Lastly, an evaluation to assess the confidence of various components of the evidence presented in the foundation assessment report.
3. The assessment of the case-study building through Visual, Empirical, Analytical and Numerical analyses by initially documenting the procedure as well as the assumptions and known limitations of the approach.
4. Followed by an evaluation of how well the results represent the case study building's damage state. Finished by a further discussion on the characteristics identified to influence the performed assessment as well if necessary the potential additions which could lead to improvements in the accuracy and robustness of results.

---

### *EXTRACT 5: Research Methodology*

The research methodology is depicted in the flowchart shown in Figure 1. The final thesis structure will closely resemble this methodology. Chapters 2 and 3 provide a comprehensive introduction and review of the necessary literature, establishing the theoretical basis for the research. Chapter 3 presents the implementation and analysis of assessments using Empirical Analytical methods. Chapter 4 focuses on the numerical evaluation of the building, along with an analysis of the characteristics and performance of the numerical models. Chapter 5 presents a material parameter identification procedure designed to enhance the accuracy of results and address uncertainties in masonry numerical analyses. Finally, Chapter 6 outlines the key conclusions, future research recommendations, and contributions of this study.



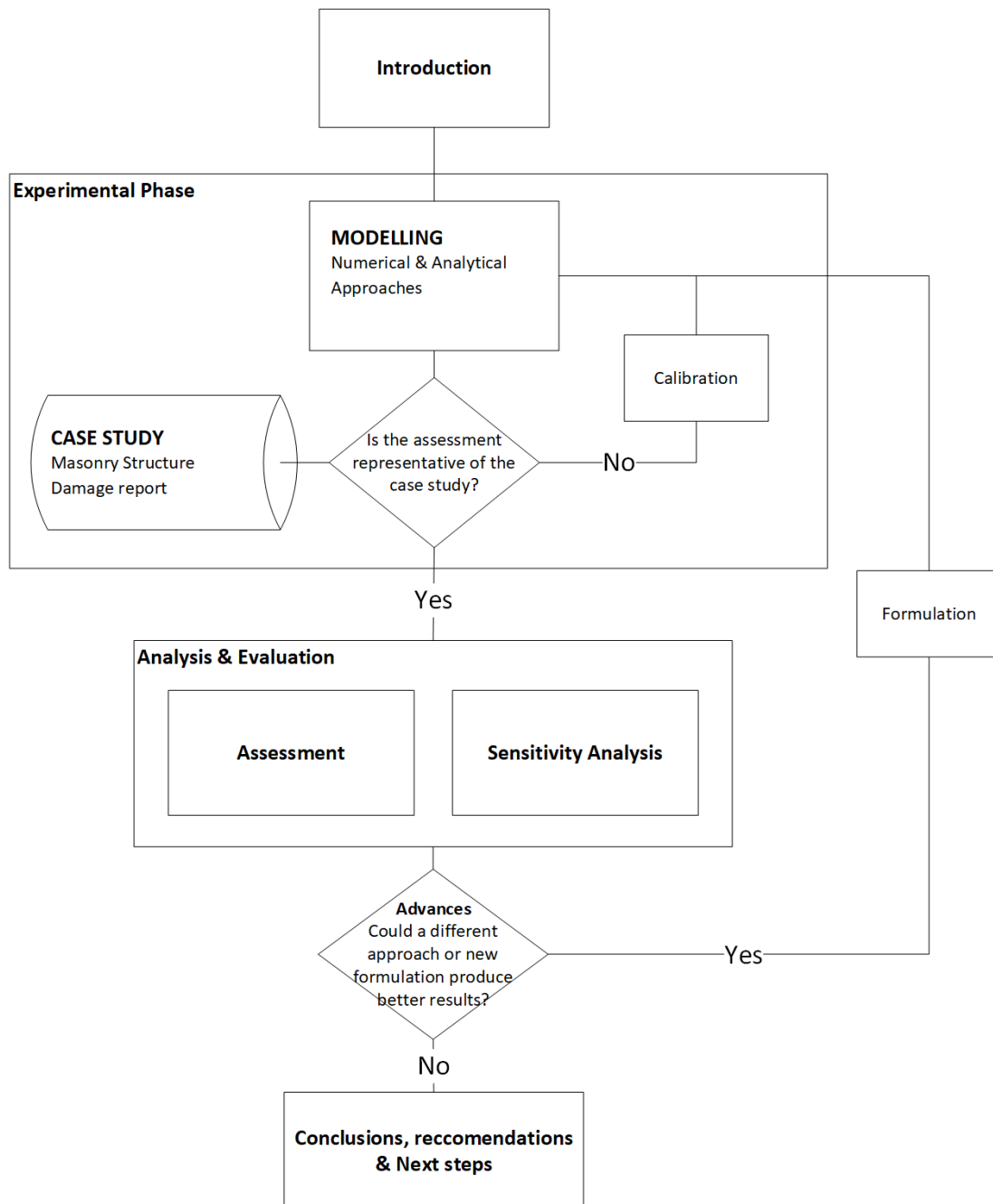


Figure 1: Research methodology

## 2. Literature review

---

This review provides a comprehensive background on subsidence processes, the behaviour of masonry, the response of masonry buildings to settlements, and an evaluation of existing assessment procedures for masonry structures affected by subsidence.

## 2.1 Land subsidence

Bagheri-Gavkosh et al. (2021) define land subsidence as the gentle settling or rapid sinking of discrete ground surface segments. Berry (1992) identifies the primary causes of this phenomenon to be: heavy withdrawal of groundwater, geothermal fluids, oil, gas, coal and sulfur through mining; hydro-compaction of sediments; oxidation-induced shrinkage of organic deposits; catastrophic sinkhole development; and other factors. These processes are categorized as either long-term differential subsidence (Kooi et al., 1998) or human-induced mechanisms (Koster, et al., 2018) based on their speed and severity.

Human-induced activities are the primary cause of severe subsidence in approximately 77% of cases globally, out of which groundwater extraction is the leading factor in 59% of these instances and commonly occurs in populated coastal deltaic areas (Bagheri-Gavkosh, et al., 2021). Both characteristics listed are shared with the Dutch coastal delta, which has become a renowned location for subsidence issues. Dinar et al. (2021) categorized the subsidence extent in this region with a worldwide relative subsidence extent index of 0.7, which indicates a region susceptible to aggravated subsidence.

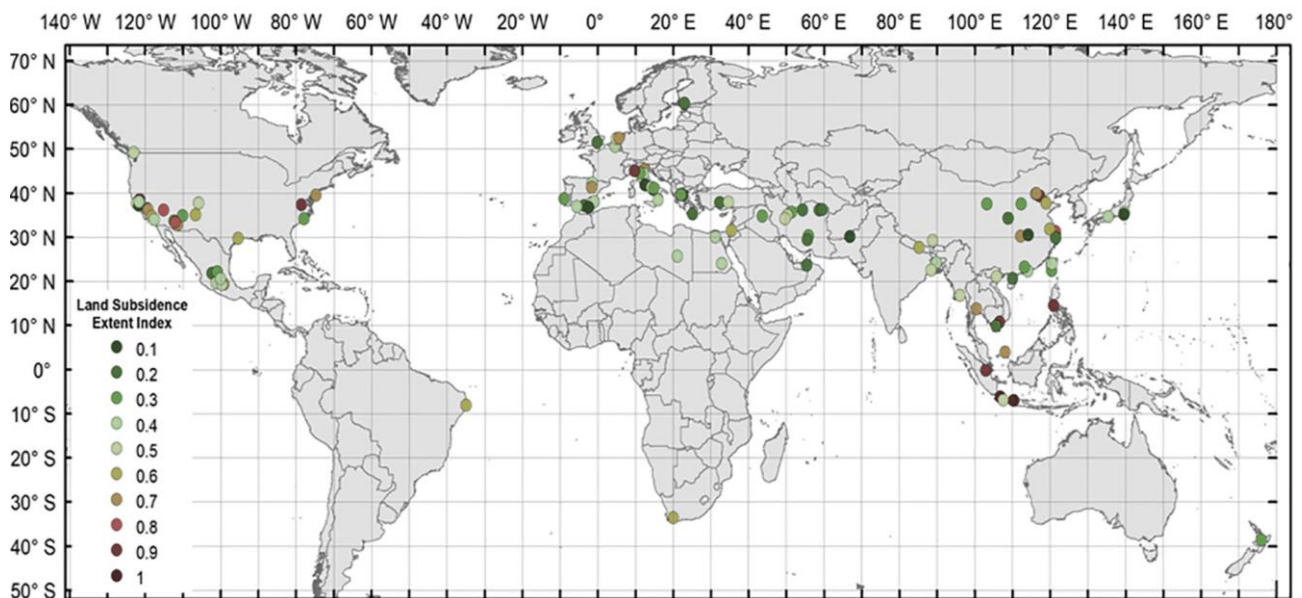


Figure 2: Global impact extent of land subsidence in worldwide investigated sites (Dinar, et al., 2021).

The central reason behind the prevalence of ground settlements in the Dutch mainland is the geological composition, van der Meulen, et al., 2007 estimated the likelihood of subsidence-susceptible soil layers being present in the Dutch coastal deltaic plain to be over 75%. Being mostly composed of peat layers, which are known to be susceptible to erosion and decomposition, large clay soil layers are known to fluctuate in size based on changing groundwater level tables. Consequently, It also produced a model accounting for both spatial variability and variability in depth of the soil compositions and his findings show that the presence of these layers occurs most in the populated regions of the western-deltaic plain correlate and therefore these regions possess higher subsidence potentials.

Historically subsidence processes in the Netherlands occurred solely due to deep subsidence drivers mainly due to clastic sedimentation, in the last millennia subsidence shifted into a combination of processes of which shallow processes became most prominent particularly based on human-induced mechanisms. These mechanisms are known to create unpredictable ground deformation profiles that

## 2.1 Land subsidence

buildings find difficult to accommodate. Therefore, changes seen in the drivers behind subsidence processes over the last millennium are a matter of concern. Usually, deep subsidence processes produce more uniform ground distortions, whilst now more common shallow processes produce more irregular distortions. This is because increasingly varied subsurface compositions due to peat extraction, accelerated oxidation processes due to climate change as well as groundwater-level lowering affect the temporal saturation of soil layers and produce distortions at much shallower depths which increase the number of distortions transferred to the surface.

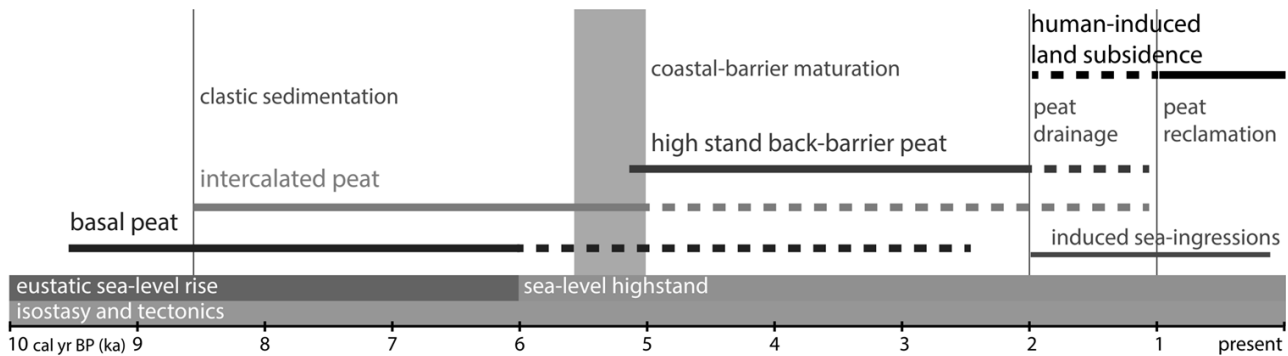


Figure 3: Schematic overview of Holocene processes in the coastal deltaic plain (Koster, et al., 2018).

Out of all soil-specific drivers, the most relevant is groundwater recession. In regions where groundwater recession takes place, the compaction of soil layers occurs due to the shift in stress from the soil's pore-water pressure into the soil itself as the water table level is reduced. Under this driver the settlements are known to be less pronounced and the influence region to be larger (Netzel, 2009). Further effects due to groundwater level lowering involve the changes to foundation capacities due to their deterioration. As the groundwater level increases, buildings on wooden foundations are more prone to fungal attacks due to increased oxidation. The deterioration of foundations can be so severe, that SBR, a set of engineering guidelines for the calculation of subsidence-induced damage, recommends that strain damage limits be restricted by 55-75% in cases where the deterioration of the foundation is severe (Netzel, 2009).

The increasing impact of human-induced subsidence adds further unpredictability to ground deformations. Usually, a combination of human-driven, geological, and structural factors collaborate to produce the final root cause for the subsidence problems across the Netherlands. A classification of all these drivers was made by Ozer & Geurts, 2021 which not only focuses on the soil behaviour but also the surface and building behaviour.

Root	Description	Cause
Influence of loads on the building	Insufficient resistance	Initial, Renovation, Aging
	Overload from use (static)	Normal use, Altered use, Renovation/extension
	Overload due to vibration	Road traffic / Rail traffic, Construction activities, Industrial activities, Earthquakes
Deformations	Specific reasons for overload	Impact of objects (e.g., collisions, falling objects), Explosion, Weather conditions (e.g., storm, wind, snow)
	Prevented deformations of the building construction	Initial, Renovation/extension, Aging / deterioration
Uneven subsidence of subsoil/foundation	Imposed deformations	Initial, Renovation/ extension, Metal corrosion, Trees & root growth
	Autonomous settlement	Constant loads (self-weight), Natural creep in heterogeneous soil
	Change in load	Renovation/extension/change in use, Nearby buildings Heightening, Excavation, and Construction of roads/railways

Root	Description	Cause
	Change in subsoil	Changes in groundwater (GW) level, Changes in GW level by work, activities (e.g., drainage of construction pits), Vibrations from the road/rail traffic (liquefaction of the soil), Vibrations from work activities
		Earthquakes, Changes in GW level through trees (e.g., extreme drought), Deep subsidence effects (elongation, bends, skews), Naturally extreme variations in GW level (e.g. extreme drought)

TABLE 1: Classification of causes of building damage (Ozer & Geurts, 2021).

De Vent (2011) also provides a classification with a more thorough breakdown of the most likely causes for damage in the Netherlands effects, these are partially depicted in Figure 4 but mainly correspond to damage caused due to Settlement and Overloading. Focussing only on settlement-induced damage it is stated that the mechanical response during settlement is affected by changes either to the loads, changing foundation behaviour or the soil capacity. Whose effects on the building behaviour are represented by observable and non-observable symptoms and damage forms.

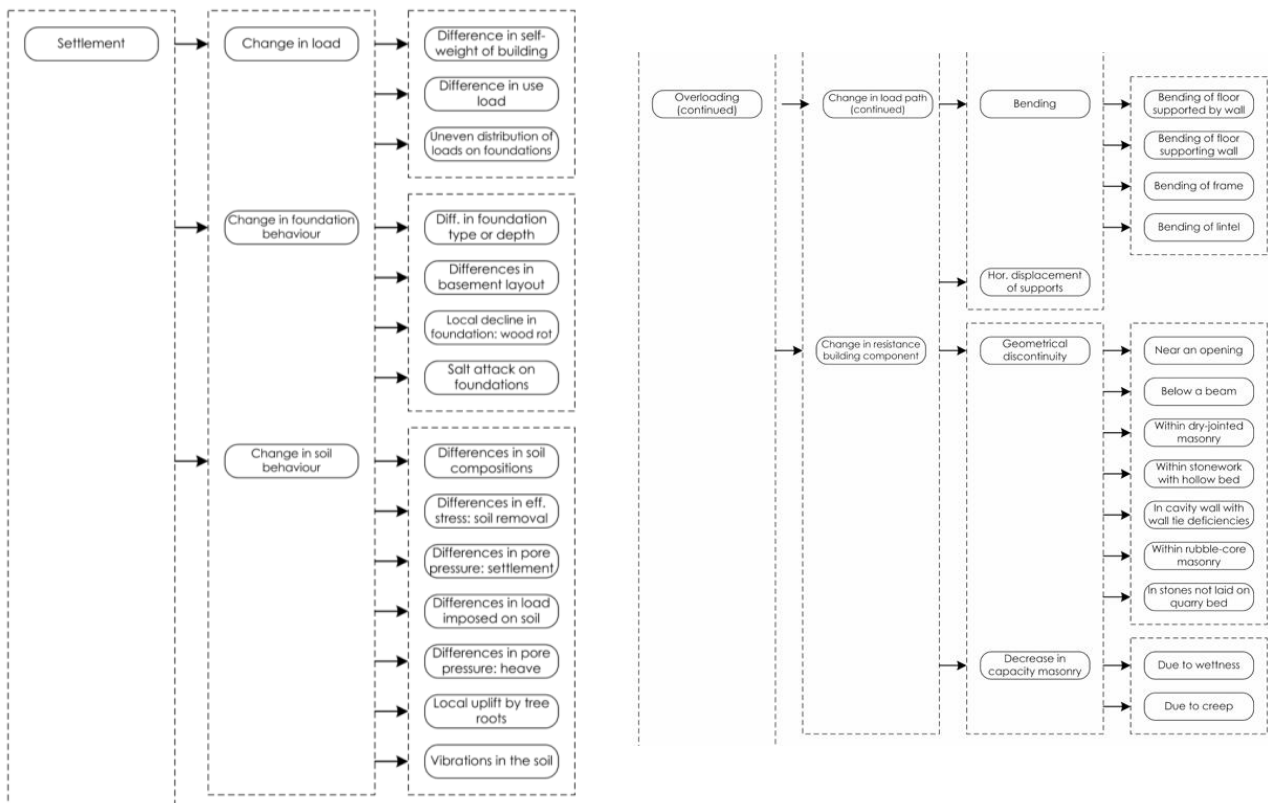


Figure 4: Overview of typical causes of structural damage in masonry in the Netherlands (de Vent, 2011).

Therefore, as can be seen, the settlements experienced by many buildings are determined by a wide combination of driving factors which work in different ways and tend to produce different deformations. Simulating the behaviour of all these is practically unfeasible and thus why recreating the soil behaviour in coupled assessments can prove such a challenge.

Nevertheless, some shared characteristics have been observed between specific subsidence drivers. In cases of settlements caused due to tunnelling and excavations, the ground deformations have been demonstrated to take a combination of sagging and hogging shapes (Rastbood, et al., 2006). Similarly, for specific subsidence drivers, such as the displacement profile produced beneath a foundation due to a loss of support can be described through a Gaussian probability function. Initially proposed by Peck, 1969,

## 2.1 Land subsidence

the Gaussian shape allows to measure the displacement at a specific location  $S(x)$  through the maximum settlement at the centreline  $S_{max}$ , and the distance from the symmetry axis to the point of inflection  $X_i$ , as shown in Figure 5.

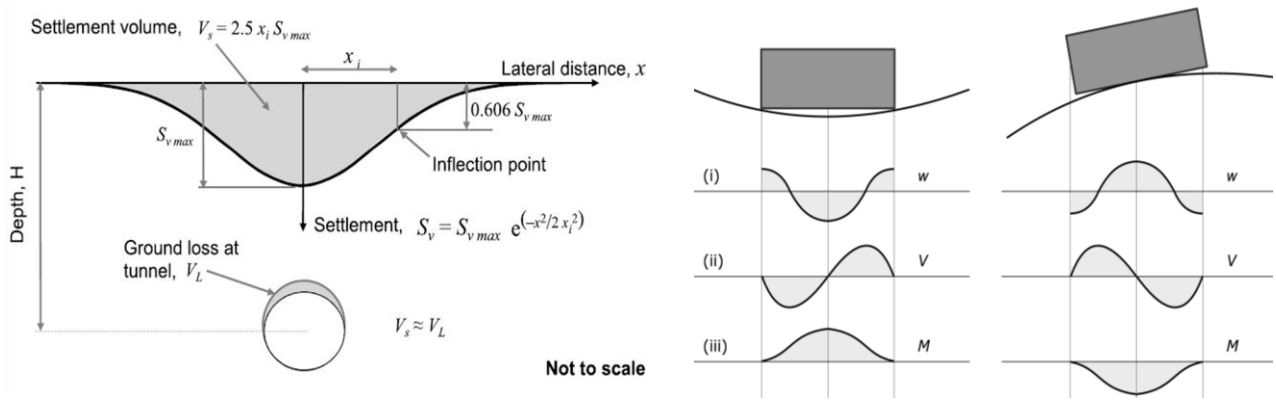


Figure 5: Use of Gaussian function to predict surface settlements (Marto, et al., 2015) and the mechanical response of sagging and hogging settlements (Ritter, et al., 2020).

Similar shapes have also been identified in urban subsidence settings. In Prosperi, et al., 2023 a Dutch subsidence survey performed on 615 building walls, reconstructed the displacement profiles for 499 of these walls. Although the displacement on the wall does not equate to the subsidence experienced by these walls they are nonetheless strongly correlated. These measured displacement fields were then split into regions with discrete shapes, which were later compared against each other. Then a database was built based on categorised displacement shapes of different buildings. The results showed a relatively even split between hogging and sagging subsidence profiles. In particular, two displacement profile shapes (Hog 2 and Sag 2) saw a greater likelihood than other shapes, these shapes corresponded to strong one-ended settlements at the point of maximum curvature. All other settlement types were in some way resembling different Gaussian shape combinations of different length scales and curvatures.

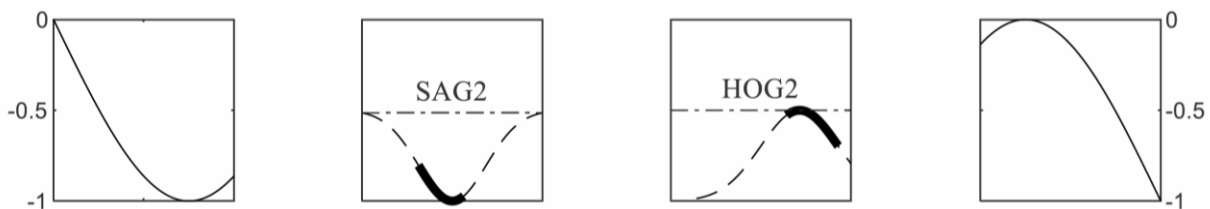


Figure 6: Most encountered displacement profile shapes in a Dutch buildings measurement survey (Prosperi, et al., 2023).

Nevertheless, the deformations a building experiences rarely match the actual subsidence acting on it. Typically, the geometrical and physical characteristics of the superstructure affect its response by reducing or altering the displacements. In many cases, the most significant factor is the spatial variation of the settlement profile and its position relative to the building. The building's location within this subsidence profile influences the curvature of the deformations, which affects both the initiation points of damage and the eventual severity of that damage. This is particularly true for unreinforced masonry buildings, where all components interact more heavily to shape the overall response. Since accounting for every component in an analysis is impractical, it is often sufficient for measurements taken at the bed to be as most likely as the final displacements experienced by the structure.

## 2.2 Masonry Structures

Masonry is one of the oldest building materials still widely used in modern construction (Lourenço, 1996; Fernandes, et al., 2009). The earliest evidence of its most common form, mud bricks, dates back to around 10,000 B.C. in ancient Egypt (Sidney, 1992). Masonry units have historically been made from materials such as clay, compressed earth, stone, or concrete. These units are typically assembled by hand, either with or without mortar, into stacks that eventually form stable structures. The stability of these structures mostly comes from the units working together in compression under their weight.

The enduring success of masonry is usually attributed to a few key characteristics: durability, fire resistance, soundproofing, and low maintenance requirements (Lourenço, 1996). However, its most fundamental qualities are the methods of easy manufacturing and simplicity. Brick units can be manufactured quickly, inexpensively, and using artisan methods, making it a highly accessible construction technique. Furthermore, the inherent simplicity of masonry allows for the construction of varied and sturdy structures without the need for heavy machinery.

As a result, masonry has been employed in numerous applications such as the construction of buildings, load-bearing walls, roads, and bridges. It has also been a historically popular material in the Netherlands as over 60% of residential facade material stock is composed of it (de Vos-Effting, et al., 2017), it is also popularly employed in Quay Walls and pavements, as is the case in most Dutch towns and cities. Despite so, the most popular use of masonry in the Netherlands is in buildings. These buildings especially in their more ancient forms tend to be 2-4 stories in height, out of which the facades and perimetral walls constitute the main load-bearing elements of the structure. These walls are usually either single wythe or cavity walls, which tend to have large openings and slender configurations.

### 2.2.1 Masonry's material properties

Masonry is an anisotropic material with different compressive and tensile strengths, and it also exhibits brittleness anisotropy, affecting its post-failure behaviour. The complexity of masonry structures is further compounded by the non-linearities arising from their composite construction. These non-linearities manifest as material-specific post-failure behaviours in individual units under compression and tension. During plastic strain, small energy releases occur at the unit-mortar interface, described by normal stress-dependent cohesive-frictional behaviour in shear and cohesive behaviour in tension. While the characterization of masonry materials is well-advanced, limitations remain in modelling the softening phase (Lourenço, 1996; Jafari, 2021). The accuracy of this characterization largely depends on the chosen modelling approach. Block-based models require more parameters to capture behaviour, while continuum models may overlook certain mechanisms but still yield valuable insights.

#### Unit material properties

Masonry units are usually clay/adobe bricks whose main properties are described through their Elastic modulus and Poisson ratio, these properties often can vary significantly due to the deterioration experienced by units when and the influence of lesser controlled manufacturing environments in older masonry manufacturing. The range of Young's modulus of clay masonry units can vary from 4-18 GPA, whilst its Poisson ratio can vary from 0.35-0.2 (Ghiassi, et al., 2019).

Softening is the name given to the material behaviour following the peak stress state where a gradual decrease of mechanical resistance occurs. A particular characteristic of this behaviour is the fracture energy i.e. the amount of energy absorbed by the material as it undergoes fracture, this characteristic corresponds to the area underneath the stress-strain graph following the peak response. Due to the anisotropic nature of masonry, this behaviour is different for vertical and horizontal loading a characteristic that also holds for the fracture energy.

#### Stress-strain curve in compression

#### Stress-strain curve in tension

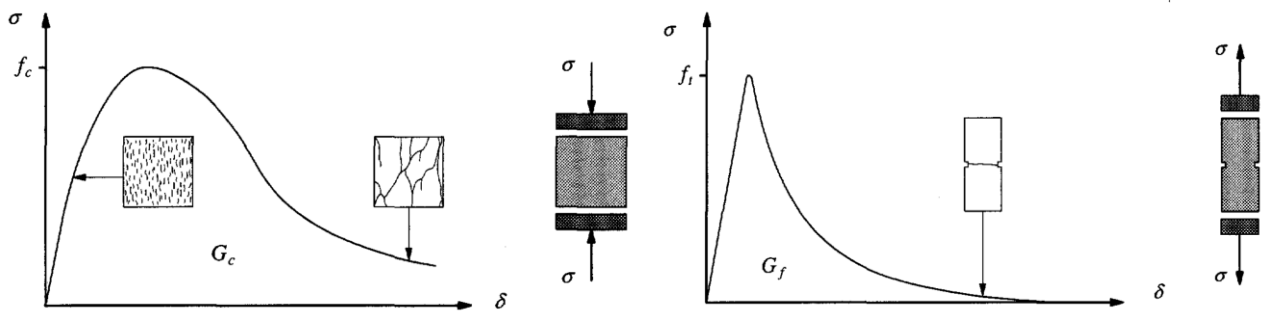


Figure 7: Material response curves for masonry units under different stresses (Lourenço, 1996).

### Mortar and brick-mortar interface material properties.

The quantification of mortar behaviour in uniaxial behaviour for compression and tension has been limited (Lourenço, 1996). Measuring the deformations on a surface that usually ranges from 2-5mm in thickness is practically unfeasible. Nevertheless, researchers such as Linag & Hong, 2011; Vindhyashree, et al., 2015 have presented relationships for the mortar in its compressive elastic range. The results from these tests follow the expected shape but further work is necessary to determine the non-linear behaviour of the material. Additionally, Jafari, 2021 also performed some bending and compression tests on general-purpose mortar the investigation showed that the flexural strength of mortar varied from 2.8-4.65 MPa whilst the compressive strength ranged from 3.8-16.1MPa.

By contrast, the characterisation of the post-peak behaviour of the brick-mortar interface has seen much more attention, since the interface constitutes the weakest link in the behaviour of masonry and is, therefore, the initiating factor before failure. This behaviour is captured through the Mode type fracture energy, which is the amount of energy necessary to create a unitary area of a crack along the unit-mortar interface. In Mode I the failure occurs in tension where the fracture energy ( $G_{f-I}$ ) can be captured by observing the area below the graph in the softening branch of the stress-strain relationship. There is a significant variance to this amount since the fracture energy is largely dependent on the net bond surface which is the effective mortar surface that remains following the shrinkage of the mortar following the placement of the masonry unit with what is assumed to be a uniform layer in the masonry units surface. In Mode II or shear failure mostly depends on the confining stress and the cohesion of the mortar the range of Mode II fracture energy ( $G_{f-II}$ ) can vary from 0.01 to 0.25 Nmm/mm<sup>2</sup>, the behaviour in this failure mode is largely governed by the dilatancy angle ( $\psi$ ) where initially the displacement occurs linearly normally and perpendicularly to the bed joint but eventually only shear displacement occurs.

Although the above shows a comprehensive quantification of parameters and mechanisms in brick-mortar behaviour by researchers, further research is still necessary to quantify effects in the behaviour of the tensile resistance in head joints between units. Further significant limitations exist in the



characterisation of the stress-strain relationship of the mortar behaviour.

### Tensile bond surface

In individual units

For a wall section

### Masonry behaviour in shear

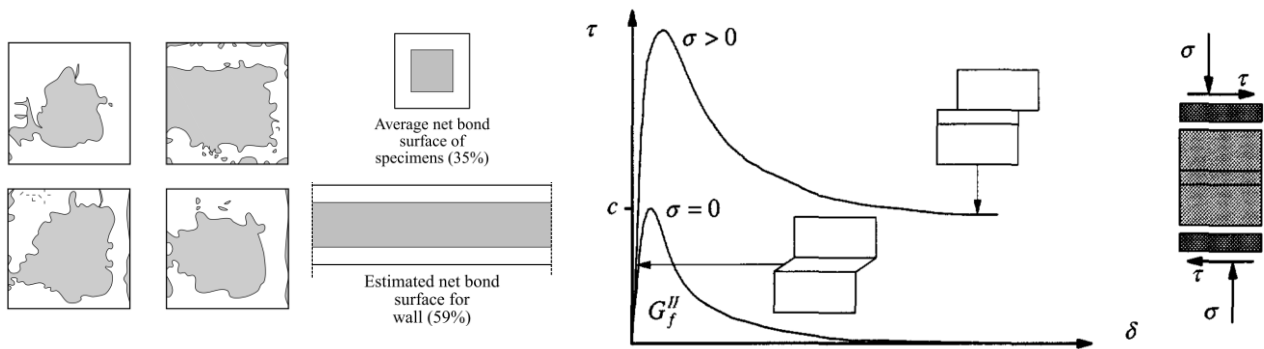


Figure 8: Factors influencing the response of the unit-mortar interface (Lourenço, 1996).

## Masonry as a composite material

When we describe masonry as a composite material, we refer to a formulation that includes both masonry units and mortar. The behaviour of these components under uniaxial compression perpendicular to the bed joints is crucial, as it aligns with the typical loading conditions of walls and piers. Under such loading, the mortar in the bed joint experiences triaxial compression, while the masonry units are subjected to compression and biaxial tension. In this state, both materials offer maximum resistance. However, in uniaxial compression parallel to the bed joints, the load-bearing capacity can be significantly reduced, ranging from 0.2 to 0.8 times the perpendicular compression capacity. In uniaxial tension parallel to the bed joints, the tensile resistance of the composite is assumed to be equivalent to the tensile bond strength, which is the weakest link. If weathering has degraded the resistance of the units or if the proportions of the bed joints and units are non-standard, the relative stiffness of both components will be affected. In such cases, the crack patterns tend to be straighter and do not necessarily follow the interfaces between units. Consequently, the stress-strain curve response becomes more irregular and brittle, with a longer plateau in the softening branch before reaching zero at higher strain levels. This response is governed by the fracture energy of the units and head joints.

### 2.2.2 Characterization of masonry's material properties

According to D'Altri, et al., 2020 to perform a reliable simulation of a masonry structure it is first necessary to characterize the material parameters through experimental tests and a detailed geometrical and structural survey. Depending on the target analysis approach characterization campaigns will take place at different scales take place, as seen in Figure 9.

When dealing with existing structures performing testing in in-situ is of utmost importance, since it is the only way to capture variabilities in the structure's material which may have stemmed from manufacturing or material time-dependent deterioration effects. This is nevertheless difficult since in-situ testing is usually most effective through invasive techniques of the original structure, and to be able to construct a well-rounded characterisation campaign multiple samples across a building will have to be extracted. In practice, this is not feasible thus, when dealing with historical buildings many efforts have been made to improve the characterisation capabilities of qualitative non-invasive techniques. (D'Altri, et al., 2020).

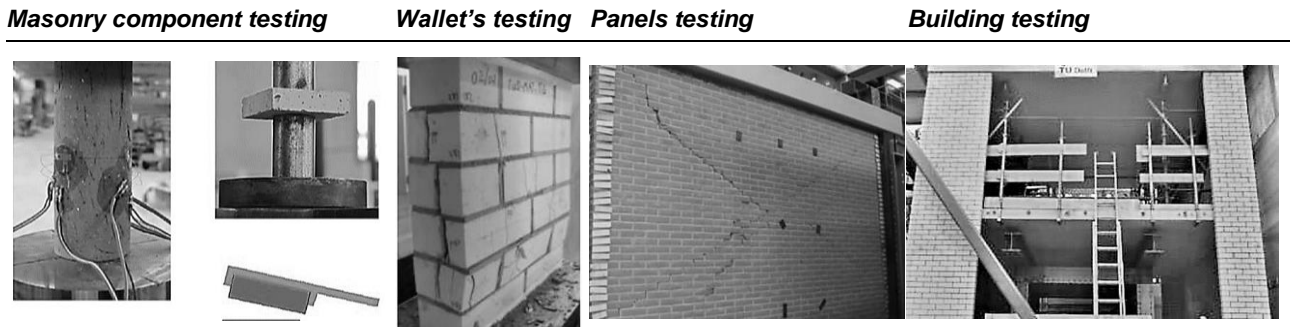


Figure 9: Experimental characterization of masonry at different scales (D'Altri, et al., 2020).

Fortunately, when dealing with urban masonry structures the uniqueness of material characteristics is much less common than in historical structures. This is why when dealing with urban structures, regions or Nationwide masonry material investigative campaigns may not just suffice but be of greater use since there no longer exist limitations on the maximum invasiveness undertaken throughout experimentation. Additionally, the greater number of available samples allows a better true characterisation of the true variance introduced to different effects, given that the investigative campaign has been able to produce testing in sufficiently different masonry material categories (i.e., masonry of different sources, sizes, age, climatological exposure etc.).

For this purpose, for Dutch-specific masonry, an investigation was carried out firstly by Jafari, et al., 2017 which characterised different categories of masonry materials and later by Jafari, et al., 2022 where the investigation performed identified and produced empirical relations between different material parameters to allow a coherent estimation of material properties under different modelling approaches given relatively few site-specific data. The materials were sourced from different regions around the Netherlands, but the samples were mostly from the northern Groningen region. The samples dated from 1910 to 2010, a period that correspond to a vast majority of existing household masonry constructions excluding the 19<sup>th</sup> century period. The values in brackets represent one standard deviation from the mean of the parameters, the typology of distribution was not provided.

Another major useful source relevant to the modelling of masonry is shown in TABLE 5 which presents a compilation of relations built by Jafari, et al., 2022 and compiled from other literature sources which allows to relate key material parameters such as the compressive strength or bond tensile resistance to other key material parameters under different modelling approaches. This allows for a much more accurate representation of the material behaviour with much lesser invasive testing.

Another popular source for masonry material parameters specific to the Netherlands has been NEN-NPR 9998:2005 this norm provides a range of non-linear material parameters for different non-linear analysis. Jafari compared the material characterisations and found that the resistance from NPR was on average 14% lower, with a maximum difference deviation of 64% in the case of the compressive fracture energy.

Masonry Type	Vertical Compressive		Horizontal Compressive		Orthogonality	
	Strength [MPa]	Young's Modulus [MPa]	Strength [MPa]	Young's Modulus [MPa]	Strength Ratio	Young's Modulus
Clay-solid < 1945	12.7 (0.15)	9347 (0.27)	10.9 (0.11)	8983 (0.26)	1.3	1.5
Clay-solid > 1945	17.7 (0.38)	9348 (0.35)	11.0 (0.23)	5470 (0.10)	1.9	2.3
Clay perforated > 1945	20.7 (0.13)	8688 (0.21)	-	-	-	-
Clay frogged > 1945	8.0 (0.05)	2575 (0.43)	-	-	-	-
Calcium silicate < 1985	12.4 (0.20)	8241 (0.21)	7.3 (0.05)	3918 (0.19)	1.7	2.1

TABLE 2: Dutch masonry compressive material properties (Jafari, et al., 2017).

Masonry Type	Bond Wrench Test ( $f_{x1}$ ) [MPa]	Horizontal Out-of-Plane Bending ( $f_{x2}$ ) [MPa]	In-Plane Bending Test ( $f_{x3}$ ) [MPa]
Clay-solid < 1945	0.33 (0.71)	0.83 (0.47)	0.61 (0.20)
Clay-solid > 1945	0.43 (0.38)	1.22 (0.09)	0.76 (0.28)
Clay-perforated > 1945	0.15 (0.20)	0.87 (0.09)	0.81 (0.43)
Clay-frogged > 1945	0.05 (0.92)	-	0.14 (0.30)
Calcium silicate < 1985	0.18 (0.33)	-	0.36 (0.59)

TABLE 3: Dutch masonry bending material properties (Jafari, et al., 2017).

Masonry Type	Initial Parameters		Residual Parameters	
	Initial Shear Strength ( $f_{v0}$ ) [MPa]	Initial Shear Strength ( $\mu$ )	Resl Shear Strength ( $f_{v, res}$ ) [MPa]	Residual Friction angle ( $\mu_{res}$ )
Clay-solid < 1945	0.30	0.80	0.06	0.71
Clay-solid > 1945	0.45	0.89	0.07	0.72
Clay-perforated > 1945	0.82	0.66	0.06	0.72
Clay-frogged > 1945	0.15	0.69	0.07	0.7
Calcium silicate < 1985	0.24	0.81	0.06	0.67

TABLE 4: Dutch masonry shear material parameters (Jafari, et al., 2017)

Property	Symbol	Unit	Clay brick masonry				CS masonry			
			Pre-1945		Post-1945		Brick masonry		Element Masonry	
			Tests	NPR	Tests	NPR	Tests	NPR	Tests	NPR
Vertical compressive strength of masonry	$f_m$	MPa	9.98	8.5	15.02	10	9.53	7.0	13.93	10.0
Horizontal compressive strength of masonry	$f_{m,b}$	MPa	10.86		11.00		6.17	7.0	9.42	10.0
Vertical Young's Modulus of masonry	$E_3$	MPa	5346	5000	7354	6000	6904	4000	8313	7500
Horizontal Young's Modulus of masonry	$E_{3,b}$	MPa	8933		5470		4177	4000	7701	7500
Vertical Compressive Fracture Energy	$G_{f-c}$	N/mm	11.93	20	20.58	15	17.42	15	20.92	20
Horizontal compressive fracture energy	$G_{f-c,b}$	N/mm	30.81		63.10		20.04	15	12.83	20
Vertical flexural strength	$f_{x1}$	MPa	-	0.15	0.43	0.3	0.13	0.15	0.58	0.60
Horizontal flexural strength	$f_{x2}$	MPa	0.62	0.55	1.23	0.85	0.59	0.55	0.73	1.00
Cohesions (initial bed joint shear strength)	$f_{v0}$	MPa	0.31	0.30	0.47	0.4	0.26	0.25	0.83	0.80
Friction coefficient in bed joint	$\mu$	-	0.73	0.75	0.76	0.75	0.77	0.60	1.48	0.80

TABLE 6: Comparison between parameters obtained by Jafari, 2021 and those from NEN-NPR 9998

Properties	Sym	Unit	Relation	Description
<b>Masonry properties</b>				
Vertical compressive strength	$z$	MPa		Direct tests or indirectly derived as recommended in Eurocode 6
Vertical Young's modulus	$E_m$	MPa	$E_m = (500 - 700)f'_m$	Masonry with conventional joint & Masonry with thin joint
Horizontal compressive strength	$f_{m,h}$	MPa	$f'_{m,h} = (0.70 - 0.80)f'_m$	
Horizontal Young's modulus	$E_{3,h}$	MPa	$E_{3,h} = 0.70E_3$	
Vertical flexural strength	$f_{x1}$	MPa	$f_{x1} = f_w$	
Horizontal Flexural Strength	$f_{x2}$	MPa	$f_{x2} = 3f_w$	
Tensile strength	$f_{t1}$	MPa	$f_{t1} = 0.8f'_w$	
Fracture energy in vertical compression	$G_{f-c}$	N/mm	$G_{f-c} = (0.88 - 5.3)f'_m$	Masonry with conventional joint
Fracture energy in horizontal compression.	$G_{f-c,h}$	N/mm	$G_{f-c,h} = G_{f-c}$	
<b>Mortar and brick properties</b> <span style="float: right;">**May range from to</span>				
Mortar compressive strength	$f_m$	MPa	$f_m = f_w/0.036$	
Mortar Young's modulus	$E_m$	MPa	$E_{3m} = (200 - 240)f_m$	
Mortar tensile strength	$f_{tm}$	MPa	$f_{tm} = (0.15 - 0.32)f_m$	
Mortar fracture energy in tension	$G_{f-tm}$	N/mm	$G_{f-tm} = 0.025(f_m/10)^{0.7}$	
Brick compressive strength	$f_b$	MPa	DIRECT TEST	
Brick Young's modulus	$E_b$	MPa	$E_{3b} = (300 - 430)f_b$	
Brick tensile strength	$f_{tb}$	MPa	$f_{tb} = (0.04 - 0.07)f_b$	
Brick fracture energy in tension	$G_{f-tb}$	N/mm	$G_{f-tb} = 10G_{f-l}$	
<b>Interface properties</b>				
Bond strength	$f_w$	MPa	DIRECT TEST	
Initial shear strength	$f_{v0}$	MPa	DIRECT TEST	
Initial Friction angle	$\mu$	DIM	DIRECT TEST	
Fracture energy in tension	$G_{f-l}$	N/mm	$G_{f-l} = 0.16f_{t1}$	
Fracture energy in shear	$G_{f-\Pi}$	N/mm	$G_{f-\Pi} = 10G_{f-l}$	

TABLE 5: Recommended mean input parameters for masonry structures (Jafari, 2021)

## 2.3 The response of masonry structures to settlements

Damage classification methods can differ depending on whether the goal is to evaluate or quantify damage. This section of the review first explores how damage is understood to develop and how masonry buildings behave under deformations. It then focuses on the methodologies used to assess damaged structures. The aim is to gain a clearer understanding of the mechanisms and behaviours that lead to both visible and hidden damage, as well as how damage progresses over time.

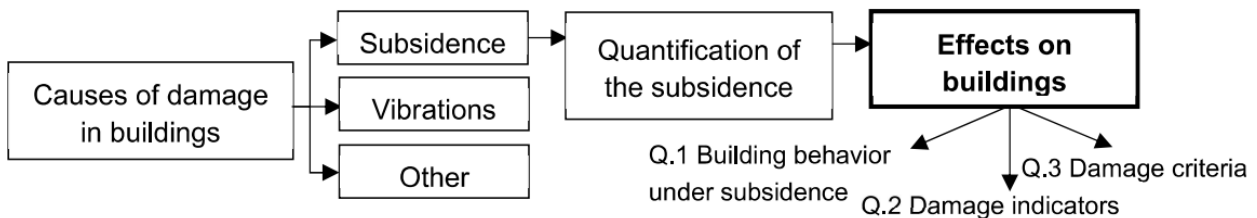


Figure 10: A simplified literature workflow for understanding the behaviour of buildings under soil subsidence (Ozer & Geurts, 2021).

### 2.3.1 Superstructural behaviour

A building's behaviour is dictated by the response of its structural system subject to the influence of its surroundings. Building deformations originate from the loss of equilibrium in one of its components such as has already been explored under changes in the foundation, nearby soil, amongst others. The effects these have on buildings are usually manifested in 3 forms: cracking, displacements, and tilts (de Vent, 2011).

Researchers have mostly focussed on correlating the above symptoms to the most relevant deformation measures. In instances where the superstructure (i.e. the section of the structure above the ground) deforms through a hogging curvature, cracks are expected to initiate at the top of the wall and propagate along the height of the wall, up to the point where a full mechanism is formed and the building begins to behave as two different units of reduced stiffness. This is similar to one ended settlement where this process takes place at the location of greatest curvature change. In sagging deformations, the process is inverse to hogging deformations yet the curvature results in the area experiencing tension to be that which tends to be stiffer, the foundation and ground floor.

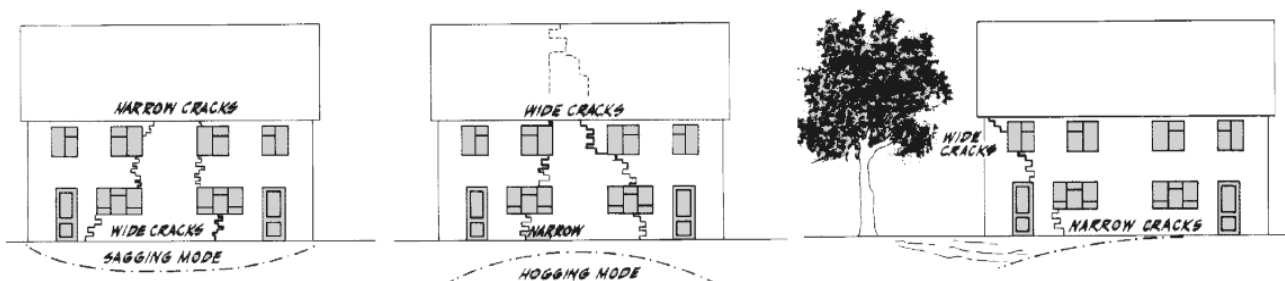


Figure 11: Distortion and cracking caused by a hogging subsidence profile (Chancery group, s.f.).

Differential settlements have been experimentally shown to demonstrate a more flexible behaviour and further accommodate the induced strains. In cases of uniform settlements, the damage is not expected to be significant as long as the subsidence is uniform along the building's entirety (Huijgen, et al., 2020),

under relative settlements (settlements happen under both major building axis) damage is much more likely especially when differential settlements take hogging rather than sagging shapes.

These effects were further studied by de Vent , 2011 who performed several Non-linear Finite Element Analyses (FEA) on a masonry beam to demonstrate the expected overall response of common settlements for masonry buildings underground settlements. The following table summarises the simulations performed to predict damage for a smeared masonry beam.

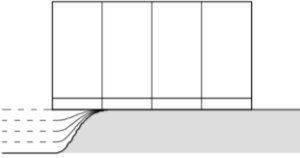

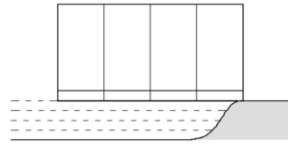
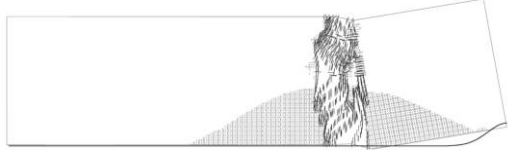
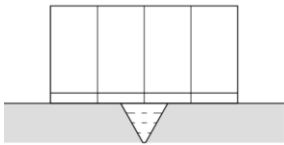
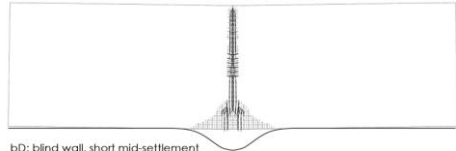
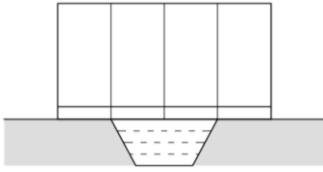
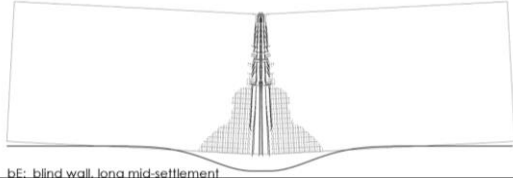
<b>Deformation Shape</b>	<b>Settlement shape</b>	<b>Numerical result</b>
Short end settlement		
Long end settlement		
Short mid settlement		 bD: blind wall, short mid-settlement
Long mid settlement		 bE: blind wall, long mid-settlement

TABLE 7: Deformations and cracking from principal deformation shapes (de Vent, 2011).

Nonetheless, cracking does not constitute the only damage form to masonry structures. Before the onset of cracking the best way to observe the effects on the superstructure is to assess its deformations. Deformations tend to follow the direction of the imposed loads yet in extreme when losses of stability happen, most commonly in masonry due to out-of-plane bending, such situations lead to unusually large deformations perpendicular to the load direction.

Lastly, the third most identifiable source of damage is tilt which refers to a segmental or full-body rotation of a building. Under this mechanism, further deformation occurs in the superstructure due to the thrust or stress redistributions in particular sections of a structure which can lead to different damage in adjacent utilities, such as sewage, and shared structural elements between bodies experiencing different deformations. Although the above includes the greatest amount of observable damage forms further damage expressions can also happen under different actions outside of settlements. A more detailed breakdown of the relation of certain processes and damage expression was made by Korswagen, et al., 2017 which accounts for weakening and spalling characteristics when masonry undergoes more micro failures.

### 2.3 The response of masonry structures to settlements

Process	Damage Expression			
	Cracking	Spalling	Blistering	Internal weakening
Overloading	✓			
Vibrations	✓	✓		
Earthquakes	✓	✓		
Wind loading	✓			
Settlements	✓			
Thermal variations	✓			
Freeze-thaw cycles	✓	✓		✓
Ageing		✓		✓

TABLE 8: Masonry damage expressions to different processes (Korswagen, et al., 2017).

In the end, the always present superstructural symptom of settlements is ground deformations. For quantification of this measure, a series of 9 main distortion measures relevant to 2D deformation profiles was devised by Burland & Wroth, 1974. Burland & Wroth, 1974 stated that these deformation measures were proposed to avoid the prior confusion in shared terminology to describe different soil deformations, These deformation parameters have become standard in characterising the deformations of the soil and are also known as Subsidence related intensity (SRI) parameters. Due to the irregularity in urban subsidence profiles these measures are useful when the characterisation of the shape, magnitude and location of regions wants to be made.

N°	Deformation Mechanism	Description	Image
1	Shortening	A change of length $\delta L$	
2	Settlement	Uniform displacement $\rho$	
3	Differential Relative Settlement	Delta settlement $\delta\rho$	
4	Rotation	Change of gradient of a straight line between two points, $^\circ$	
5	Tilt	Rigid Body Rotation	
6	Relative rotation	Rotation between the straight line of two points relative to the tilt	
7	Angular strain	Summation of rotation from two reference lines positive = sag, negative = hogging	
8	Relative deflection	Maximum displacement relative to the straight line connecting two reference points at a distance L.	
9	Deflection Ratio	Deflection over length	

TABLE 9: Definition of settlement deformation mechanisms (Burland & Wroth, 1974).

When assessing the condition of a structure, especially through visual inspection, it's important to recognize that not all deviations from the original building state are caused by subsidence. There are many instances where deformations and cracks are intentionally engineered to counteract other effects. For example, in the Netherlands, buildings are sometimes constructed with intentional tilts, known as "op vlucht gebouwd" (built on flight), to help with rainwater management. These inclinations are often mistaken for subsidence damage. Similarly, some buildings in the Netherlands were engineered with

counter-tilts to anticipate future soil deformations. Other common features that are sometimes misinterpreted as cracking damage include expansion joints in masonry buildings, which are designed to allow for thermal expansion by leaving space along certain sections of the structure. Recognizing these characteristics is crucial when conducting assessments. However, it's worth noting that these engineered features are exceptions rather than the norm.

### 2.3.2 Substructural behaviour

These above SRI deformation measures have been shown under specific scenarios to correlate well with masonry building damage. Nevertheless, this correlation is strongly dependent on the substructural building features that influence the foundation's capacity and behaviour. This is shown in Prosperi, et al., 2023 as the informativeness of different SRI parameters to building damage levels across different foundation types showed the correlations against damage states to be much more pronounced between buildings with shallow foundations, with weaker correlations being present amongst buildings with piled foundations.

Notably, for shallow foundation structures, the rotation and angular distortion appeared to have the strongest correlation with observed damage, although all SRI parameters demonstrated a degree of correlation with damage. This suggests that shallow foundation buildings are more sensitive to shallow deformations. In the study, strong correlations were found in shallow foundation buildings through rotation and angular distortion.

The vulnerability of shallow foundation buildings is a matter of concern for Dutch homes. Although few comprehensive publicly available surveys exist on building foundation typologies, shallow foundations remain a popular foundation type in Dutch homes, particularly in older structures. In studies such as Peduto et al. (2016) from a sample size of 706 buildings, 180 were found to rest on shallow foundations approximately 25%. In a different sample from Prosperi, Korswagen, Korff, Schipper, and Rots (2023), involving a sample of 386 buildings, 124 were identified to have shallow foundations. This highlights how a large amount of homes are at risk and also emphasizes the large role the substructural behaviour of the building has in predicting masonry damage.

Nevertheless, the foundation typology is a single characteristic within a foundation system researchers such as Burland & Wroth, 1974; Korff, 2009 also emphasise the importance of the soil structure interaction (SSI), in influencing damage estimates. SSI, tends to constitute a main limitation in many assessment methods as the frictional contact debonding and slipping between the building's foundation and the applied deformations by the soil is a highly time-dependent and difficult-to-simulate phenomenon in analytical and numerical models (Burland & Wroth, 1974). In numerical models, this behaviour is captured either through using rough, intermediate, or smooth interfaces, with the choice of aforementioned being based on the desired accuracy of the model. While accurately accounting for SSI generally leads to more precise results, lazy implementations can also introduce additional uncertainty into Finite Element Models.

Furthermore, some researchers have noted the necessity to include SSI only under specific circumstances. Similarly, Dhadse, Ramtekkar, and Bhatt (2020) argue that the foundation's response is more influenced by the behaviour of softer materials/components and that SSI behaviour is largely dictated by the relative stiffness of the foundation and soil.

### 2.3.3 Definition of damage & assessment indicators

Damage can be defined as the manifestation of a lack of performance in a structure (de Vent, 2011), it can also be classified due to its severity i.e., risk or likelihood to cause a loss of performance. In masonry structures, its most identifiable representation is cracking. In instances of subsidence phenomena cracks tend to concentrate around locations where maximum structural distortion occurs (Korff, 2009), with often the cracks features allowing to interpret the responsible mechanisms for the damage (de Vent, 2011; Korff, 2009). A crack's direction allows one to infer the direction of the principal stresses and the displacement along its length can hint as to the direction and magnitude of loading.

Cracking damage has been most popularly classified according to Burland J. B., 1977 Damage Levels. Damage Levels relate crack widths and the reparability of the damage, to a structural damage state. More updated classifications based on Burland, 1977 are also now adopted in CEN, 2022 engineering design norms which continue to classify cracking damage according to its crack width and reparability.

<b>DL</b>	<b>Damage Class</b>	<b>Tensile strain limit [%]</b>	<b>Description</b>	<b>Crack Width [mm]</b>	<b>Ease of repair</b>
0	Negligible	0-0.05	Hairline crack Damage is generally restricted to internal wall finishes.	<0.1	
1	Very Slight	0.05-0.075	Close inspection may reveal some cracks in external brickwork or masonry	<1	Fine cracks that are easily treated during normal redecoration
2	Slight	0.075-0.15	Cracks may be visible externally; doors and windows may stick slightly	2-3	Cracks easily filled. Re-decoration is probably required. Recurrent cracks can be masked by suitable linings. Some repointing may be required to ensure water-tightness
3	Moderate	0.15-0.3	Doors and windows sticking; service pipes may fracture; weather tightness often impaired.	Up to 5 locally	Cracks require some opening up and can be patched by a mason. Repointing of external brickwork and possibly a small amount of brickwork may be replaced.
4	Severe	>0.3	Windows and door frames distorted; floor sloping noticeably; walls leaning or bulging noticeably; some loss of bearing in beams; service pipes disrupted	5-15	Extensive repair work involving breaking out and replacing sections of walls, especially over doors and windows
5	Very Severe		Beams lose bearing; walls lean badly and require shoring; windows broken with distortion; danger of instability.	>15	Requires a major repair job involving partial or complete rebuilding

TABLE 10: Damage classification criteria according to (CEN, 2022).

Nonetheless, Burland J. B., 1977 classification has two main limitations. First, its classification heavily relies on the crack's width. Furthermore, its classification is also discrete with damage differentiation between classes being more difficult. These two limitations although not significant for overall damage assessments do complicate the accurate depiction of time-dependent damage as well as the accuracy of the assessments.



For this reason, Korswagen, et al., 2019 developed a metric to continuously classify masonry damage through Burland, 1977 classification via a single dimensionless damage parameter  $\Psi$ . This parameter evaluates further damage features such as the number of cracks and their crack lengths. Through  $\Psi$ , masonry specimens of 0.1mm crack-widths correspond to a value of one ( $\Psi=1$ ), cracks up to 1mm correspond to a value of 2 ( $\Psi=2$ ) and cracks of up to 4mm correspond to a value of 3 ( $\Psi=3$ ).

The parameter only accounts for cracks with a thickness greater than 0.1mm as this threshold is argued to be the limit through which human visual inspections can begin to identify cracks, as also employed in CEN, 2022. Another benefit of this parameter is that it can evaluate damage states between walls and for full structures accounting for the necessary reparability implications for a given damage state and a wall of a specific size.

The computation of the parameter is performed through the following expressions. In the expressions  $n_c$  refers to the number of cracks in the wall,  $\widehat{c}_w$  is the width-weighted and length-average crack width (mm),  $c_w$  is the maximum crack width and,  $c_L$  is the crack length (mm). With the following being the damage evaluation according to the parameter  $\Psi$ .

<b>Description</b>	<b>Expression</b>						
Light damage evaluation ( $\Psi$ ) for single-wall	$\Psi = 2 \cdot n_c^{0.15} \cdot \widehat{c}_w^{0.3}$	<b>Damage state</b>	<b>DS0</b>	<b>DS1</b>	<b>DS2</b>		
Calculation of the weighted crack width for a single wall	$\widehat{c}_w = \frac{\sum_{i=1}^{n_c} c_{w,i}^2 \cdot c_{L,i}}{\sum_{i=1}^{n_c} c_{w,i} \cdot c_{L,i}}$	<b>Damage Level</b>	<b>DL0</b>	<b>DL1</b>	<b>DL2</b>	<b>DL3</b>	<b>DL4</b>
Psi parameter for a structure consisting of N walls	$\overline{\Psi} = \frac{\sum_{i=1}^N \Psi_i \cdot A_i}{A_T}$	Damage parameter	$\Psi < 1$	$1 < \Psi < 1.5$	$1.5 < \Psi < 2.5$	$2.5 < \Psi < 3.5$	$\Psi > 3.5$
Absolute damage comparison between walls	$\Psi'_i = \Psi_i \cdot \frac{A_i}{A_m}$	Approximate crack width	N/A	0.1mm	1mm	5mm	15mm
Estimated cost of repair of a structure	$Z = Z_0 + \overline{\Psi} \cdot A_T \cdot \zeta$						

Equation 1: Damage parameter ( $\Psi$ ) formula and damage parameter categories (Korswagen, et al., 2019).

Thus, current state-of-the-art damage assessments currently mostly involve cracking damage with deformations and tilts being mostly used in an empirical scale form. That said, current crack-based damage metrics in the case of on-site specimens can heavily rely on visual interpretations if adequate measurement equipment is not used. Due to these possible limitations Korswagen, et al., 2017 emphasize different terminologies to differentiate the purpose and implications from different masonry damage assessment benchmarks.

Through these definitions Damage States (DS) refer to the general state of the specimen with DS 0 referring to no damage, DS 1 to light damage, and DS 2 to structural damage. It also argues to use of Perceived Damage States (PDS) when the damage level cannot be quantifiably evaluated or the Damage Level evaluation has been made solely through the visual state of the specimen.

## 2.4 Damage assessment procedures for Masonry Structures subjected to settlements

A focal point of this thesis is to demonstrate the suitability of state-of-the-art assessment methods outside of universally popular numerical analysis techniques. Different analysis methods have remained successful for specific problems outside shallow subsidence or human-driven processes but continue unknown if they can be applied to subsidence-specific settlements. Furthermore, numerical analyses possess strong barriers to use as numerically based solutions require training and experience to manage the effects modelling decisions and assumptions may have over the results. With specific considerations for the analysis of masonry homes being less discussed.

Therefore, the following section aims to review the existing assessment techniques for settlement-induced masonry damage assessments. The review aims to highlight method the methodology, its underlying assumptions, and limitations identified by researchers, to present a comprehensive review that documents the necessary implications for future users.

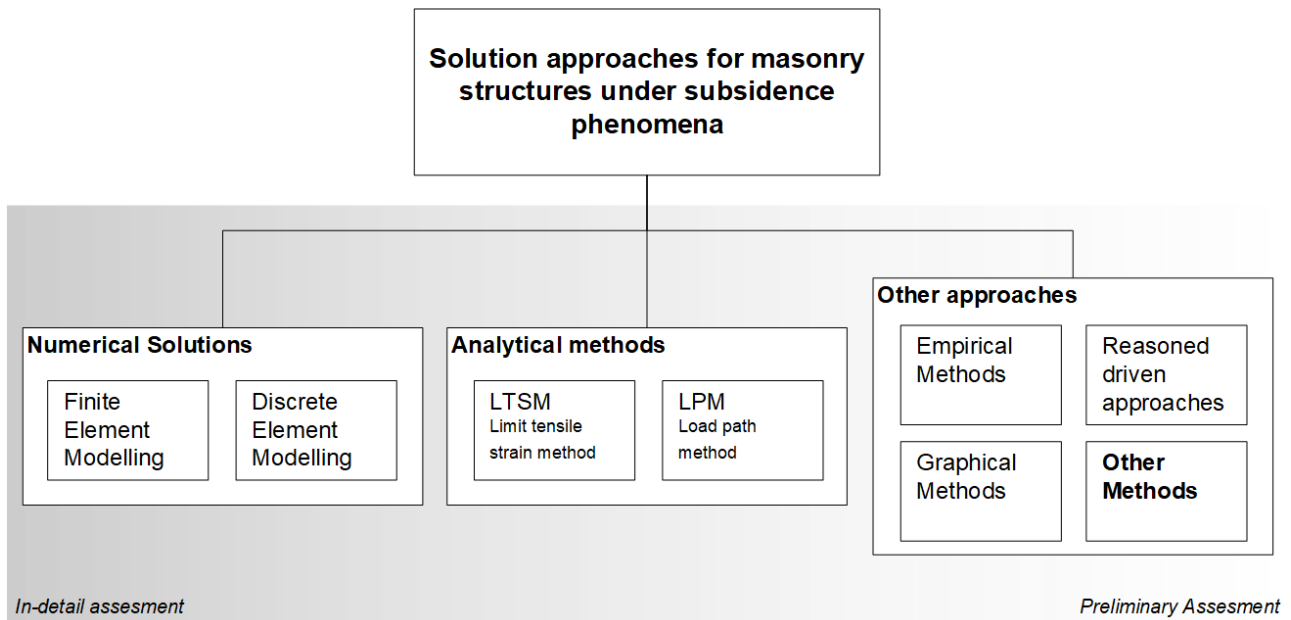


Figure 12: Classification of masonry structure assessment methods.

The review found that possible assessment methods can be categorised as follows. Firstly, analytical methods, are methods which make use of elementary structural mechanics theory to approximate the behaviour of the building through equivalent forms and formulations such as Newtonian-based formulations. A subset of these is analytical-empirical which also combines experimental tests to approximate the behaviour of a mechanical scheme, this corresponds to the Limit Tensile Strain method (LTSM) and Load Path Method (LPM).

In second place there is numerical methods, which formulate the behaviour of a structure by discretizing its different counterparts based on a set of mechanical element formulations characterised by their material characteristics and numerically approximated most popularly, Finite Element Modelling (FEM) and Discrete Element Modelling (DEM). In last place, there is a set of distinct approaches which are a mix of purely empirical and visual. Empirical methods, a historically popular approach, have been

performed through Subsidence related Intensity (SRI) parameters, which relate the deformations with the damage on a building, and lastly, Visual assessments which are those that study the visual evidence and provide possible hypotheses.

### 2.4.1 Empirical methods: Empirical based literature thresholds

Empirical methods establish relationships between target variables through observation and measurement of phenomena across various domains (Dan, 2017). Researchers often use these methods to link damage to factors associated with building deformation. By simplifying often complex, problems into a manageable set of variables, empirical methods provide a practical approach for engineers. However, these methods also pose significant limitations. Often, they oversimplify problems and can therefore make them unsuitable to particular analysis instances. Despite so, empirical methods have been widely used in research and engineering design codes to streamline the assessment process.

#### Subsidence-related intensity thresholds from (inter)national guidelines

The prominence of empirical methods in engineering most likely stems from the approachability to different engineers of different backgrounds and the practicality they provide. In instances of Masonry structures and ground settlements, Dutch-specific regulations exist adapted from Eurocode 6 and Eurocode 7, the foremost relates to assessing the capacity of masonry buildings and the latter in geotechnical design. Other relevant design or building state norms specific to the Netherlands include CUR, 1996 (a structural design norm specific to construction in soft soils), in this norm, further limits are proposed relating a building's damage state to its vertical rotation ( $\Phi$ ). Other measures also include those proposed by the municipalities of Rotterdam and Amsterdam which use a range of SRI parameters.

The first set of available limits are found in Eurocode 7, they establish the acceptable angular distortions experienced by the foundation. In the case of open or infilled frames and load-bearing elements composed of masonry elements, the soil's angular distortion ( $\beta$ ) varies from 1/2000 and 1/300, whilst usually for different structures values of 1/500 are considered acceptable in the SLS. These limits change between the shape of the deformation, with them being more stringent when the deformations are under hogging shapes rather than sagging deformations.

The main limitation of norms and legislation that set specific limits is that they are most applicable to new constructions. As a result, these standards may lead to overly optimistic assessments when applied to existing structures. Additionally, new constructions often differ significantly from older ones due to engineering practices, construction techniques, and materials.

#### Subsidence-related intensity thresholds from previous studies

Furthermore, the greatest amount of empirical building damage limits are found in the literature. These limits are too many to be discussed individually but on the whole, they relate SRI and strain measures to possible damage instances. Not all are related to the damage levels which is why Perceived damage states that correspond to the damage prescription have been assigned levels from different literature sources. In these sources, a greater prevalence of thresholds use either the Angular distortion ( $\beta$ ) and the Deflection ratio ( $\Delta/l$ ). Nevertheless, there also is a second set of thresholds which relate to the tensile strains and are more popularly employed under the Limit Tensile Strain Method (LTSM) as it allows to produce strain estimates for a building.

## 2.4 Damage assessment procedures for Masonry Structures subjected to settlements

SRI parameters [ $\beta, S_v, \phi$ ]				Building strains [ $\epsilon$ ]						
Explanation	Criteria	Values	Limit for	Source	Explanation	Criteria	Values	Limit for	Source	
Angular distortion	$\beta$	3.33x10 <sup>-3</sup>	Cracking in wall panels	Skempton & McDonald(1956)	Angular distortion	$\beta$ per $\epsilon$	$\beta = 1 \times 10^{-3}$	Negligible damage	Boscarding and Cording (1989)	
		6.66x10 <sup>-3</sup>	Structural damage				$\epsilon = 0.5 \times 10^{-3}$	Very slight		
Max. diff. settlement	$\Delta ST$ (max)	32mm	In sand (all foundations)		Horizontal Strain		$\beta = 1.5 \times 10^{-3}$	Slight		
		45mm	In clay (all foundation)				$\epsilon = 0.75 \times 10^{-3}$			
Max settlement	$ST$ (max)	51mm	Isolated foundations in sand soil		Horizontal strain	$\epsilon$	$\beta = 3.25 \times 10^{-3}$	Moderate to severe	Burland, et al. (1977)	
		76mm	Isolated foundations in clay soil				$\epsilon = 1.5 \times 10^{-3}$	Visible cracks		
		51-76mm	Raft foundation in sand				$\beta = 6.5 \times 10^{-3}$	Onset of visible cracking		Base et al. (1966)
		76-127mm	Raft foundation in clay				$\epsilon = 3 \times 10^{-3}$	Onset of visible cracking		Burhouse (1969)
Deflection ratio per L/H	$\Delta/l$ per L/H	0.3x10 <sup>-3</sup>	for L/H $\leq 2$ Sagging	Polshin & Tokar (1957)	Tensile strain	$\epsilon$	$\beta > 6.5 \times 10^{-3}$	the onset of cracking	Mainstone (1971)	
		1x10 <sup>-3</sup>	for L/H = 8 Sagging				$\epsilon > 3 \times 10^{-3}$	Visible cracking		
Angular distortion	$\beta$	5x10 <sup>-3</sup>	First visible cracking to no infill structures	Wood (1958) Information taken from Son (2003)	Tensile strain	$\epsilon$	0.5x10 <sup>-3</sup>	Negligible damage	Son and Cording(2005)	
Angular distortion	$\beta$	2.2x10 <sup>-3</sup> to 3.6x10 <sup>-3</sup>	The first visible cracking to happen in brick panels and walls				0.75x10 <sup>-3</sup>	Very slight		
		1x10 <sup>-3</sup>	First visible cracking to brick walls with openings				1.67x10 <sup>-3</sup>	Slight		
Angular distortion	$\beta$	1x10 <sup>-3</sup> - 2x10 <sup>-3</sup>	Cracking of clay brick units with mortar	Bozuzuk (1962)			3.33x10 <sup>-3</sup>	Moderate to severe		
Angular distortion	$\beta$	2x10 <sup>-3</sup>	Safe limit for no cracking	Bjerrum (1963)						
		3.33x10 <sup>-3</sup>	Cracking in panel walls							
		6.66x10 <sup>-3</sup>	Considerable cracking in panel and brick walls							
Angular distortion	$\beta$	2.5x10 <sup>-3</sup>	Cracking	Meyerhof (1953)						
Angular distortion	$\beta$	3.33x10 <sup>-3</sup>								
Angular distortion	$\beta$	Hogging Z	Cracking unreinforced load-bearing wall	Meyerhof (1982)						
		0.5x10 <sup>-3</sup>								
		Sagging Z								
		2x10 <sup>-3</sup>	Cracking of infilled frames							
		4x10 <sup>-3</sup>	Cracking of frame structures							
Settlement	$S_v$	100-220mm								
Angular distortion	$\beta$	Sagging: 0.5-3.3x10 <sup>-3</sup>	Damage	CEN (2007) (EN 1997-1)						
		Hogging: 0.25-1.6x10 <sup>-3</sup>	Standard for open or infilled frames and load-bearing brick walls							
		Sagging: 2x10 <sup>-3</sup>	Serviceability limit state For many (new) structures							
		Hogging: 1x10 <sup>-3</sup>								
Rotation	$\Phi$	<2x10 <sup>-3</sup>	No damage	CUR (1996) Dutch regulation for buildings on shallow foundations						
		2x10 <sup>-3</sup> to 3.3x10 <sup>-3</sup>	Aesthetic Damage							
		3.3x10 <sup>-3</sup>	Structural Damage							
		>10x10 <sup>-3</sup>	Risk for residents							
Angular Dist	$\beta$	20x10 <sup>-3</sup>		SWD (2009) Amsterdam municipality						
Settlement rate	$S_{max}$	4mm/y	Demolition of the building							
	$\Delta S_{max}$	2 mm/y								
Vertical Tilt	$\omega$	< 1/66	Good	IGWR (2009) Rotterdam Municipality						
		1/66 -1/50	Acceptable							
		1/50 , 1/33	Poor							

TABLE 11: Compiled Strain and SRI thresholds for different damage levels (Ozer & Geurts, 2021)

## 2.4.2 Analytical methods: Limit Tensile Strain Method and Load Path Method

The analytical method involves using a set of approaches that apply deductive and scientific reasoning to represent a real-world system through mathematical formulations. These formulations capture the underlying principles and relationships that govern the process. Ideally, such methods provide a direct synthesis of the problem and are not as subject to uncertainties. For masonry structures, these formulations may include systems like frames, beams, or springs to model the behaviour of masonry or building elements under loads and deflections, thereby approximating the behaviour of the system.

### 2.4.2.1 Limit Tensile Strain Method (LTSM)

Arguably the most popular analytical method has been the Limit tensile strain method (LTSM). This method approximates the mechanical response of the building through an equivalent beam making use of Timoshenko beam theory. It then calculates the expected strains based on the estimation of a fictitious point load which is approximated through the expected deflection of this load on the beam, which is measured through the deflection ratio calculated based on the green field profile. From which the final strains are approximated through the Timoshenko formulations and a linear elastic assumption behaviour from the beam. Based on the strain levels these are then compared against a set of empirical limits of the damage levels expected from tested masonry beams under such a deflection.

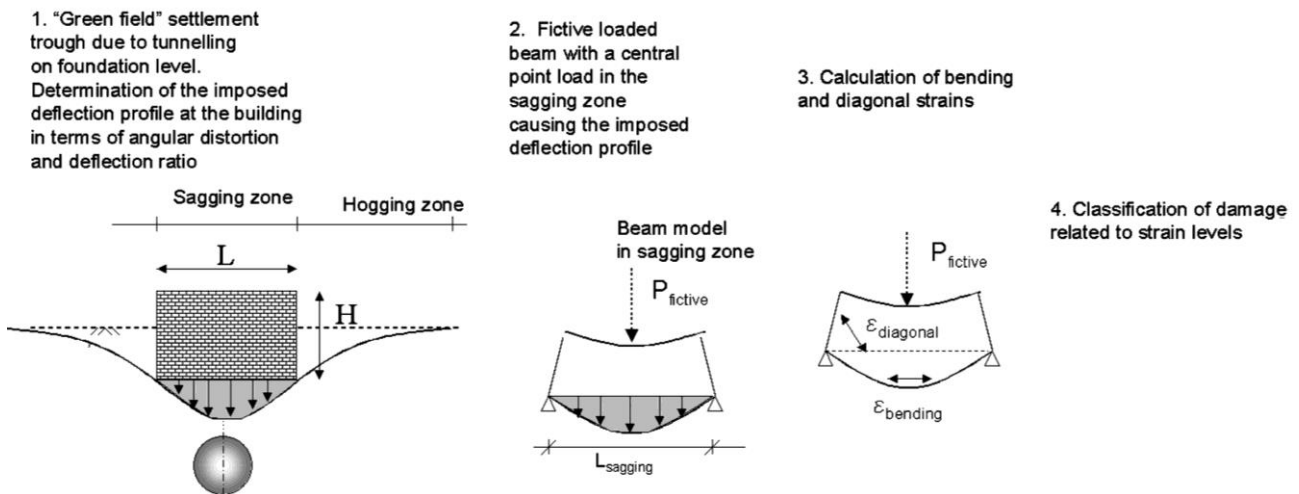


Figure 13: LTSM approach scheme (Netzel, 2003).

The original formulation is based on Burland and Wroth (1974), it uses the deflection ratio to approximate the fictive point load and thus the strains. Nevertheless, other formulations make use of the angular distortion and are considered more suitable for problems with greater shear contributions.

Loading	Max Strain - Bending	Diagonal Strain - Shear
Point Load	$\frac{\Delta}{L} = \left[ \frac{L}{12t} + \frac{3I}{2tLH} \frac{E}{G} \right] \epsilon_{b_{max}}$	$\frac{\Delta}{L} = \left[ 1 + \frac{HL^2}{18I} \frac{G}{E} \right] \epsilon_{d_{max}}$
Uniformly Distributed Load	$\frac{\Delta}{L} = \left[ \frac{5L}{48H} + \frac{3I}{2tLH} \frac{E}{G} \right] \epsilon_{b_{max}}$	$\frac{\Delta}{L} = \left[ \frac{1}{2} + \frac{5HL^2}{144I} \frac{G}{E} \right] \epsilon_{d_{max}}$

Equation 2: LTSM formulas by Burland and Wroth (1974) altered by Mair et al. (1996) (Korff, 2009).

The method operates under several further assumptions with the main limitations identified by various researchers (Netzel, 2003; Potts & Addenbrooke, 1997) summarized below. Generally, it is recognized that the LSTM provides a conservative approach for estimating building strains, serving as a preliminary procedure to identify instances where a more detailed structural evaluation is warranted.

**Assumptions:**

- The assessment procedure is decoupled: Greenfield displacement is initially calculated and subsequently applied to an idealised model of the structure.
- The building is only represented by a two-dimensional weightless beam with isotropic elastic material properties. Non-linear effects are not accounted for.
- The greenfield profile is directly applied onto the beam, and foundation and SSI contributions to the system are often neglected. In other words, the ground deformations are assumed to be fully transferred constituting a conservative approach.
- The stiffness of the beam is evaluated through parameters that relate to the dimensions and the material of the structure which makes it difficult to evaluate the contribution of different building characteristics.
- For long buildings, the part of the building where the settlement shape does not surpass 1mm in depth is not accounted for and therefore cantilever effects are not incorporated.

Burland & Wroth, 1974 evaluated the response of the LSTM formulations and showed how the strains are mostly governed by flexural mechanisms, as for L/H ratios greater than 1.3 the flexural strains outweigh those of shear strains. Nevertheless, the strain limit from which the shear-to-bending contribution happens changes based on the E/G ratio but at the same L/H ratio. Therefore, particular attention has to be given to correctly estimating the elastic resistance of the equivalent beam.

Approximating the elastic to shear modulus of a building is at best challenging. The elastic and shear response of a building is based on an interaction of material, geometric and assembly conditions/characteristics of a building. Initially Burland & Wroth, 1974 differentiated the response of the building by a factor of 2.6 for unreinforced masonry walls and 12.5 in the case of framed masonry buildings. This was then further elaborated by Son & Cording, 2007 which determined the ratio based on the opening percentage of the façade.

<i>E/G ratio</i>	<i>Description</i>	<i>Source</i>
2.6	Wall with no openings	(Burland , et al., 1977)
12.5	Framed Structure	
3.4	Wall with no openings	
8	Wall with 10% openings	(Giardina, et al., 2013)
11	Wall with 30% openings	
2.6	Wall with no openings	(Son & Cording, 2007)
4.5	Wall with 10% openings	
7.5	Wall with 20% openings	**Ks/Kn = 1
11	Wall with 30% openings	

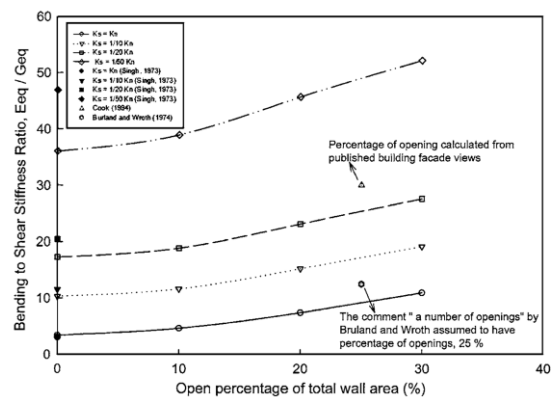


Figure 14: Different recommended E/G ratios for the LSTM.

The second major factor influencing the resistance from the fictitious beam response is the second moment of area. Burland, et al., 1977 state these values should be determined through a value of  $H^3/12$  in the case of sagging and through  $H^3/3$  in the case of hogging. There a slight modification occurs as the location of the neutral axis is assumed to change based on the deformation mechanism, although not realistic of traditional beam behaviour, a  $H/2$  distance is to be used under sagging deformations and  $H$  is to be the distance in the case of hogging deformations.

There exist many other relevant additions developed to the LTSM, a very popular one is the relative stiffness method proposed by Potts & Addenbrooke, 1997, this formulation aims to account for SSI effects and the main limitation in the original LTSM method contributing to producing conservative results. Other interesting additions to the LTSM include modification factors to account for existing damage and different settlement rates, SBR, 1998 proposes to increase the tolerable strain limits by a percentage factor the slower the settlement rate is. Similarly, reduction of the tolerable strain limits are also proposed when damage is originally present in the building.

### 2.4.2.2 Load Path Method (LPM)

The second most popular analytical method available in the assessment of settlement-experiencing masonry structures is the Load path method (LPM) (Schlaich, et al., 1987). This model is an extension of the strut and tie model (STM) prevalent in the analysis of reinforced concrete structures. The method maintains the existing capabilities of the STM mainly: it can approximate rocking, unit-to-unit slip, interface frictional cohesive behaviour, tensile cracking and crushing, but it has been expanded to allow capturing the brick's tensile cracking brittle response through residual models. (Gagliardo, 2021).

Under this approach, the model's focus is the prediction of damage and crack pattern initiation/propagation not the estimation of its ultimate limit resistance. This is done by searching the load path associated with the lowest value of the total strain energy among the different load paths in equilibrium for different assumed mechanisms called “states”. These states are divided into five distinct phases: State 0 (Unstressed structure), State 1 (Stress regime without cracking), State 2 (First cracking instances), State 2a (Crack propagation), and State 3 (Ultimate Limit State).

**State 1: Equilibrium**

**State 2 & 2a: Strut & Tie Model, Final Load Paths and Mechanism**

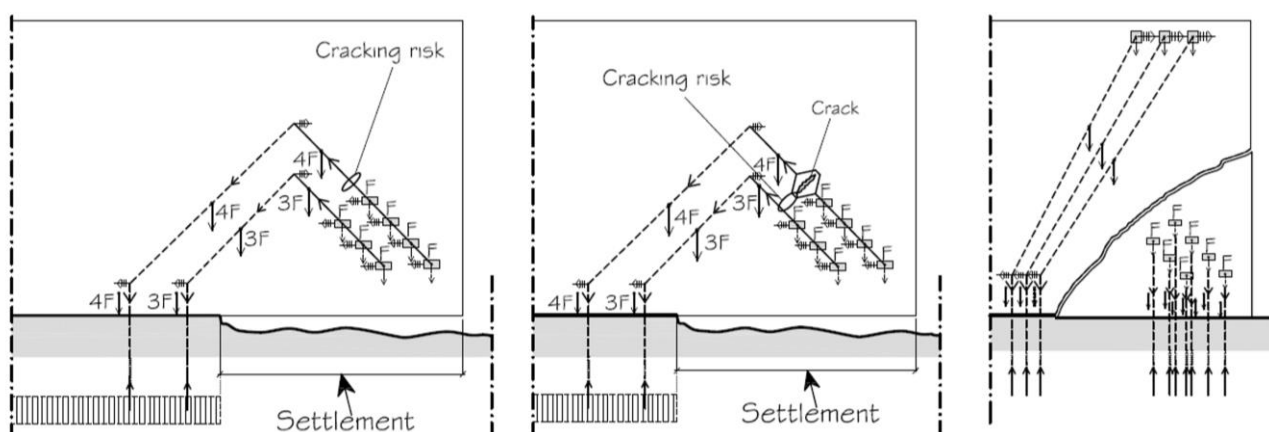


Figure 15: LPM on one ended settlement in a (State 1), b-c-d (State 2) (Palmisano & Elia, 2015).

State 0 represents the initial condition of the structure before any loads are applied, with no internal stresses or deformations. State 1 is when only gravity loads or other non-damage-inducing loads (e.g., self-weight) are applied. The structure experiences internal stresses but remains uncracked, maintaining equilibrium with straightforward vertical load paths. State 2 involves the application of additional external loads (e.g., settlements or lateral forces), leading to the first instances of cracking. In this state, Load paths are adjusted to maintain equilibrium and new cracks form. State 2a, is when the existing cracks propagate, and new cracks appear as the load is increased. State 3 marks the ultimate limit state, where the “wall” reaches its capacity and collapse is assumed.

Although in the demonstrated example the masonry element constitutes a simplified wall the versatility of the load path method in part helps address some limitations from the LTSM, mainly that the crack widths cannot be estimated nor the location of damage. Furthermore, the LPM can be used to account for the effects the geometry of the masonry element can have on the crack pattern and location.

Nevertheless, it is still not able to simulate the post-failure behaviour of the cracks as it just assumes that the cracks continue to propagate along the increasing stress path with no stress redistribution effects. It also does not account for masonry’s anisotropy and can lead to not entirely realistic crack patterns. Also due to the heavily assumption-based procedure, the assessment can be lengthy and time-consuming.

### 2.4.3 Numerical Methods: Masonry Finite Element Analysis

With increasingly widespread access to computational resources, the use of numerical analysis in structural engineering has become increasingly standard. The adoption of masonry numerical analysis has increased in popularity in part because of the great advancements by researchers in the last half century (Prosperi, et al., 2023; D’Altri, et al., 2020; Lourenço, 2014) mostly by developing the accurate simulation of the characteristic masonry behaviour via the finite element method. Masonry Finite Element Analysis (FEA) differs from other materials due to the construction methods’ heterogeneity and discontinuity.

The two main approaches micro and macro scale modelling fundamentally differ based on the explicitness of the masonry modelling. In masonry micro-modelling the analyses require the detailed modelling of behaviour through interfaces and non-linear material properties, whilst macro-modelling techniques must replicate failure mechanisms from different parts and different material resistance. Further difference also stems from how damage is represented at different damage states. At low damage levels, models must accurately simulate cracking, and account for material non-linearities necessitating the updating of material parameters in specific regions of the material. As this damage progresses, these principles remain, but additional considerations become necessary based on the modelling approach and targeted simulated behaviour which may have to introduce contact non-linearities and geometrical non-linearities. Nevertheless, advances in the formulations of material, displacement and energy equilibrium behaviour have allowed the assessment possibilities of masonry structures to be close to every possible loading scenario and configuration (D’Altri, et al., 2020).

#### 2.4.3.1 FEA solutions methods: Linear, Non-linear, Quasi-static, and Dynamic approaches

Masonry finite element analysis, as well as general FEA, mostly takes three different analysis forms: Linear static analysis, Nonlinear analysis and Dynamic analysis. Linear static analysis is the most



employed, it is used in situations where the structures are not expected to surpass the elastic state yet characteristics such as stress distributions, displacements at specific locations or support reactions are still relevant information as the elastic response of the structure is at interest. In this analysis method, the problem can be formulated by a system of equations which if well set have a singular solution. In second instance and most popular in the analysis of damage experienced by masonry structures is non-linear analysis. In this analysis, the response of material parameters, geometric effects and contact response is assumed to be non-linear, which in practical terms means that the problem formulation is state-dependent.

This means that the numerical formulation of the problem changes between each state and the problem's stiffness matrix is updated per time step. To solve such a problem an incremental-iterative analysis procedure is carried out, which through user-defined steps the response is iteratively calculated at all of those steps, simulating the progression of non-linear effects throughout the problem. These non-linearities are numerically approximated through displacement control or arc-control methods, which results in the problem no longer having a singular solution but rather an infinite number of solutions dependent on the stability of your solution method based on the step size, number of iterations and convergence tolerance as well as the problem formulation.

In the last case, there also is dynamic analysis whose specifics won't be dwelled too much since it is not relevant to this research. Where in essence, either time-discretised analysis or modal analysis is performed. Time-discretized analysis, approaches are similar to non-linear analysis where the solution of a problem is estimated at each time step. This analysis can also incorporate non-linear analysis which would then involve the iteration through time and state to allow the simulation of the detailed response due to time-dependent forces and state-dependent phenomena at each timestep. The second major form and most popular due to its lesser computational cost is modal analysis, which evaluates the time-dependent response of a structure by evaluating its mode of vibration and natural frequencies where then the dynamic response is estimated by the introduction of the time-dependent forces into the vibration modes. This analysis is most popular in the analysis of masonry structures under seismic actions, an effect that they are notoriously vulnerable to because of their poor ductility.

The previous breakdown covers most major analysis types, but quasi-static analysis stands apart as a less common category. This method is mainly used for issues like subsiding masonry, creep, and thermal effects, where time dependence is assumed to be minimal or linear. While this assumption may not always hold, especially during significant damage events, it helps simplify complex masonry analyses.

### **2.4.3.2 FEA masonry material modelling: Micro and Macro modelling**

When masonry analyses are being made a model proposition that strikes a balance between precision and complexity has to be made. Despite great advances in computing processing capabilities non-linear finite element analysis remains extremely computationally expensive, billions of computations are made to approximate a structure's final state and its behaviour throughout the process. Following this rationale, different masonry modelling approaches based on the interested mechanical scheme have been broken down into different modelling families. The most popular schemes include Block-based models, Continuum homogeneous models, Macro element models and geometry-based models.

Block-based models are those primarily concerned with modelling the block behaviour of masonry units and masonry texture. This approach allows for the most precise simulation of the masonry mechanical

interaction and is expected to best simulate crack patterns. Continuum models constitute those where the masonry is modelled as a deformable body where the constitutive law is defined by a direct approach, calibrated laws based on experimental tests or homogenization procedures where the structural-scale response is encompassed in a single material response, these models usually strike a balance between computational efficiency and damage representation accuracy and are the most popular for the analysis of larger masonry structures and elements.

Macro-element models are those where structures are simplified into piers and spandrels based on the interpretation by an engineer of the structural behaviour of the building. Macro-element models are often used in seismic performance and global stability of masonry structures. Lastly, geometry-based models are models that through the structure’s geometry and limit-analysis investigate if the structure remains in equilibrium and to investigate potential collapse mechanisms.

### Micro modelling models

Block-based models include the most realistic modelling approaches. Due to the implicit mechanical restraint offered by the explicit modelling of the masonry bond in walls and corners, the overall structural stiffness in place and out of plane is well represented. Additionally, these models can depict failure modes without further interpretation. However, their high computational expense due to having 8 more elements to represent a single masonry element limits their application to individual panels additionally, the explicit modelling of the elements makes it time-consuming. In this family of numerical approaches, there are two main types: Interface element-based approaches where two-phase micro modelling is issued for historic masonry and cyclic behaviour analysis and, textured continuum-based approaches which separate the modelling of blocks and joints without interfaces. Other approaches include contact-based approaches, such as DEM and Block-based limit analysis predict collapse loads and failure mechanisms without the use of FEA, both methods outside the scope of this work.

Block-based models which employ the FEM mostly employ micro-modelling, this approach to different levels of detail models the units, mortar behaviour and interface behaviour between both elements. The two main variants are two-phase micro-modelling or simplified micro-modelling, a model where the mortar is modelled through a single interface of no thickness that can account for the crushing, debonding and slipping of the mortar, as well as the general brick behaviour and, three-phase micro-modelling, where the mortar is explicitly modelled and connected to the brick elements through discrete interfaces. This last approach represents the most realistic representation of the masonry yet is prohibitively computationally expensive which is why it’s mostly reserved for small-scale investigations against laboratory specimens.

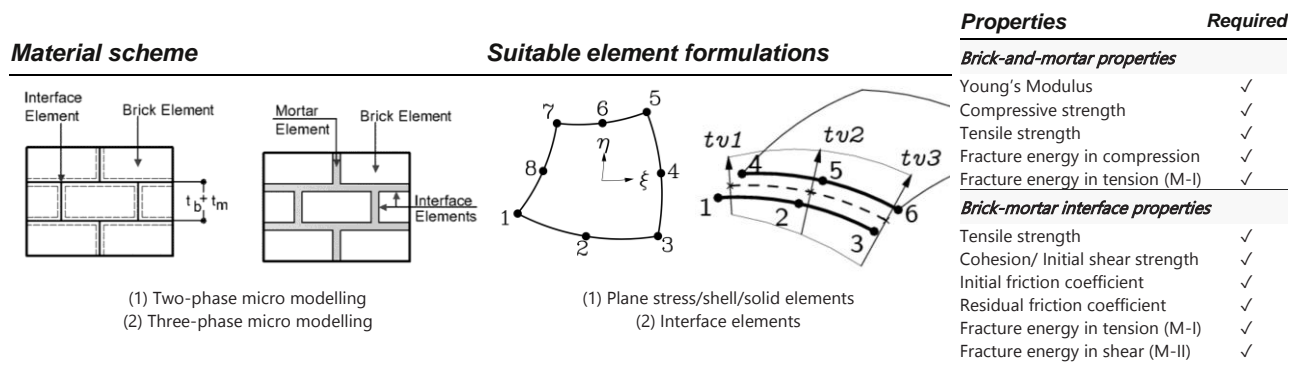


Figure 16: Block-based modelling strategies (Asteris, et al., 2015; DIANA FEA BV, 2024)

## Macro modelling

Continuum approaches comprise those where the composite masonry behaviour is defined in a continuous deformable body. This approach reduces the computational expense of the analysis but increases the complexity of forming a coherent constitutive model. It is in this characteristic where the main differentiation within continuum homogenous stems, the way through which the composite material is characterised, the two main characterisation techniques are: direct, or structural homogenization approaches that constitute the eventual macro-modelling material model.

Direct approaches constitute the most popular approach this is because they offer a computationally acceptable way to capture the dominant mechanisms, mainly tension softening and brittleness anisotropy. The simplest set of these direct approaches is no-tension material models, although not very realistic they present a good starting point for investigations into the structural behaviour of a wall as in the design of masonry structures all load-bearing masonry elements are designed to be in a compressive state.

The second simplest form of continuum models base their behaviour on non-linear constitutive laws based on fracture mechanics, damage mechanics or plasticity theory, these models are called smeared crack models and are the most popular direct approach form which allows relatively easy simulation of the main mechanisms which occur in masonry. They nevertheless still have some limitations based on their mesh-sensitivity in crack energy dissipation, caused due to the regularization of the fracture energy in the continuum and the influence meshing has on the length and pattern of the crack. The most popular laws in the FEA of masonry available in the software package Diana are the Total Strain Based Crack Model (TSCM) and the Engineering Masonry Model (EMM).

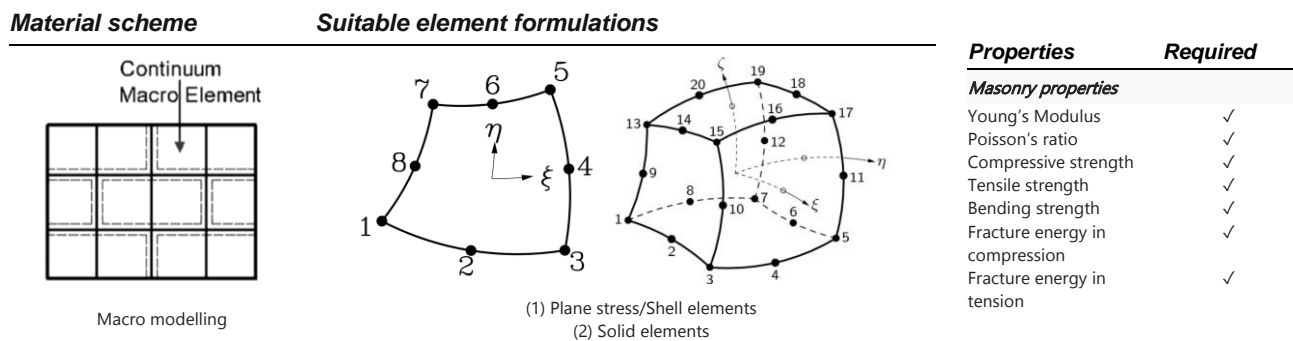


Figure 17: Continuum homogeneous modelling strategies (Asteris, et al., 2015; DIANA FEA BV, 2024)

The Total Strain-based Crack Model (TSCM) is an isotropic material model usually used to predict crack initiation, propagation and softening in concrete. Its behaviour is based on a user defined elastic stress-strain relationship, and user defined softening behaviour. In masonry analysis, the most relevant softening branches used are Brittle (No-tension), Linear or Exponential (Most relevant to masonry), or multi-linear.

The main model characteristic is it allows cracking to happen in any direction when the first principal stress surpasses the material's tensile strength. When this happens cracking strains are smeared over the element, perpendicular to the principal direction, through a user-defined crack bandwidth formulations which by default is determined through based on the element size and order. When cracking occurs fracture energy is released to maintain equilibrium with the applied work, and under the rotating crack definition cracks are allowed to rotate base on changes of the direction of the maximum principal stress.

## 2.4 Damage assessment procedures for Masonry Structures subjected to settlements

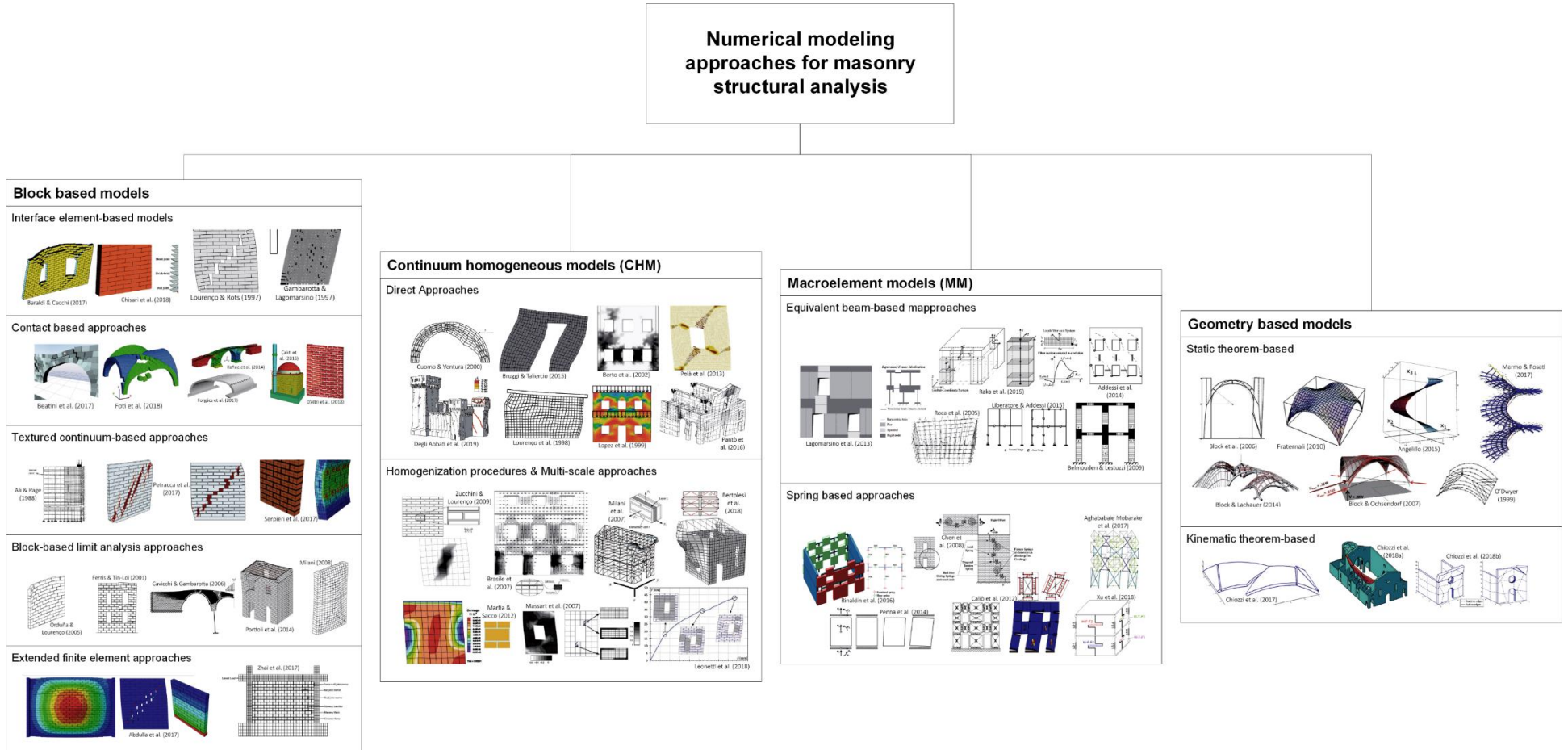


Figure 18: Numerical modelling strategies for masonry structures an adaptation of D'Altri, et al., 2020.

The second major constitutive law is the Engineering masonry model, this material model is an orthotropic material model with a non-linear compressive behaviour whose shear bed joint resistance can be described through the Mohr-Coulomb criterion. This material model is suitable for plane stress elements and shell elements.

The material model by default can evaluate a number of failure Mechanisms: tension, compression and shear sliding (1-3 in the figure below) the remaining are evaluated depending on the user-defined failure mechanisms, for failures perpendicular to head joints and bed-joints the model will also evaluate horizontal tensions and compression (Mechanisms 1-5), by user definition, define of the head-joint resistance as a function of friction (Mechanisms 1-4), disregard head-joint failures (Mechanisms 1-3) or through a staircase crack angle ( $\alpha$ ) dictating the diagonal tensile resistance based on the masonry bond and possible failure progression through the mortar joints (Mechanisms 1-3,6). The definition of these failure Mechanisms allows to rationalise the possible cracking directions with the element x-component for bed-joint failures in the y-component for head joint failures and the diagonals based on the user-specified angle.

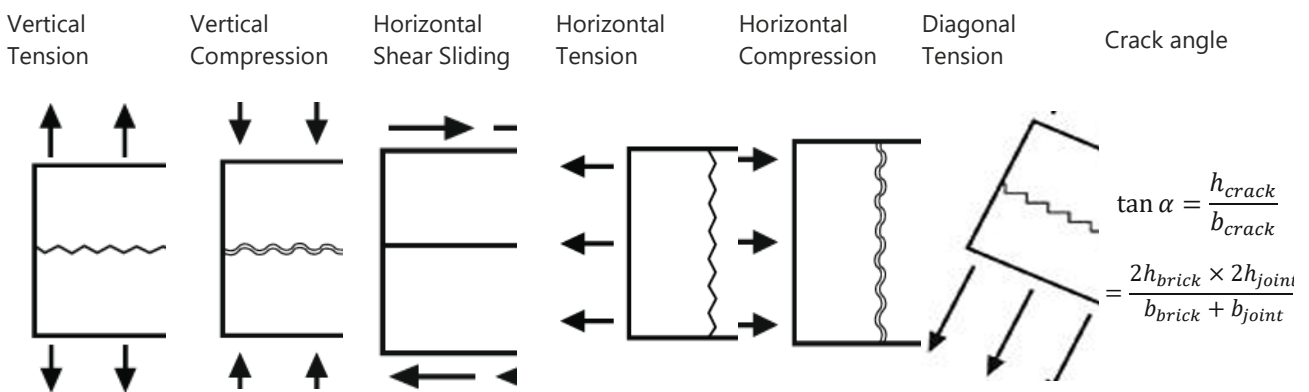


Figure 19: Failure mechanisms considered by the engineering masonry model, and estimation of crack angle (Lisanne, 2019).

The model is known to be more capable of capturing masonry diagonal cracks which prominent in rocking motions and one-end-heave or one-ended settlement patterns (Those where shear stresses have a greater influence), it has also been shown to present good results in shear walls under light damage, and shows better energy dissipation than the TSCM (Lisanne, 2019).

However, some limitations have been identified. The characteristic diagonal staircase cracks tend to appear steeper than those observed in experimental results, and the crack patterns are generally more diffuse. Additionally, the material model occasionally can have numerical stability issues (Lisanne, 2019).

### 2.4.5 Modelling approaches specific for settlement-induced Masonry Structures

The review of numerical modelling approaches so far has focussed on the simulation of the masonry. Nevertheless, settlement-specific considerations are also made when the analysis of masonry structures concerns settlement-specific behaviour. Recently Finite Element Analysis (FEA) specific to urban subsidence has gained more attention through the research of Alessandrini, et al., 2015; Sangirardi, et al., 2020; Grant, et al., 2021; Erturk Atmaca, et al., 2023; Prosperi, et al., 2023; Prosperi, et al., 2023.

The classification of settlement-specific numerical models primarily concerns the modelling approach undertaken for the subsoil behaviour. Models are either coupled, semi-coupled or uncoupled models. Coupled models explicitly incorporate both structural and subsurface behaviour, these models are the preferred choice for analysing structures of increased complexity (Korff, 2009; Burland & Wroth, 1974), semi-coupled approaches are used when the composite substructure-structural behaviour wants to be simulated with a lesser computational expense. In these models, the analysis of ground movements is applied to an interface that may include both soil and foundation or solely the soil-foundation interaction. Uncoupled models, on the other hand, focus exclusively on the superstructure, with settlements directly applied to the building.

The application of masonry models for subsidence processes has not been as widespread examples include Sangirardi et al. (2020) which performed a set of NLFEA to two different case studies, Erturk Atmaca et al. (2023) who assessed the collapse risk of masonry structures subjected to subsidence due to adjacent excavations through semi-coupled and coupled strategies. Further models were also implemented in Giardina, 2013 which implemented a range of coupled semi-coupled and uncoupled models to predict masonry damage due to tunnelling settlements.

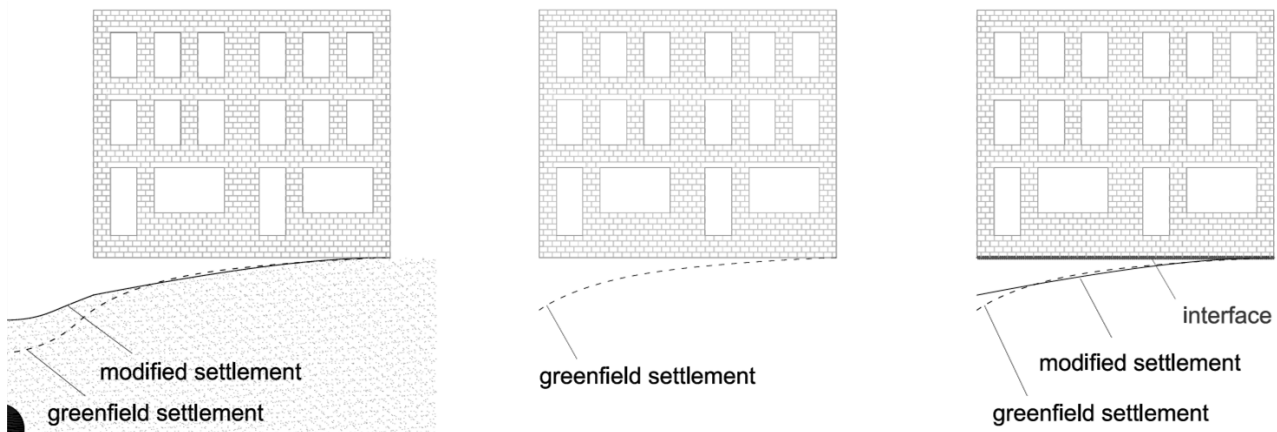


Figure 20: Subsoil modelling approaches for settlement-induced building damage. Coupled (Left), uncoupled (centre) and semi-coupled (right) (Giardina, 2013).

Yet the most relevant research on the capabilities of FEA in the assessment of settlement-induced masonry structures is found in Prosperi, et al., 2024; Prosperi, et al., 2023; Prosperi, et al., 2023. In Prosperi, et al., 2023, different structural schemes were made to investigate the effects of unidirectional 3D settlement profiles. It assessed the set of model types which included 2D façade models, similar to those in Sangirardi, et al., 2020, a 2D beam-façade composite models which aim to represent the contribution of adjacent walls, and a variation to also account for the substructural behaviour, and a set of 3D models focused on only representing the façade, outer perimeter of the building and explicit

building itself. The 2D modelling propositions were done through plane stress elements and 3D models with shells, all of which made use of a smooth interface from which the displacements were applied.

The findings demonstrated the effectiveness of equivalent 2D models to depict well the behaviour of the structure and were also computationally much more efficient. Further conclusions drawn included simplified façade models demonstrated to under-represent the damage patterns predicted in the structure by a factor ranging from 2 to 7 times, with 3D models also presenting higher damage levels.

### 2.4.5.1 Settlement induced Finite Element Model sensitivity effects

In the context of subsidence-affected structures, Rots, Korswagen, Eguren, and Longo (2021) conducted a sensitivity analysis of masonry models under settlement in Groningen, using finite element analysis (FEA) to assess the damage expected to masonry facades.

The study found that different foundation types could influence damage levels by 25% to 50%, while pre-existing damage amplified predicted damage by factors of 2 to 17. Substructural modelling using semi-coupled models increased damage by 9.5 times compared to uncoupled models. Material properties also played a key role, with sagging profiles experiencing damage 13-20% earlier and hogging profiles 20-30% earlier. The research highlighted that materials with lower resistance accommodate deformations better, reducing damage. Notably, the elastic modulus was identified as a critical parameter, as a higher modulus can delay the onset of damage when tensile strength is held constant.

Further sensitivity studies on subsidence-induced masonry structures were conducted by Prospero et al. (2023), with a focus on various topological features of masonry facades, substructure characteristics, soil properties, and general model parameters. The study found a strong correlation between the retrieved angular distortion values and the applied distortion, indicating that more deformable models generally resulted in higher levels of damage. Additionally, the research demonstrated that several factors, including weak masonry material properties, higher length-to-height (L/H) ratios, settlement shape, building mass, presence of transverse walls, and elastic parameters, exhibited high sensitivity in influencing the final damage states of the facades.

Lastly, Giardina, 2013 found for a set of analyses on masonry buildings settled due to tunnelling settlements that the parameters that had the biggest influence on the analysis damage level were the soil structure interface stiffness followed by the masonry fracture energy and the Tensile Strength.

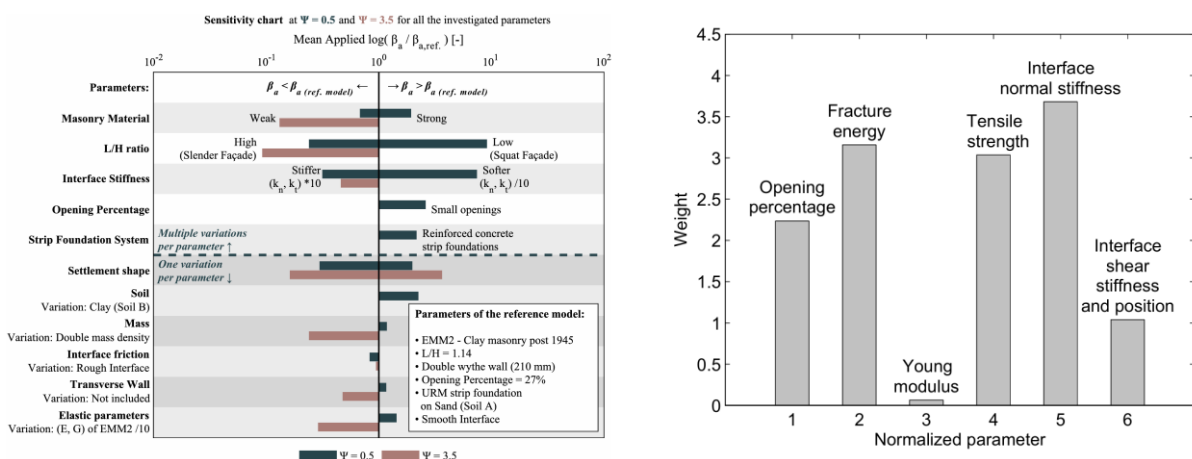


Figure 21: Sensitivity analysis on settlement experiencing FE Models (Prospero, et al., 2023; Giardina, 2013).

## 2.5 Calibration of Finite Element Models

In subsidence-involved masonry problems, uncertainties can arise from several sources, including but not limited to, difficult-to-measure soil deformations, soil-structure interactions, naturally varying properties of masonry and mortar, irregularities in the geometry of masonry units and mortar joints, challenges in accurately characterizing mortar properties and fracture energies, and possible presences of pre-existing damage. Therefore, given the breadth and depth of these uncertainties, it is impractical to account for all of them comprehensively. This is why engineers often rely on informed engineering judgment to interpret results which are founded on uncertainty-riddled problems.

Often in the literature, the terminology model verification, validation and calibration is used interchangeably. For this purpose, Atamturktur, et al., 2010 provides a good breakdown of the difference between the three. Verification focuses on ensuring the mathematical correctness of the model, specifically checking whether the numerical solution is precise and the equations are being solved correctly. Validation is concerned with accurately representing real-world phenomena. In the context of Finite Element Models, this involves selecting appropriate boundary conditions, topology, material laws, and loading conditions to ensure the model reflects the physical reality accurately. In such instances model correlation techniques, i.e. procedures that involve the comparing of analytical results with empirical observations (Atamturktur, et al., 2010), help achieve correlation between the model outcomes and observed data. When such a correlation is achieved, the underlying assumptions and modelling approach are considered valid. Conversely, discrepancies are attributed to either inaccurate parameters or flawed modelling decisions. Calibration is specifically employed to address inaccuracies in parameters and has historically been accomplished through manual trial-and-error methods as well as sensitivity analysis.

Calibration comes into play when there is a discrepancy between model predictions and physical evidence. It involves fine-tuning the model's parameters to better align with the observed data, thereby improving its accuracy, it is most effective for models that exhibit higher sensitivities. Calibration is a crucial step within the broader process of validation. Therefore, calibration takes an inverse problem role, when this is done in a deterministic fashion the problem turns into, what model features need updating to reduce the residual measure between measured and computed model solutions targets (Seung-Seop & Hyung-Jo, 2016).

### 2.5.1 Successful calibration instances of Finite Element Models

A relatively new research area is the implementation of automatic deterministic calibration techniques. These methods involve the algorithmic calibration of modelling input parameters based on key performance indicators (KPIs) derived from the model. Historically, automatic FEA calibration has primarily relied on gradient-based methods and least squares approaches. However, gradient-based techniques often face challenges in highly non-linear problems, where the efficiency of gradient tracing is reduced. To mitigate these issues, researchers have explored non-gradient-based calibration algorithms, such as direct search methods and particle swarm intelligence methods through PSO (Particle Swarm Optimisation).

Despite offering a systematic calibration process, these methods have been constrained by the extensive number of input combinations required to optimize parameter selection. This poses a significant limitation, given the computational expense associated with updating finite element (FE) models,



especially in high-fidelity contexts (Ramancha, et al., 2022). Consequently, these alternative strategies remain relatively novel, with their application predominantly limited to numerical demonstrations and small-scale structural models under controlled laboratory conditions. These methods have been even less prevalent in their implementation of real-world structures and especially in high-fidelity FE models (Liu, et al., 2021) therefore, more efficient solution search methods could potentially allow more widespread model calibration.

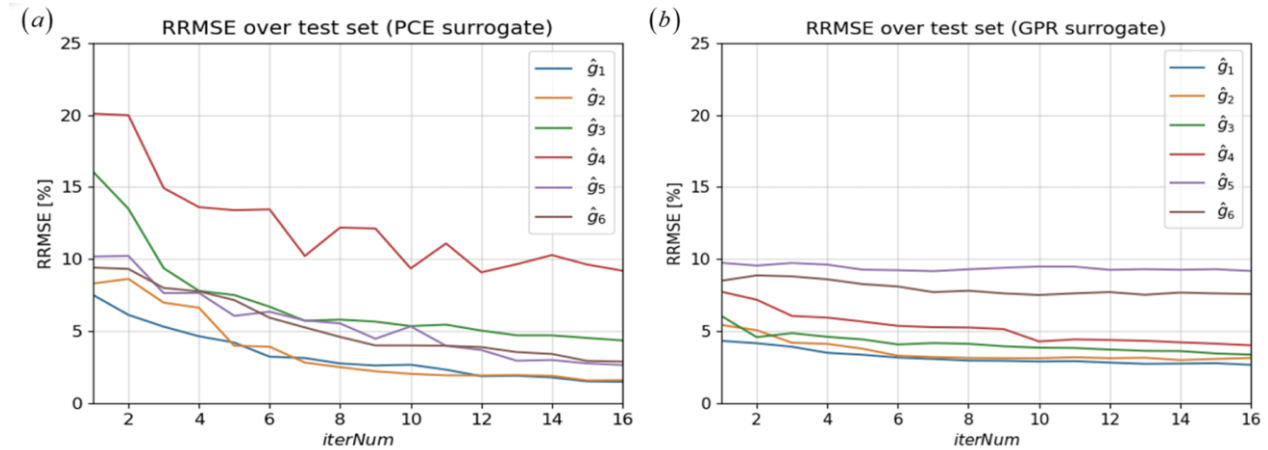


Figure 22: RMSE for the calibration procedure through both surrogates (Ramancha, et al., 2022).

Arguably the most successfully implemented FEM calibration procedure was performed by Ramancha, et al., 2022 which used a set of surrogates in Polynomial chaos expansion (PSO) and a Gaussian Process (GP) along with a quasi-random search technique through Sobol sampling to calibrate the Finite Element Model of a locked gate. The procedure whose Finite Element Model expense was 00:02:10 [hh:mm:ss] for a total procedure time of approximately 15hrs demonstrated that the use of surrogates for the calibration procedure reduced the calibration time by a factor of four.

The application of such methods to masonry FEA has been less common, and also not been applied to crack models. Bartoli, et al., 2017 also used Bayesian model updating to calibrate the Young’s modulus of linear modal dynamic analyses of historic masonry towers. Kibriya, et al., 2024 made use of different particle swarm intelligence optimisation methods paired with a CNN to calibrate 4 model variables by recreating the load-displacement curve of an arch and using the CNN to reproduce the failure mechanism of the arch which was calculated through the Discrete Element Method (DEM).

## 2.5.2 Bayesian optimisation: a possible solution

Bayesian Optimization (BOPT) is an effective approach for sample-efficient optimization of expensive-to-evaluate black-box functions. Applications range widely between aerospace engineering, materials science and civil engineering (Ament, et al., 2023). The usual characteristics of suitable BOPT problems are a combination of any of the following properties:

- The set of inputs is of a dimensionality  $D$ , which is not too large, but approximately less than 20.
- The objective function is continuous and is “expensive to evaluate”, in that a feasible number of evaluations is limited usually in the range of a few hundred.
- The objective function lacks known solution space features such as concavity or linearity that would make it easy to optimise and the overall behaviour is “Black-box”

- The objective function is non-differentiable
- The focus is to find the global optimum rather than a local optimum (Frazier, 2018)

The first main component in the BOPT framework is the Gaussian process (GP). The use of a Gaussian process is both the central component and the underlying reason for the improved capabilities of BOPT against other automatic calibration methods based on non-probabilistic kernel methods (Krauth, et al., 2017). This is because the GP is a non-parametric model, previously used approaches in FEM calibration, such as least-squares or Particle swarm optimisation (PSO), it directly uses the observations to map the solution space. BO leverages its probabilistic surrogate model along with the second main component in the algorithm, the acquisition function, to dictate when and where to explore or exploit current solution space positions, this being in its most basic and popular formulation.

```

Place a Gaussian process prior on  $f$ 
Observe  $f$  at  $n_0$  points according to an initial space-filling experimental design. Set  $n = n_0$ .
while  $n \leq N$  do
  Update the posterior probability distribution on  $f$  using all available data
  Let  $x_n$  be a maximizer of the acquisition function over  $x$ , where the acquisition function is computed using
  the current posterior distribution.
  Observe  $y_n = f(x_n)$ .
  Increment  $n$ 
end while
Return a solution: either the point evaluated with the largest  $f(x)$ , or the point with the largest posterior
mean.

```

Figure 23: Basic pseudo-code for the Bayesian optimisation procedure (Frazier, 2018).

A Gaussian process is a collection of random variables represented by a joint Gaussian distribution with mean  $m(x)$ , and covariance  $k(x, x')$ , expressed as,  $y(x) \sim \mathcal{GP}(m(x), k(x, x'))$ . For a set of inputs  $X = \{x_1, x_2, \dots, x_n\}$ , and their corresponding target values  $f = \{f(x_1), f(x_2), \dots, f(x_n)\}$ , the evaluation of new observations can be incorporated by a procedure known as Bayesian Model Updating. The process begins with a GP with prior distribution, assumed to be Gaussian,  $\mathcal{N}(f; m, K_{X,X})$ , which has zero mean,  $m$ , and covariance  $K_{xx}$ . Since at many times the observed targets are assumed to be noisy evaluations of a true function, an observation model  $y_i = f(x_i) + \epsilon_i$ , is adopted, with noise drawn from a zero mean and unit variance Gaussian distribution,  $\epsilon_i \sim \mathcal{N}(0, \sigma_n^2)$ .

Then by maximising the evidence or marginal likelihood and employing Bayes theorem the posterior distribution can be achieved, the results of this are also Gaussian which is why it can maintain its probabilistic interpretation,  $\mathcal{N}(\mu(x^*), \sigma^2(x^*))$ . The posterior expressed by its mean,  $\mu(x^*) = k_{x^*,X} K_{X,X}^{-1} y$ , and covariance,  $\sigma^2(x^*) = k(x^*, x^*) - k_{x^*,X} K_{X,X}^{-1} k_{X,x^*}$ . By iteratively performing this procedure repeatedly the GP continues to further improve its understanding of the solution space and be more certain and better approximate the regions where the best solution is most likely to be found.

<b>Prior</b>	<b>Marginal Prior</b>	<b>Employ Bayes</b>	<b>Arrive at posterior</b>
$p(f   x)$ $= \mathcal{N}(f; m, K_{X,X})$	$p(y   x)$ $= \mathcal{N}(y; m, K_{X,X} + \sigma_n^2 I)$	$p(f   X, y) = \frac{p(y   f) p(f   X)}{p(y   X)}$	$p(f(x^*)   X, y, x^*)$ $= \mathcal{N}(\mu(x^*), \sigma^2(x^*))$

Equation 3: Gaussian process formulation when employed for a regression task.

One of the most important architectural decisions influencing the Gaussian Processes (GPs) capability to capture the underlying patterns is the adequate selection of an appropriate kernel. GPs are vulnerable

to spectral biases, they tend to over-smooth the actual solution, as mostly happens due to the inadequate selection of a kernel which prevents the identification of region-specific discontinuities. Therefore, it is crucial to choose a kernel that aligns with the most likely characteristics of the data. Among the many available options, the Matérn kernel is the most popularly employed due to its flexibility and capabilities, making it well-suited for modelling covariance in situations with unknown or irregular structures.

The Matern kernel makes use of the modified Bessel function of the second kind,  $K_\nu$ , which governs how covariance changes between distant points, a gamma function,  $\Gamma(\nu)$ , plays the role of normalizing the kernel and determining the differentiability of the covariance function. Additionally, the kernel also incorporates the Euclidian distance between observations  $r = (|\mathbf{x} - \mathbf{x}'|)$ , the variance parameter  $\sigma^2$ , length scale  $l$  and, smoothness parameter  $\nu$ . The calibration of these parameters allows the model to non-parametrically capture the covariance between input features, and guide the combinatorial behaviour of the different variables to achieve the desired changes of the target.

$$K(\mathbf{x}, \mathbf{x}') = \sigma^2 \frac{2^{1-\nu}}{\Gamma(\nu)} \left( \frac{\sqrt{2\nu} r}{l} \right)^\nu K_\nu \left( \frac{\sqrt{2\nu} r}{l} \right)$$

---

*Equation 4: Matern Kernel formulation and covariance matrix for a sinusoid function.*

The kernel parameters are tuned using an evidence maximization function, which directly evaluates the probability of observing the data under the chosen model without relying on approximations. This process is crucial for Gaussian Processes (GPs) to operate as non-parametric models. By maximizing the evidence function during training, the model selects hyperparameters that best fit the observed data, leading to more accurate and reliable surrogate models.

In this case, the exact marginal log likelihood (MLL) is used as the evidence measure. The MLL is the default choice when transitioning from weight-based learning methods to non-parametric models like GPs. It consists of three key components: the data fit term, which measures how well the model predicts the observed outputs; the complexity penalty, which helps prevent overfitting by discouraging overly complex models; and a normalization constant, which ensures the likelihood is properly scaled.

$$\log p(y | X) = -\frac{1}{2} \mathbf{y}^\top (K(X, X) + \sigma_n^2 I)^{-1} \mathbf{y} - \frac{1}{2} \log |K(X, X) + \sigma_n^2 I| - \frac{n}{2} \log 2\pi$$

---

*Equation 5: Exact Marginal Log Likelihood.*

The final major component and differentiator of BOPT with other surrogate-based methods is the acquisition function. The most commonly used acquisition function is Expected Improvement (EI). EI is predicated on the principle of selecting the next evaluation point in an optimization process that maximizes (or minimizes, depending on the objective) the improvement of the best-observed outcome.

The process begins by identifying the best result obtained from previous evaluations, which serves as a reference point. The surrogate model, such as a Gaussian Process, is used to approximate the objective function, from which its optimization process starts by initializing multiple points to search for the next best location. The acquisition function, often Expected Improvement (EI), estimates the potential improvement at each candidate point by comparing it with the current best-known result. The point that maximizes this expected improvement is selected as the next location to evaluate, it does so by also

accounting the uncertainty in this evaluation. This approach iteratively refines the best-known solution by choosing the most promising points at each step, guiding the optimization towards the global optimum.

While a range of alternative acquisition functions exist, primarily Knowledge Gradient and Entropy Search, they are generally considered more specialized and are only necessary when the primary assumption of EI—that the main benefit of sampling comes from improvement at the sampled point—is not fulfilled (Frazier, 2018). The acquisition function presented below is the Log Expected Improvement (LEI), a variation of the EI function discussed above. The use of Log acquisition functions is recommended based on the findings of Ament et al. (2023), which proved the benefits of log-based acquisition in addressing diminishing gradient issues impacting the optimization of the acquisition function. The formulation seen on the right corresponds to the analytical expression of this acquisition function.

$$A_{\text{LogEI}}(\mathbf{x}) = \mathbb{E}[\log(\max(1, f(\mathbf{x}) - f_{\text{best}}))] \quad \alpha_{\text{LogEI}}(\mathbf{x}) = \log(\sigma(\mathbf{x})) + \log[(\mu(\mathbf{x}) - f_{\text{best}})\Phi(Z) + \sigma(\mathbf{x})\phi(Z)]$$

Where,  $Z = \frac{\mu(\mathbf{x}) - f_{\text{best}}}{\sigma(\mathbf{x})}$

---

*Equation 6: Log Expected Improvement (LEI) Acquisition function and its analytical formulation.*

The procedure above outlined, takes place, in every iteration in the BOPT algorithm, it may seem long and time-consuming, yet in situations where the evaluation of the objective function is expensive, i.e. a single evaluation takes minutes to be performed this trade-off is a worthy sacrifice.

### 2.5.3 Detailed Insights into Bayesian Optimisation algorithms

When selecting a GP surrogate, key considerations include the type of noise (homoskedastic, heteroscedastic, or fixed), whether multi-output or single-output predictions are needed, and whether the optimization involves handling multiple tasks (multi-task models) or mixed feature spaces. In the context of FEM calibration, noise is generally not a primary concern unless the robustness of the FEM is questionable. Instead, the focus is often on managing multiple model features, which can be either discrete or continuous, such as may be in the case of masonry crack models, failure modes, crack-bandwidth regulations or softening curve choice.

Another crucial decision is the choice of acquisition function. Analytical acquisition functions like Expected Improvement (EI), Upper Confidence Bound (UCB), and Probability of Improvement (PI) are widely used for selecting single candidate points ( $q=1$ ). These functions are particularly relevant to FEM optimization approaches due to their inherently sequential nature. However, this characteristic can slightly limit their optimal performance. Figure 24 demonstrates that for various dimensionalities  $d$ , Bayesian Optimization (BOpt) problems typically identify the best solution within approximately 50-300 evaluations. This efficiency makes these methods well-suited for calibrating expensive black-box functions. The figure also highlights how using logarithmic variants of the Expected Improvement acquisition functions was shown to significantly enhance performance by effectively addressing shattered gradients. This simple variation in performance through different acquisition functions underscores how an improper problem formulation can lead to sub-optimal results.

The other main influencing factor in the capability of BOpts solution is the choice of Hyperparameters which are mostly involved in tweaking the behaviour of the acquisition function. In Improvement based acquisition functions this refers to exploitation-exploration trade-off. This follows the optimisation of

the surrogate, if more samples are selected, more different locations are evaluated (exploration), whilst if more restarts are prescribed the region around that best location in that region is ensured to be found (exploitation).

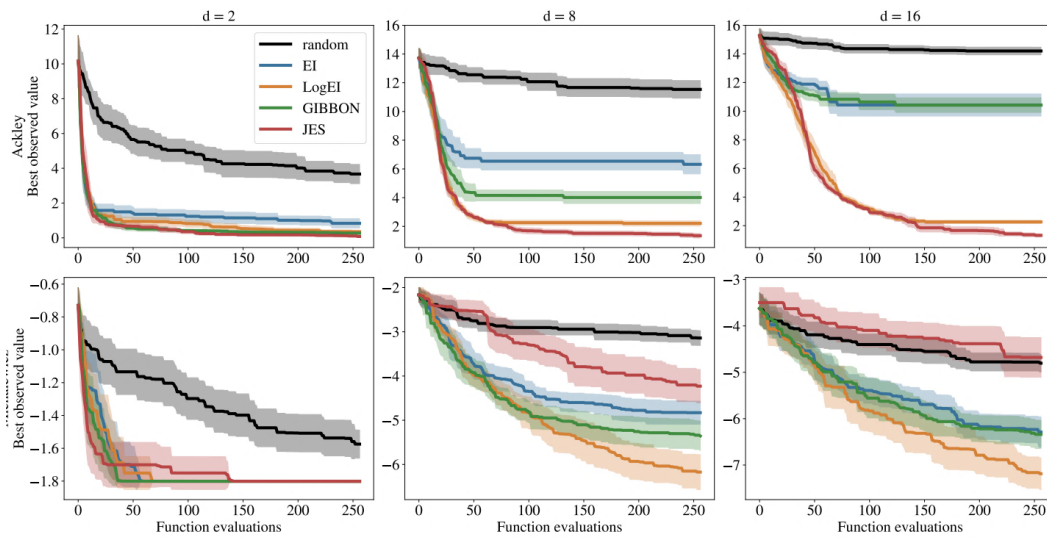


Figure 24: Objective function evaluation on the severely non-convex Ackley benchmark problem (Ament, et al., 2023).

A frequently overlooked aspect of optimization methods is the selection of the initial search technique, which is particularly critical in Bayesian Optimization (BOpt) problems. The initial sample provided to the surrogate model must promote a balanced exploration of the solution space; otherwise, there is a significant risk of inefficient computation or failure to identify the global optimum. In BOpt, where the number of evaluations typically ranges in the low hundreds, traditional methods like grid or random search are inadequate for high-dimensional problems, especially when the initial sample size is small (10-50). In such cases, quasi-random methods such as Sobol sequences or Latin Hypercube sampling substantially enhance the efficiency and robustness of BOpt by ensuring a more uniform distribution of sample points across all dimensions, thereby increasing the informativeness and coverage of the space.

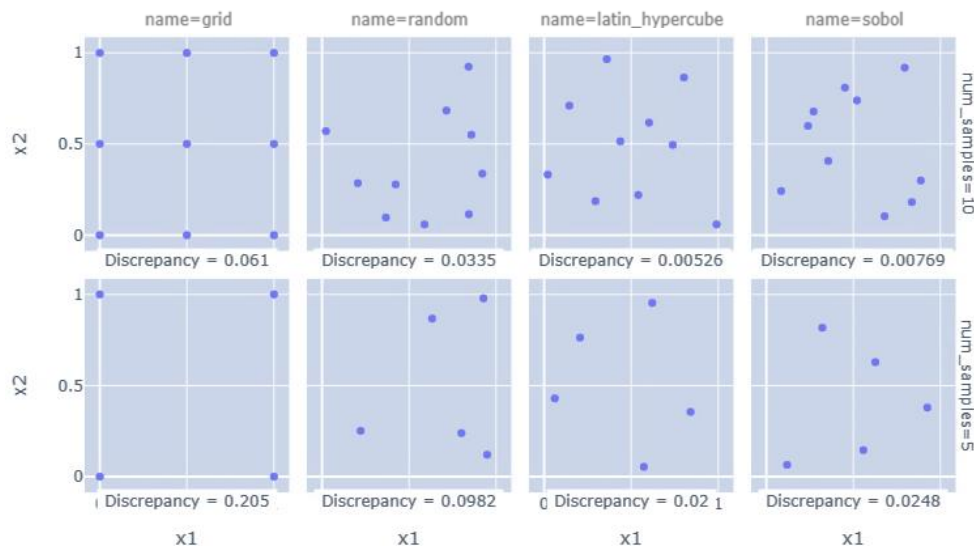


Figure 25: Illustration of worsening discrepancies of traditional vs pseudo-random search techniques in low sample spaces (Baird, 2024).

## 2.6 Conclusions

The findings from the literature review first highlighted that the characterisation and understanding of the processes behind subsidence-based settlements are well-known. The spatial variation of the displacement profiles has been thoroughly investigated for tunnelling, excavation and seismic-induced settlements and has been shown to take sagging and hoggin profiles. In urban-specific subsidence scenarios, the shape of the displacement profiles has also been examined by investigating the likelihood of different shapes from measurement surveys carried out on buildings. For a survey of 600 walls, one-ended settlement through sagging and hogging shapes were the most commonly occurring settlement profiles.

Research on the characterisation of masonry as a composite material showed that the physical masonry material properties have been characterised based on different masonry types, and different ages for Dutch-specific masonry. Furthermore, the empirical relationships to determine Finite Element Modelling material parameters for different masonry modelling approaches are also available and allow accurate material characterisation in numerical analysis for different masonry material modelling approaches. Nevertheless, the uncertainty in the physical masonry material properties and empirical relationships is still large.

The review on the response of masonry buildings to settlements showed to be influenced significantly based on the subsidence shapes being outlined above. The effect the displacement profile had on damage was demonstrated to influence the cracking location and crack profile, which were also influenced by façade and building characteristics. The superstructural response to other drivers outside of subsidence is also well studied with de Vent, 2011 presenting a thorough compilation of sources that relate to most possible damage/driver combinations.

The characterisation of damage is currently made through deformations expressed through Soil Related Intensity parameters (SRI), whilst cracking damage is evaluated through a set of Damage Levels related by the maximum crack widths or a continuous Damage Parameter ( $\Psi$ ), that accounts for the maximum crack-width, crack length, and the number of cracks.

The influence of the substructure on the superstructure response was demonstrated to be the main underlying factor in the presence of damage. Although the relevance of Soil, Foundation and SSI was not thoroughly reviewed, the greater susceptibility of buildings with shallow foundation systems has been identified to be more pronounced under similar deformation levels. By evaluating the still large number of homes with shallow foundation systems from building surveys it is confident to say that many Dutch homes remain vulnerable to settlement-induced damage.

The field which was most reviewed is the simulation of the superstructural building response. A range of different assessment procedures namely, visual, empirical, probabilistic, analytical, and numerical procedures currently allow the damage assessment and estimation of the building response under different problem characteristics.

The most popular methods, firstly, empirical methods demonstrated a varied set of experimentally correlated determined thresholds suitable to approximate Damage Levels under specific scenarios. The Limit Tensile Strain Method (LTSM), appeared the most popular non-computational approach and it can

evaluate the damage not only to different settlement troughs but also incorporate further subsidence process features such as settlement rates and façade features to calibrate the estimated strains expected on the building. The Load Path Method (LPM) is been less popular analytical method but presents the only non-computational method able to assess the cracking location and crack progression.

By far the most popular damage assessment method in literature is Finite Element analysis. Model variations in settlement-induced masonry damage are numerous but In instances of larger masonry elements and lighter damage in the form of cracking the superstructural modelling approach is preferred through a smeared crack modelling approach. This approach is favoured as it allows an accurate estimation of damage severity, location and behaviour in a computationally efficient manner. Further differentiation is also made upon the modelling of the reproducing of the settlements but all Coupled, Semi-coupled and Uncoupled modelling approaches have seen success under different problems.

When it comes to the representation of the masonry through a continuum-smeared cracking approach the two most possible constitutive laws in the software Diana FEA are the Total strain-based crack model (TSCM) and the Engineering masonry model (EMM). Both material laws possess some strong characteristics that influence the performance and results of the models, but both also constitute popular approaches for the simulation of masonry. In specific instances, the influence of the masonry Young's modulus and Tensile strength was demonstrated to have the greatest influence on model results.

Further, research has also focussed on the relevance and influence of different building topological features and model schemes. Research in this domain demonstrated that the capabilities of 2D models quite well equate to those of full-fledged 3D counterparts. Further work included the effect building characteristics such as adjacent walls or sub-structure components and building façade characteristics have on the amount of damage expected on models. The sensitivity of explicit model features showed that higher damage levels can be expected in buildings with slender facades, weaker material parameters, stiffer interfaces depicting SSI, not including adjacent walls, and the disregard for modelling the building's foundation system.

Lastly, calibration procedures for FE models are still in their early stages. Most current approaches validate model results through sensitivity studies, which help account for the influence of uncertainties on outcomes. Automated calibration analyses have primarily focused on experimental scenarios and dynamic analyses, with limited applications in real-world scenarios which have happened with computationally inexpensive models. In this context, probabilistic and surrogate-based optimization methods have been popular due to their ability to reduce the number of objective function evaluations. Research has largely concentrated on refining these procedures and assessing their impact on the process duration, rather than on the potential benefits they can offer. Bayesian Optimisation demonstrated a suitable optimisation approach for the necessities of the optimisation of expensive but lower dimensional Finite Element Models.

# **3. Case study selected for the damage assessment**

---

This section presents a review of the case study used in this research to evaluate the accuracy of settlement-induced damage assessment methods. Both the information from the Foundation Assessment report has been analysed to determine the structure's characteristics and quantify the building's damage state.



In the Netherlands, when buildings experience settlements, foundation inspection campaigns are often conducted by independent external contractors to evaluate whether damage instances observed in the superstructure indicate the inability of the foundation to prevent further settlements. KCAF (Kennis Centrum Aanpak Funderingsproblematiek)—the institution responsible for addressing subsidence-related damage to buildings across the Netherlands—has contributed to managing foundation problems by promoting research, providing lists of accredited inspection contractors, and together with several municipalities, sharing the results from foundation assessments in hundreds of homes.

The quality of these foundation assessments can vary significantly depending on the contractor and the scope of the evaluation. Some reports provide detailed analyses of damage and measurements, while others can be part of broader neighbourhood measurement campaigns and are mostly focused on measuring deformations from buildings and not damage representations and documenting building features. Nevertheless, for higher damage scenarios, the reports of set homes are not as usually made publicly available due to homeowner financial interests. Whilst in some instances some assessments have been made available following the demolition of the structure.

One of these reports has been the focus of this thesis. The report documents the findings from a survey conducted in June 2019 to the building in question. The building is a detached 2-layer single-wythe unreinforced masonry building. Its construction dates to 1961, and it boasts 2 floors and a cellar. The final damage state is known due to the good visual evidence available in the report. Further information in the form of displacement and tilt measurements, and building characteristics are also available as a more thorough damage documentation effort was made when compared to most foundation studies. It is important to note that the purpose of this report was not scientific, but to provide an overall assessment building assessment to determine the necessity to intervene in the building's foundation system, as well as provide an initial quota for the expected costs of retrofits.

In this instance, the main conclusion drawn by the inspectors was that the building's foundation capacity was insufficient given the beneath soil conditions and measured deformations. The conclusions advocated that countermeasures should be retrofitted in a 1-5 years period to the building following the assessment date. Consequently, the building was demolished circa 2019 due to the assessed insufficiency from the foundation to prevent future settlements.



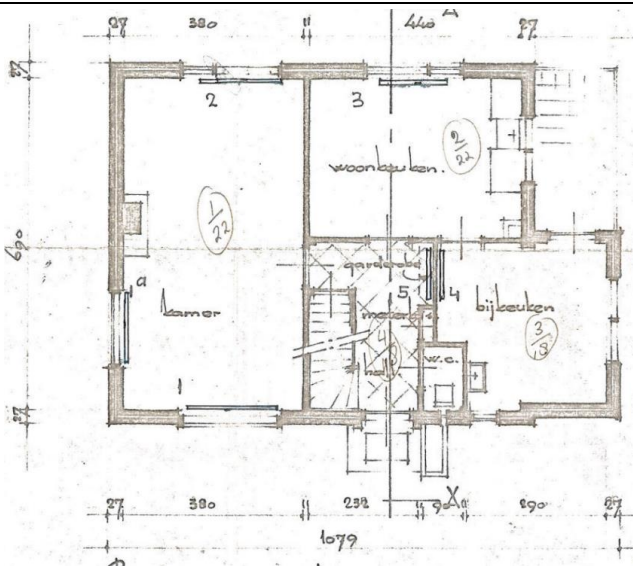
*Figure 26: Adaptation sketch of the case study building*

### 3.1 The building's superstructure

The building has two floors, the ground floor has an extension on the eastern side of the house, this extension is a balcony on the first floor. The first floor geometry resembles a quadrilateral with the primary axis of this quadrilateral being 10.8m in length for the ground floor and in the case of the first floor being 8.85m, the secondary axis is 7m in length with a height to the top of the second floor of 5.25m. There is a central staircase of approximately 3.5m by 3.75m and two main partition walls dividing the inner area of the building, although these are not structurally relevant.

The building's roof is composed of a queen spandrel roof truss of webs size 180x80mm and top cords size 200x80mm, additionally, there are horizontal purlins over which the slated roof is supported. This truss is oriented along the major axis of the building, and it is sustained on the outer walls of the Northern and Southern sides of the building. There also is an underneath cellar, approximately 2m in depth which is located on the southward-facing side of the building.

**1st-floor plan view**



**Building profile view**

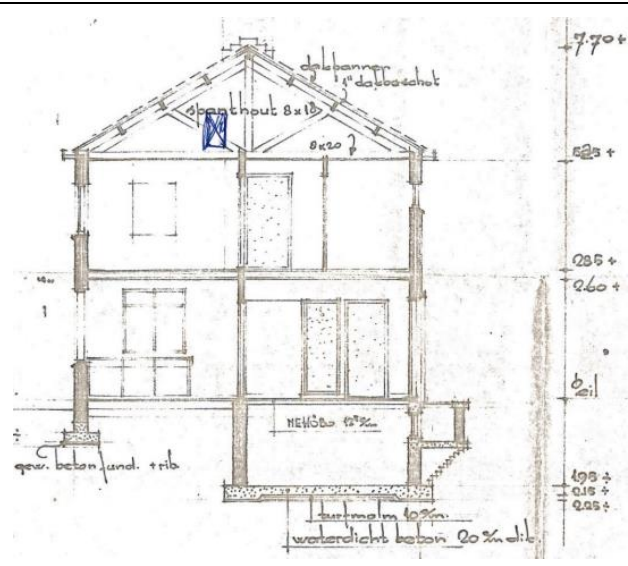


Figure 27: Archive architectural drawing of case study building

The main structural component in the building are the unreinforced single-wythe masonry cavity walls that have a combined thickness of 270mm and a single cavity of unspecified will be assumed to be 70mm in width, no further information is available on any shear connectors between leaves. All the above information has been taken from the provided architectural drawings from the plan and profile views of the building. The masonry bond used in these walls is a Flemish wall garden bond where a longitudinal unit (protruding into the interior of the building) is placed every 3 units. By counting the number of bricks and comparing the building plan dimensions, it has been determined that the masonry units are close to Dutch standard sizing with an approximate dimension of 61x200x100mm [h,l,w], and varying mortar thicknesses ranging from 2 to 5mm.

Furthermore, the internal leaf of the building makes up the main load-bearing component of the structure due to the presence of concrete lintels on the inside leaf above the openings. The building façade opening types are also varied, 2 doors and 8 window typologies are present around the entire perimeter.

In the case of Wall 2, the northern-facing wall of the building, there are two sets of openings whose sizes

have been approximated by the counting of the units along their perimeter. The smaller opening is approximated to be 1400x940mm[h,w] in size whilst the larger opening is approximated to be 2100x1250mm [h,w] in size.

Since there is no registry of major modifications made to the structure, it is assumed that the masonry façade units date to the building's first construction, 1961. Therefore, the material properties of these have been approximated through a combination of Jafari, et al., 2022; Jafari, et al., 2017, these can be available in the Appendix.

## 3.2 The building's substructure

As will be discussed the structure has suffered significant damage. The driver behind this damage has been the settlements which have happened due to the soil subsidence, the nearby soil composition and foundation characteristics are necessary components to understand to estimate the likelihood and magnitude of displacements experienced by the building.

As can be seen in Figure 28 the building's foundations are relatively irregular, the foundation on the Northern side of the building is a strip footing, whilst the foundation on the Southern side of the building is the concrete raft foundation at the building's cellar. The size of both of these foundations is also evident, although it is not obvious if the raft spans the entire main axis length of the building the width of the concrete raft when compared to strip footing is evident. Possibly this may be an issue as the resistance provided by one side of the foundation may be greater than the resistance on the Northern side of the building. Furthermore, and possibly more problematic is the asymmetric depth at which both of these foundations is located which has been approximated to happen at different depths.

Further information on the nearby soil is available due to two perforation samples have been made nearby to the building, one date to the construction of the building itself from 1961 and another is available from publicly available perforation data, this sample was taken at a location 1km east of the building, but no information is provided about the exploration date. Both constructed lithology graphs show similar soil layer compositions. There are variations as to the thickness and thus the relative location of soil layers but in all, the open data samples help validate the original exploration made at the building's location. The building's soil profile has only been shown for the first 25m as these are the most influential soil layers. The soil layers show a primary soil composition of sands especially at lower depths. Nonetheless, the soil composition, near-surface is significantly different with mostly clay layers being located close to the foundation level and another 4 metres below that, some small peat layers are also located at around 7m below surface level. No water table measurements were made available, but the water table is possibly quite high due to the nearby presence of a large canal.

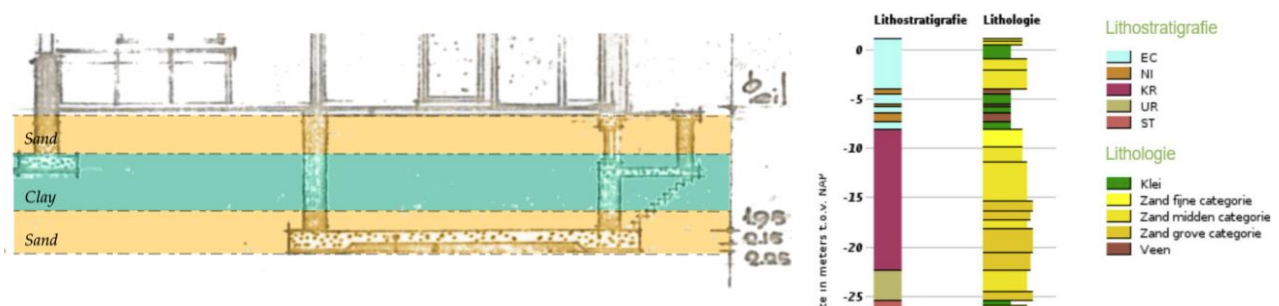


Figure 28: Approximated lithology at building foundation level and Borehole sample lithological graph.

### 3.3 The buildings' damage state

The near-surface soil layer compositions are most likely a problematic source for the settlements. The presence of a clay layer near the depth of the northern foundations' depth can be a further cause for the asymmetric resistance offered by the foundation system. Clays are soil layers that are susceptible to temporal variations in their thickness due to compaction, and swelling processes that occur due to changing loads and water tables. In the case of also nearby fine sands these layers are prone to varying resistance based on their saturation because of hydroplaning effects and their erodibility under higher water contents due to fluctuating water tables.

The identified discrepancies all most likely hint at the imbalanced resistance from both foundation systems although, the above reasoning is highly assumptious. The main driver behind the soil's resistance remains to be unknown in the water table location. Therefore, for this example, the soil simulation and analyses may pose an uncertain undertaking because of changing water tables as well as other temporal effects in weathering, non-linearity in soil properties and irregular spatial distribution of soil layers.

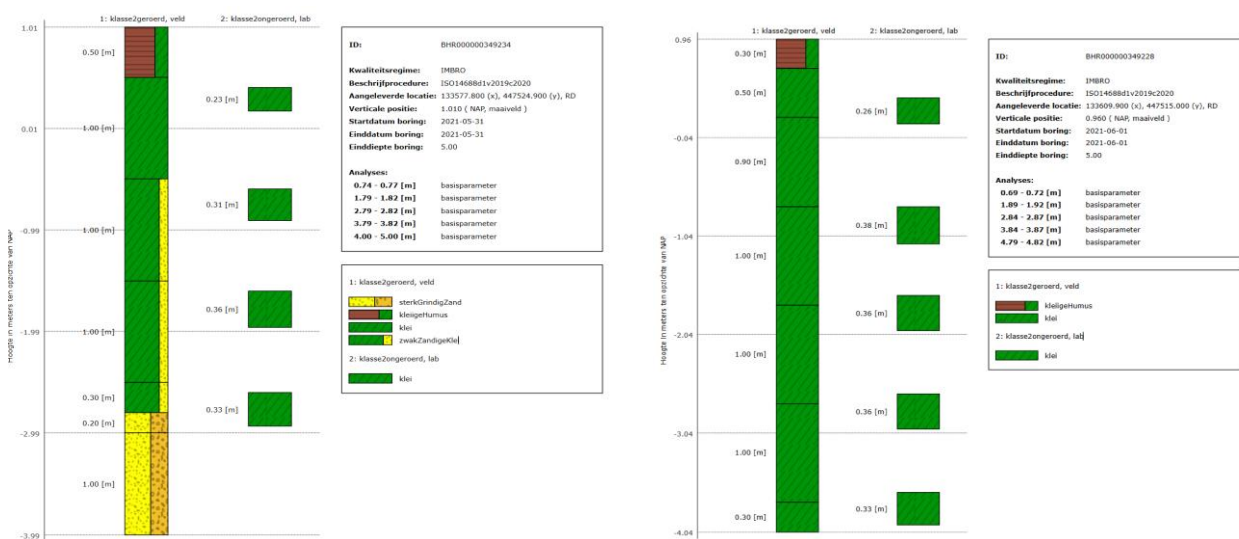


Figure 29: Open data CPT exploration around 1km east of the building.

### 3.3 The buildings' damage state

According to Korswagen, et al., 2019 and in a similar fashion to de Vent, 2011 there are three major damage forms to masonry buildings particularly when dealing with light damage to structures, these are cracking which indicates a permanent and visible loss of cohesion, permanent deformation changes to the building original state and permanent translations or rotations such as tilting or uniform settlements. In the case of a building, all these forms are present and have been measured and provided through the foundation assessment report in different forms.

The primary form of damage observed was cracking. To assess cracking, both its extent and severity were considered, accounting for crack size and impact on the building. TABLE 13 shows the damage distribution, with cracks identified using façade features and Google Earth images prior to demolition. Each crack was assigned a unique ID for classification in further analysis.

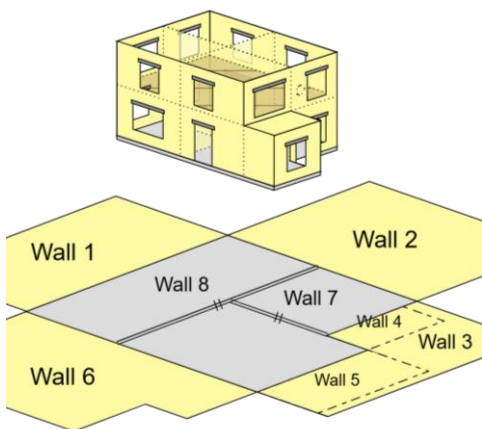
Nevertheless, the evaluation of the building's damaged state is a complicated task, as several key limitations underpin the documentation from the foundation assessment report.

- It is not clear if the crack widths relate to the average crack width or the maximum crack width.

- For those cracks which do not carry any crack-width estimates, the estimation of certain crack-widths has been done by the author based on the images. TABLE 13 indicates such cracks through those that use the close equals to symbol,  $\approx$ .
- For the damage quantification, the crack's crack lengths have also all had to be estimated. This is a simpler task than the estimation of the crack widths as the number of discursing units offers a good reference, but also introduces further uncertainty into damage estimates.
- The crack length estimates for inner-leaf damage were more complicated due to the exterior mortar coating in the walls, making it not impossible to count the number of units
- It is not clear how thorough a damage documentation campaign was carried out. This is a greater matter of concern for the inner leaf, as the building's wallpaper may hide otherwise evident cracking damage.

In all, the report documented the presence of 10 principal cracks in the structure, cracks which have been estimated to range up to 4mm in width. Most cracks have been identified to be concentrated in the north-facing façade of the building, Wall 2. These cracks mostly begin around the openings, and close to the concrete lintels. A second major cracking focal point has been the close to the building's central staircase in the partition walls, these are not as structurally relevant and it is not obvious if the partition walls are also masonry components.

The damage quantification of the structure was made through Korswagen, et al., 2019 damage parameter, a measure most relevant to the classification of "light damage" in the structure, nevertheless, the damage classification by Burland & Wroth, 1974 is also made. The final estimated damage measures are presented in TABLE 12 which the  $\Psi$  parameter has been approximated through Equation 1, along with the used wall naming convention for the structure. The evaluation provides damage estimates on a per-wall basis and also offers an overall building evaluation. As can be observed the majority of the building is mostly undamaged with two walls demonstrating concernable damage particularly the wall in the northern facade of the building (Wall 2) beginning to enter into structurally relevant damage states. Further light damage is also present in the interior leaf of Wall 1, with the rest of the structure remaining relatively undamaged. The overall building evaluation does present a "light damage" scenario which seems a fair evaluation given the documented evidence.

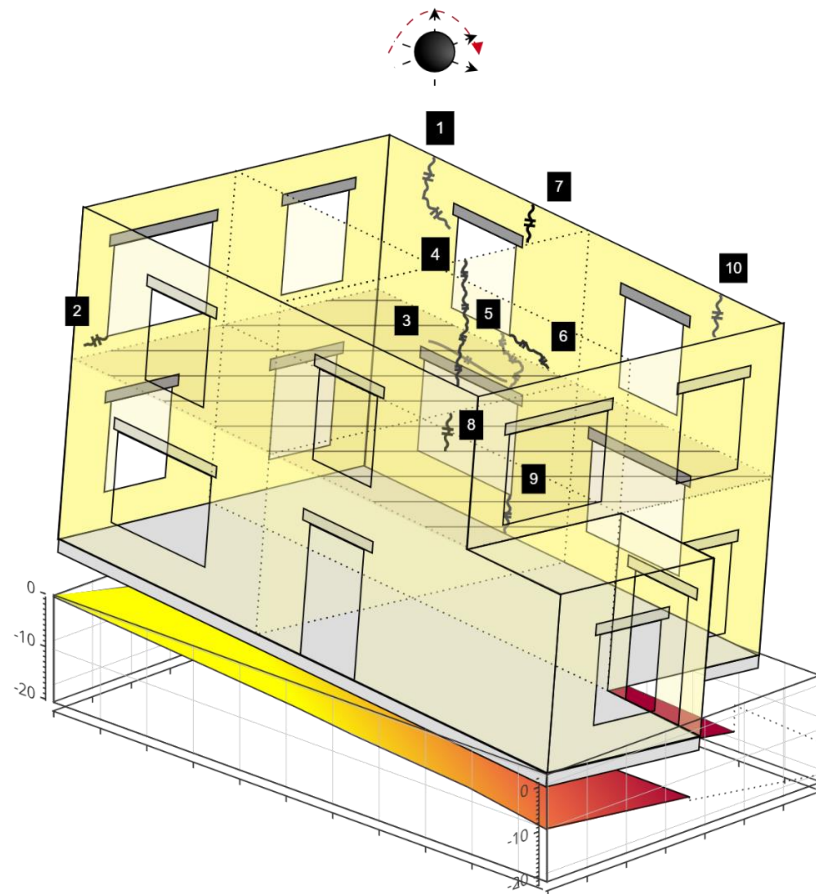


Wall	Area [mm <sup>2</sup> ]	$c_w$	$\Psi_w$ Outer	$\Psi_w$ Inner	$\Psi_w$	DL <sub>wl</sub>	$\Psi_{Building}$
1	390600	2.0	0	2.46	2.46	DL2	1,88 DL2
2	464625	2.9	3.53	3.01	3.7	DL4	
3	166950	0	0	0	0	DL0	
4	49020	0	0	0	0	DL0	
5	96720	0	0	0	0	DL0	
6	517980	0	0	0	0	DL0	
7	362250	0,01	N/A	N/A	0,502	DL0	
8	257250	0	N/A	N/A	0	DL0	
<b>Damage state</b>			<b>DS0</b>	<b>DS1</b>			<b>DS2</b>
<b>Damage Level</b>			<b>DL0</b>	<b>DL1</b>	<b>DL2</b>	<b>DL3</b>	<b>DL4</b>
Damage parameter		$\Psi < 1$	$1 < \Psi < 1.5$	$1.5 < \Psi < 2.5$	$2.5 < \Psi < 3.5$	$\Psi > 3.5$	
Approximate crack width		N/A	Up to 0.1mm	UP to 1mm	Up to 5mm	5-15mm	

TABLE 12: Building damage parameter  $\Psi$  assessment as per Korswagen, et al., 2019.

### 3.3 The buildings' damage state

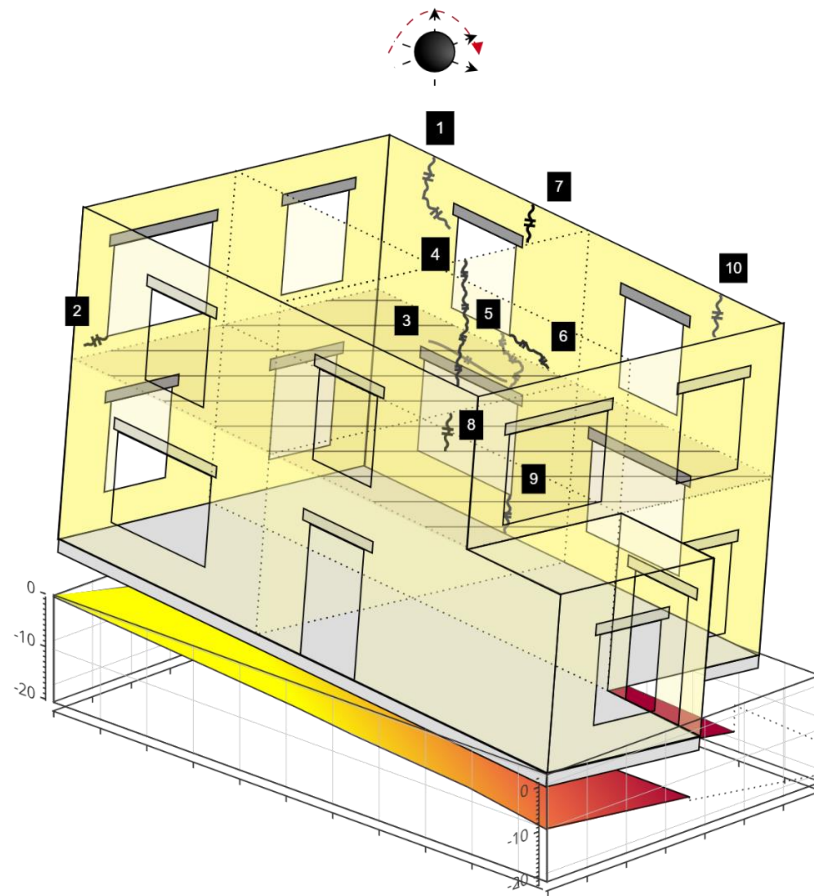
**Building state diagram**



Crack ID	Wall ID	Image	Class	Description	Crack Width	Crack Length
1	2		DL3	Tension due to settlement of the left-ward section of the wall.	4mm	885mm
2	1		DL2	Cracking on left building wall	≈2mm	1670mm
3 & 5	2		DL3	[3] Dilation crack [5] Operation lintel	[3] ≈3mm [5] ≈3mm	[3] 868mm [5] 670mm
4	7		DL3	Hairline Crack	≈0.1mm	2000mm
6	2		DL3	Differential settlement of the lintel towards the easter profile of the Building.  Previously repaired crack.	>3mm	1200mm

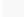
### 3. Case study selected for the damage assessment

#### Building state diagram



Crack ID	Wall ID	Image	Class	Description	Crack Width	Crack Length
7	2		DL1	Interaction of settlement and lintel	≈2mm	600mm
8	7		DL1	A crack formed most likely due to bearing stress	≈0.1mm	500mm
9	2		DL0	Formed dilation	≈1mm	994mm
10	2		<DL2	Possible operation rafter wood	≈2mm	980mm

Indicates:

 Locations where damage has been measured

 Locations where damage has been estimated

TABLE 13: Schematic damage review of the case study building.

### 3.3 The buildings' damage state

Not all damage manifested itself as cracking, due to the settlements the building also experienced significant deformations and tilt. These damage measures were evaluated through a set of skew measurements which were measured by evaluating the deformations of the bed joints around the perimeter of the building. These skew measurements only provide displacement values at discrete locations along a wall surface which gives rise to more jagged displacement profiles. This is dissimilar to the usual shapes of subsidence induced settlements found in the literature which is why the quadratic interpolation of these measurements may provide a more realistic estimate of the deformation profile. In case the 3D settlement profile was required these values were cubically interpolated for the buildings surface.

The original deformation chart shows a maximum deformation is 188 mm in the northeastern corner of the house. Nevertheless, the greatest differential settlement was experienced over the smaller axis of the building with a maximum deformation of 150mm in the western wall of the building, whilst the opposite relative settlement was 84 mm. Therefore the relative settlements occur over both orthogonal axes of the building indicating that the overall deformation gradient is SW-NE.

Interestingly, the magnitude of the deformations did not necessarily coincide with the damage concentration, as in the longer axis of the building and on the wall with the smaller settlement, the southern wall, was the focal point of damage. This same wall is situated above the strip footing and may therefore indicate that the severity of the settlements did not play as great a role as did the relative stiffness of the southern side of the building. Because little to no damage happened on the Northern side despite still experiencing significant deformations. The deformation gradient also possibly hints at the possibility that the building asymmetric layout may have had in the deformations as the extrusion on the eastern side of the building appears to be cantilevering the deformation along that side of the building as the deformation gradients are significantly smaller.

#### Deformations on the ground floor

#### 1st-floor levelling

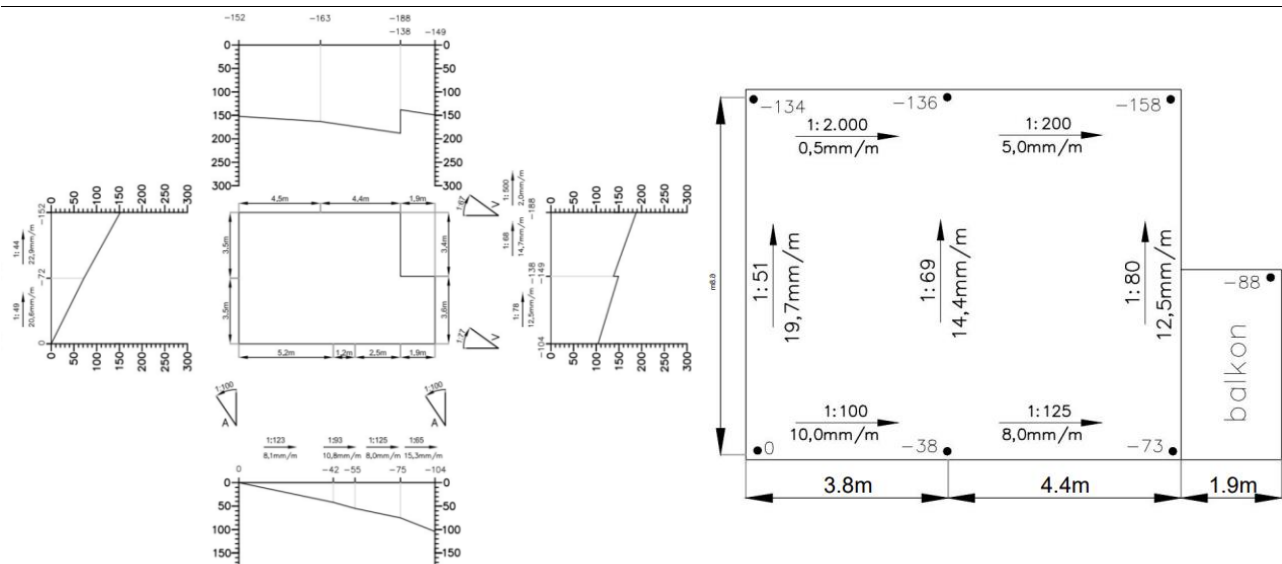


Figure 30: Building skew measurements and building settlement surface approximation.

If quadratically interpolating the displacements one can observe that in certain regions the angular distortions of the building may be overestimated since the profile takes a more concave profile, whilst when using linear interpolation, the relative displacement at regions of inflexion may be too big and lead to unrealistic cantilever effects or locally severe curvatures.



Further deformation measurements were taken through the lead joint measurements and ribbon levelling measurements. Although no description was provided for the methodology used to take these it seems that the lead joint measurements were taken by measuring the tilt from the ground-level bed joints up to a metre above ground. Whilst no information is provided for the Ribbon joint levelling these correspond to the tilts at different floors of the building.

TABLE 14 shows the amount of rotation observed for the different walls, with the distortion classifications showing the assessors' opinion on the severity of the tilts. The most significant tilts occur on the western wall/over the shorter axis of the building, as is expected given the settlement measurements. The lead measurements show how the significant horizontal tilts in the northern and eastern walls experienced the greatest tilts, deforming by 15cm and 30cm, 1m above the ground. The magnitudes of these rotations present a greater rotation along the minor axis of the building. Therefore, Walls 2 and to a lesser extent 3,4, out-of-plane bending effects are most likely influencing the damage forms observed in those walls. On the contrary, the opposite walls, Walls 1,6 will not be subject to the thrust generated by the building rotations as they will be supported on the inside by the building. As it may not be surprising the rotations should be most damaging to Wall 2 as the rotations measured over the shorter building axis are greater. Assuming the building behaves as a rigid body, the potential deformation of the structure has been attempted to be illustrated in the figure in TABLE 18.

Position	Ribbon joint levelling [ $\Delta_{z,max}$ ]					Lead joint measurement [ $\Delta_{x,y,max}$ ]					
	Deformation [mm]	Distance [m]	Tilt [mm/m]	Rotation	Classification	Deformation [cm]	Distance [m]	Tilt [mm/m]	Rotation	$\Delta$ Rotation	Classification
Wall 1	80	3.5	22.9	1:44	Extreme	5	1	5	1:200	1:0	Small
Wall 2	50	3.4	14.7	1:68	Extreme	15	1	15	1:67	[1:7,1:10]	Extreme
Wall 4,6	25	4.4	5.7	1:175	Significant	30	1	30	1:33	1:10	Extreme
Wall 6	29	1.9	15.3	1:65	Extreme	10	1	10	1:100	1:0	Significant

TABLE 14: Building rotational deformations

### 3.3.1 Evaluation of the foundation assessment report's completeness and robustness

Although this assessment report presented a much more thorough examination than most of its counterparts. Much information for an accurate building assessment is missing. Therefore, cautionary reasoning must be used when making use of the report. For this purpose, the different components of the report will be reviewed to quantify the quality of the available information for this thesis's scope. In general terms, this thesis's author is confident in the evidence and discussion presented in the report. This conclusion has been made given the overall correlation between the just presented damage concentration, building characteristics and measured displacements. The overall, picture of the problem seems coherent. It also believes that the archival data is sufficient for relatively accurate dimensioning for the numerical and analytical representation of the building.

This said, the author believes the damage assessment could have been carried out in a more detailed manner would the measurement campaign had happened for research purposes. Although the levelling measurements carried out should suffice (building rotations and displacements), this same precision was not made when evaluating the cracking damage. The cracking documentation could have been much more insightful with the shapes of the crack's initiation location and the maximum crack width of all cracks (since only some cracks had a specified thickness). This is inconvenient for this study assessment,

### 3.3 The buildings' damage state

but it is also possible that lesser documented cracks were believed quite unperceivable by the assessor, or their Damage Level (DL) was sufficiently low to not be sufficiently noticeable/not sufficiently large for precise measurements without more specialist equipment to be carried out. Therefore, in this regard, the quantification of cracking damage should be done with care.

<b>Source</b>	<b>Assessment by assessors</b>	<b>Assessment by author</b>
Architectural archival information	Sufficient	Sufficient
Soil exploration	Sufficient	Sufficient
Water table measurements	Not performed	Not performed
External Damage assessment	Insufficient	Insufficient
Internal Damage assessment	Insufficient	Insufficient
Ribbon joint measurements	Insufficient	Fair
Lead joint measurements	Insufficient	Fair
Floor levelling measurement	Insufficient	Fair
Construction assessment	Insufficient	Fair
Environmental assessment	Sufficient	Sufficient
Geotechnical assessment	Insufficient	Fair
Material Assessment	Insufficient	Insufficient

TABLE 15: Foundation assessment report confidence assessment.

Nevertheless, the overall assessment of the report is more optimistic than the assessors themselves it can be determined that the assessment report provides sufficient insights for an analysis to be carried out but also has some major limitations. Despite so, when compared to other foundations assessment reports it is pleasing to know that this assessment was carried out in a better manner than most, with many of its shortcomings potentially happening due to a lack of interest of the assessors to continue documenting the building since they had already demonstrated the necessity for upgrades to the buildings foundation system. Therefore, the limitations may not be necessarily due to the carelessness of the assessors and should be relied upon with caution. Overall, the assessment sufficiently serves this study's scope.

# **4. Damage assessment through empirical and analytical procedures**

---

The following section concerns the assessment of the building through non-computational based assessment procedures. Section 4.1 consists of a visual assessment of the building, 4.2 Is an empirical based damage assessment and 4.3 is an Analytical empirical assessment through the Limit Tensile Strain Method.

## 4.1 Visual investigation

The great progress in state-of-the-art techniques has led structural engineers to be able to perform better assessments, yet it can be argued that the notoriety of numerical tools such as Finite element analysis has led to less emphasis being placed on visually assessing or reasoning a building's structural state. Although this is for good reason — since often intuitive and visual approaches can be highly unobjective or highly dependent on an individual's experience and capacity as a structural engineer — it is also true that many fundamental characteristics of a building's current state may be overlooked when little attention is placed to the assessment of the building's condition, layout or characteristics before performing structural analysis. Visual assessments allow the identification of relevant information that may be relevant in the structural formulation of the problem and may interfere with the limitations of a chosen analysis method. With this in mind, de Vent, 2011 made a breakdown of the damage mechanisms present in masonry structures under different possible hypotheses. These were then combined into a diagnostic decision support tool that helps diagnose mechanisms occurring at a micro level and influencing the global behaviour of the building. De Vent, 2011 states that the use of the diagnostic tool must be employed by.

### Application of the Diagnostic Decision Support Tool by de Vent, 2011

The diagnostic tool demonstrated a reliable support tool when reasoning masonry damage. Despite several hypotheses being posed in its use for all damage instances, the final hypothesis appeared to agree with the overall behaviour seen in the building or building section. The last column in TABLE 16 shows how all hypotheses bar one appear to agree well with the mechanism. Nevertheless, it must be noted that the evaluation of tilts and deformations (also possible through the diagnostic decision tool), was not able to be tested due to the case-study building documentation being focused on cracking damage forms.

On an individual basis, the evaluation identified that the main causes for the cracks were either Vertical on-ended settlements, Vertical mid-heave settlements, and thrusts on the masonry caused by the concrete lintels. These hypotheses allowed us to categorise the damage forms into two influencing categories: those governed by the settlement of the building, and those which seem to form by the interaction of building façade characteristics with the deformations of the wall. Cracks 1,5,7,8,9 were identified to belong to the first hypothesis set and cracks 2,3,6 to the second. In addition to the individual mechanisms further global mechanisms were also identified by locations and combination of individual mechanisms. In the case study building this was apparent in a single case, where the left side detaches from its right side caused by the continuous crack that transverses through the openings and the wall's height.

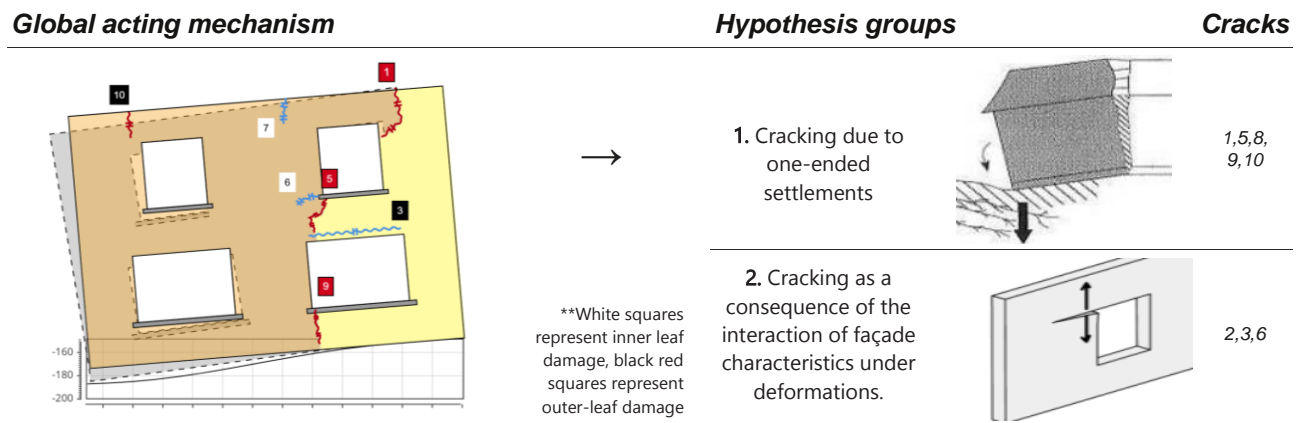

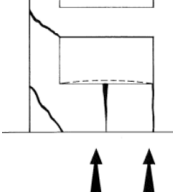

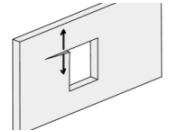

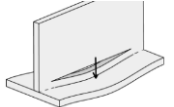
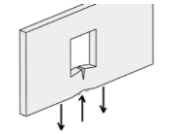

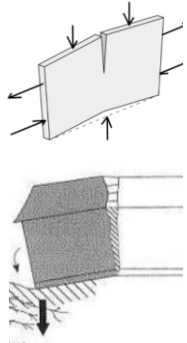


Figure 31: Representation of damage hypothesis categories (de Vent, 2011).

4. Damage assessment through empirical and analytical procedures

Crack ID	Image	Previous Details	Reasoning					Assessment				
			Type	Material	Geometry	Direction of crack	Condition +1	Condition +2	Damage pattern	Hypothesis	Scheme	True
1		Damage: DS1 - DL3 Width: 4mm Length: 885mm	Crack	In composite masonry	In column or wall	Combination of directions / Diagonal	Crack widest at top	At a corner	[Pattern 31] Corner diagonal crack Can also be pattern 37	Vertical settlement: One-end-settlement		✓
2		DS1 - DL2 ≈2mm 1670mm	Crack	In composite masonry	In column or wall	Horizontal	At a corner	Near an opening	[Pattern 19] Horizontal crack near an opening	1) Vertical settlement: All types 2) Overloading, change in load path: Bending, horizontal thrust, lintel, floor		✓
3 & 5		DS1 - DL3 ≈2mm 8mm	Crack	In composite masonry	In column or wall	Horizontal	Halfway the length	Near the roof or floor level	[Pattern 20] Horizontal crack near roof or floor	Overloading due to change in load path		✓
		[5] 1670mm	Crack	In composite masonry	In column or wall	Vertical	Widest at top	Below an opening	[Pattern 22] Vertical tapered crack below an opening	Vertical settlement: Midheaven		✓
4		DS1 - DL3 ≈0.1mm 2000mm	Crack	In composite masonry	In column or wall	Vertical	Tapered towards one end	Widest at top + At top of the building	[Pattern 23] Vertical tapered crack at the top of a building	Vertical settlement : one-end-settlement		✓

4.1 Visual investigation

Crack ID	Image	Previous Details	Reasoning					Assessment				
			Type	Material	Geometry	Direction of crack	Condition +1	Condition +2	Damage pattern	Hypothesis	Scheme	True
6		DS1 - DL3 >3mm 1200mm	Crack	In composite masonry	In column or wall	Horizontal	Near an opening		[Pattern 19] Crack in the wall near the opening	Vertical settlement mid-heave		✓
7		DS1 - <DL2 ≈1mm 994mm	Crack	In composite masonry	In column or wall	Vertical	Widest at top	At the top of the building	[Pattern 23] Vertical tapered crack at the top of the building	Vertical settlement: one-end-settlement		✓
8		DS1 - DL1 ≈0.1mm 500mm	Crack	In composite masonry	In column or wall		Vertical		<b>Cannot identify logical reasoning</b>			x
9		≈0.5mm 994mm	Crack	In composite masonry	In column or wall	Vert	Tapered towards one end	1. Widest at top or bottom -> Below an opening. 2. Widest at bottom 3. One widest at the top one widest at bottom	1. [Pattern 22] The tapered crack is widest at the top below an opening. 2. [Pattern 24] The tapered crack is widest at the bottom 3. [Pattern 25] Tapered crack one widest top one widest bottom	1. Vertical settlement mid-heave  2-3. One end settlement/ one end heave		✓

TABLE 16: Damage classification assessment and hypothesised rationale according to de Vent 2011.

## 4.2 Empirical assessment

The thresholds gathered from the literature review and shown in TABLE 11 were incorporated into a building assessment tool module called “BRICKS”, two empirical databases were made relating the SRI parameters and the strain limits to the different building damage approximations made in the sources. A second algorithm was made to calculate the SRI parameters for any displacement profile introduced, this script was used with the perimetral displacement profiles from the case study building from which a report is produced which is then used through an “EM\_assess” function for the evaluation of the thresholds is made and the final damage evaluation of the parameter is made for the different sources. Another function “EM\_plot” can then be used to visualise the results in a data matrix heatmap for all individual sources. The results from this procedure are shown in TABLE 18.

The author seeks to emphasize certain key characteristics when constructing the empirical limits databases, both for the SRI and strain limits.

- Not all limits boast continuous evaluation scales, many limits take a binary approach to determining whether damage has taken place or not. The first appearance of cracking was set to correspond to a DL 1 assessment.
- Not all limits related their evaluations to the more standardized damage measures such as Burland & Wroth, 1974 DL’s. Therefore to standardize the evaluation process, the author unified their assessments according to Burland & Wroth, 1974 but also presents in the interactive tool the true source evaluation when hovered.
- Often, different sources are relevant to particular instances, such as foundation typologies, soil types and building characteristics. The consulting of the source and its assumptions is recommended when a true evaluation is made according to any source.

When making use or interpreting the results of the tool the above considerations are necessary to maximise the likelihood of making accurate assessments.

### 4.2.1 Results from the empirical assessment

In general terms, the results from the mixed empirical assessment show a good correlation with the approximated damage levels calculated in the case study evaluation. By taking an informed median damage level —The median damage level from the different limits accounting for the assessments whose scale does not range from DL 0-5— the empirical assessments predicted Wall 2 should demonstrate a severe damage scenario (DL 4), whilst the assessment was also able to identify the damage severity in walls 3-6 which corresponded to a no damage level (DL 0).

On the contrary, the evaluation was not able to approximate the damage level (DL 2) expected from Wall 1, this was the only instance where damage was misidentified. Although the results are promising, the small sample size, as well as relatively similar subsidence patterns across all walls, and the little variance between walls prevent further conclusions from being drawn. Nevertheless, they do help illustrate one of their first applications of many empirical SRI limits to a real-world example and that an informed use of the assessment method can lead to correct damage estimates.

On an individual SRI basis, the results show the angular distortion to best correlate with the observed

## 4.2 Empirical assessment

Damage states at both higher and lower damage levels. This aligns with literature findings which also have found that the angular distortion demonstrates a high correlation against damage although, as will be shown this SRI parameter may have some limitations under particular profile shapes.

Further observations can be made based when observing the relative incapability of specific SRI parameters and sources to correlate to the observed damage. Firstly focussing on the sources, it can be observed how engineering norms-based sources demonstrate a mix of conservative and lenient damage estimates. In the case of the literature source IGWR (2009) the relative rotation limits should be overlooked for most sources as they generally are too lenient and are not able to predict any damage instance in all evaluations always predicting no damage (DL0) in all walls.

In the case of CUR (1996), the evaluation is to the contrary, the limits appear too strict with damage being predicted on all walls. Furthermore, severe damage was predicted on Walls 1,3,6 when damage is only present on Walls 1,2. This is most likely in part due to the nature of the settlement profile acting on the building which favours more distortion-based parameters, nevertheless, for many walls with more uniform profiles such as in Walls 1,3,4,5, the assessments were still inconsistent. These observations also align with the conclusions of Prosperi, et al., 2023, which also highlighted optimistic values in international codes based on his simulations.

The poor efficacy of CUR (1996) is an important limitation of this assessment. Its poor assessments did not allow the possibility to use the rotation  $\Phi$  to evaluate the damage in the walls. This is very unfortunate, as this source was the only one that made use of the building rotation, a parameter that should be most informative in the instances of the inclined settlements, i.e. those uniform over one axis observed in arguably five out of six walls (Walls 3,4,5 and possibly Walls 1,6), which in all possibly hindered the ability to predict damage state in Wall 1.

A simple exercise can be made by calibrating the rotation limit of DL2 to  $\Phi_{DL2} \approx 2.0E-02$ . As is shown in TABLE 17 such a small change could have very positive effects on the overall damage evaluation made through the empirical limits. Although just a proposal, it helps emphasize that further limits based on  $\Phi$  could help the informativeness of an SRI parameter suitable for a common subsidence shape in buildings with stiffer responses.

<b>Wall</b>	<b>Wall 1</b>	<b>Wall 3</b>	<b>Wall 4</b>	<b>Wall 5</b>	<b>Wall 6</b>
Rotation [ $\Phi$ ] <sup>Rank</sup>	2.3E-02 <sup>*1</sup>	1.1E-02 <sup>**3</sup>	5.8E-03 <sup>***4</sup>	9.4E-03 <sup>***5</sup>	1.5E-02 <sup>**2</sup>
Actual Damage Level	DL2	DL0	DL0	DL0	DL0
CUR (1996)	DL4	DL4	DL3	DL3	DL3
Adjusted [ $\Phi_{DL2} \approx 2.0E-02$ ]	DL2	DL0	DL0	DL0	DL0

TABLE 17: Building Rotation thresholds calibrated based on the damage levels of the different walls of the case study building.

The last determined inaccurate source was Skempton & MacDonald, 1956 evaluation through the maximum relative displacement ( $\Delta S_{max}$ ). This source only predicts the onset of damage but appeared too lenient which predicted cracking to occur in most walls but this was not the case.

Overall, the evaluation was able to determine with adequate judgement the damage state for the case-study building a large amount of variance and exceptions exist within this assessment for the possibility of misuse is high. Nevertheless, it proved a sufficiently informative tool for a more rapid assessment of a given structure.



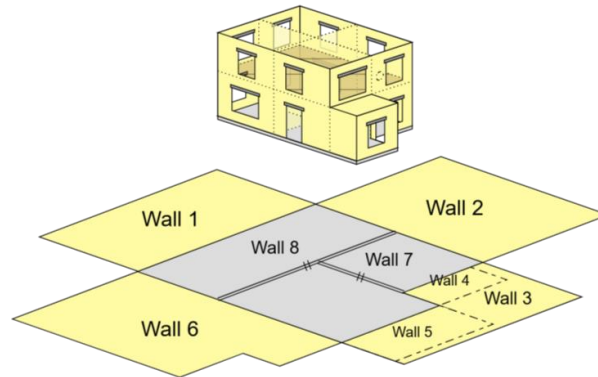
#### 4. Damage assessment through empirical and analytical procedures

##### Building layout & values

##### Wall ID

##### Empirical assessment

##### Damage Evaluation

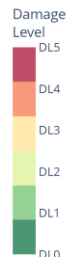
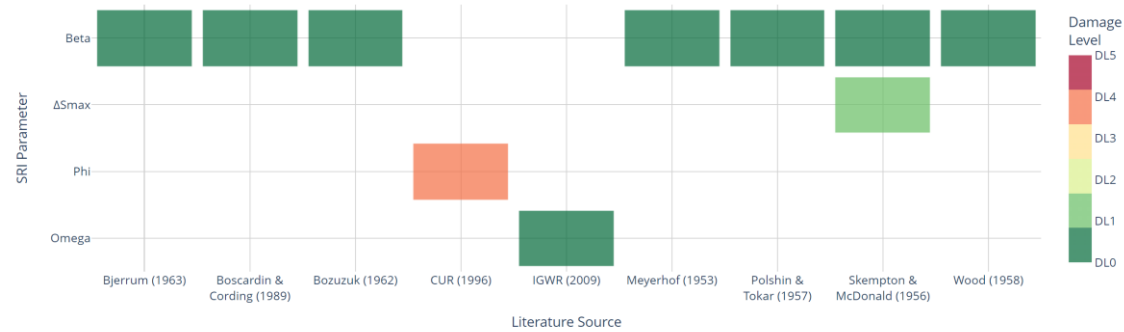


Wall N°	$\Delta S_{max}$	D/L	drat	$\omega$	$\phi$	$\beta$
Wall 1	152	2.2E-02	4.0E+00	1.0E-02	2.3E-02	1.3E-04
Wall 2	36	4.0E-03	7.2E+00	1.2E-03	5.7E-03	3.9E-02
Wall 3	39	1.1E-02	0.0E+00	1.1E-02	1.1E-02	0.0E+00
Wall 4	11	5.8E-03	0.0E+00	5.8E-03	5.8E-03	0.0E+00
Wall 5	34	9.4E-03	0.0E+00	9.4E-03	9.4E-03	0.0E+00
Wall 6	104	9.6E-03	7.8E+00	3.9E-03	1.5E-02	0.0E+00

TABLE 18: SRI parameters for the case study building

\*\*A colour scale is used to highlight the different damage levels: Green levels depict small to negligible damage, yellow colours relate to "light damage", red colours relate to "structurally significant damage"

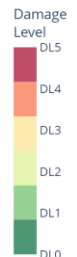
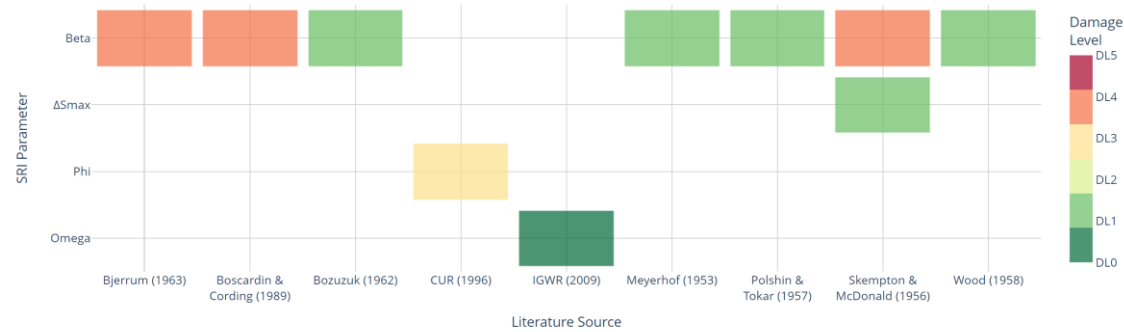
1



DL 0  
None

Actual:  
DL 2

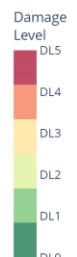
2



DL 4  
Moderate  
to severe

Actual:  
DL 4

3

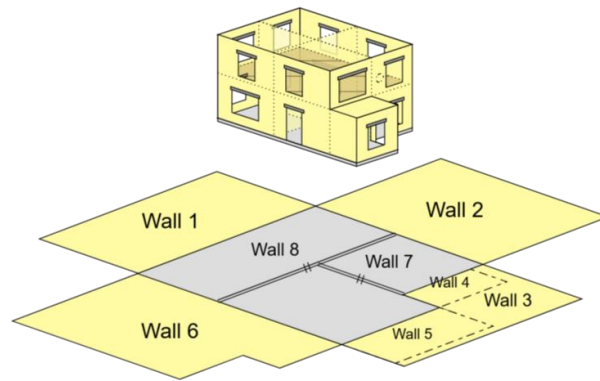


DL 0  
None

Actual:  
DL 0

## 4.2 Empirical assessment

### Building layout & values



Wall N°	$\Delta S_{max}$	D/L	drat	$\omega$	$\phi$	$\beta$
Wall 1	152	2.2E-02	4.0E+00	1.0E-02	2.3E-02	1.3E-04
Wall 2	36	4.0E-03	7.2E+00	1.2E-03	5.7E-03	3.9E-02
Wall 3	39	1.1E-02	0.0E+00	1.1E-02	1.1E-02	0.0E+00
Wall 4	11	5.8E-03	0.0E+00	5.8E-03	5.8E-03	0.0E+00
Wall 5	34	9.4E-03	0.0E+00	9.4E-03	9.4E-03	0.0E+00
Wall 6	104	9.6E-03	7.8E+00	3.9E-03	1.5E-02	0.0E+00

TABLE 18: SRI parameters for the case study building.

\*\*A colour scale is used to highlight the different damage levels: Green levels depict small to negligible damage, yellow colours relate to "light damage", red colours relate to "structurally significant damage"

### Wall ID

### Empirical assessment

### Damage Evaluation

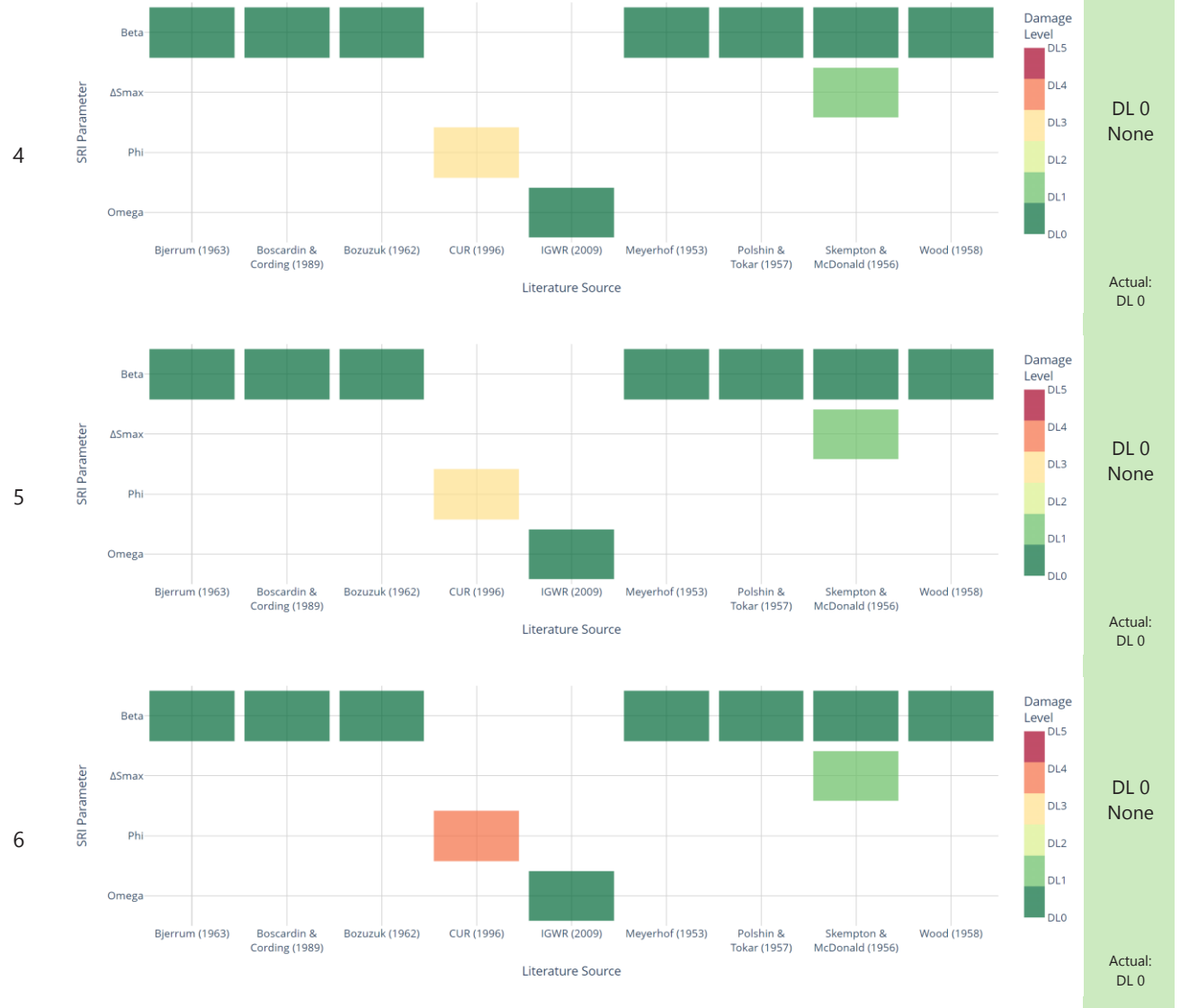


TABLE 19: Building damage assessment according to a set of compiled empirical thresholds.

### 4.3 Analytical assessment

The Limit Tensile Strain Method (LTSM) is the most widely used analytical approach for assessing damage to masonry buildings subjected to settlements. Originally developed by Burland & Wroth in 1974, this method was designed to predict structural damage caused by tunnelling-induced settlements. In this study, the application of the LTSM is adapted to accommodate the unique conditions of this assessment mainly, that the foundation assessment report provides the final measured deformations, and the application of a greenfield profile is not necessary.

Nevertheless, this adjustment eliminates a source of conservatism inherent in the original procedure. Usually when the greenfield profile is applied the full transfer of displacement is assumed to happen when usually this doesn't take place. Many parameters including the empirically derived E/G ratio and strain limits have been determined through the original method. Consequently, the direct use of the building measurements may result in more accurate or possibly less conservative damage predictions. This remains unknown but for comparison, a second procedure aiming to reproduce the original method was also devised, a greenfield profile reconstruction method.

Numerically implementing this procedure involved the development of many constituent parts. Therefore, a breakdown of these components is shown in TABLE 25 and TABLE 29.

#### Approximating the elastic resistance of the walls

A main limitation of the LTSM is the accurate determination of the equivalent E/G ratio from the building to accurately determine the resistance of the building. This factor must be determined semi-empirically based on facade topology characteristics: the building typology, and the opening percentage. For this analysis, the eventual E/G ratios were determined by interpolating the values from Giardina, et al., 2013 based on the geometric information for the different walls presented in TABLE 20.

Wall N°	Length [m]	Height [m]	L/H	Thickness [mm]	Area [m2]	Opening Area [m2]	Opening %	E/G Ratio
Wall 1	7.45	7.7	0.96	27	34.25	4.86	15	8.6
Wall 2	8.85	5.25	1.68	27	37.09	9.36	25	10.3
Wall 3	7.45	7.7	0.96	27	24.35	4.984	20	9.6
Wall 4	1.94	2.85	0.68	27	8.09	1.68	20	9.6
Wall 5	3.4	2.85	1.19	27	9.15	1	10	8.1
Wall 6	10.79	5.25	2.05	27	47.58	4.42	10	7.6

TABLE 20: Wall characteristics and E/G ratio estimations.

#### Approximation of the relative deflection

Although the first approach involves the direct use of the displacement profile, the relative deflection ratio for all the walls has to be calculated, for this purpose, an algorithm was built and also used in the determination of the SRI parameters.

The algorithm works as follows, firstly the sign of the second derivative is measured at all measurement locations, when a change in the sign of the second derivative takes place, this point is identified as an inflexion point, with positive second derivatives where identified as hogging regions and negative second derivatives where identified as sagging regions. New regions were determined to start following an inflexion point unless an overlapping region was detected due to an inflexion point being located at the

following measurement location under which a shared region was located which shared the adjacent measurement locations. Knowing the regions and the measurement locations belonging to each the relative displacement of each region is computed by taking the vertical distance from the measurement location to the normal taken between all two points in that region, from which the maximum is returned as the final deflection ratio.

## Reconstructing the Greenfield profile

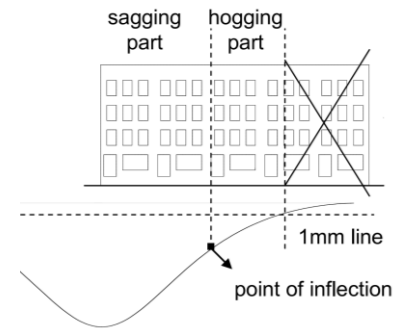
The LTSM originally estimated the greenfield profile by calculating the volume of soil lost due to the construction of a tunnel based on Peck, 1969. Therefore, through this method, the greenfield profile is aimed to be computed by reproducing the best possible Gaussian shapes for the measured displacement profiles for each wall.

The procedure firstly estimates the relative location of the wall by centring the maximum skew measurement of the wall, to the centre of Gaussian shape and equating the maximum displacement  $S_{max}$ . Then by making use of a gradient-based method the unknown parameters, in this case  $X_i$  the distance from the symmetry axis to the point of inflection, is computed to give the minimum discrepancy between values. The use of the gradient-based method allows for a more transferable method to different deformation functions not just the Gaussian shape.

Algorithm	Curve Reconstruction Using Gaussian Shapes
1:	<b>function</b> FITFUNCTION( <i>i_guess</i> , <i>tolerance</i> , <i>step</i> , <i>function</i> = Gaussian shape)
2:	Initialize <i>x_soil</i> , <i>y_soil</i> , <i>z_soil</i> , self.process["params"]
3:	<b>for</b> all <i>wall</i> ∈ self.house <b>do</b>
4:	Determine <i>x_gauss</i> and <i>y_normal</i> based on <i>y_data</i> minimum index
5:	Calculate optimized_parameters using <i>curve_fitting</i>
6:	Find root iteratively using FINDROOTITERATIVE
7:	Generate <i>x_gauss</i> and <i>x_normal</i> for fitted curve
8:	Store parameters in self.process["params"]
9:	<b>end for</b>
10:	Generate mesh grid <i>X</i> , <i>Y</i>
11:	Interpolate <i>z_gaussian</i> on grid using <i>griddata</i>
12:	Store <i>x</i> , <i>y</i> , <i>z_gaussian</i> in self.soil["soil"]
13:	<b>end function</b>
14:	<b>function</b> FINDROOTITERATIVE( <i>guess</i> , <i>parameters</i> , <i>tolerance</i> , <i>step</i> )
15:	Initialize output using Gaussian shape
16:	<b>while</b>   <i>output</i>   > <i>tolerance</i> <b>do</b>
17:	Update guess by step
18:	Recalculate output using Gaussian shape
19:	<b>end while</b>
20:	return guess
21:	<b>end function</b>

Wall	Reference length	$S_{max}$	$X_{inflection}$
Wall 1	[-7.0, 21.0]	-137.38	3.05
Wall 2	[-54, 71]	-177.1	14.04
Wall 3	[-15, 28]	-179.33	4.92
Wall 4	[-13, 31]	-147.02	4.79
Wall 5	[-17, 24.5]	-131.43	4.79
Wall 6	[-9.2, 30.8]	-87.80	-4.58

TABLE 21: Obtained Gaussian parameters for different walls



EXTRACT 6: Script to fit the subsidence measurements to Gaussian shapes.

The reconstructed parameters for the case study building are shown in TABLE 21. Figure 32 shows the final reconstructed greenfield profile for the building. In this figure, the reconstructed Gaussian shapes are depicted by dashed lines whilst the solid lines represent the actual measurements taken from the building. The full displacement profile for the building was obtained by cubically interpolating the reconstructed Gaussian shapes demonstrating that the possible influence region for the settlements in the building may be up to 15m. The procedure roughly can reproduce a full greenfield profile, but it also shows that irregularities do form close to the building extension where the interpolation of the different Gaussian shape measurements from the eastern walls causes an irregular ground deformation.

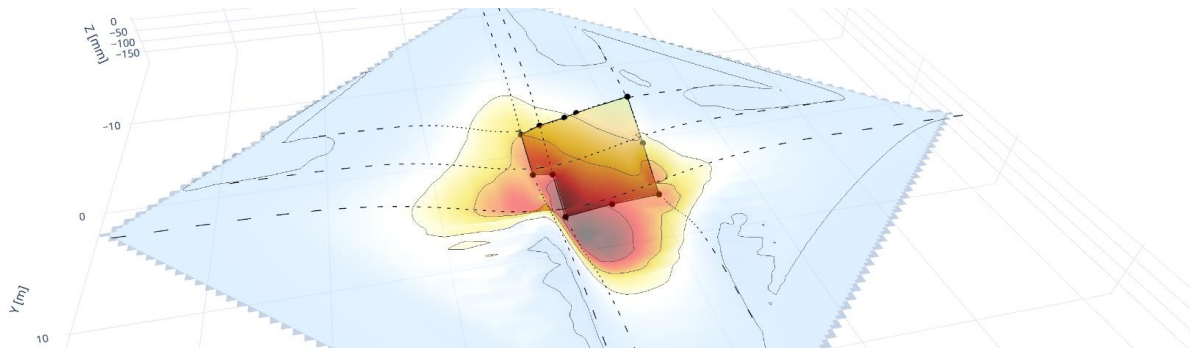


Figure 32: Soil subsidence profile approximation

## Final procedure

The procedure then applies the relative deflection values to the formulations shown in Equation 2 from which the strain estimates for each wall are obtained. These values are then compared to the strain-based empirical limits compiled in TABLE 11, which were then evaluated through the ‘EM\_assesment’ function used in the empirical assessment which led to the final damage estimates. The final evaluations are the squares shown inside the beam and similarly to the Empirical assessment, not all sources correlate damage in its full spectrum, but some sources also only predict the onset of cracking which corresponds to a DL1.

### 4.3.1 Approach 1: Direct use of the building displacements

The results from LTSM evaluation through the actual measurements show that 4/6 walls have been correctly assessed, i.e. all undamaged walls. Overall, the relatively uniform displacement profiles show that most walls undergo a uniform displacement profile out of which none predict damage to occur. In those walls where the deformation is less uniform, a single sagging region was detected in Wall 6 with a very small deflection ratio. The rest of the displacement profiles undergo one-ended settlements, and the only significant deflection ratio is approximated in Wall 2 and 6.

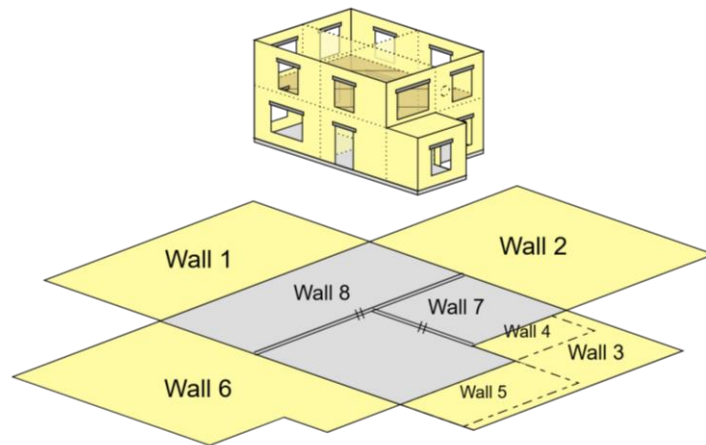
In the case of wall 6 the hogging is sufficiently small that it does not translate to a significant strain level, although a single source does predict the initial cracks may have begun to form in this wall through the most lenient strain measure in Mainstone (1971). In Wall 2 the deflection ratio is similar but the hogging region is much greater and therefore damage is predicted to be present. In the case of the Wall 2 assessment Boscardin & Cording (1989) is very close to the DL 4 estimate therefore the relative accuracy of this assessment is still relatively good. Once again the assessment in Wall 1 is where the biggest difference against the building is seen.

Wall N°	Damage Level	$\epsilon_{Total}$	$\epsilon_{Bending}$	$\epsilon_{Shear}$	$\epsilon_{B,Hogg}$	$\epsilon_{B,Sagg}$	$\epsilon_{S,Hogg}$	$\epsilon_{S,Sagg}$	$\epsilon_{Horizontal}$	$\Delta_{Hog}$ [mm]	$\Delta_{Sag}$ [mm]	$l_{hog}$ [mm]	$l_{sag}$ [mm]
Wall 1	0	1.68E-04	1.68E-04	0.00E+00	1.68E-04	0.00E+00	6.91E-04	0.00E+00	0.00E+00	4.0	0.0	7000	0.0
Wall 2	3	1.52E-03	2.74E-03	1.52E-03	2.96E-04	0.00E+00	9.59E-04	0.00E+00	3.04E-03	7.2	0.0	8900	0.0
Wall 3	0	0.00E+00	0.00E+00	0.00E+00	0.00E+00	0.00E+00	0.00E+00	0.00E+00	0.00E+00	0.0	0.0	0.0	0.0
Wall 4	0	0.00E+00	0.00E+00	0.00E+00	0.00E+00	0.00E+00	0.00E+00	0.00E+00	0.00E+00	0.0	0.0	0.0	0.0
Wall 5	0	0.00E+00	0.00E+00	0.00E+00	0.00E+00	0.00E+00	0.00E+00	0.00E+00	0.00E+00	0.0	0.0	0.0	0.0
Wall 6	1	3.51E-04	3.51E-04	0.00E+00	3.51E-04	2.26E-04	2.20E-03	8.16E-05	0.00E+00	7.8	2.7	4400	6400

TABLE 22: All approximated strain values according to the LTSM through approach 1

### 4.3 Analytical assessment

#### Building layout & values



Wall N.º	$\epsilon_{Total}$	$\epsilon_{Bending}$	$\epsilon_{Shear}$	$\Delta_{Hogging}$ [mm]	$\Delta_{Sagging}$ [mm]	$L_{Hogging}$ [mm]	$L_{Sagging}$ [mm]
Wall 1	1.68E-04	1.68E-04	0.00E+00	4.0	0.0	7000.0	0.0
Wall 2	1.52E-03	2.74E-03	1.52E-03	7.2	0.0	8900.0	0.0
Wall 3	0.00E+00	0.00E+00	0.00E+00	0.0	0.0	0.0	0.0
Wall 4	0.00E+00	0.00E+00	0.00E+00	0.0	0.0	0.0	0.0
Wall 5	0.00E+00	0.00E+00	0.00E+00	0.0	0.0	0.0	0.0
Wall 6	3.51E-04	3.51E-04	0.00E+00	7.8	2.7	4400.0	6400.0

TABLE 23: LTSM strain values according to approach 1

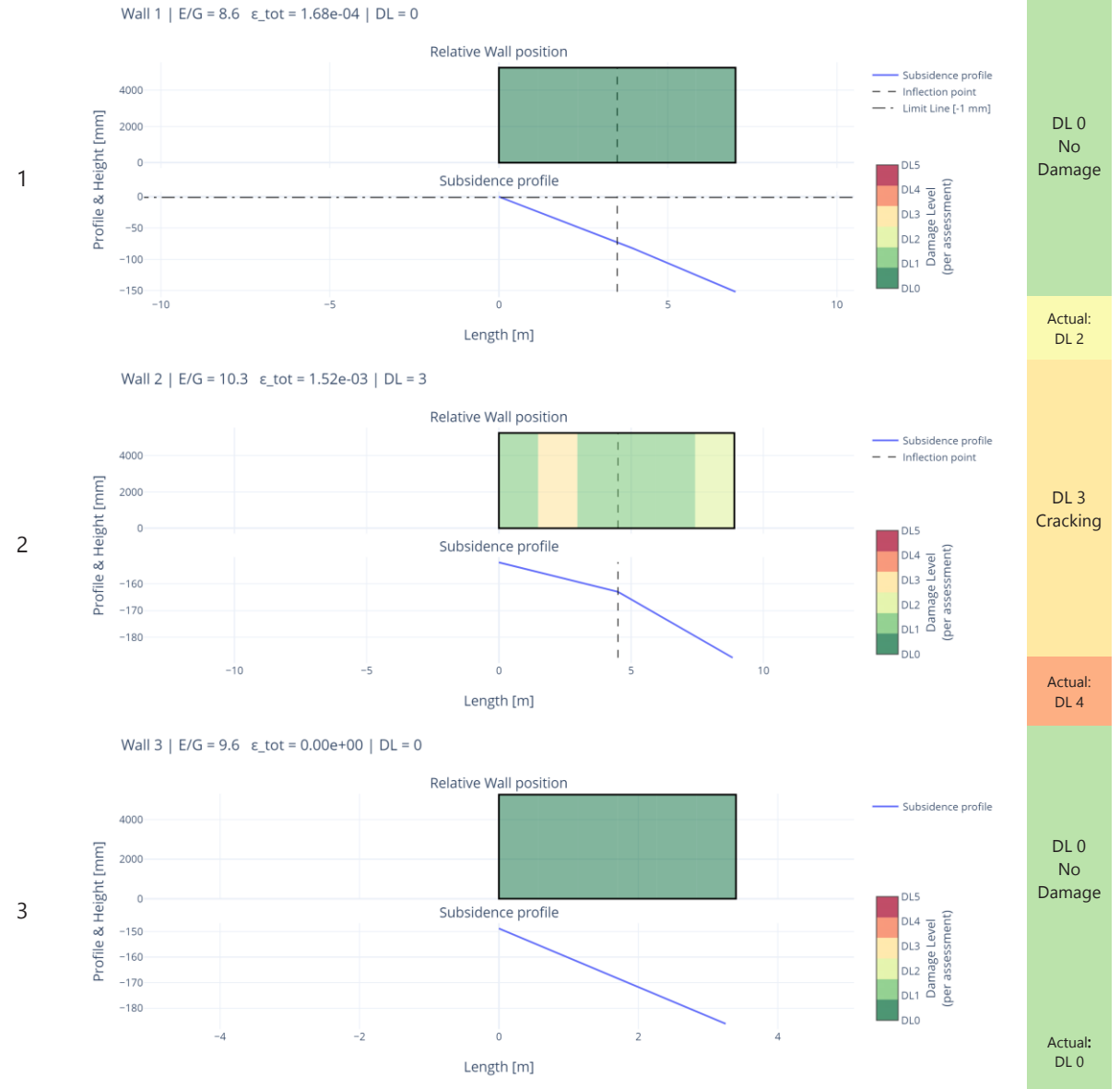
Wall N.º	Inflection points	Regions	Region lengths	Inflexion coordinate	$\Delta W_{zone}$
Wall 1	[0]	[1]	[7.0]	[3.5]	[4.0]
Wall 2	[0]	[1]	[8.9]	[4.5]	[7.20]
Wall 3	[0]	[1]	[3.4]	[0]	[0]
Wall 4	[0]	[1]	[1.90]	[0]	[0]
Wall 5	[0]	[1]	[3.6]	[0]	[0]
Wall 6	[5.2, 6.4]	[-1, 1]	[5.2, 5.60]	[5.2, 8.9]	[2.6875, 7.84]

TABLE 24: Identified regions for the displacement profile

#### Wall ID

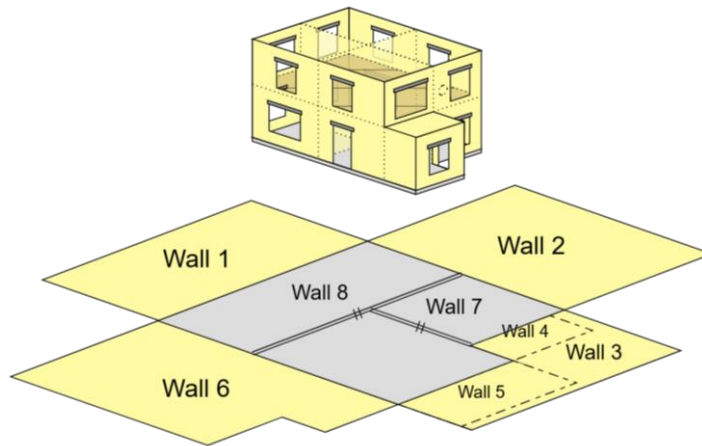
#### LTSM scheme

#### Damage Evaluation



#### 4. Damage assessment through empirical and analytical procedures

##### Building layout & values



Wall N.º	$\epsilon_{Total}$	$\epsilon_{Bending}$	$\epsilon_{Shear}$	$\Delta_{Hogging}$ [mm]	$\Delta_{Sagging}$ [mm]	$L_{Hogging}$ [mm]	$L_{Sagging}$ [mm]
Wall 1	1.68E-04	1.68E-04	0.00E+00	4.0	0.0	7000.0	0.0
Wall 2	1.52E-03	2.74E-03	1.52E-03	7.2	0.0	8900.0	0.0
Wall 3	0.00E+00	0.00E+00	0.00E+00	0.0	0.0	0.0	0.0
Wall 4	0.00E+00	0.00E+00	0.00E+00	0.0	0.0	0.0	0.0
Wall 5	0.00E+00	0.00E+00	0.00E+00	0.0	0.0	0.0	0.0
Wall 6	3.51E-04	3.51E-04	0.00E+00	7.8	2.7	4400.0	6400.0

TABLE 23: LTSM strain values according to approach 1

Wall N.º	Inflection points	Regions	Region lengths	Inflexion coordinate	$\Delta W_{zone}$
Wall 1	[0]	[1]	[7.0]	[3.5]	[4.0]
Wall 2	[0]	[1]	[8.9]	[4.5]	[7.20]
Wall 3	[0]	[1]	[3.4]	[0]	[0]
Wall 4	[0]	[1]	[1.90]	[0]	[0]
Wall 5	[0]	[1]	[3.6]	[0]	[0]
Wall 6	[5.2, 6.4]	[-1, 1]	[5.2, 5.60]	[5.2, 8.9]	[2.6875, 7.84]

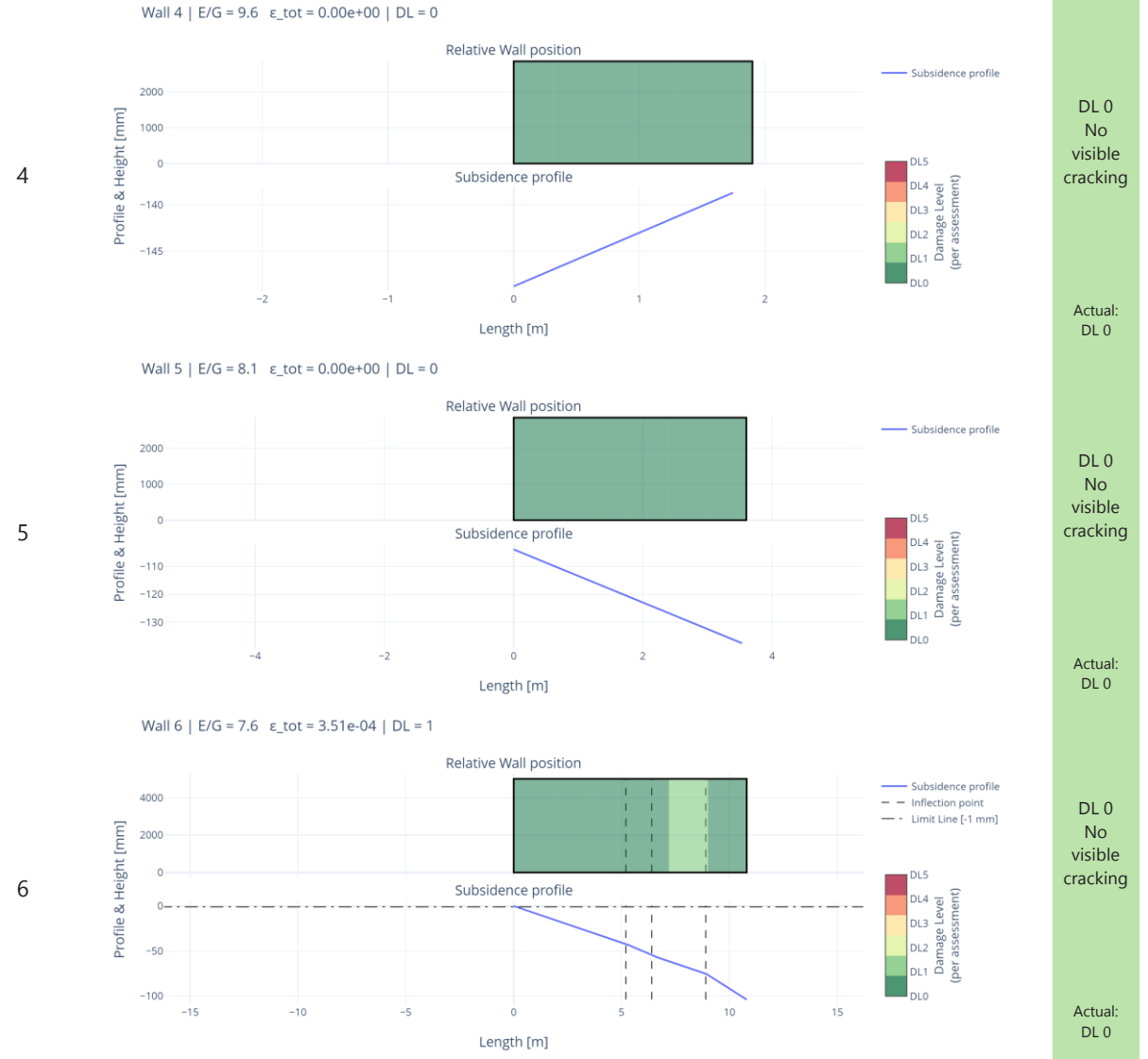
TABLE 24: Identified regions for the displacement profile

TABLE 25: Schematic breakdown of the LTSM results through direct application of skew measurements.

##### Wall ID

##### LTSM scheme

##### Damage Evaluation



### 4.3.2 Approach 2: Extrapolating the greenfield profile from the wall measurements

TABLE 29 shows the visual scheme of the problem for all walls, the reconstructed, the location of the inflexion point, and the positioning of the limit line. The LTSM through the reconstruction method estimated correctly the damage level in 5 out of 6 walls, with once again Wall 1 being incorrectly assessed. With no literature source predicting damage on Wall 6. The evaluations on Wall 2 were correctly made through all assessments, with 5/6 assessments, all assessments that predicted the onset of cracking and Boscardin and Cording (1989), Son and Cording (2005) was the only incorrect assessment which yielded a DL3 which similarly to the measurement results was very close to the DL 4 threshold.

The method shows in the case of one-ended settlements to aggravate the deflection ratios when the wall location is only situated within a single region either hogging or sagging which is why the deflection ratio on Wall 2 is overestimated when compared to approach 1 and underestimated in the cases of Walls 1,6. Furthermore, in walls with uniform tilted settlements such as Walls 3,4,5 the deflection ratio is also overestimated but not sufficient for any damage assessments to predict damage.

Wall N°	Damage Level	$\mathcal{E}_{Total}$	$\mathcal{E}_{Bending}$	$\mathcal{E}_{Shear}$	$\mathcal{E}_{B,Hog}$	$\mathcal{E}_{B,Sag}$	$\mathcal{E}_{S,Hog}$	$\mathcal{E}_{S,Sag}$	$\mathcal{E}_{Horizontal}$	$\Delta_{Hog}$ [mm]	$\Delta_{Sag}$ [mm]	$L_{Hog}$ [mm]	$L_{Sag}$ [mm]
Wall 1	0	1.17E-04	1.17E-04	0.00E+00	1.17E-04	7.81E-05	6.72E-04	3.11E-05	0.00E+00	2.2	0.6	3947.2	3052.8
Wall 2	4	3.24E-03	3.24E-03	1.52E-03	0.00E+00	2.06E-04	0.00E+00	6.93E-05	3.04E-03	10.2	2.9	0.0	8900.0
Wall 3	0	1.11E-04	1.11E-04	0.00E+00	0.00E+00	1.11E-04	0.00E+00	4.40E-05	0.00E+00	3.5	1.0	0.0	3400.0
Wall 4	0	2.00E-04	2.00E-04	0.00E+00	0.00E+00	2.00E-04	0.00E+00	7.90E-05	0.00E+00	3.4	1.0	0.0	1900.0
Wall 5	0	1.81E-04	1.81E-04	0.00E+00	0.00E+00	1.81E-04	0.00E+00	6.35E-05	0.00E+00	3.3	1.0	0.0	3600.0
Wall 6	0	1.76E-04	1.76E-04	0.00E+00	1.76E-04	1.20E-04	5.39E-04	4.46E-05	0.00E+00	2.8	0.9	6218.7	4581.3

TABLE 26: All approximated strain values according to the LTSM through approach 2.

## 4.4 Conclusions

The preliminary assessment methods posed as generally effective and approachable alternatives for evaluating the case study. Whilst some of these methods have already been popularly employed in other fields, the assessments demonstrated that through an informed use, and in some cases accurate consideration of their limitations, these methods proved efficient alternatives for performing damage assessments. Notably, they also complement one another as they focus on different effects observed in the building. For instance, when only visual evidence is available, the diagnostic tool allows to hypothesise possible rationale behind damage forms; if only the building/soil deformations are known, the empirical methods can be applied; and when a more comprehensive set of information that accounts for façade features and the deformation as well, the LTSM can be used.

### Visual assessment

The visual assessment proved a reliable assessment methodology to be used along with basic structural engineering judgement. The hypothesis posed by the tool for the different damage forms appeared to agree with the documented behaviour of the building, it was identified this was the case in 8/9 different damage forms. The tool is most suitable in instances where damage documentation is best available in the form of visual evidence such as photographs taken in site inspections. The analysis made on the damage of the structure was a positive first step to reassure the possible behaviour identified by the



report. Nevertheless, given the many hypotheses that stem from the evaluation of each damage form, it is possible that with limited supporting evidence more erroneous assumptions can be made, and thus it is more difficult to identify shared failure hypothesis supporting global structural behaviour.

### **Empirical assessment**

The empirical assessments demonstrated a fair evaluation procedure in cases where only the deformations of the structure are known. This procedure requires the review of the relevant literature as well as the determination of the SRI parameters for either each of the individual walls or the building as a whole, although this last procedure was not made. The final evaluations made from all walls demonstrated accurate predictions in 5/6 Walls which hints that an informed use of the tool can allow the successful prediction of the likelihood of identifying damage.

This said, the procedure demonstrated to have some major limitations. On the whole, the robustness of the evaluations through most SRI parameters was good, and limitations in the assessments were mostly due to the relevance of the literature sources themselves. This was especially the case with limits taken from norms & legislations, these demonstrated to have the worst correlation with the observed damage. Further possible limitations were shown when the subsidence pattern takes the form of uniform settlements, this is a major limitation, but possibly with further emphasis on new limits based on the tilt the robustness to different subsidence shapes could be improved. The results from the remaining evaluations corresponded to the findings shared in the literature, which state the use of these limits is most suitable in buildings with shallow foundations, and also that the correlation of the Angular Distortion ( $\beta$ ) and the Deflection ratio ( $\Delta/L$ ) is better than other SRI alternatives.

### **Analytical assessment**

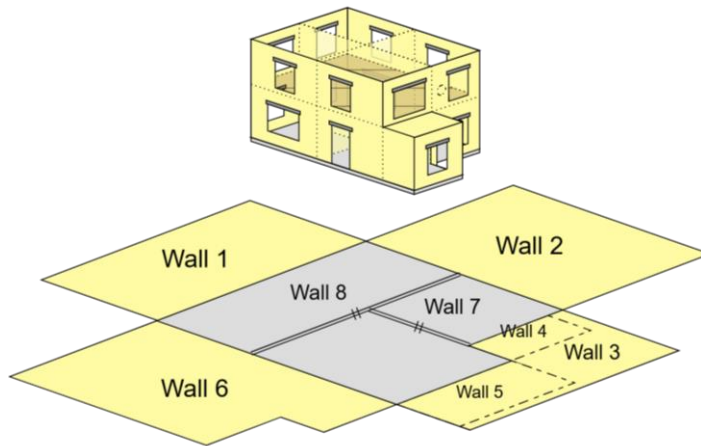
The analytical assessment through the Limit Tensile Strain Method showed good accuracy in estimating the final damage levels. This was due to the good correlation between the strain limits and damage levels from Son & Cording (2007). The strain level for Wall 2 under the LTSM ( $\epsilon=1e-03$ ) was approximately an order of magnitude away from the less conservative results obtained by the FEA ( $\epsilon=1e-02$ ), yet the damage level and an interpolation of a fictitious PSI parameter was very close  $\Psi=3.5$ .

The evaluation of the procedure through the different soil deformation shapes correlated with its expected damage effects, and the use of the Gaussian shapes aggravated the damage estimates. For all Walls unless the wall was split in both regions. The effect of the increase in the deflection ratio was not as big as expected. Nevertheless, the main limitation of the LTSM remains its applicability under the direct use of the displacement profile and suitability under tilted displacement profiles. Further testing is necessary as the range of observable Damage states and displacement profiles in the case study was not too varied. Although for this instance the procedure appeared to be relatively accurate.

Furthermore, the capabilities were greatly improved by the addition of Son & Cording, 2007 findings which allowed for interpolation of the E/G ratio which governs the elastic resistance of the formulated masonry beam which highlights the importance of accounting for further additions to the method based on the problem (such as including slenderness and settlement rate effects). This study advocates for the use of greenfield profile reconstruction, although this method has some limitations which have been addressed, its use better aligns with the LTSM evaluation of deformations through the deflection ratio and possibly also help reconstruct a more severe greenfield profile that may act on the building.

## 4.4 Conclusions

### Building layout & values



Wall N°	$\epsilon_{Total}$	$\epsilon_{Bending}$	$\epsilon_{Shear}$	$\Delta_{Hogging}$ [mm]	$\Delta_{Sagging}$ [mm]	$L_{Hogging}$ [mm]	$L_{Sagging}$ [mm]
Wall 1	1.17E-04	1.17E-04	0.00E+00	2.2	0.6	3947.2	3052.8
Wall 2	3.24E-03	3.24E-03	1.52E-03	10.2	2.9	0.0	8900.0
Wall 3	1.11E-04	1.11E-04	0.00E+00	3.5	1.0	0.0	3400.0
Wall 4	2.00E-04	2.00E-04	0.00E+00	3.4	1.0	0.0	1900.0
Wall 5	1.81E-04	1.81E-04	0.00E+00	3.3	1.0	0.0	3600.0
Wall 6	1.76E-04	1.76E-04	0.00E+00	2.8	0.9	6218.7	4581.3

TABLE 27: LTSM strain values for approach 2

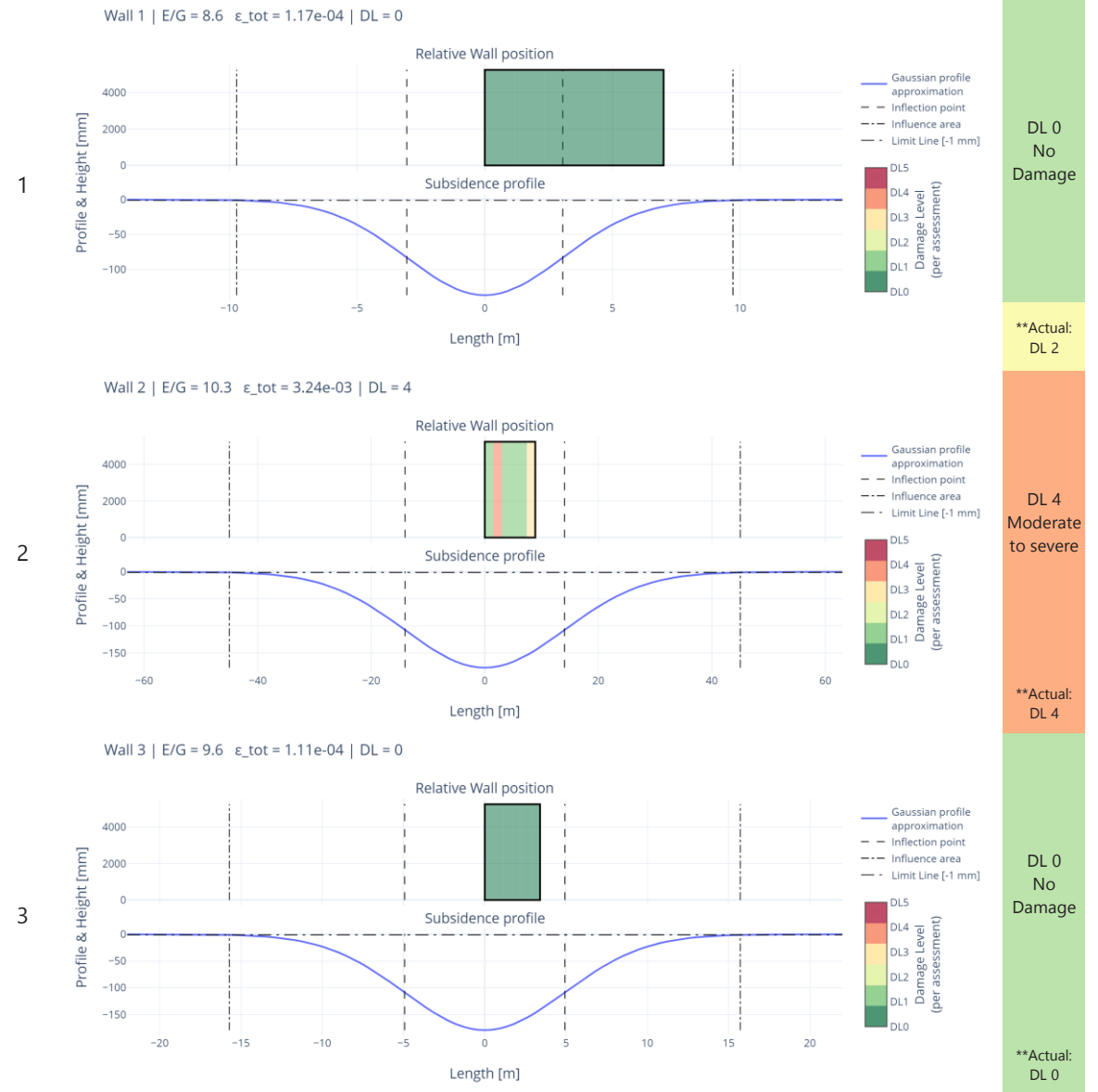
Wall N°	Reference length	$S_{max}$	$X_{inflection}$
Wall 1	[-7.0, 21.0]	-137,38	3.05
Wall 2	[-54, 71]	-177,1	14.04
Wall 3	[-15, 28]	-179,33	4.92
Wall 4	[-13, 31]	-147.02	4.79
Wall 5	[-17, 24.5]	-131.43	4.79
Wall 6	[-9.2, 30.8]	-87.80	-4,58

TABLE 28: Parameters for fitted Gaussian shapes per wall

### Wall ID

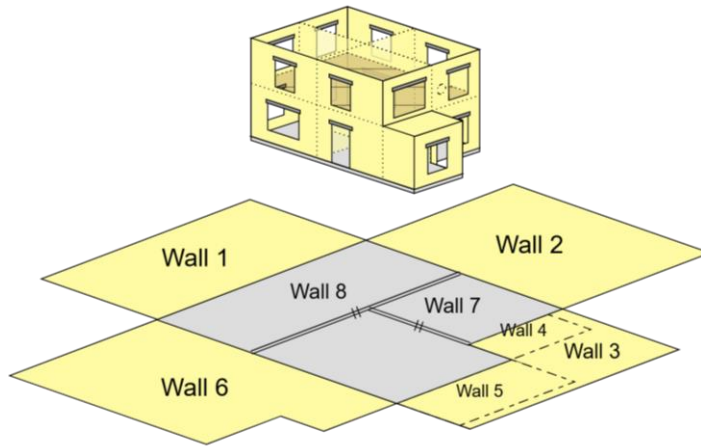
### LTSM scheme

### Damage Evaluation



#### 4. Damage assessment through empirical and analytical procedures

##### Building layout & values



Wall N°	$\epsilon_{Total}$	$\epsilon_{Bending}$	$\epsilon_{Shear}$	$\Delta_{Hogging}$ [mm]	$\Delta_{Sagging}$ [mm]	$L_{Hogging}$ [mm]	$L_{Sagging}$ [mm]
Wall 1	1.17E-04	1.17E-04	0.00E+00	2.2	0.6	3947.2	3052.8
Wall 2	3.24E-03	3.24E-03	1.52E-03	10.2	2.9	0.0	8900.0
Wall 3	1.11E-04	1.11E-04	0.00E+00	3.5	1.0	0.0	3400.0
Wall 4	2.00E-04	2.00E-04	0.00E+00	3.4	1.0	0.0	1900.0
Wall 5	1.81E-04	1.81E-04	0.00E+00	3.3	1.0	0.0	3600.0
Wall 6	1.76E-04	1.76E-04	0.00E+00	2.8	0.9	6218.7	4581.3

TABLE 27: LTSM strain values for approach 2

Wall N°	Reference length	S_max	X_inflection
Wall 1	[-7.0, 21.0]	-137,38	3.05
Wall 2	[-54, 71]	-177,1	14.04
Wall 3	[-15, 28]	-179,33	4.92
Wall 4	[-13, 31]	-147.02	4.79
Wall 5	[-17, 24.5]	-131.43	4,79
Wall 6	[-9.2, 30.8]	-87.80	-4,58

TABLE 28: Parameters of fitted Gaussian shapes per wall.

##### Wall ID

##### LTSM scheme

##### Damage Evaluation

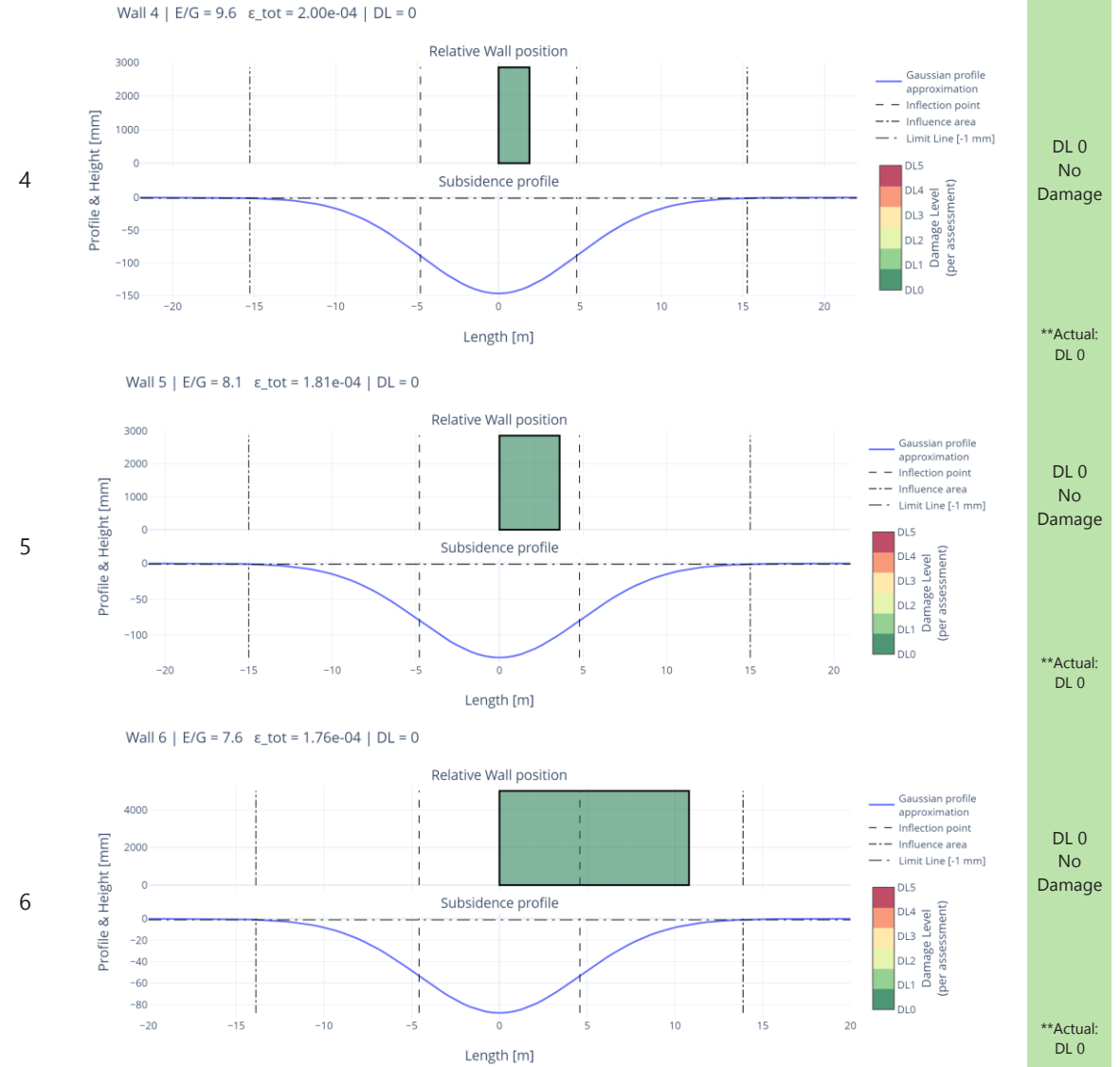


TABLE 29: Breakdown of the LTSM results through the reconstruction of greenfield profile

# **5. 2D Finite Element Analysis damage assessment**

---

The following section is the Numerical Finite Element damage analysis of the case study building. This section firstly presents the methodology in section 5.1, it then presents the models in 5.2 and lastly, presents the results 5.3 and conclusions sections 5.4.

## 5.1 Methodology

The numerical modelling of structural masonry is one of the most complex challenges in structural engineering research and practice (Asteris, et al., 2015). Finite Element (FE) modelling offers a flexible and highly precise method for estimating the mechanical response of structures. However, its successful application requires careful consideration of a large number of parameters, which are often influenced by modelling assumptions necessary to achieve the desired analysis results and are conceptually understood by the analyst.

The results from Empirical/Analytical assessments, usually preliminary or flagging assessment procedures, both identified Wall 2 as the only likely wall to be damaged. Furthermore, the empirical/analytical assessments were not able to provide information on the location of damage, its shape and its severity. Carrying a Finite Element Analysis of Wall 2 will allow us to simulate these damage characteristics and thus carry out a more in-depth study.

The first set of model analyses will be simple through a 2D scheme of Wall 2. A 2D scheme allows to evaluate the results and validate its use for either further 3D modelling approaches or flag existing model limitations. Furthermore, such an approach conceptually should work well with the cracking pattern seen in Wall 2, whose more vertically profiled and tapering cracks hint that in-plane effects are mostly responsible for the damage, although the out-of-plane effects (due to the differential settlement, and the large documented rotations may also be influencing the damage on the wall). Nevertheless, the out-of-plane effects are Expected to be taken up by the adjacent perpendicular walls.

By the end, the successfulness of the results will be evaluated according to a set of relevant attributed to Finite Element Models: precision, representing the structure's expected response or aligning with available evidence; robustness, producing consistent results under varying solution parameters; and accessibility, minimizing the complexity and number of considerations needed for correct implementation.

<b>Precision</b>	<b>Robustness</b>	<b>Accessibility</b>	<b>Features of interest</b>
Damage severity similarity	Material Sensitivity	Modelling complexity	Constitutive law
Damage location similarity	Mesh Sensitivity	Convergence Time & Stability	Topological influence
			Solution method

**TABLE 30: Model evaluation criteria and studied model features.**

A key aspect to emphasize in this analysis methodology and evaluation is the approach to assessing model accuracy based on damage severity. This is typically done using either the Burland & Wroth (1974) Damage Levels or the Damage Parameter ( $\Psi$ ) introduced by Korswagen et al. (2019). The damage parameter has been widely used when evaluating FEA results, the formulation of  $\Psi$  (Equation 1) uses the maximum crack width to estimate the damage parameter. Yet, for this set of analyses, the Damage Parameter ( $\Psi$ ) has been calculated using the mean crack width.

These values will be compared against the same evaluation made in TABLE 16 based on the available pictures from the assessment report. This decision will result in significantly lower damage parameters for the different models. A small comparison of the effect this decision has is provided on Page 161, but the effect approximately equates to a reduction of  $-1 \Psi$  in the evaluations.

This evaluation will also be carried out through the 2D modelling approach but through a set of variations based on the main non-explicit finite element modelling choices, or model Features of Interest—A non-explicit modelling choice refers to a modelling choice not relevant to the physical representation of the wall. In settlement-induced masonry damage models, the primary variants between models refer to the selection of the most appropriate macro-modelling constitutive law and the accurate topological representation of the structure.

All analyses were performed through the commercial software Diana 10.8, a popular Finite Element Analysis software. The machine used for the analysis had the following specifications: Processor - Intel(R) Core(TM) i7-1065G7 CPU @ 1.30GHz 1.50 GHz, RAM - 16.0 GB. Background tasks were minimized during the analysis, and all analyses were carried out in a single thread to reproduce the available resources consistently between models. Further results and analysis are available in the appendix, while the main conclusions and observations have been discussed in the main body.

## 5.2 Finite Element models

The two main modelling decisions which could influence the discretization of the model are the choice of constitutive law and the model topology scheme chosen to represent the wall. The model topology will be kept constant whilst different constitutive laws, the most popular within macro-modelling approaches: The Total Strain-based Crack Model and the Engineering Masonry Model will be used in the analysis.

### 5.2.1 Geometry, discretization & loads

Arguably, the most important characteristic of masonry crack models is the model topology. An important characteristic of the case study building is its use of single-wythe masonry cavity walls. The building plans show how the outer leaf serves an architectural role whilst the inner leaf serves as the main load-bearing component. Considering these roles, an adequate simulation of the behaviour of the inner leaf is of greater interest to the structural behaviour of the structure nevertheless, the performance of the outer leaf is also of interest, structurally and scientifically due to its more varied damage pattern and being a fully unreinforced masonry wall, which better allows evaluation of the material model as less components are at play.

Since a 2D modelling scheme of Wall 2 was used, separate models to represent the inner and outer leaves of the walls were made. Wall 2's relative simplicity, being symmetrical as well as having few façade details. The schemes for inner and outer leaves are relatively similar, the support conditions are fixed vertical displacements along the entire base of the wall and a horizontal restraint at the rightwardmost corner of the building, as this location is where the wall will pivot and also is the location where the relative displacement is zero.

The façade geometry uses Regular 4-node plane-stress elements with a linear integration scheme were chosen. A default mesh element size chosen for the base model was 200mm whose mesh was specified to be of Hexa/quad typology although due to the topology of the façade and mesh size, some triangular elements are also present in the mesh.

The loading conditions change between both models. Firstly, the support reactions from the roof have been assumed to be equally transmitted between the inner and outer sections of the wall, and thus the reactions from the weight of the roof are equal in both models, these were assumed to happen at four

different locations and are greater towards the centre of the wall where the influence area between roof trusses is greater than at the edges, these reactions are only present along Wall 2 and Wall 6 (Assumptions and calculations are shown in the Appendix). The last remaining similarity between the inner and outer leaf models are the openings size and location, and the subsidence trough applied to them.

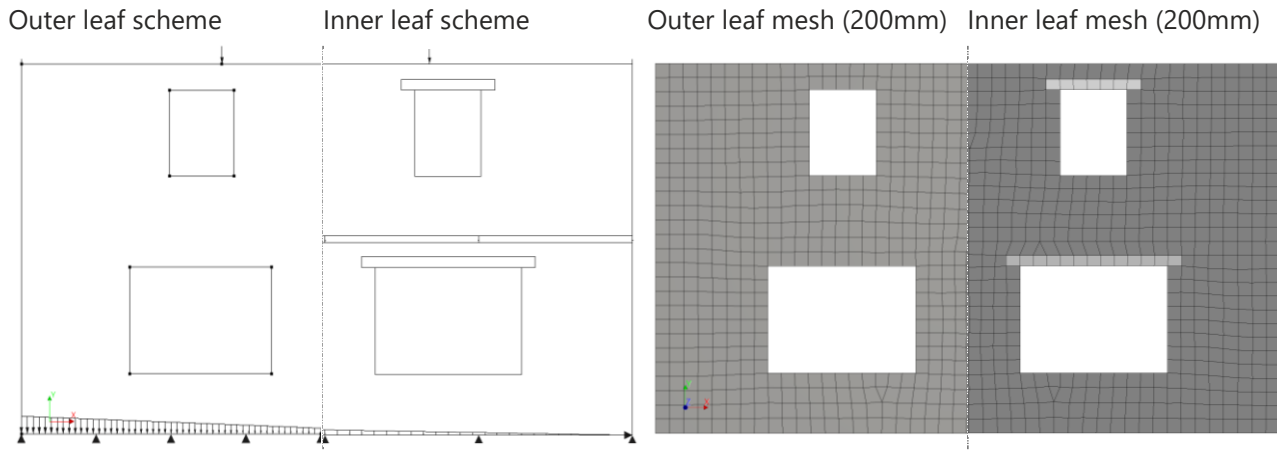


Figure 33: Model and mesh schemes for Wall 2 Outer-Inner.

The main difference between the models is the incorporation of the concrete lintels which were modelled as linear elastic elements, as they are expected to be reinforced according to NEN-EN 845 standards, the width of these is equal to the width of the opening plus two masonry units' length (200mm), this is the same for all openings, the thickness of the lintel is also constant at 100mm. Lastly, the contribution of the self-weight of the first floor is only applied to the inner leaf as a UDL based on the floor reactions (estimated contributions shown in the Appendix).

The loads on the structure were applied in two load cases: the building loads, which include the compressive force exerted by the roof, and the building settlement. The first load case was applied in 30 load steps with standard tolerances, ensuring convergence in all norms. The subsidence trough, was applied in 720 steps, which corresponds to 0.05mm per step, and the convergence criterion was an energy norm with a threshold of 0.001. A Quasi-Newtonian solution method through the Broyden-Fletcher-Goldfarb-Shanno algorithm was used to achieve faster convergence and robustness from possible high non-linearities.

## 5.2.2 Analysis and problem limitations

The anticipated limitations for the modelling approach are mostly based on the modelling rationale that has had to be made in part due to the little information available from the report, and the chosen 2D modelling scheme, these include the following,

- The applied displacement profile corresponds to the final measured deformations measured on the building; therefore the iterative load application will not reproduce the time history experienced by the building.
- The material properties of the building are unknown and mostly likely irregular.
- Out-of-plane deformations caused by the buildings' differential settlements will not be accounted for
- Box behaviour offered by the entire building's façade, adjacent walls and interior of the building was not accounted for.

- Both leafs have been assumed to act independently, possible shared stiffness provided by wall ties or window frames has not been accounted for.
- There is full joint interaction between lintels and masonry (no interface).
- The inner leaf wall has been assumed to be a continuous masonry wall and not split by the first floor.

Despite the limitations mentioned above, the most critical factors are believed to be the box-like building influence on the resistance of the structure, the interaction between masonry and lintels, and the modelling of the first floor. The omission of box-like behaviour is expected to limit the overall resistance of the building. Similarly, neglecting the interaction between lintels and masonry may lead to an overestimation of lintel deformation preventing further deformation by the masonry.

In the building plans, the floor between the ground level and cellar is labelled as "Nehobo," indicating a concrete floor. However, no such indication is made for the first floor. For Wall 2, a conservative approach was taken by modelling only the support conditions provided by the floor to the inner leaf, rather than fully introducing an element to separate the top and bottom sections of the wall. This approach avoids overestimating the restraint provided by a concrete element, which could artificially increase the overall resistance. Nevertheless, choosing not to model the floor as a separate element may result in increased crack propagation, as the model does not account for the additional stiffness a concrete floor could provide.

### **5.2.3 Model 1: Analysis through the Total Strain based Rotating Crack-Model (TSCM)**

The first analysis was performed through the TSCM its definition has assumed the material response to be elastic in compression and to have an exponential softening tensile behaviour. The crack rotation axis was selected as rotating with a Rots crack-bandwidth specification. The material parameters were obtained from the studies of Jafari, et al., 2017 and Jafari, 2021 where some material properties were estimated through the relations available in the latter (The material values and estimation of model parameters are available in the Appendix). The relevance of Jafari's work has been broken down in this study literature review, but in the authors' opinion, it presents the most accurate and in-depth available material characterisation campaign of age and brick typology-specific material parameters which in the case of this case study the most similar where those characterised in Jafari's study as solid-bricks post 1940. Other empirical relations available in Jafari, 2021 were then used for the estimation of model parameters. Additionally, physical non-linear effects have been prescribed due to the expected softening behaviour of the masonry.

### **5.2.4 Model 2: Analysis through The Engineering masonry model (EMM)**

The second set of models was analysed using the EMM. All model parameters remain unchanged except for the new material parameters in the EMM formulation. A key feature of the engineering masonry model is the user-defined, a priori definition of the tensile failure mechanism. The mechanisms capture different effects, making it challenging to decide which one is most suitable for a given scenario if the crack pattern cannot be observed.

In the case of Wall 2 of the building, most cracks occur along the bed and head joints. Therefore, using



a head-joint failure type, either by direct input or through a friction definition, would be an acceptable choice. Under this assumption, the relevant material parameters, especially for the tensile and shear failures would be based on the mortar's material properties.

The second possibility for Wall 2 is to evaluate staircase cracks. The crack pattern shown in Figure 34 shows a pronounced diagonal crack, this crack is believed to happen due to the following two factors. First, the Flemish Garden bond, this bond is a highly irregular bond typology, the arrangement of the units causes the diagonal tension to shift between crack segments, as the sections with the successive transversal units will reduce the crack angle and the section with the longitudinal unit will produce a steeper crack angle. Secondly, it is possible that the slenderness of the façade may be producing shear stresses whose interaction with the tensile stresses from the bending may produce more diagonal cracks, this hypothesis was in part also observed by the diagonal strain estimates from the LTSM results.

Lastly, inspecting the crack pattern in the outer leaf of Wall 2 shows an additional failure mode in the masonry, failure in the masonry units, and 3 tensile failures have been able to be identified in the middle portion of crack 6. As this failure happens at multiple locations in the specimen, and given the superior tensile strength offered by the units, it is possible that the overall resistance by Wall 2's masonry to be higher than usually expected, when the tensile resistance is assumed to be determined by the tensile resistance of the mortar. This complicates an accurate estimation of the material resistance, and it is also not clear if this failure is also present in the inner leaf.

The analysis parameters were mostly kept the same as in the Total-strain-based crack model, a continuation criterion for no equilibrium iterations was also set anticipating possible convergence issues given by the EMM. The material parameters significantly deviate due to the failure type and the material anisotropy of the constitutive law additionally the shear characteristics of the masonry are also considered, a breakdown of all parameters is available in the appendix.



Figure 34: Observation of failures in the middle portion of the crack pattern in Wall 2

<b>Model Elements</b>	<b>Building Element</b>	<b>Element type</b>	<b>Element ID</b>	<b>Interpolation order</b>	<b>Mesh type</b>	<b>Mesh size</b>	<b>Thickness [m]</b>
	Building façade	Regular Plane stress	Q8MEM T6MEM	Linear	Hexa/Quad	200mm	0.1
	Concrete Lintels	Plane stress	Q8MEM	Linear	Hexa/Quad	200mm	0.1
<b>Iterative scheme</b>	<b>Load Class</b>	<b>Load steps</b>	<b>Solution method</b>	<b>Max iteration N°</b>	<b>Convergence Norms</b>	<b>Convergence tolerance</b>	<b>Satisfy all norms</b>
	Building Loads	30	Quasi-Newton Raphson (BFGS)	100	Displacement Force	0.001 0.01	TRUE
	Building Settlement	720	Quasi-Newton Raphson (BFGS)	1000	Energy	0.001	TRUE
<b>Material Model</b>	<b>Name</b>	<b>Young's Modulus [MPa]</b>		<b>Mass density [kg/m3]</b>		<b>Poisson ratio</b>	
	Linear Elastic Concrete	31000		2400		0.2	
	<b>Name</b>	<b>Crack Orientation</b>	<b>Tensile Behaviour</b>	<b>Crack bandwidth</b>	<b>Compressive Behaviour</b>		
	Clay-solid >1945 (Jafari, et al., 2022)	Rotating	Linear-crack energy	Rots	Elastic		
	<b>Young's Modulus [MPa]</b>	<b>Poisson ratio</b>	<b>Mass density [kg/m3]</b>	<b>Uniaxial tensile strength [MPa]</b>	<b>Mode, I Fracture Energy [N/m]</b>	<b>Residual tensile strength</b>	
	9348 ±0.35	0.15	1805	0.34	28	0	

TABLE 31: W2 – TS Model parameters breakdown.

<b>Model Elements</b>	<b>Building Element</b>	<b>Element type</b>	<b>Element ID</b>	<b>Interpolation order</b>	<b>Mesh type</b>	<b>Mesh size</b>	<b>Thickness [m]</b>
	Building façade	Regular Plane stress	Q8MEM T6MEM	Linear	Hexa/Quad	200mm	0.1
	Concrete Lintels	Regular Plane stress	Q8MEM	Linear	Hexa/Quad	200mm	0.1
<b>Iterative scheme</b>	<b>Load Class</b>	<b>Load steps</b>	<b>Solution method</b>	<b>Max iteration N°</b>	<b>Convergence Norms</b>	<b>Convergence tolerance</b>	<b>Satisfy all norms</b>
	Building Loads	30	Quasi-Newton Raphson (BFGS)	100	Displacement Force	0.001 0.01	TRUE
	Building Settlement	720	Quasi-Newton Raphson (BFGS)	1000	Energy	0.001	TRUE
<b>Material Model</b>	<b>Name</b>	<b>Vertical Young's Modulus [MPa]</b>	<b>Horizontal Young's Modulus [MPa]</b>	<b>Shear Modulus [MPa]</b>	<b>Mass density [kg/m3]</b>	<b>Poisson ratio</b>	
	Clay-solid >1945 (Jafari, et al., 2022)	9348 ±0.35	5470	1250	1805	N/A	
	Linear Elastic Concrete		31000	N/A	2400	0.2	
	<b>Name</b>	<b>Compressive Strength [MPa]</b>	<b>Fracture Energy in compression [N/m]</b>	<b>Friction angle [rad]</b>	<b>Cohesion [MPa]</b>	<b>Fracture Energy in shear [N/m]</b>	
	Clay-solid >1945	17.7	54693	0.67	0.35	283	
	<b>Head Joint failure type</b>	<b>Bed-joint strength [MPa]</b>	<b>Minimum Head joint strength [MPa]</b>	<b>Fracture Energy in tension [N/m]</b>	<b>Residual tensile strength [MPa]</b>	<b>Stepped diagonal angle [rad]</b>	
	1: Tensile strength defined by friction	2.79	1790	28	0	0.6	
	2: Diagonal staircase cracks	0.34	N/A	55.04	0	0.6	

TABLE 32: W2 – HJ, S model parameters breakdown.

## 5.3 Model 1: TSCM results

In general terms, the analysis results from the Total Strain-based Rotating Crack Model show a good similarity to the case study observations. The model stands out by its capability to reproduce the damage location and its shape but also appears to present limitations in its crack-width overestimations that highlight how the results tend to present conservative damage estimates which can depending on the situation influence the final crack pattern accuracy. The robustness of the model was mixed as the stability of the convergence of the model was strong, but the model analysis duration was relatively long and the model in the outer leaf analysis did present mesh sensitivity effects.

### 5.3.1 Model precision: Damage severity and similarity

The results from the outer leaf analysis present a DL4 with  $\Psi_{W2O-TS}=4.53$  which is a 29% overestimation against the observed damage level ( $\Psi_{W2}=3.53$ , DL4). They also show a large continuous crack that spans most of the wall's height and passes diagonally through the openings on the right-hand side of the wall, this crack tapers from top to bottom and begins with a relatively vertical profile which then tilts diagonally in its middle portion and in its bottom portion. These cracks form a mechanism where the left-hand side of the wall and the right-hand side detach and begin to behave more as two individual components, this can be observed in the overall displacements of the wall being discontinuous to the ones on the right-hand side, this same effect was also identified in the case study but was predicted to be of a lesser extent due to the smaller crack widths.

Overall, the crack pattern resembles relatively closely the one on Wall 2 in its location and shape although, the superior portion of the crack is located above the top right opening in the actual building. Although cracks particularly cracks 3,10 situated above the bottom right opening and at the top left section of the wall were not able to be predicted. The model does show some limitations when trying to predict the crack widths as the maximum crack width is roughly 5.5 times the width estimated in the building. This applies to the tapering of the crack as well, as the tapering is expected to range the maximum crack widths by 3mm but in the analysis, this happens by about 20mm.

Inner-leaf results don't present as accurate a damage picture, the model damage presents a DL4 with  $\Psi_{W2I-TS}=3.93$  a 31% damage overestimation. Crack pattern shows a main crack which spans the entire height of the building which differs quite strongly from the one in the case study building, where two cracks of approximately 3mm were expected.

These cracks had initially been simulated by the model as the first one began at the bottom left corner of the top right opening and the other began left of the lintel in the top right opening. Nevertheless, the damage state of these cracks in terms of their crack width and length was so large that both cracks coalesced and then continued to grow. Therefore, in this instance, the model's capability to simulate the cracks was still good but its damage overestimation influenced the final dissimilarity between the results and the case study, this is truer for the inner leaf results.

### 5.3.2 Convergence and mesh sensitivity

The most important characteristic of the TSCM convergence is that it rarely fails to converge, this is a useful trait of the material model which is beneficial when dealing with material uncertainties. It was also

### 5.3 Model 1: TSCM results

observed that the constitutive law fails to converge only when the material parameter input selection is extreme. Nevertheless, the solution time for the models tends to be quite high when compared to its counterpart, the solution time from the outer leaf model was 01:25:40 [hh:mm:ss] whilst for the inner leaf model the solution time was 00:55:57 [hh:mm:ss], relatively lengthy times when compared to the EMM. The number of iterations required for equilibrium per load step was relatively high and was correlated with the damage level. The number of crack formations per time step was also quite high.

The last main TSCM characteristic study was the model's mesh sensitivity. Further analysis where made with mesh sizes of 0.1m and 0.05m. In terms of the damage pattern the mesh sensitivity effects were relatively small, the damage appeared to be localised better with the finer mesh. Nevertheless, much larger sensitivities were experienced in the maximum crack widths, particularly in the outer leaf model where  $cw_{max}$  changed from 21.5mm, 14mm to 19mm, these changes happened in the cracks located at the top of the wall which changed in location and width and since these were the widest their impact to the damage parameters was consequently also the greatest. The mesh sensitivity effects in the inner leaf model were not as great as  $cw_{max}$  remained at 22mm but the mean crack width decreased as the tapering was better simulated through the finer mesh and decreased by 14%.

Therefore, the over-representation of damage varies considerably between the inner and outer leaf analyses. Trying to reproduce similar results requires the outer leaf for half of the total displacement profile to be applied whilst in the inner leaf a quarter of the displacement profile has to be applied. This shows that either the in-plane resistance of the wall in the models is much lower or that the capability of the wall to accommodate the settlement is less. This is most likely the former, as the presence of the lintels, appears to stiffen the response of the wall producing smaller deflections in the inner leaf models. It appears that the effect this increased stiffness has on the damage is that the deformations are more concentrated in the cracks. This hints that the issue may reside in that the simulation of the masonry behaviour should be more flexible.

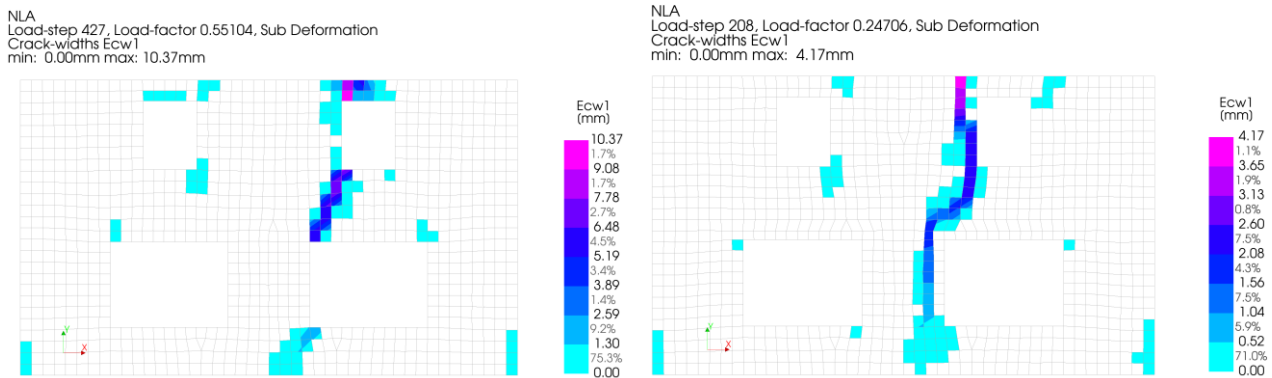


Figure 35: Crack patterns at load factors where  $\Psi_{Analysis} = \Psi_{Model}$ .

Lastly, the linear elastic behaviour of the lintels was validated in these analyses. Throughout most of the analysis, the lintels are acting in the elastic stage. Between  $\lambda=0.37-0.47$ , the tensile stress in the cantilever portion of the lintel ranges from 2-2.5 MPa, which is approximately the limit for unreinforced c25/30 concrete. At these same load ranges, the crack pattern is influenced as it shifts upward, as the stress redistributes around the lintel surpassing the masonry's tensile strength of 0.344 MPa demonstrating a micro effect due to the resistance of the lintels. This effect may only be realistic in the case that the lintels are unreinforced which should not be the case.

Model	Outer Leaf	Inner Leaf
<p>Mesh Size: 200mm</p> <p><math>\Psi_{W20} = 3.7</math></p> <p><math>\Psi_{W21} = 4.09</math></p>	<p>NLA Load-step 750, Load-factor 0.99936, Sub Deformation Crack-widths Ecw1 min: 0.00mm max: 21.52mm</p>	<p>NLA Load-step 750, Load-factor 0.99936, Sub Deformation Crack-widths Ecw1 min: 0.00mm max: 21.31mm</p>
<p>Mesh Size: 100mm</p> <p><math>\Psi_{W20} = 4.47</math></p> <p><math>\Psi_{W21} = 3.4</math></p>	<p>NLA Load-step 750, Load-factor 0.99936, Sub Deformation Crack-widths Ecw1 min: 0.00mm max: 14.16mm</p>	<p>NLA Load-step 750, Load-factor 0.99936, Sub Deformation Crack-widths Ecw1 min: 0.00mm max: 22.83mm</p>
<p>Mesh Size: 50mm</p> <p><math>\Psi_{W20} = 4.85</math></p> <p><math>\Psi_{W21} = 4.06</math></p>	<p>NLA Load-step 750, Load-factor 0.99936, Sub Deformation Crack-widths Ecw1 min: 0.00mm max: 19.15mm</p>	<p>NLA Load-step 750, Load-factor 0.99936, Sub Deformation Crack-widths Ecw1 min: 0.00mm max: 22.76mm</p>

TABLE 33: First principal crack width at last load step for all Total Strain based Crack Model models.

## 5.4 Model 2: EMM results

The EMM results demonstrate much less conservative damage analysis results for Wall 2, the final crack patterns resemble the case study's damage but can differ at particular locations. The model's strongest trait is that the crack-widths are much more realistic although they still present slight overestimations of the expected damage. On the whole, the balance between damage shape similarity and damage severity similarity appears to be relatively strong.

For the analysis through the EMM, the definition of the constitutive law was not completely able to be determined beforehand as the definition of the failure mode and its material parameters was initially uncertain. Therefore, an analysis of the outer leaf through the two most suitable failure mechanisms was made. To let the results decide the most suitable approach. Following these analyses, it was evident that the analysis through the Head Joint failure mode (Model: EMM-HJ) was poor. The results demonstrated a very light crack pattern with a poor representation of the amount shape and severity of damage. This along with a weaker theoretical rationale for the model — as the observed tensile failure in the units would better correspond to a staircase failure— sufficiently discouraged the use of this failure mode for further analyses in Wall 2. Therefore, the results of the staircase failure material definition were decided to be used as the final model.

### 5.4.1 Model precision: Damage severity and similarity

The EMM-staircase model result demonstrated a balanced set of capabilities. The crack magnitudes from the EMM were much closer. Average crack widths were usually 2.5 times their expected values but maximum crack widths at specific locations along the crack length did still present much larger crack - widths. The less conservative damage estimates are also more apparent when evaluating the damage parameter scores ( $\Psi_{W2O-EMMS}=3.7 [+5\%] \rightarrow \Psi_{W2}=3.5$ ,  $\Psi_{W2I-EMMS}=4.09 \rightarrow \Psi_{Observed}=3 [+36\%]$ ), these are much lesser than with TSCM and are relatively close to the actual case study.

The final crack pattern similarities were also more balanced. The outer leaf crack pattern differentiated itself by being less conservative, as the main crack did not eventually span the whole wall's height as the crack at the bottom of the wall was smaller, which prevented the mechanism on the left side of the wall not to fully forming. Furthermore, Crack 5 (Middle) of the wall was also similar as the crack shifted from diagonal to vertical, as was also documented in the damage report. Furthermore, Crack 1 (Top right) also appeared close to the top right opening closer to its actual location than in the TSCM.

The inner leaf crack pattern similarity was also strong, Crack 6 (Bottom left corner of the top right opening and Crack 7, the crack left-ward of the lintel of the top right opening were well represented in their length, shape and average crack width.

Nevertheless, one of the greatest limitations of EMM results stems from its tendency to smear damage. Additionally, the EMM often generates unexpected cracks, as shown on the right side, where cracks approximately 500mm in length and with a maximum width of 5mm influence the damage parameter in the analysis. Finally, the model is still unable to capture Cracks 3 and 10 in the outer leaf analysis.

## 5.4.2 Convergence and mesh sensitivity

The main limitation of the EMM was the model robustness mainly its sensitivity effects on the convergence behaviour and the mesh sensitivity. After multiple analyses the model was demonstrated to be very sensitive to the combination of material inputs under specific deviations in the overall material definition, under which the material model begins to fail to converge in many load steps.

This said the only model which failed to converge on all iterations was the coarse mesh outer leaf model. In this analysis, a single iteration failed to converge (Figure 36), with the energy criterion being far from the threshold and also not appearing to decrease over the 1000 iterations. Although no further non-converged steps followed this loading step and the results and damage continuation appear natural, this still hampers the robustness of the results as they lose uniqueness in their solution.

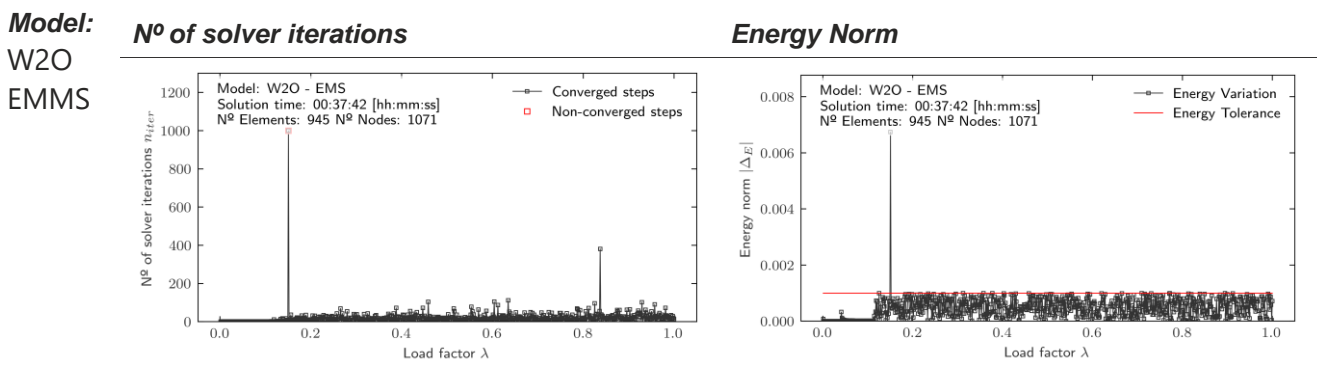


Figure 36: Convergence behaviour of W20 – EMS

Further sensitivity effects were also identified through different mesh sizes. In the outer leaf models, this sensitivity appeared to be greater, changes to the crack shape are evident as new cracks are shown above the top right corner of the bottom right opening, and changes to Crack 5 (Middle) are also present as the crack profile now changes from originally being diagonal to a vertical profile, into a fully diagonal profile in the 100mm mesh and a vertical/diagonal profile in the 50mm mesh. Furthermore, the maximum crack widths deviate considerably as they increase from 8mm to 15mm to 21mm. In the outer leaf analysis, the variance between models is such that no mesh size can be determined accurately, but the 200mm mesh produces the most resembling results. Lastly, the mesh sensitivity also influenced the convergence of the models as no convergence issues were identified in any models, including the outer leaf model.

In the inner leaf models, the mesh sensitivity was much lesser an initial decrease in the maximum crack width and crack lengths for Cracks 6,7 happened following the first mesh refinement, but the last two sets of results appear very similar and accurate when compared to the expected crack patterns. Furthermore, the crack on the left-hand side of the wall was also not simulated.

5.4 Model 2: EMM results

Model	Outer Leaf	Inner Leaf
Mesh Size: 200mm $\Psi_{W20} = 3.7$ $\Psi_{W21} = 4.09$	NLA Load-step 750, Load-factor 0.99936, Sub Deformation Crack-widths Ecw1 min: -0.00mm max: 8.54mm 	NLA Load-step 750, Load-factor 0.99936, Sub Deformation Crack-widths Ecw1 min: -0.00mm max: 17.79mm 
Mesh Size: 100mm $\Psi_{W20} = 4.47$ $\Psi_{W21} = 3.4$	NLA Load-step 750, Load-factor 0.99936, Sub Deformation Crack-widths Ecw1 min: -0.03mm max: 15.39mm 	NLA Load-step 750, Load-factor 0.99936, Sub Deformation Crack-widths Ecw1 min: -0.16mm max: 9.24mm 
Mesh Size: 50mm $\Psi_{W20} = 4.85$ $\Psi_{W21} = 4.06$	NLA Load-step 750, Load-factor 0.99936, Sub Deformation Crack-widths Ecw1 min: -0.01mm max: 21.02mm 	NLA Load-step 750, Load-factor 0.99936, Sub Deformation Crack-widths Ecw1 min: -0.04mm max: 10.04mm 

TABLE 34: First principal crack width at last load step for all Engineering Masonry Models models.



## 5.5 Conclusions

Overall, the Finite Element Analysis results were able to reproduce comparable crack patterns and the severely damaged state of the wall. The analysis was able to reproduce the global behaviour in the wall, mainly the partial separation of the left-hand side of the wall against its right side in the outer leaf models, whilst in inner leaf models the behaviour was more similar in the EMM class of models. Furthermore, Figure 37 depicts the final crack patterns for the best two models. It shows that 5/7 cracks are present. It also shows that the locations and shapes of the cracks are comparable to the building although small crack pattern features such as the specific location of certain cracks and their shape don't present the equal crack observed on Wall 2.

Further limitations are also observed in the model benchmark scores, the RMSE scores show an average deviation of approximately  $1\Psi$  and 4.7mm in the case of the damage parameter and crack-widths respectively. The convergence of all models was similarly strong, and the baseline models took on average around 50 minutes to run. Only a single model did not converge on all load steps. Furthermore, the mesh objectivity of the different models was also demonstrated to influence the crack patterns as changes to the mesh size resulted in changes to analysis results.

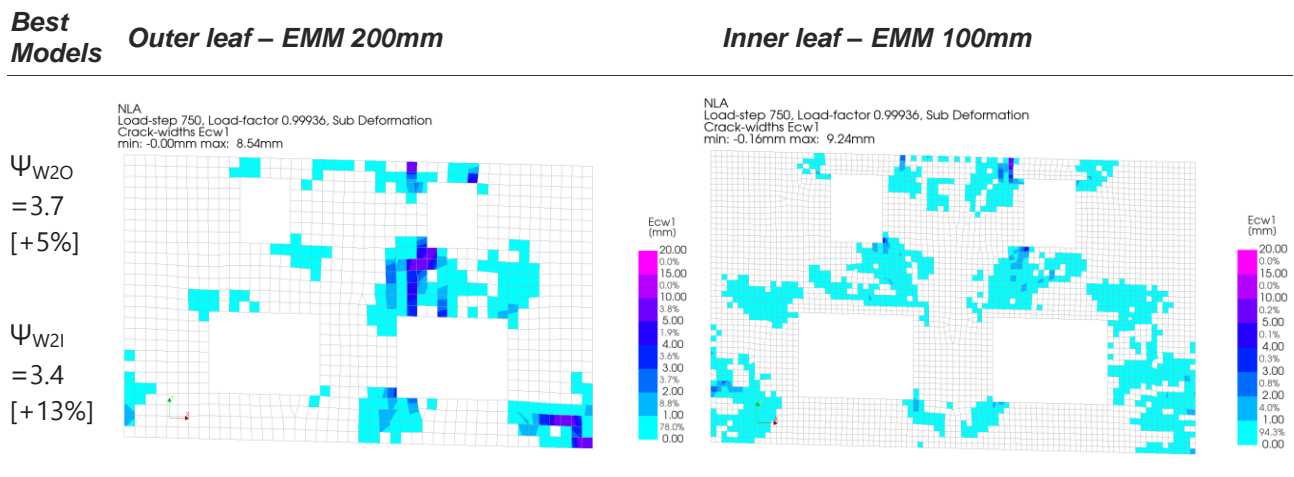


Figure 37: Best FEA results: Their crack patterns, damage parameters and percentage difference.

Outside of the general accuracy of the FEA results, interesting effects are also observed by evaluating the difference outcomes due to the three model differentiators: (1) the presence of lintels, (2) the influence of mesh size, and (3) the impact of the constitutive law.

### 5.5.1 Key Factor 1: Evaluating the influence of the lintels by Comparing Inner Leaf and Outer Leaf Models

The most significant difference between the models lies in the comparison between the inner and outer leaf models, particularly regarding the influence of the lintels and the surcharge from the first floor, which notably affects the crack patterns. In both models, crack initiation occurs at the bottom left corner of the top right opening. However, the subsequent crack patterns differ; the diagonal crack profile (Cracks 1, 4, 10) is not reproduced in the inner leaf models but instead, a new crack (Crack 4) forms to the left of the top right lintel.

This behaviour likely takes place due to the stiffening influence by the lintels. The magnitude of this

effect can be studied by evaluating the relative displacements of Node A (bottom left-hand side of the wall) and Node B (Top left-hand side of the wall) of the inner and outer leaf models (TABLE 36 – Model stiffness).

These comparisons indicate a significantly ductile response in the outer leaf model, as the ratio of vertical displacements between Node A and Node B is nearly equal. In contrast, the inner leaf model shows a ratio of less than 1, suggesting a stiffer response. Additionally, this difference becomes more apparent when examining the horizontal displacements of the top node, which reveal that the horizontal displacement of Node A is much greater in the outer leaf than in the inner leaf, indicating that settlement effects are more detrimental to the unreinforced masonry façade.

### 5.5.2 Key Factor 2: Model's mesh objectivity

TABLE 47 presents the effect of mesh size on the Damage Parameter ( $\Psi$ ) and the percentage differences in crack width between models. The results indicate that no consistent relationship can be established between mesh size and damage assessment for the wall. When analysed on a per-model basis, the influence of mesh size on damage assessment varies significantly some models show a general decrease, others an increase, while others show an initial decrease and then increase, indicating no consistency between models.

This variability suggests that mesh size has no clear impact on the results. Such findings pose limitations on the reliability of model results or the suitability of other numerical solution parameters. Even when achieving full numerical convergence and making use of a strict tolerance criterion, solutions still deviate in terms of the damage level and also in the cracks patterns, as only one set of models presented good mesh objectivities.

Therefore, for this set of analysis, the best conclusion that can be made is that the damage in the wall can deviate by a standard deviation of  $\sigma_{\Psi} = 0.23 \Psi$  and  $\sigma_{CW} = 2.3 \text{ mm}$  and 95<sup>th</sup> percentile confidence interval of 0.45  $\Psi$  and 4.5mm, with further changes to the crack pattern shape, also possibly being moderate i.e. some cracks may change shape, but this is more influenced based on the choice of constitutive law.

### 5.5.3 Key Factor 3: The influence and behaviour of the constitutive laws

The final major influencing factor between the models was the constitutive law. Unlike the other two factors, the influence of the constitutive law is determined by the user, allowing results to be tailored according to the characteristics of the chosen law. As demonstrated in TABLE 33 and TABLE 34, the choice of constitutive law impacts the maximum crack widths and the crack pattern shapes, therefore the choice of constitutive law in these analyses was demonstrated to have the following effects.

#### Total Strain based crack model

The Total Strain-Based Crack Model can be best characterised as a reliable model. The accuracy of results is sufficiently such that crack patterns showed to be similar and the damage produced tended to be localised. Nevertheless, on the contrary, the material model demonstrated produced conservative crack widths and overall conservative damage states. This can have an influence on the crack patterns when the scenario at hand may be very influenced by an increase in the crack widths and crack lengths. Which

was the case in the inner leaf models. Furthermore, the use of the TSCM was demonstrated to provide a less resistant simulation of the masonry as shown by the larger horizontal displacements and larger Damage levels and crack-widths.

The robustness of the model was demonstrated to be acceptable but significantly better than its counterpart as mesh sensitivity effects were smaller and only present in the outer leaf models. Furthermore, the numerical behaviour of the model demonstrated good convergence. Due to a greater number of crack formations, its analysis times are slightly larger. Its last major feature is its much easier definition. The model has much fewer material parameters, which paired with its good convergence and robustness make it a more user-friendly model.

#### **Capabilities**

- User-friendly
- More localized damage
- Strong convergence

#### **Limitations**

- Conservative crack width estimates
- Higher analysis times

### **Engineering masonry model**

The EMM can be best described as a less user-friendly model that, when properly applied, has the potential to offer the highest accuracy. Both best results for the outer and inner section of Wall 2 were provided by this model as its results tended to demonstrate closer maximum crack width similarities and to a lesser extent crack pattern shape similarities. Results usually tended to reproduce the main cracks but also produced cracks not present in the case study. Its simulation of the masonry behaviour was more stiffer than in the TSCM. Furthermore, when good convergence is seen in a model its analysis times tend to be considerably faster.

#### **Capabilities**

- More optimistic crack patterns
- Faster analysis times

#### **Limitations**

- High mesh sensitivity
- Less user friendly
- Tendency to simulate unexpected cracks and produce smeared damage patterns
- Convergence issues

Despite its strengths, the EMM also demonstrated significant limitations that affect its user-friendliness. A major drawback is the a priori definition of the failure mode, as demonstrated by the differences between the Head-Joint and Staircase failure mode analysis results. This along with the necessary careful consideration for the definition of material parameters to match the masonry failure, made the model more challenging to use.

Furthermore, the constitutive law is highly sensitive to mesh size changes which greatly impact the number, widths, and shape of the cracks. Other major limitations involved difficulties in achieving full convergence can also be challenging due to the models' convergence sensitivity to the relationship between material properties which must fall within a specific range against each other for acceptable convergence. If this is not achieved poor convergence is likely which complicates its application to real-world scenarios such as this one where the accurate definition of material properties is more challenging.

<b>Model</b>		<b>Model Accuracy</b>		<b>Model robustness</b>		<b>NCS</b>	
		<b>Damage Parameter [<math>\Psi</math>]</b>	<b>Max Mean Crack Width [mm]</b>	<b>Damage similarity</b>	<b>Mesh objectivity</b>		<b>Solution time [hh:mm:ss]</b>
TSCM	Outer 200mm	4.53 [+29%]	9.45 [+136%]	Acceptable		01:25:50 [2.32]	0
	Outer 100mm	4.31 [+23%]	8.56 [+114%]	Acceptable	Acceptable	03:52:31 [6.28]	0
	Outer 50mm	4.87 [+39%]	10.16 [+154%]	Acceptable		09:18:16 [15.1]	0
	Inner 200mm	3.93 [+31%]	9.56 [+218%]	Poor		00:55:577 [2.56]	0
	Inner 100mm	3.81 [+27%]	8.63 [+187%]	Poor	Good	03:23:56 [8.07]	0
	Inner 50mm	4.09 [+36%]	7.87 [+162%]	Poor		08:58:08 [22.36]	0
		RMSE= 1.02 $\sigma=0.19$	RMSE= 5.58 $\sigma=0.68$	Acceptable	Acceptable	$\mu=04:39:00$ $\sigma=03:20:00$	$\mu=0$
EMM	Outer 200mm	3.7 [+5%]	3.79 [-5%]	Acceptable		00:36:58 [1]	1
	Outer 100mm	4.47 [+27%]	6.51 [+62%]	Acceptable	Poor	01:36:32 [2.61]	0
	Outer 50mm	4.85 [+38%]	8.31 [+107%]	Acceptable		07:52:43 [14]	0
	Inner 200mm	4.09 [+36%]	10.18 [+239%]	Acceptable		00:25:16 [1]	0
	Inner 100mm	3.4 [+13%]	3.10 [+3%]	Good	Acceptable	02:23:36 [5.68]	0
	Inner 50mm	4.06 [+35%]	5.66 [+88%]	Good		07:38:48 [18.15]	0
		RMSE= 0.94 $\sigma=0.40$	RMSE= 3.73 $\sigma=2.5$	Acceptable	Poor	$\mu=03:25:00$ $\sigma=03:08:00$	$\mu=0.17$
<b>Overall</b>		RMSE= 0.98 $\sigma=0.33$	RMSE= 4.7 $\sigma=2.3$	Acceptable	Acceptable	$\mu=04:02:22$ $\sigma=03:17:34$	$\mu=0.085$

TABLE 35: Analysis benchmark scores for the different models.

Values in brackets indicate the deviation of model results compared to the case study. Certain parameters are evaluated qualitatively on a scale of Excellent (all cracks correctly located or minimally influenced by mesh size), Acceptable (most cracks correctly located with minor mesh influence), and Poor (few cracks correctly predicted with significant mesh influence). Final evaluation criteria include the Root Mean Squared Error (RMSE) and Standard Deviation ( $\sigma$ ) provided for each model family and the overall models evaluation. NCS = Non-Converged steps

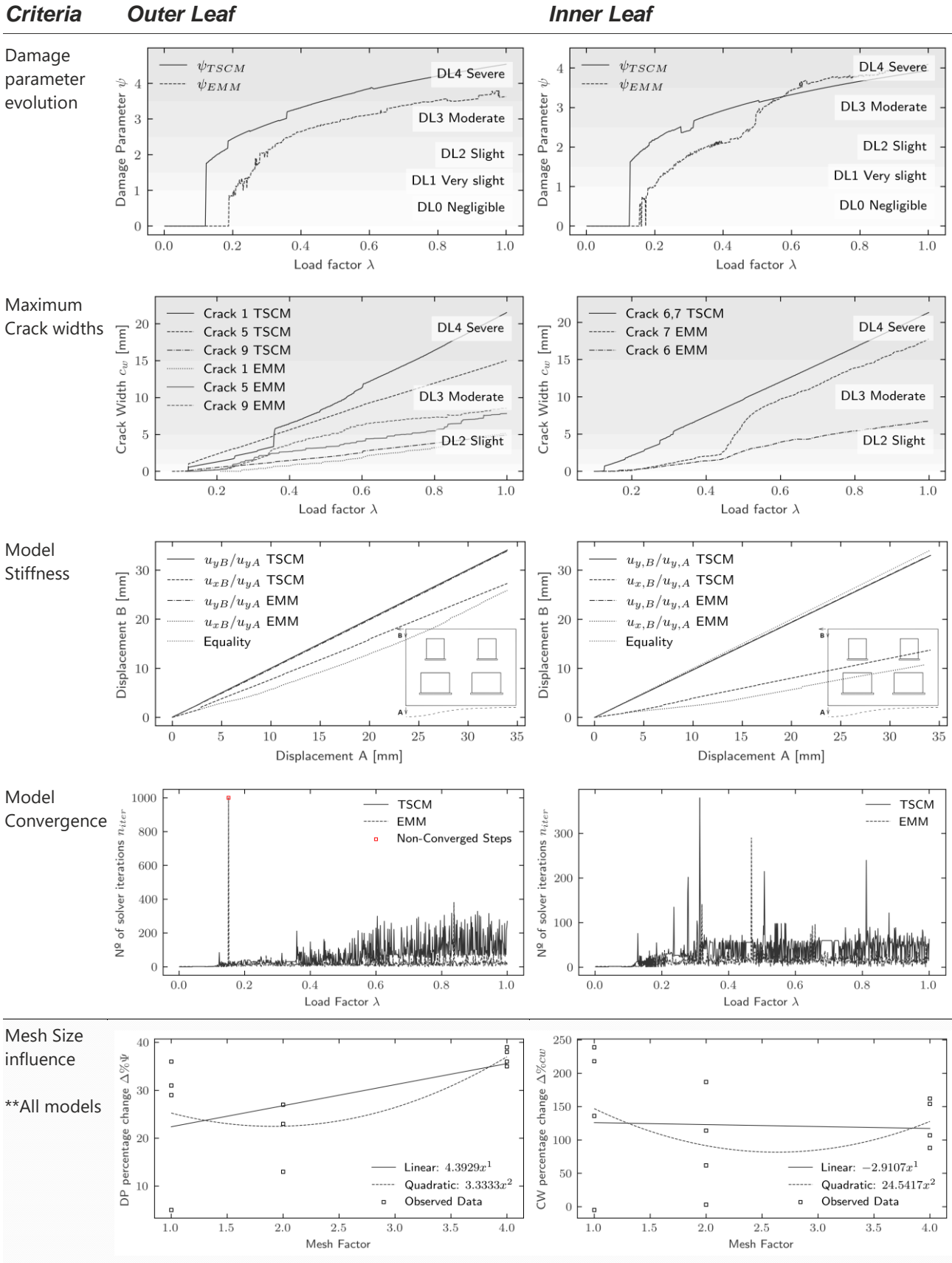


TABLE 36: Cross-Model Evaluation of Damage Evolution, Crack Width Progression, Displacement, Numerical Stability, and Mesh Influence (200mm Models)

# 6. Material parameter identification for light settlement-induced masonry damage

---

The following section presents an algorithm suitable for the determination of FEM model parameters developed specifically for computationally expensive FEM. This algorithm is used to improve the FEA results from Section 5, and also used to provide further information on the behaviour of the popular masonry material models.

## 6.1 Introduction

The Finite Element analysis of the structure provided a comprehensive set of results that accurately captured the damage distribution on the northern side of the building. The most accurate predictions for the inner leaf were obtained with the W2I-EMM-100mm model, which closely approximated the observed crack patterns. In contrast, the outer leaf results, while generally satisfactory, show potential for further improvement if reduction to the conservative crack width estimates can be achieved, as the produced crack patterns in FEA results for all variants were fairly resembling of the case study's crack pattern.

For the Total Strain-based Crack Model (TSCM), the model successfully reproduced the crack patterns but significantly overestimated the damage level. Similarly, the Engineering Masonry Model (EMM) also captured the crack patterns accurately but also exhibited a lesser degree of damage overestimation, which nonetheless remained present.

Nevertheless, FEA results at much smaller load factors showed good resemblance with the expected damage. Furthermore, the crack pattern on the outer leaf of the wall demonstrated that two failure modes were present, failures in the bed-joints and in the units which originally made an accurate definition of the material resistance challenging. Therefore, it raises the question of whether a more precise definition of the material parameters is possible and if this would help better approximate the expected analysis results.

Atamturktur, et al., 2010 states the robustness of an analysis is often contingent upon the precision of its input parameters. This is particularly critical in the context of multi-scale problems, such as in the case of subsidence-induced masonry damage, the calibration of parameters referring to the structure, substructure and their interaction play a vital role in the accurate depiction of the damage response on the superstructure.

Despite systematic and automatic FEA calibration methods that allow for the best determination of these parameters already existing, existing methods have been constrained by the extensive number of input combinations required to optimize parameter selection. This poses a significant limitation to the possible applications of these approaches, given the computational expense associated with updating finite element (FE) models, especially in high-fidelity contexts (Ramancha, et al., 2022). Alternative strategies have so far remained relatively novel, their application has predominantly been limited to numerical demonstrations and small-scale structural models in laboratory conditions with full-scale real-world structures being less common (Liu, et al., 2021).

To bridge this gap, this study proposes to implement a new optimisation approach for FEM calibration. A probabilistic surrogate-based optimization approach known as Bayesian optimization (BOPT). BOPT is an iterative algorithm that combines machine learning with optimization techniques, to offer the advantage of reducing computation time by minimizing the number of evaluations required of the objective function, in this case the Finite Element Model. This reduction is achieved through an acquisition function that balances an exploration and exploitation trade-off in each iteration, informed by a probabilistic understanding of the solution space provided by a surrogate, in this instance a Gaussian Process (GP).

## 6.2 Optimisation problem formulation

The primary goal of the calibration is to accurately align the FEM (Finite Element Method) model with its ground truth. Given the models that the baseline models already demonstrated good crack pattern accuracy, the focus of the optimisation is to reduce the damage level in the models.

To achieve this, possible uncertainties in input parameters are addressed by formulating an inverse problem, where these uncertainties are systematically changed to best reproduce the expected results. This is done through an objective function which measures how closely the FEM model approximates the true solution.

$$OF = \min_{\theta} E \left[ L \left( \mathcal{N} \left( f_{\text{FEM}} \left( \theta_{\text{i,var}}, \theta_{\text{fix}} \right), \sigma^2 \right) \right) \right] \quad \theta_{i,\text{min}} \leq \theta_i \leq \theta_{i,\text{max}} \quad \forall i \in \{1, \dots, n\}$$

*Equation 7: Calibration objective function.*

As shown in Equation 7, the objective is to minimize the variable parameters  $\phi$  in conjunction with the fixed parameters  $\lambda$ . The FEM evaluation yields an outcome that may include uncertain observations, characterized by a variance  $\sigma^2$ . These outcomes are then processed through a loss function, specifically the Huber loss, which is compared against the target model values. The expectation of this loss function is what we aim to minimize, thereby ensuring the FEM model's outputs are as close as possible to the true solution.

Nevertheless, the set of variable parameters should preferably not be optimised along solution parameters, such as mesh-size convergence criteria and step size. This separation is essential to maintain stationarity in the FE solution. Since a set of validated numerical solution procedure parameters was not evident from the FE damage assessment. A less computationally expensive set of solution parameters was chosen, with a model mesh size of 200mm and 360 load steps (0.1mm/step).

### 6.2.1 Choosing target features and optimisation parameters for continuum crack models

The informativeness of the target features, also known as comparative features ( $\phi$  in Equation 7), is fundamental for defining a well-posed Bayesian Optimization (BOpt) calibration problem. Target features are measures that can effectively evaluate the accuracy and quality of the model's results, providing a robust basis for comparison. Conversely, the calibration parameters should exhibit a high sensitivity to changes in the model's response, ensuring that their variation significantly influences the results. Choosing appropriate target features and calibration parameters enables the optimization to navigate the parameter space more effectively and converge on an improved solution.

#### Choosing a model target

A suitable target is one whose adequate calibration will best represent the desired solution. This parameter has preferably been able to be analytically determinable to be effectively incorporated into the loss function. Given that our targeted feature for the analysis is to reduce the models' damage severity and maintain the damage similitude. The damage severity was calculated using the Damage Parameter proposed by Korswagen et al., 2017  $\Psi$ , which through use of a crack-detection algorithm the crack



lengths and their average widths were determined to compute the Damage Parameter. Nevertheless, such a parameter is not available when aiming to evaluate damage similitude, which if not accounted for can pose a significant limitation as possible gains in Damage Level reductions may come at a cost of worsened crack pattern similarity.

Other studies, such as Kibriya et al. (2024), addressed this issue by utilizing computer vision to ensure consistent damage mechanisms between models and comparing extracted features from contour plots across different analyses. (Ajitkumar, 2022) similarly made use of computer visions to evaluate crack similarities. While this approach was feasible, incorporating an additional machine learning model would have unnecessarily increased the complexity of the procedure with potentially limited benefits. Therefore, the damage similarity was eventually not evaluated in the loss function.

## Optimisation parameters

Given that the focus of the calibration procedure will be on the outer leaf model, which is an unreinforced masonry wall, only the Masonry material parameters will possibly influence the results. As few explorations of continuum crack-model parameters exist to date and the results between them can vary identifying the most suitable material parameters was not immediately clear. In Bejarano-Urrego et al. (2018) the tensile model parameters, specifically tensile strength and Mode I fracture energy, were shown to have the most significant influence on analysis results, Giardina, 2013 also argued that interface stiffness along with tensile strengths and fracture energy were also the most influential parameters. And Prospero, et al., 2023 also demonstrated the interface stiffness to have a significant influence but also showed that the Elastic parameters could also have a large influence on results.

Therefore, all studies underscore a broad mix of parametric importance to various masonry material characteristics in different scenarios. This suggested that a comprehensive exploration of multiple parameters may be most beneficial. However, such a decision must be made with caution as higher dimensionality problems require further evaluations and particularly in low-data regimes can affect the quality of results. Therefore, given the lack of a clear compromise, this study evaluated all material properties which carried uncertainty in Jafari (2021), as long as the number of parameters was less than 20.

TABLE 37 presents the final set of chosen variables for both material models. Only continuous material parameters were chosen. The final bounds for the calibrated model parameters were determined using the relationships in TABLE 5, and the physical material properties and uncertainties based on the values in TABLE 2, TABLE 3, and TABLE 4. By using the 95<sup>th</sup> CI physical material parameters, assuming the parameters were normally distributed. Through using the unit's compressive strength, the mortar's bond wrench strength and the elastic parameters, the final model material properties were estimated with the values in between brackets constituting the lower and upper bound material parameters.

This procedure occasionally resulted in unrealistically large material parameters for clay masonry. For instance, the coefficient of variation for the shear modulus was reduced from 500 to 200 to prevent the model from exploring negative shear resistance values. Overall, this adjustment enables an evaluation of the material model's behaviour under extreme parameter conditions, which will be a key focus in the subsequent investigation. But it should also be borne in mind that the behaviour of the material models at the extremes may not be as relevant to the overall results.

## 6.2 Optimisation problem formulation

Property class	Total strain-based crack model				Engineering masonry Model			
	Parameter	Type	Selected [✓,○]	Input	Parameter	Type	Selected [✓,○]	Input
Elastic Material Properties	Young's Modulus [MPa]	Continuous	✓	[2936,15759]	Vertical Young's Modulus [MPa]	Continuous	✓	[2936,15759]
		Continuous	✓		Horizontal Young's Modulus [MPa]	Continuous	✓	[4397,6542]
	Poisson ratio	Continuous	○	0.2	Shear Modulus	Continuous	✓	[860,1643]
	Mass density [kg/m <sup>3</sup> ]	Continuous	○	1950	Mass Density [kg/m <sup>3</sup> ]	Continuous	○	1950
Compressive parameters	Reduction model	Discrete	○	No reduction	Compressive Strength [MPa]	Continuous	○	17.7
	Compressive behaviour	Discrete	○	Elastic	Fracture energy in compression [N/mm]	Continuous	○	54693
FTS at compressive strength					Discrete	○	4	
Cracking parameters	Tensile strength [MPa]	Continuous	✓	[0.23,0.45]	Failure mode	Discrete	○	Staircase Failure
	Mode I Fracture Energy [N/mm]	Continuous	✓	[0.0216,0.034]	Bed-joint tensile strength	Continuous	✓	[0.23,0.45]
	Residual tensile strength [MPa]	Continuous	○	0	Fracture Energy in tension [N/mm]	Continuous	✓	[0.0216,0.034]
	Tensile Curve	Discrete	○	Linear crack energy	Residual tensile strength [MPa]	Continuous	○	0
	Crack Orientation	Discrete	○	Rotating	The angle between diagonal crack and bed-joint [rad]	Continuous	○	0.6
	Crack Bandwidth Specification	Discrete	○	Rots				
Shear parameters					Cohesion [MPa]	Continuous	○	0.35 [0]
					Friction angle [rad]	Continuous	○	0.67 [0]
					Fracture energy in shear [N/mm]	Continuous	✓	[0.021,0.033]

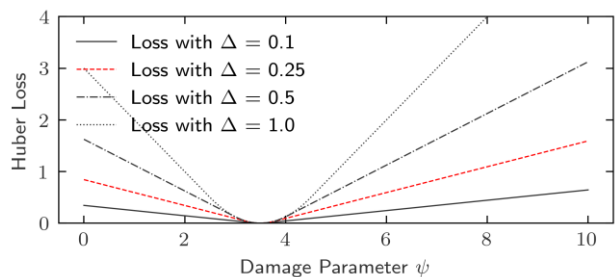
TABLE 37: Breakdown of the Finite Element Model's material parameters and optimisation bounds.

### Building a Loss Function

The last necessary component left is to quantify the loss. A Huber Loss function was selected due to its smooth transitions from quadratic to linear convergence when the absolute difference from the target exceeds a user-specified threshold,  $\Delta$ . This loss should help smoothen the loss computations and present a more uniform understanding of the effect the changes in material parameters have on the analysis.

The quadratic boundary  $\Delta$  was set to 0.25, as this value effectively captures the majority of model evaluations with a loss below 1, while also highlighting the complexities that may arise when optimizing within this boundary. Additionally, a penalty condition was incorporated to guide the solution space based on specific model evaluations. Convergence was defined by models that did not diverge and successfully achieved convergence in subsequent load steps. If a model failed to meet this criterion, a damage parameter of 7 was automatically assigned, as it corresponded to a loss of 1 when  $\Delta=0.25$  as was chosen.

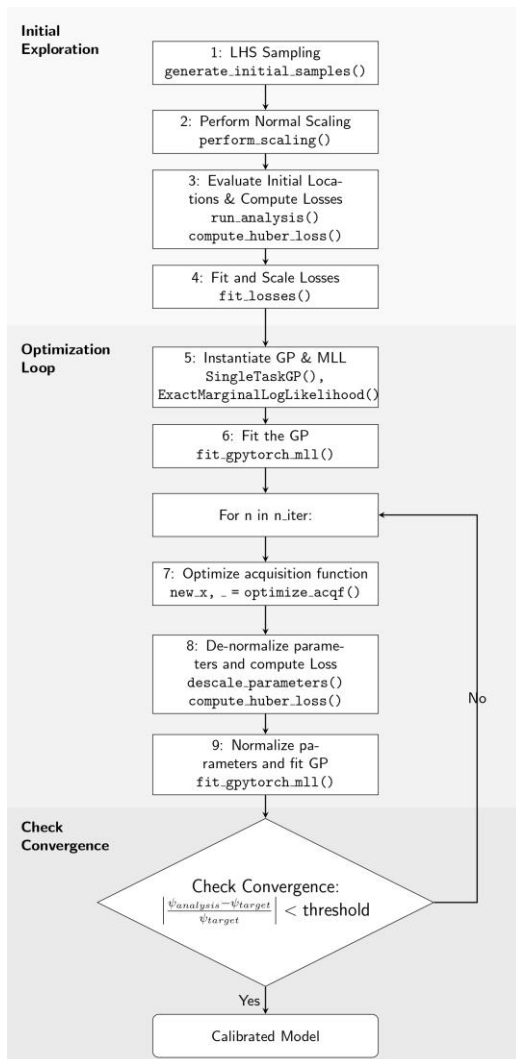
$$L_{\delta}(a, b) = \begin{cases} \frac{1}{2}(a - b)^2 & |a - b| \leq \delta \\ \delta \cdot \left(|a - b| - \frac{\delta}{2}\right) & |a - b| > \delta \end{cases}$$



Equation 8: Huber Loss function under different Delta parameters

## 6.3 Optimisation algorithm

EXTRACT 7 shows the pseudo-algorithm and flowchart for the procedure, and highlights how this can be split into 3 main steps the Initial exploration, The Optimization Loop and the Convergence/Benchmarking steps. The first step in the initial exploration is to define the targets, in this case: What damage Parameter do we want to obtain?, then the solution bounds are defined by using Jafari, 2021 mean values and coefficient of variation from TABLE 2,12,13 to calculate the 95th percentile confidence interval for the eventual model parameters. This was done by assuming the values to be normally distributed —as no material distribution shape was provided. TABLE 37 shows how the upper and lower confidence interval values may at times be unrealistic nevertheless, the outline procedure was not changed.



**Algorithm** FEA calibration through Bayesian Optimization

**Initialization:**

Initialize model parameters, bounds, and target damage parameters. Initialize scalers for the material parameters using `fit_targets()`.

**Initial Exploration:**

Generate initial grid samples across the parameter space using `generate_initial_samples()`.

Scale the initial samples using `perform_scaling('targets', 'scale', samples)`.

**Evaluation:**

**for** each sample in scaled samples **do**

Run FEM analysis using `run_analysis(sample, model_index)` to calculate the damage parameter  $\psi$ .

Compute the loss using `loss_function(sample)` based on the difference between  $\psi$  and the target values.

Fit the losses using `fit_losses()`.

Rescale the loss values using `perform_scaling('loss', 'scale', loss)` and store them.

**end for**

**Optimization Setup:**

Initialize and fit the GP model using `SingleTaskGP(X_init, Y_init)`.

Fit the model using `fit_gpytorch_mll(mll)`.

Define the acquisition function using `LogExpectedImprovement(gp_model, best_f)`.

**Bayesian Optimization Loop:**

**for** iteration in `range(max_iterations)` **do**

Optimize the acquisition function using `optimize_acqf(acq_func, bounds)` to propose new material parameter samples.

De-scale the proposed samples using `perform_scaling('targets', 'descale', new_x)`.

Run FEM analysis on the de-scaled samples using `run_analysis(new_x_unnorm)`.

Compute the loss using `loss_function(new_x_unnorm)`.

Update the GP model with the new data using `gp_model.set_train_data(inputs, targets)`.

Re-fit the GP model using `fit_gpytorch_mll(mll)`.

Monitor results and check for convergence or early stopping using `early_stopping()`.

**if** convergence criteria met **then**

**Break**

**end if**

**end for**

EXTRACT 7: Proposed Finite Element model BOPT calibration approach.

Having set the bounds an initial set of “n\_samples” is sampled from a Latin Hypercube Sampler (LHS). A procedure was chosen to allow handling discrepancy issues with dimensionality and the low number of samples due to the high cost of the evaluation of the objective function. Once the samples were made these were scaled, via MinMaxScaling, a procedure that transforms the values from a range from zero to one to prevent magnitude differences between the variables that dominate in the numerical procedures.

The optimization procedure begins by fitting a Gaussian Process (GP) to the initially known data points, essentially modelling them as a multivariate normal distribution. This process involves maximizing the likelihood of the model's hyperparameters. These hyperparameters are critical values that influence the behaviour of the GP, particularly by shaping its autocovariance function, or kernel. Key hyperparameters include the Length Scale (which determines how strongly the model correlates with distant points, and the Differentiability (Controls the smoothness or irregularity of the autocovariance function). These optimised parameters After fitting the GP with the optimized hyperparameters, the iterative optimization loop starts. The loop is set with a maximum of 200 evaluations and includes a stopping criterion, where the process will halt if a solution is found within 1% of the target Damage Parameter.

The looped optimization then starts by optimizing the acquisition function, which determines the next location to evaluate. This evaluation involves identifying the most promising locations based on the GP's current understanding of the solution space. The process begins with generating multiple initial search locations (`raw_samples`), which are mostly semi-randomly distributed across the solution space. These locations are then optimized to identify the best minima. Given that these evaluations often converge to local rather than global minima, a parameter `n_restarts` is set. This parameter defines the maximum number of times the gradient-based optimization can restart near the regions where it initially got stuck, thereby increasing the likelihood of escaping local minima. Among all the best-found locations, each is evaluated using the `LogExpectedImprovement` acquisition function. The location that offers the greatest potential for improvement—based on its mean and associated uncertainty—is selected as the next combination of material parameters to evaluate.

This final step is what sets Bayesian Optimization (BOpt) apart from other surrogate-based methods: it leverages a probabilistic model of the solution space to guide evaluations, making it a highly efficient solver. However, this approach also has certain drawbacks, such as sensitivity to model assumptions and the potential for computational complexity, which must be carefully considered during the optimization process. Once the new location is found the models' input parameters are descaled, the model is run, the damage parameter is found, the loss is computed by evaluating possible penalties and comparing its value to the target, the targets are scaled and a new GP is fitted for the procedure to take place again until the maximum number of iterations of the convergence criterion is met.

### 6.3.1 Hyperparameter selection for a continuum crack model

While Bayesian Optimization (BOpt) procedures remain consistent across different problems, specific considerations can prove beneficial when it is applied to Finite Element Method (FEM) analyses. All of these decisions constitute Hyperparameters, which are parameters that are user-defined decisions which influence results.

In the context of Continuum crack models, one of the primary considerations is the selection of an appropriate surrogate. Usually in BOpt architectures probabilistic surrogates such as Gaussian Process (GP) are typically used. The choice of GP is usually based on two characteristics: the nature of the data (continuous or discrete) and the level of expected uncertainty (noise) from the evaluations.

In this particular case, where only a single objective—the damage parameter—is being tracked, all optimised variables are continuous, and the noise is expected to be small and random due to small changes in the numerical solution between non-penalised converged models, a `SingleTaskGP` was determined as the most suitable model.

Further considerations for this GP have to be made upon its choice of likelihood and autocovariance function. An ExactMarginLikelihood was chosen due to the low number of evaluations and its exact precision, whilst a Matern Kernel was also chosen as it is regarded as the most versatile kernel. The default differentiability of 2.5 was unchanged as the value is sufficiently high to allow the model to generalise well the data and not be prone to overfitting. The length scale parameter, which controls the correlation distance between parameters was set with the default prior and was introduced as part of the Likelihood, meaning that it was optimised in every iteration to ensure that the GP model could adequately capture the underlying patterns in the data without being too sensitive to small variations.

The final and equally important decision involves the choice of acquisition function. An improvement-based acquisition function is particularly effective when you have confidence that the Gaussian Process (GP) can accurately capture the underlying solution space. Among the available options, improvement-based functions have generally been the most popular due to their ability to effectively balance exploration and exploitation.

In this context, the traditional Expected Improvement (EI) function is often considered the most balanced choice, as it manages the exploration-exploitation trade-off in a relatively unbiased manner. To address potential challenges such as non-convexity in the solution space—especially arising from the non-linearities inherent in FEM models—the sampling strategy was adjusted. Specifically, a 3/5 ratio favouring exploration was implemented to ensure a more thorough search of the solution space. This strategy helps to avoid premature convergence to local optima, which is a common risk in highly non-linear and complex optimization problems.

<b>Component</b>	<b>Procedure</b>		<b>Kernel</b>		<b>Acquisition Function</b>		
Decision	Exploration/ Optimisation		Mater Kernel		LogExpectedImprovement		
Hyperparameters	N° Initial Samples	Max iterations	Smoothness	Length scale	Parallel Evaluations	Raw Samples	N° Restarts
Value	25	200	2.5	**Likelihood	1	25	15

TABLE 38: Algorithm components and hyperparameters.

### 6.3.2 Limitations

The calibration procedure in this study faced several limitations, primarily stemming from computational constraints and the nature of the optimization problem. One key limitation relates to the modest number of samples and restarts, which was necessary due to the high computational demand of the numerical simulations. While a more comprehensive search would typically include hundreds of samples, the available computational resources restricted the number of initial evaluations. Consequently, the chosen sample size had to be smaller than the total number of evaluations typically required. This constraint may have limited the ability to fully explore the solution space, particularly if the initial Gaussian Process (GP) model did not adequately capture the complexity of the problem. As a result, while the chosen approach is well-suited for the problem at hand, the trade-off between sample size and computational feasibility might hinder the thoroughness of the search and the robustness of the final solution.

Another limitation concerns the lack of parallel evaluations due to restrictions within DIANA's Python API, which forced the number of parallel evaluations to be set to one ( $q=1$ ). Although this did not significantly impact the overall optimization performance, it did limit the efficiency of the process, as

only one evaluation could be conducted at a time. Consequently, the total number of iterations was limited to 200, which is significantly lower than other optimization techniques like Particle Swarm Optimization which often require an order of magnitude more iterations. While 200 iterations typically represent the point of diminishing returns in well-posed Bayesian Optimization (BOpt) problems, this constraint could reduce the capability to identify a global optimum, especially if the problem is highly non-convex or complex.

Further, the robustness of the objective function, represented by the finite element model, is assumed to provide reasonable estimates of the ground truth. However, it is also acknowledged that some level of noise might be present in these estimates, which could impact the precision of the optimization results. The challenge lies in balancing model accuracy against generalization. Overfitting the model can increase the non-convexity of the problem and complicate the solution procedure, while an overly generalized model may fail to capture critical local minima. Consequently, the final solution is unlikely to represent the true global minimum, emphasizing the importance of properly tuning the Gaussian Process (GP) to ensure a balanced representation.

Moreover, the inherent limitations of the GP model become evident in this context, as the small number of evaluations (approximately 200) restricts its ability to accurately capture the complexity of the high-dimensional, continuous problem. Lastly, a notable limitation of this study is the focus on a single objective—the Damage Parameter. By primarily optimizing this parameter, other important features such as crack pattern similarity and model stability might not be fully accounted for, even though they were guided by analytical benchmarks. Consequently, the conclusions derived from the optimization may not be universally applicable to other related problems or failure mechanisms.

### 6.3.3 Implementing the automatic calibration procedure

The Bayesian optimization approach was implemented using the open-source library BoTorch (Balandat, et al., 2020), a project stemming from the machine learning framework PyTorch. BoTorch was released in 2020 at Facebook to enhance the efficiency of backend infrastructure and the tuning of hyperparameters in ranking models in social networks. A selection of BoTorch's models, acquisition functions and optimisation modules were used to build an optimisation algorithm suitable for the optimisation of FE-based masonry crack models. The eventual script was run on an Azure VM with Processor – AMD EPYC 7763 64-Core 2.44 GHz, and Memory - 32.0 GB. In this analysis, all threads were allowed to be used and the scripts were run through in-built python interpreter and Python API in Diana 10.8.

The architecture and its algorithm were tested on the Branin problem, a not too non-convex benchmark optimization problem. The algorithm developed in this research was compared to other Botorch-based alternatives utilizing similar Improvement-based acquisition functions, and against the general search algorithm Sobol. The performance of the proposed algorithm was found to be comparable to that of BoTorch's qEI variant, with minor differences observed between runs, likely attributable to the influence of heuristics on the solution. The overall problem's regret (or best-found solution) exhibited an inverse logarithmic trend, characterized by a stepped progression. The final results indicated that the solver's capabilities were on par with those of BoTorch's solution and outperformed the general search method Sobol. This served as an initial validation for the model and was deemed sufficiently capable of solving non-linear problems under good problem formulations.

## 6.4 Material parameter identification results

The results of the material parameter identification procedure are presented using four types of visualizations: an optimization progression plot, a comparison between the mean and best models, two sets of contour plots showing the bivariate mean and variance near the optimal solution, and contour plots illustrating the covariance between parameters. Note that not all iterations are included, as analyses penalized based on convergence criteria have been pre-processed. This filtering step has been applied to all presented plots and analyses.

### 6.4.1 Damage assessment results

Firstly, Figure 38 displays the best damage parameter score across iterations (left) and the corresponding damage parameter score for each specific iteration (right), providing insights into the optimization process over time. The results from the analysis demonstrate that the material parameter identification procedure was overall successful. The process effectively reduced the damage state of the models closer to its target for both material models. Its implementation also demonstrated more effectiveness on the EMM than on the TSCM where the gains were limited.

The damage parameter reduction was more pronounced for the EMM model, which also exhibited an overall greater sensitivity to material parameters, as can be observed by the variance in its damage estimations which could fluctuate by  $1.5 \Psi$ . Due to the models' sensitivity, the procedure was able to identify the combination of material parameters which was relatively close to its targeted damage state. By contrast, the gains on the TSCM were limited, and the model demonstrated to be less sensitive as variations in the material parameters didn't often produce large changes in the damage parameter its variance being around  $0.5 \Psi$ .

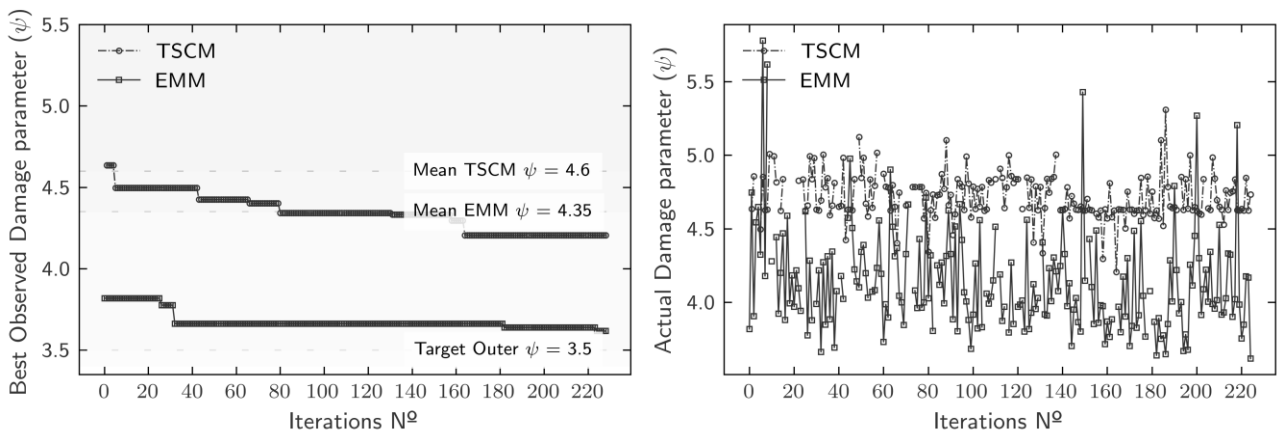


Figure 38: Damage parameter lowest value and values as a function of model iterations

TABLE 39 presents the mean and best crack patterns, damage parameters, difference to the target, loss, and material parameter values and percentiles for both models. It can be observed that a small loss of crack-pattern accuracy has occurred on both models, but the overall shape remains relatively similar therefore the gains in precision in the damage state did not come at a large crack-pattern accuracy cost.

A difference in the EMM mean results against the original FEA results happened due to the changes in the numerical solution procedure in the optimisation as the number of load steps was reduced from 720 (0.05mm/step) to 360 (0.1mm /step). In this model, the crack pattern improved as it was able to be

produced on the right side of the wall where the damage is located, but was still poorer than the standard 200mm mesh analysis in 5.4.

The TSCM calibrated model was able to reduce its maximum crack width by 4mm, but it was also able to estimate a smaller Crack 9 (Inferior left corner bottom right opening) which led to a 20% decrease in the damage level. The material parameters also show how the TSCM was better optimised by resorting to the extreme values either in the 95<sup>th</sup> or 5<sup>th</sup> CI, these material parameters are also likely optimistic for clay masonry units and mortar and most likely represent an unrealistic resistance by the masonry. But they also show a loss in correlation as the estimation of the tensile strength and tensile fracture energy is both approximated by bond wrench resistance for the tensile strength its maximum values were used but for the tensile fracture energy its minimum values were used.

In the EMM the maximum crack width was reduced by 50%, but the main cracks present in the outer leaf Cracks 1,5,9 have been better predicted approximated being a maximum of 4mm as in the case study. Nevertheless, other cracks are also present as with most other performed EMM analyses. The final material parameters obtained also appear uncorrelated as the Vertical and Horizontal Young's Modulus CI are inversely correlated. This is also true for the tensile resistance and the tensile fracture energy. The rest of the parameters appear to follow their natural behaviour.

### 6.4.2 Discussion on the optimisation Procedure

The damage parameter optimisation progression demonstrated a usual BOpt optimisation improvement shape, initial gains were much greater and became less as more exploration of the solution space took place. The amount of improvements achieved at later iterations may also hint that the optimization problem faced two relatively non-convex solution spaces, which appears to be the case as the contour plots in TABLE 40 and TABLE 41 show.

The final solution spaces also help illustrate firsthand the workings of the GP's. In the TSCM the solution space shows a clear local minima and maxima. Since the best solution location has to be in the plot this means that the true global minima (marked with X) was close but had been regularised out. By contrast, the fit of the EMM was much better, aside from irregularities with Vertical Young's Modulus, the Global Minima was always located within the lowest psi region. Although the mismatch in the case of the TSCM was not too significant it does illustrate the possible limitations that using a surrogate has. Nevertheless, the limitations exist in any regression problem, and in all the performance of the GP for a high dimensional space with only approximately 225 samples was strong.

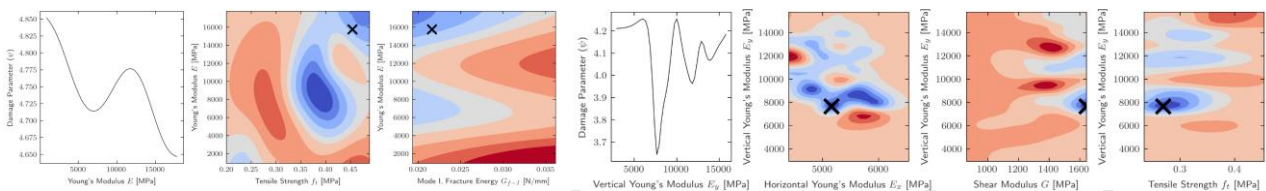


Figure 39: Comparison of surrogate limitations, unable to capture true global minima (left) EMM (right).



6. Material parameter identification for light settlement-induced masonry damage

	<b>Parameters</b>	<b>Mean model</b>	<b>Parameters</b>	<b>Calibrated Model</b>
<b>Total Strain based rotating crack model</b>	Total Loss: 0.2087	NLA Load-step 361, Load-factor 1.0000, Sub Deformation Crack-widths Ecw1 min: 0.00mm max: 21.93mm	Total Loss: 0.1455	NLA Load-step 361, Load-factor 1.0000, Sub Deformation Crack-widths Ecw1 min: 0.00mm max: 17.84mm
	$\Psi_{\text{Mean,TSCM}}$ : 4.46 [+27%]  Material Parameters: $E_x=9348$ [MPa] $f_t=0.34$ [MPa] $G_{f-I}=0.0283$ [N/mm]		$\Psi_{\text{Cal,TSCM}}$ : 4.2 [+20%]  Material Parameters: $E_x=15760$ [MPa] 95 <sup>th</sup> Percentile $f_t=0.454$ [MPa] 95 <sup>th</sup> Percentile $G_{f-I}=0.02$ [N/mm] 5 <sup>th</sup> Percentile	
<b>Engineering masonry model</b>	Total Loss: 0.1787	NLA Load-step 361, Load-factor 1.0000, Sub Deformation Crack-widths Ecw1 min: -0.02mm max: 15.10mm	Total Loss: 0.0097	NLA Load-step 361, Load-factor 1.0000, Sub Deformation Crack-widths Ecw1 min: 0.00mm max: 8.25mm
	$\Psi_{\text{Mean,EMM}}$ : 4.34 [+24%]  Material Parameters: $E_x=9348$ [MPa] $E_y=5470$ [MPa] $G=1250$ [MPa] $f_t=0.344$ [MPa] $G_{f-I}=0.55$ [N/mm] $G_{f-II}=0.283$ [N/mm]		$\Psi_{\text{Cal,EMM}}$ : 3.64 [+4%]  Material Parameters: $E_x=8613$ [MPa] 45 <sup>th</sup> Percentile $E_y=5158$ [MPa] 37 <sup>th</sup> Percentile $G=1643$ [MPa] 76 <sup>th</sup> Percentile** $f_t=0.267$ [MPa] 18 <sup>th</sup> Percentile $G_{f-I}=0.03$ [N/mm] 64 <sup>th</sup> Percentile $G_{f-II}=0.027$ [N/mm] 37 <sup>th</sup> Percentile	

\*\*Global CI. Full bounds were constrained by changing  $\sigma^2 = 500 \rightarrow 200$

TABLE 39: Results comparison between identified against mean material parameters analysis results

**GP Mean and variance against material parameters**

*At best solution*

**Model Mean**

**Model Variance**

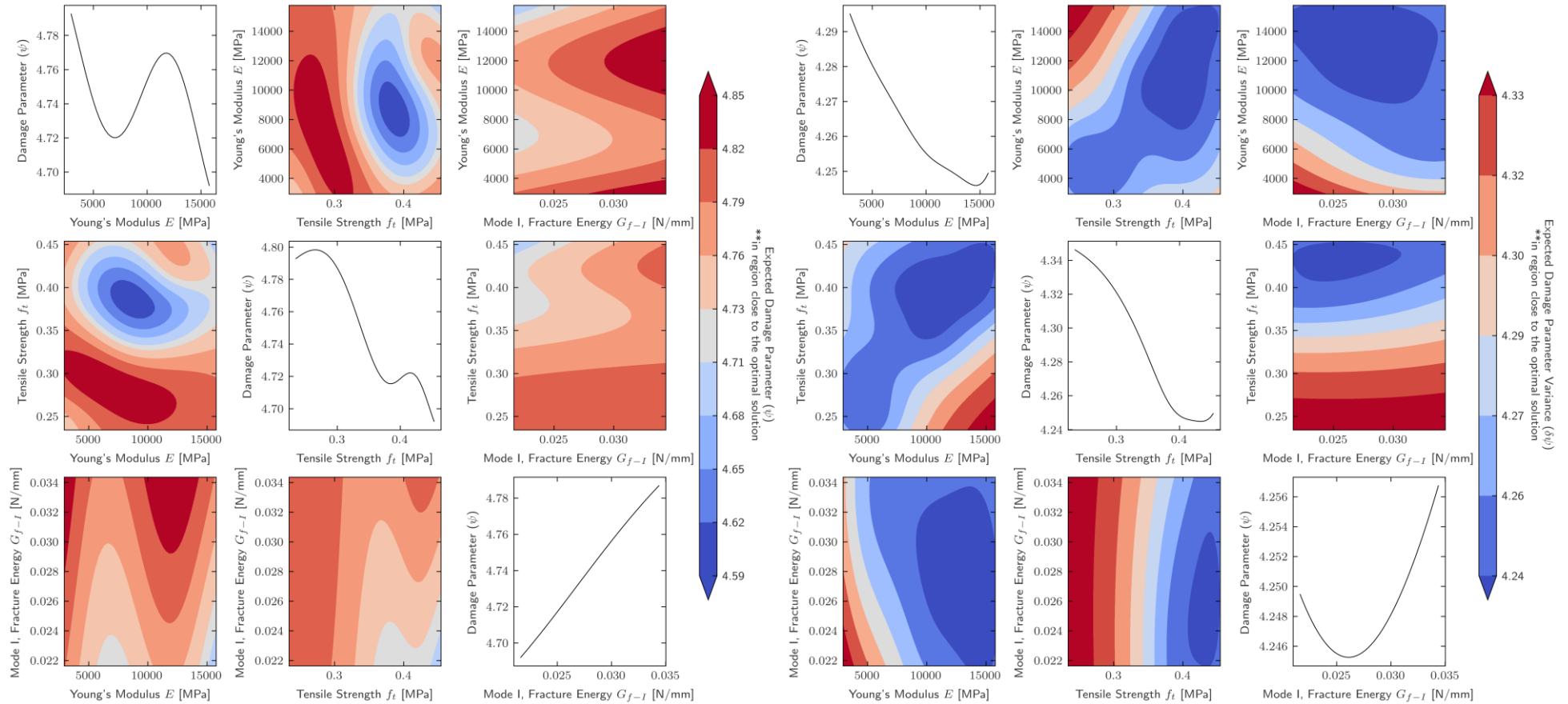


TABLE 40:  $\Psi$  Mean and variance for the TSCM at region close to the best solution.

**GP Mean and variance against material parameters**

*At best solution*

**Model Mean**

**Model Variance**

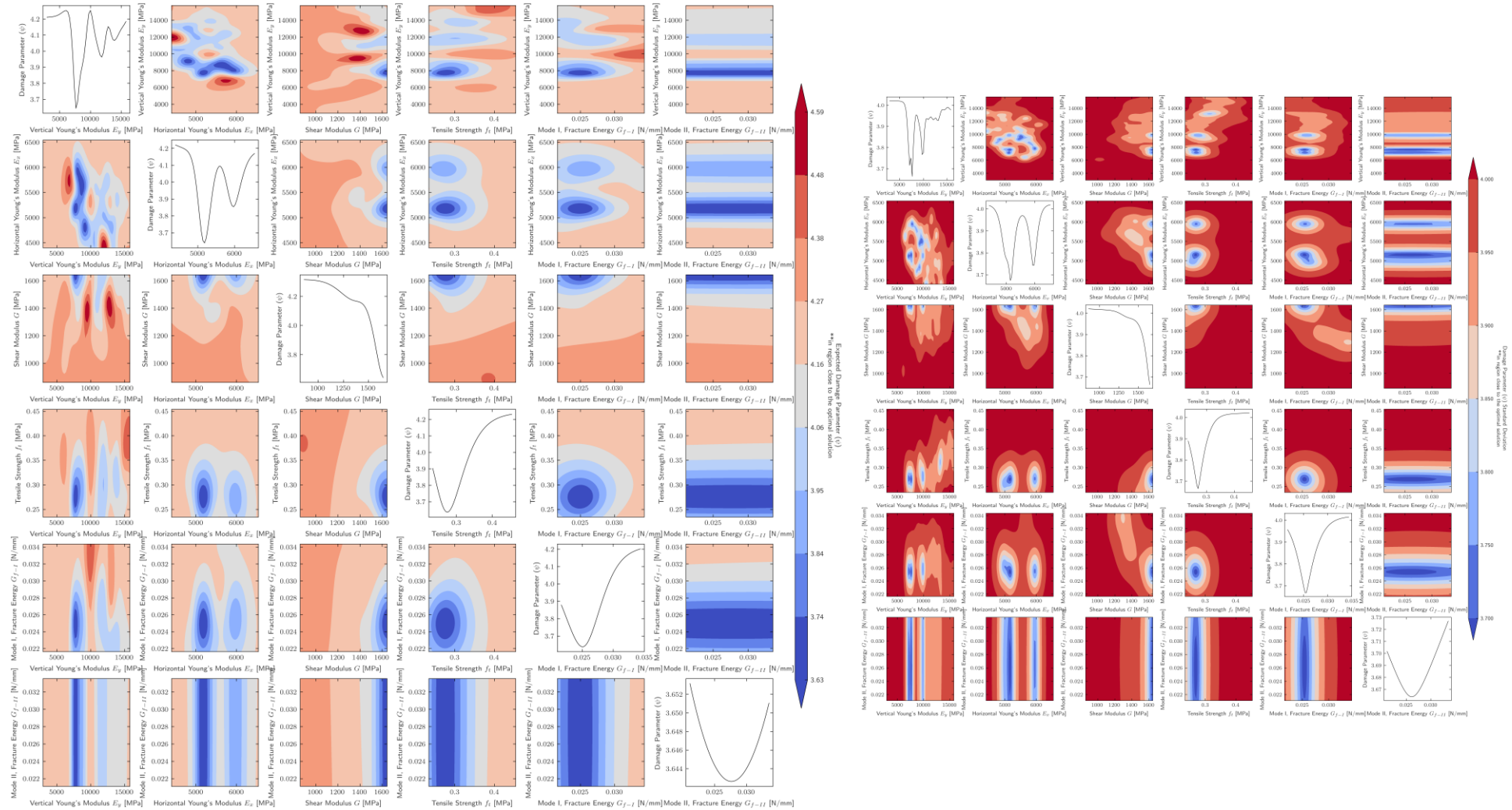


TABLE 41:  $\Psi$  Mean and variance for the EMM at region close to the best solution.

## 6.5 Observations about the material model behaviour

The influence of different material parameters on the constitutive behaviour can be analysed due to the straightforward design of the outer leaf model, which consists of a plain, unreinforced masonry wall with fixed openings. As the size of the openings remains constant, variations in the material properties primarily govern the model's response, making it easier to derive conclusions from the different simulations.

The first approach for evaluating the material parameter influence involves calculating feature importance scores using a Random Forest Regressor. This method correlates material parameter combinations with their respective loss values, identifying which parameters most significantly reduce the prediction error. The resulting importance weights are presented in TABLE 42. The second method assesses the material model parameters by plotting them against the mean Damage Parameter predicted by the surrogate model (TABLE 40 and TABLE 41). The same Gaussian Process (GP) model is used but with adjusted noise and length-scale constraints for improved accuracy. Similarly, TABLE 43 displays the model's Kernel with variance (diagonal plots) and covariance (off-diagonal plots). Covariance is highest where the Damage Parameter changes most, like at minima and maxima. All contour plots show the bivariate influence of the material parameters against the damage parameter at the optimal solution, keeping other parameters constant at their best values.

### 6.5.1 General Observations

The feature importance scores agree that the shared most important parameter across both constitutive laws was the masonry's Young's Modulus, followed by the tensile strength and the fracture energy. These scores are slightly different to those in Giardina, 2013 as in this study a much greater importance is placed on the elastic resistance, but similarly agrees with the relative importance of the tensile strength.

The high feature importance of Young's Modulus appears mechanistically accurate, as a stiffer elastic response leads to lower strains in the masonry under the same applied displacement. Lower strains correspond to lower stress levels, reducing the likelihood of the tensile strength of the masonry being surpassed and reducing the probability of crack initiation. However, in the case that the applied displacements are large enough to reach or exceed the tensile strength of the material, the higher stiffness can lead to more concentrated stresses in localized regions resulting in fewer but more severe cracks. The differences between both studies likely lie in the difference between the models as Giardina, 2013 used a 3D semi-coupled modelling approach whilst this study used a 2D coupled modelling approach.

<b>Model</b>	<b>Feature importance Scores</b>					
TSCM	Young's Modulus 0.47		Tensile Strength 0.33		Mode – I Fracture Energy 0.19	
EMM	Vertical Youngs Modulus 0.18	Horizontal Young's Modulus 0.15	Shear Modulus 0.14	Tensile Strength 0.17	Mode-I Fracture Energy 0.14	Mode -II Fracture Energy 0.19

TABLE 42: Benchmarking of calibration gains and feature importance scores.

The results from the GP's mean and Kernel present a different picture to those from the feature

importance scores. These plots show that close to the optimal solution the fracture energies appear to have a greater importance on the results, whilst the elastic parameters appear to have the smallest effect. Furthermore, both the model means show non-convex solutions more in the case of the EMM, this means that smooth correlations between the material values and the damage are not present in both material models. Nevertheless, since these are more “local effects” the conclusions drawn from the feature importance scores are more transferable to the entire problem.

### 6.5.2 Total Strain based crack model observations

The distribution in the damage parameter evaluations for TSCM showed that the damage parameter usually fell relatively closer to the lower percentile of all evaluations (Figure 38). Occasional increases in the estimate occasionally happened but the overall variance remained relatively similar and small. This indicates that the TSCM damage overestimation identified in the previous section of FEA may be more driven by the constitutive law formulation or suitability to masonry analysis rather than the material parameters.

The TSCM results show a clearer influence by specific material parameters. Young’s Modulus followed by the Tensile Strength and lastly, the fracture energy having the most impact. The importance of the Elastic modulus is expected as deformations in the wall that don’t happen elastically must happen inelastically in this case in the form of cracking. Following upon this it is then also reasonable that the second most influential parameter is the tensile strength as it will determine the stress limit from which cracking will occur. Lastly, the fracture energy may be the least influential overall, but the GP mean and covariance close to the best solution does show that around these regions its influence was most important.

The best solutions material parameters (TABLE 39) as well as the GP’s mean contour plots (TABLE 40) show that the reduction of the damage parameter in the TSCM resorts to extreme material parameter resistances. Due to the smaller number of material parameters in the TSCM, the results in table TABLE 40 provide a much more comprehensive understanding of the full model behaviour. Given that the Tensile fracture energy relationship with Young’s Modulus and Tensile Strength is linear is most regions by focussing on the contour plots (2,1/1,2) and superposing the linear fracture energy influence strong global observations can be made.

Firstly, it is obvious that the material parameter relationship against the material parameter is non-convex mostly influenced by Young’s Modulus which shows a correlation with the Tensile strength, this relationship appears to suggest that stronger material values correlate with lesser damage. This observation is more evident for the Tensile strength than the Young’s Modulus. This statement stands contrary to the results from the feature importance scores. This may indicate that further considerations most likely also influence the damage estimates, most likely topological model features.

Lastly, the solution appears to show that the correlation of the fracture energy against the other parameters is not just inverse but appears to be uncorrelated as can be seen in TABLE 43. This does not follow the material parameter relationships from Jafari, et al., 2022. That supports a linear correlation between Bond Wrench Strength, Tensile Strength and Fracture Energy. By the contrary, TABLE 43 shows a strong correlation between Young’s Modulus and the Tensile Strength, although their covariance is circular due to the minimum proximity the shape of the circle is very symmetrical indicating a strong correlation.

### 6.5.3 Engineering Masonry Model observations

Before presenting the observations from the EMM analysis, it's important to address a significant limitation that may affect these findings: the influence of the specific failure mode associated with the EMM, concerning the behaviour of Wall 2. Given that depending on the failure mechanism taking place on the masonry it is possible that the influence of certain material parameters disproportionately influences the damage level estimates in the model. For example, if failure in the joints is taking place due to solely a shear failure, it is expected that the shear parameters may play a greater influence in determining the ultimate resistance of the specimen. Therefore, the following conclusions from the EMM model may not be generalizable to other failure modes or the EMM constitutive law as a whole. Nevertheless, despite these limitations, the findings still provide valuable insights into the model's behaviour.

The feature importance scores for the EMM show relatively equally important scores between material parameters, although the importance of the Young's Modulus and the tensile strength is still relevant the shear fracture also achieved the highest feature importance score.

The EMM also demonstrated to value most an adequate combination of material parameters rather than extreme material parameters as was the case in the TSCM. This is evident in the final material parameter CI's from the model's best solution, showing a range of different CI's between material parameters. Similar conclusions can also be made from inspecting the results from the GP (TABLE 41), these show a quite non-convex constitutive law behaviour, where all features aside from the Shear fracture energy show a large influence on the damage state of the wall due to their large variance of psi. This in part may also be why the EMM model's damage values demonstrated a high variance between iterations. Obtaining an adequate combination of most material parameters appears necessary for lower damage level estimates (Figure 38).

The shear fracture energy behaviour was also an interesting characteristic of the EMM behaviour. This material parameter behaved similarly to the tensile fracture energy behaviour in the TSCM. The material parameter was shown to be independent of the rest of the material parameters. Furthermore, based on the results from TABLE 41 it appears its feature importance to be small, its variance close to the optimal solution is the smallest which should correspond to a low feature importance score, which stands contrary to its feature importance score. It is possible that as its formulation in Jafari, et al., 2022 the unit's compressive strength creates a too dissimilar correlation against bond wrench resistance values and elastic parameters. The second possibility is also the behaviour of the constitutive law.

The correlations between most material parameters are weak. TABLE 41 shows that while the vertical and horizontal Young's Modulus exhibit similar behaviour, neither is correlated with the damage parameter. Unlike the TSCM, tensile strength also shows no correlation with the elastic properties. Additionally, non-linear material properties have a more pronounced convex effect on the damage state compared to elastic properties. This is evident from the highly irregular patterns observed in the plots of the first and second rows and the first to third columns. Overall, the model's behaviour appears satisfactory, as key parameter correlations are evident. However, the non-convexity of the solution space raises concerns as it potentially affects the model's numerical stability. Furthermore, This issue might be related to the model's elastic behaviour, as the model's non-linearities could worsen convexity.

**Material parameter covariance**

**TSCM Kernel**

**EMM Kernel**

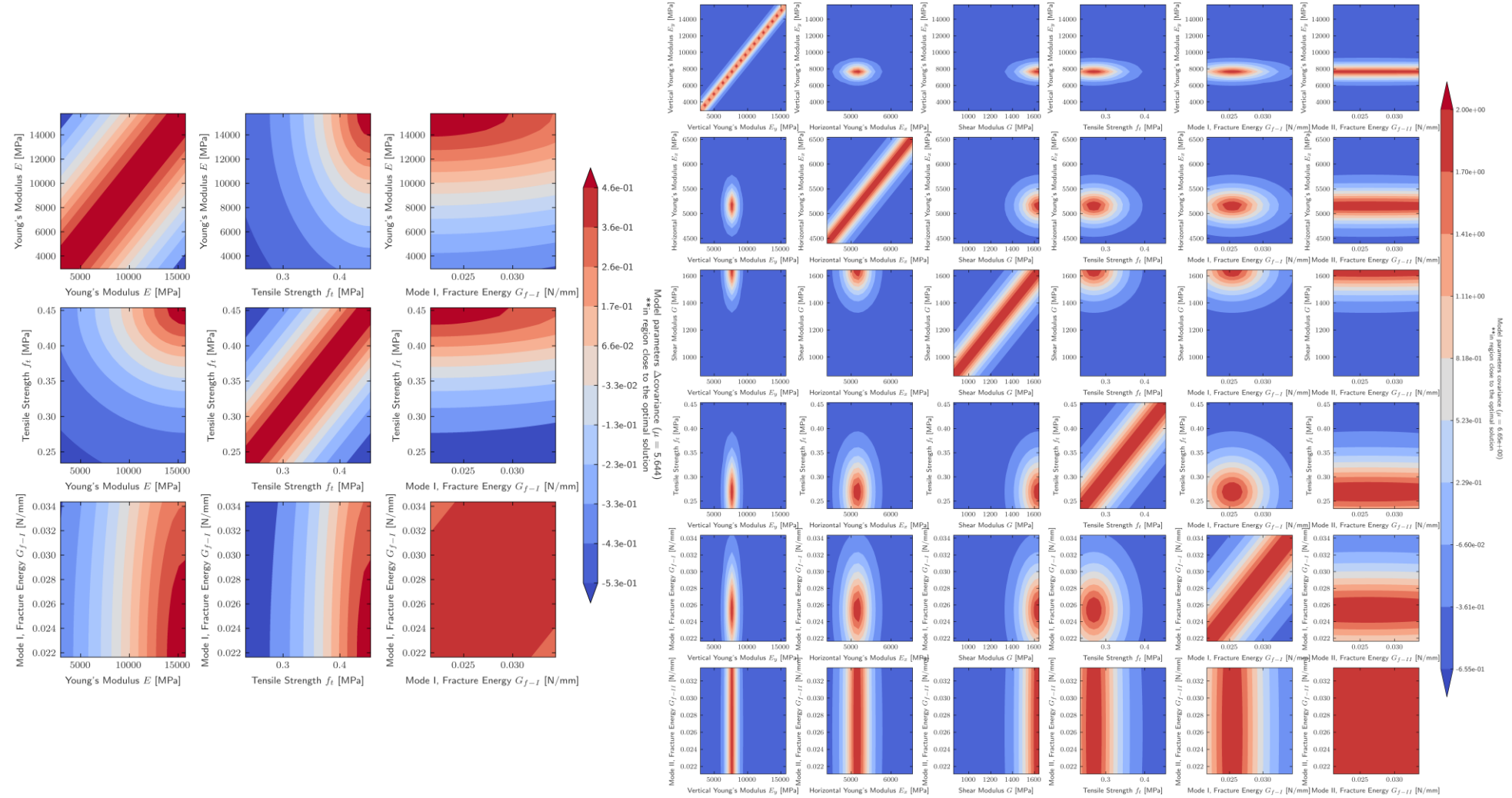


TABLE 43: Parameter covariance as understood by the GP's Matern kernel for the calibration of the EMM and the TSCM

## 6.6 Conclusions

The BOpt implementation demonstrated that the parameter identification in higher-fidelity finite element models is feasible. It also shows that the non-linear response of continuum crack models is still interpretable by a Gaussian processes surrogate model and that optimization can take place.

The procedure was able to reduce the damage level for both model families. The TSCM damage parameter reduction was limited, whilst the EMM's was able to be sufficiently reduced to its target. The final crack patterns presented changes to their original results, but these changes were not major. Furthermore, mainly due to the reduction of crack widths throughout the results, the analyses for Wall 2's outer leaf were able to be marginally improved.

This improvement was not sufficient and a one-to-one analysis of the wall was achieved. Throughout the different model evaluations, the changes in the material parameters were able to influence the crack patterns in major ways as well as the crack widths. Nevertheless, Cracks 3 and 10 have been unable to be reproduced in any model.

The material parameters changes to the TSCM appear to influence previously simulated crack patterns, or changes to the mechanism in the wall, which changed from the left to the right-hand side of the wall. The influence of material parameters on the EMM crack patterns and crack widths was much greater demonstrating that the material parameters did have a much greater influence on results. This is why the optimisation procedure may be more suited for its use under this model.

- BOpt was able to successfully identify more suitable parameters for a computationally expensive FEM.
- Improvement to the models took place, but a one-to-one damage representation was not able to be produced.
- Optimization reduced damage for both models yet, TSCM gains were limited and the EMM against met the target damage level.
- EMM's higher sensitivity in its crack width and damage level indicates that the optimization procedure can be a suitable addition to this model.

The optimisation procedure was also able to highlight the workings of the material models as well as add to previous existing findings on the influence of model parameters on FEM damage assessments.

It is believed that the stronger correlation between the Elastic Modulus and the Tensile Strength in the TSCM led to the maximum damage parameter reduction achieved via more extreme CI material parameter values. Whilst the larger non-convex relationships between material parameters in the EMM led to the maximum damage reduction being achieved through a specific combination of material parameter CI's, this is also observed in a more balanced set of feature importance scores.

The investigation demonstrated that the material model constitutive relationships produce non-convex relationships between different material parameters. In the case of the EMM this was truer between elastic parameters. Young's Modulus was found to be more influential than previously reported, suggesting that elastic properties may play a more critical role. The correlation between Tensile fracture energy (TSCM) and the shear fracture energy (EMM) in the material models appeared to be inverse to the expected physical correlations found in Jafari, 2022.



# 7. Conclusions

---

This Chapter discusses and consolidates the findings of this research project. It starts with the list of highlights and contribution in section 7.1. In section 7.2., the research questions are answered whilst section 7.3 presents the recommendations for future research.

## 7.1 Research contributions

The main scientific contributions of this thesis can be summarized as follows:

**RC 1.** This thesis is among the first to apply a comprehensive range of damage assessment methods to a full-scale masonry building that has experienced actual subsidence-induced damage.

**RC 2.** This thesis provides a comprehensive benchmarking of the accuracy of damage assessment methods for masonry buildings affected by subsidence.

This thesis demonstrates that damage levels and crack patterns in masonry buildings can be effectively approximated using current assessment methods. However, it also uncovers key limitations that influence the accuracy, reliability, and applicability of these methods across various scenarios. These findings highlight the need for further refinements to enhance assessment precision and extend the range of conditions under which these methods can be reliably employed.

**RC 3.** This thesis demonstrated the possible accuracy achieved when using a topologically equivalent representation in a 2D Finite Element Analysis.

This thesis explored the range of results a geometrically explicit, macro-modelling, uncoupled 2D Finite Element Model can generate when subjected to a known settlement-induced displacement profile. The study found that, while the best models produced relatively accurate crack patterns, the estimated crack widths still deviated by approximately 5 mm from observed values.

**RC 4.** This thesis developed a Material Parameter identification algorithm suitable for use in high-fidelity Finite Element Models.

A material parameter identification algorithm was developed and successfully implemented to identify the optimal FEM model parameters for a desired set of results. This algorithm was also efficient enough to allow the optimisation of computationally expensive Finite Element Models.

**RC 5.** The thesis provided a comprehensive breakdown of the material parameter influence for the two main masonry constitutive laws available in the software package Diana FEA.

This thesis performed a study of the two most suitable masonry constitutive laws, the Total Strain Based Crack Model (TSCM) and the Engineering Masonry Model (EMM). The investigation outlined their fundamental behaviour and demonstrated that specific material parameters' behaviour did not behave similarly to their physical correlations outlined in the literature.

## 7.2 Returning to the research questions

Revisiting the research questions outlined in 1.2 the answers to the research questions are as follows:

**RQ 1.** To what extent can current solution methods based on state-of-the-art approaches predict a masonry building's state when undergoing a subsidence process?

The damage state of a masonry building under subsidence-induced settlements can be approximated fairly accurately. Visual assessments allow the hypothesising of mechanisms based

on damage characteristics, which in this case study allowed to identify the main mechanisms acting on the building, one-ended settlement.

The Empirical assessment and Limit Tensile Strain Method were able to estimate the damage levels in 5/6 walls. Both methods demonstrated an inability to assess the damage in a wall that underwent tilted settlements. Empirical assessments demonstrated a much greater variability between individual assessments and a greater necessity to employ engineering judgment. The results from the Limit Tensile Strain method were demonstrated to be robust.

Finite Element Analyses were able to reproduce crack patterns, crack widths and the overall behaviour of the masonry element. Nevertheless, a tendency to overestimate the severity of these damage forms was present. The FEA results were able to reproduce 5/7 cracks, it also did so with good crack similarities. Crack patterns were shown to be more localised in the TSCM and more smeared in EMM. Nevertheless, FEA results demonstrated to be subject to uncertainties based on the numerical solution parameters, mainly the mesh size. This influence on the mean crack width error was approximately 4.5 mm and 1  $\Psi$ . Eventually, the above differences were able to be reduced through the material parameter identification algorithm nevertheless, these gains came at a small crack pattern similarity cost.

**RQ 2.** Given that an approach has a level of success, what are its characteristics and limitations in assessing the mechanistic behaviour of a structure? And under what circumstances should these methods be adopted in practical scenarios?

Visual assessments should be used only when physical evidence of damage is available, and a deeper understanding of the building's behaviour is sought. Empirical and analytical methods are suitable as preliminary assessment tools to evaluate the likelihood of damage being currently present or to occur in the future and what is its likely severity. Finite Element Analysis should be employed when a comprehensive reproduction of the building's behaviour is required, especially when detailed damage features such as crack locations and shapes are important to the evaluation.

Chronologically the assessment methods characteristics and limitations identified are as follows.

### **Visual Assessment**

The Visual assessment aided by de Vent, 2011 demonstrated limitations when the determinations of damage characteristics had to be made, as having to determine the damage shape and tapering was not always easy with the visual evidence. Based on this, the likelihood for wrong choices to be made in the Diagnostic tool's decision trees is large which eventually influences the final hypothesis made.

### **Empirical Assessment**

The Empirical assessment is a relevant approach when the deformation of the building is known and a faster assessment method is also warranted. The empirical assessment demonstrated that the suitability of particular sources and SRI parameters are more relevant than others. For this case study the angular distortion ( $\beta$ ) proved the most informative SRI parameter as well as angular distortion-based sources.

On the contrary, the analysis demonstrated a high likelihood of wrong results therefore performing the assessment “in scale” through all SRI parameters and sources helped address this limitation as engineering judgment was able to be employed to arrive at the most likely overall damage state.

The variability of results was particularly relevant to Engineering norm limits which in the case of CUR (1996) demonstrated to be conservative and in the case of IGWR (2009) demonstrated to be too lenient.

### **Analytical Assessment – LTSM**

The main characteristic of the Limit Tensile Strain Method (LTSM) is that it demonstrates a more robust assessment. Expected conservatism in the method was not present, with the method providing relatively accurate results. The method was also unable to approximate the damage state for the Wall with the tilted displacement profile. Both displacement profile methods used demonstrated good accuracy. Although the greenfield profile reconstruction produced more conservative damage estimates.

### **Finite Element Analysis**

The main characteristic of the FEA concerned the accuracy to which it could reproduce damage. On the whole, it proved the most conservative method of all analyses made on the case study building. And its results demonstrated a better suitability to predict structurally relevant damage, rather than lighter damage. This is so, as the analyses demonstrated the worst capabilities when having to reproduce independent cracks (Cracks 3 and 10) which were not associated with the main damage mechanism formed on the outer leaf composed of Cracks 1,5 and 9.

Its second main characteristic was its damage overestimation. This led TSCM inner leaf models to produce mechanisms do not present in the building, whose results produced cracks 10 times the length and 5 times the expected widths. In EMM models the damage overestimation proneness leads to the simulation of cracks appearing between layers of vertically stacked units on the right side of the wall.

Nevertheless, FEA’s main limitation was the variance in results under changing mesh sizes. Global mesh size influence was approximated to have a standard deviation of  $\sigma = 0.33 \Psi$  and  $\sigma_{CW_{max}} = 2.3\text{mm}$  showing no consistency in these deviations between different mesh sizes. The observed mesh size influence help demonstrate that the validation of FEA results for such models is imperative. Alternatively, conclusions drawn from results must account for the possible magnitude in deviation in crack widths and crack patterns.

**RQ 3.** For different assessment methods, what is the influence different parameters have on the evaluations?

### **Visual Assessment**

The visual assessment was most influenced by an already mentioned limitation in the difficulty of assessing crack features through visual evidence. This was discussed to influence the ability to

---

correctly use the decision tree.

### **Empirical Assessment**

The most influential factor in the Empirical assessment was the source, which showed that literature-based SRI limits had the greatest accuracy. Furthermore, it is also possible the shallow foundation typology from the case study building allowed the better use of SRI parameters for the damage assessments and also positively influenced the accuracy of results.

### **Analytical Assessment**

The Limit Tensile Strain Method (LTSM) was most influenced, by the use of the modified E/G ratios based on Son & Cording's (2009) recommendations, which make use of the facades opening percentage. Before this adjustment, the original E/G ratios proposed by Burland & Wroth (1974) yielded very poor strain approximations and consequently poor damage level estimates, emphasising the importance of accurately determining the elastic resistance of the beam.

### **Finite Element Analysis**

For the Finite Element Analyses the influence of most model decisions and parameters is significant. Initially, the uncertainty from unknown material parameters was most problematic, specifically in the EMM material parameter definition. Nevertheless, once sufficiently accurate results are produced the mesh size influence is demonstrated to be the greatest influencing factor.

Additionally, while topological model features were not extensively studied, the inclusion of lintels in otherwise identical inner and outer leaf models had a significant impact on the stiffness of both models. This led to changes in the location and magnitude of damage which shifted from a severe diagonal crack to a milder crack pattern in the EMM inner leaf results and a large significant crack in TSCM results.

The material parameters showed a significant influence, particularly near their mean in the EMM models which showed the greatest sensitivity in the elastic parameters. This was also similarly true for the TSCM although its sensitivity was less. The influence of the tensile strength was also determined to be significant.

## **7.3 Recommendations for future research**

**RQ 4.** What improvements might be necessary to current solution methods to make them more precise and robust?

Future improvements to current solution methods should primarily focus on enhancing their robustness and precision. Future research on analytical and empirical assessments could explore how to better predict damage under uniform and tilted settlement profiles. Future research could also evaluate the accuracy of assessments under a more varied range of subsidence patterns and building damage levels to validate if the accuracy and damage assessment characteristics observed in this study are also shared under different building topologies and displacement profiles.

The Finite Element Analyses of the case-study building could also be carried through other 3D or equivalent approaches. Such approaches could account for out-of-plane effects caused by the differential settlement which have not been explored. Furthermore, more 3D approaches could evaluate if the FEA results would produce less conservative crack patterns in Wall 2 by providing further resistance form the building. Other considerations could also include to evaluate the influence topological features such as to use interface elements for the lintels and the influence the modelling approach selected for the first floor in the inner leaf can have on results.

Lastly, further research on the influence numerical solution parameters have on the results could help address limitations on the robustness of results by evaluating the tightness of energy norms or finer load step sizes, to confirm if results limitations observed correspond to the behaviour of masonry material models.

# Appendix 1: FE Model parameters and results

---

This appendix includes the calculation of all the parameters used for the discretization of the FE models used in Section 5. It then includes a brief discussion on the FEA results according to both constitutive laws and the crack pattern development for each of the different models.

## Appendix 1.1: Calculation of building element contributions

Since the mechanical schemes of the numerical analyses aim to reduce the modelling burden and computational time, 2D modelling schemes were chosen. These do not inherently account for Other building elements such as walls, floors or beams explicitly and thus require modelling assumptions to replicate their presence. The identified main building components that may play such a role on Wall 2 are the roof and the first floor. These two elements will act mostly in compression compressive loads from the floors and roof may also play a significant role in reducing the amount of cracking by introducing a greater level of prestress to the unreinforced masonry façade. Additionally since they act at different positions, they may also influence the amount of damage between the top half of the wall and the bottom half. Yet, it is important to estimate their behaviour precisely so as not to introduce further uncertainty into the analysis. Therefore, the following has been the rationale chosen to approximate the behaviour of these elements.

### Calculating the roof's support reactions

Starting, an estimation of the reactions of the roof truss on the perimetral walls was made. The truss that supports the roof runs longitudinally along the longer axis of the building (along Wall 2 and Wall6) although the number of trusses in the building's roof is not known the analysis will assume that there is a truss at the start and end of the roof and two intermediate trusses. For the analysis, the weight of the elements for the influence zone of each truss has been approximated by assuming the support reactions at the ends of the truss are smaller.

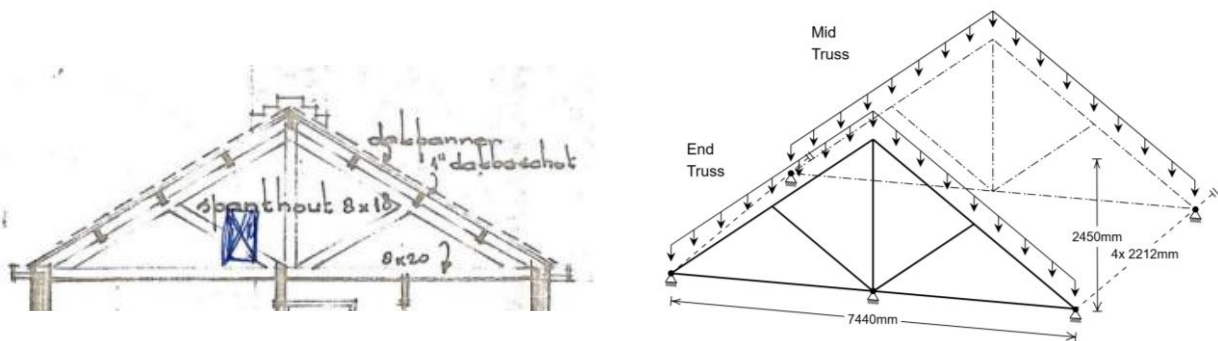


Figure 40: Truss mechanical simplification

#### Calculation

##### Cross sections (from building plan):

Cross section 1: 8", 20" [w,h]  $A_1 = 0.1\text{m}^2$ , Cross section 2: 8", 20" [w,h]  $A_2 = 0.09\text{m}^2$

$V_{CS-1} = 0.09 \cdot (4.45 \cdot 2 + 2.45 + 3.41 \cdot 2) = 1.64\text{m}^3$ ,  $V_{CS-2} = 0.1 \cdot (3.72 \cdot 2) = 0.744\text{m}^3$ ,  $V_{Total} = 1.7097\text{m}^3$

Although no further information is available About the wood type this most likely is a hardwood therefore it will be assumed to be Oak strength grade D30 ->  $\rho_{mean} = 350\text{ [kg/m}^3\text{]}$

##### Roof elements weight:

Slate,  $w = 38\text{ [kg/m}^2\text{]}$ , Insulation foam  $w = 2\text{ [kg/m}^2\text{]}$ , Other  $w = 30\text{ [kg/m}^2\text{]}$

Roof SW:  $w_{tot} = 70\text{ [kg/m}^2\text{]} = 687\text{ N/m}^2$

Beam SW:  $w_{tot} = 640 \cdot 1.71 \cdot 9.81 = 10.8\text{kN}$

#### Output





**Calculation**

Category A use (EN-1991):  $q_k = 2 \text{ kN kN/m}^2$  (Very conservative)  $\rightarrow q_k = 0.5 \text{ kN kN/m}^2$

Although no information is available about the flooring wood type this most likely is a soft wood was used and therefore it will be assumed to be C24 timber  $\rightarrow \rho_{\text{mean}} = 420 \text{ [kg/m}^3\text{]}$

Self-weight:

Floor 1 area:  $A_1 = 8.3 \times 6.9 = 57.27 \text{ m}^2$ , Distributed load  $q_k = (0.1 \times 0.25 + 0.5) = 0.75 \text{ kN/m}^2$

Floor 1 self-weight:  $w_{\text{tot}} = 0.75 \times 57.27 = 42.95 \text{ N/m}^2$

**Support reactions:**

$V_x = 0.75 \times 8.3 \times 0.5 = 3.11 \text{ kN/m}$ ,  $V_y = 0.75 \times 6.9 \times 0.5 = 2.58 \text{ kN/m}$

$\alpha = L_1/L_2 = 1.20 \rightarrow \alpha_x = -0.0468$ ,  $\alpha_y = -0.0325$  ( $\gamma = \text{Longer edge}$ )

$M_x = \alpha_x \times q_k \times L_1 \times L_2 = 4.02 \text{ kN/m}$ ,  $M_y = \alpha_y \times q_k \times L_1 \times L_2 = 2.8 \text{ kN/m}$

**Output**

Weight of the structure

**CALCULATION 2: Estimation of first floors reactions on walls.**

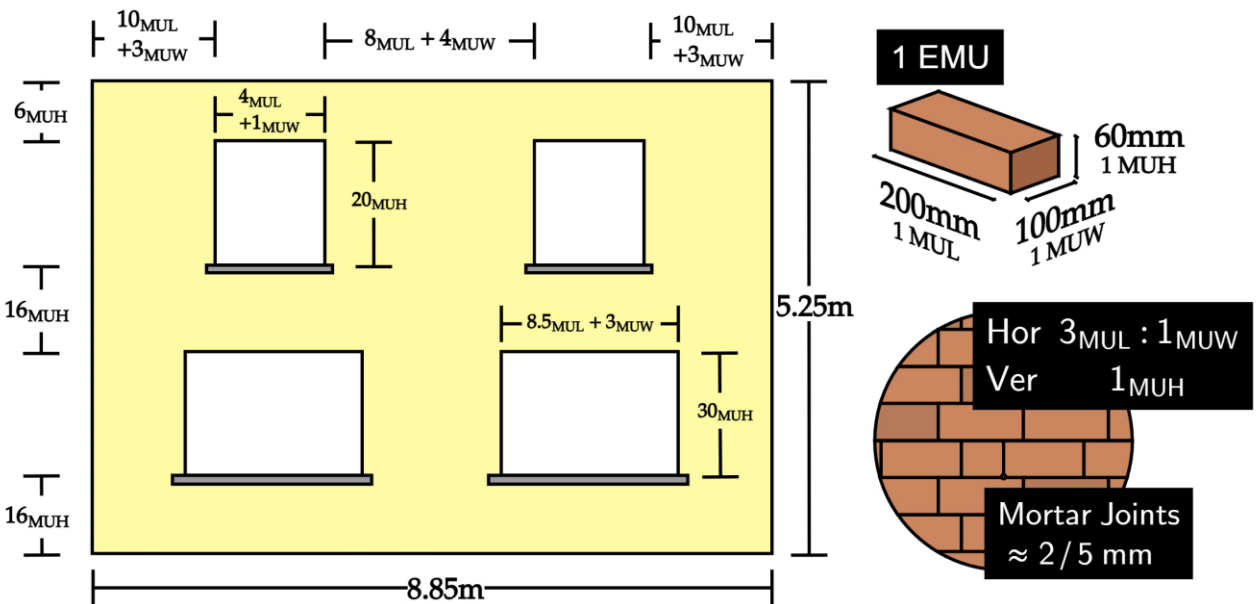


Figure 42: Approximated Wall 2's dimensions

## Appendix 1.2: Determination of the material parameters through Jafari, 2021

A possible factor that can complicate the convergence or robustness of the results is modelled uncertainty introduced by the material parameters. For this purpose available literature allows the determination of material parameters according to age and typology additionally, the research from Jafari also presents a thorough study of the relation between material and model parameters. First, the most similar material parameters are determined by Jafari, et al., 2017 where according to the material classification of Solid-Clay bricks post-1945 the parameters are the following,

Material	Vertical compression test		Horizontal compression test		Bending properties			Shear properties		
	Compressive Strength [MPa]	Young's Modulus [MPa]	Compressive Strength [MPa]	Young's Modulus [MPa]	Bond wrench test [MPa]	Horizontal out-of-plane bending test	In-plane bending test	Shear modulus [MPa]	Initial shear strength [MPa]	Initial friction coefficient [Rad]
	$f_m$	$E_m$	$f_{m,h}$	$E_{3,h}$	$f_{x1}$	$f_{x2}$	$f_{x3}$	$G$	$f_{v0}$	$\mu$
Clay-solid >1945	17.7 ± 6.73	9348 ±3271	11.0 ±2.53	5470 ±547	0.43 ±0.07	1.22 ±0.11	0.76 ±0.21	1252 ±550	0.35	0.67

TABLE 44: Reference material parameters from Jafari, 2021 based on case study specifications

Yet if the EMM is used further information is required on the shear properties, particularly the shear modulus. For this purpose, further material parameters from Jafari, et al., 2022 were used, of a sample of similar example, “Molenweg” a building from 1920 whose masonry is also solid-clay, and therefore similar to the case-study building.

Database of shear properties obtained from tests on cores and on companion specimens.

Objects	Shear tests on cores							Shear-compression tests on companion triplets/panels					
	$\alpha$ (No.)	<sup>1</sup> Failure(No.)	<sup>2</sup> $f_{core}$	<sup>3</sup> $f_{core}$	$f_{0,core}$	$\mu_{core}$	<sup>2</sup> $G_{core}$	$f_p^b$ (No.)	<sup>1</sup> Failure(No.)	$f_c$	$f_o$	$\mu$	<sup>2</sup> $G_w$
			MPa	MPa	MPa	-	MPa	MPa		MPa	MPa	-	MPa
MAT-3 Replicated clay masonry	40 (3)	ST (3)	1.33 (7)	1.58 (7)	0.22	0.80	-	0.20 (3)	S (3)	0.30 (23)	0.15	0.79	296 (27)
	45 (3)	ST (2), T (1)	0.60 (25)	0.60 (25)	-	-	-	0.60 (2)	S (2)	0.61 (11)	-	-	297 (12)
	50 (3)	ST (2), T (1)	1.43 (16)	1.20 (16)	-	-	-	1.00 (3)	S (3)	0.91 (11)	-	-	248 (9)
MAT-4 Replicated clay masonry	45 (5)	ST (4), T (1)	1.07 (32)	1.07 (32)	0.22	0.80	284 (56)	The same as MAT-3					
	50 (6)	S (6)	0.50 (37)	0.42 (37)	-	-	169 (32)						
	55 (6)	S (6)	0.62 (45)	0.44 (45)	-	-	162 (53)						
Molenweg <sup>3</sup> Existing clay masonry	45 (2)	S (1), ST (1)	1.00 (40)	1.00 (40)	0.35	0.67	1252 (44)	0.20 (3)	-	0.36 (14)	0.34	0.48	-
	50 (2)	S (2)	0.90 (27)	0.76 (27)	-	-	326 (42)	0.60 (3)	-	0.79 (1)	-	-	-
	55 (2)	S (2)	0.63 (48)	0.44 (48)	-	-	241 (-)	1.00 (3)	-	0.73 (15)	-	-	-

TABLE 45: Masonry shear material properties from tests on cores and triplets (Jafari, et al., 2022).

In the case of the EMM, the values for the minimum head-joint tensile resistance were determined by using the lower bound of the mortar tensile strength as it is assumed that these mortar joints are of lesser quality than the bed joints. The running bond on the structure was a Flemish Garden bond and thus the longitudinal against transversal units occur every 3 and alternate between successive unit rows, therefore the calculation of the stepped diagonal angle has to be made between two transversal units. The rest of the parameters were approximated through the relations available at TABLE 5.

For those models which include concrete lintels the determination of the material parameters was not as straightforward. Little research is available on concrete lintels from masonry structures which account for their deterioration. Nevertheless, this deterioration is expected to be very small when compared to the masonry as these are located on the inside of the building. In the model these were assumed as linear elastic, this decision was made as no cracking has been documented in any of the lintels and therefore accounting for their non-linear behaviour if cracking occurs may impact the results in the masonry, nevertheless throughout the analysis a tensile limit of 2-5MPa will be reviewed to ensure these should

not enter their softening stage. The most suitable material properties were taken from Korswagen, et al., 2021 which also performed some FEA in the study of the onset of light damage on shear walls with concrete lintels the parameters used in the analysis where  $\rho = 2.4 \text{ ton/m}^3$ ,  $E = 31 \text{ GPa}$ ,  $\nu = 0.2$ .

**Calculation**

**Output**

<p><b>For the total strain crack model:</b></p> $f_m = 17.7 \pm 6.73 \text{ Mpa}, \quad f_w = f_{x1} = 0.43 \pm 0.07 \text{ Mpa}$ <p>Tensile strength:  <math>f_{t1} = 0.8 \times f_w = 0.8 \times 0.43 = 0.344 \text{ [Mean]}, 0.8 \times 0.05 = 0.04 \text{ [LB]}</math></p> <p>Mode 1 fracture energy in tension:  <i>Mortar compressive strength:</i>  <math>f_m = f_w/0.036 = 0.43/0.036 = 11.94 \text{ Mpa}</math></p> $G_{f-tm} = 0.025 \times (f_m/10)^{0.7} = 0.025 \times (11.94/10)^{0.7} = 0.0283 \text{ N/mm}$	<p><b>TSCM</b></p> <p><i>Tensile strength based on masonry values</i></p> <p><i>Fracture energy based on mortar</i></p>
<p><b>For the Engineering masonry model:</b></p> $f_m = 17.7 \pm 6.73 \text{ Mpa}, G_{xy} = 1250 \pm 550 \text{ Mpa}, f_w = f_{x1} = 0.43 \pm 0.07 \text{ Mpa}$ <p>For head-joint failures determined by tensile strength head-joint defined by friction,  Mortar tensile strength:  <math>f_m = f_w/0.036 = 11.94 \text{ Mpa}</math></p> $f_{tm} = (0.15 - 0.32) \times f_m = 0.235 \times 11.94 = 2.79396 \text{ Mpa [Mean]}, 0.15 \times 11.94 = 1.791 \text{ [LB]}$ <p>Minimum head-joint strength:  <math>f_{tm-HJ} = LB[f_{tm}] = 1.79 \text{ Mpa}</math></p> <p>Fracture energy in compression:  <math>G_{f-c} = (0.88 - 5.3)f'_m = 3.09 \times 17.7 = 54.693 \text{ N/mm}</math></p> <p>Fracture energy in tension:  <math>G_{f-tm} = 0.025 \times (f_m/10)^{0.7} = 0.025 \times (11.94/10)^{0.7} = 0.0283 \text{ N/mm}</math></p> <p>Fracture energy in shear:  <math>G_{f-\Pi} = 10G_{f-l} = 10 \times 0.0283 = 0.283 \text{ N/mm}</math></p> <p>For stepped diagonal crack,  Tensile strength:  <math>f_{t1} = 0.8 \times f_w = 0.8 \times 0.43 = 0.344 \text{ [Mean]}</math></p> <p>Mode 1 fracture energy in tension:  <math>G_{f-l} = 0.16 \times f_{t1} = 0.16 \times 0.344 = 0.055 \text{ N/mm}</math></p> $G_{f-tb} = 10 \times G_{f-l} = 0.55 \text{ N/mm}$ <p>Fracture energy in compression:  <math>G_{f-c} = (0.88 - 5.3)f'_m = 3.09 \times 17.7 = 54.693 \text{ N/mm}</math></p> <p>Fracture energy in shear:  <math>G_{f-tm} = 0.025 \times (f_m/10)^{0.7} = 0.025 \times (11.94/10)^{0.7} = 0.0283 \text{ N/mm}</math></p> $G_{f-\Pi} = 10G_{f-l} = 10 \times 0.0283 = 0.283 \text{ N/mm}$ <p>Stepped diagonal/ bed-joint angle:  <math display="block">\tan \theta = \frac{h_{crack}}{b_{crack}} = \frac{2 \times h_{brick} + 2 \times h_{joint}}{b_{brick} + b_{joint}} = \frac{4 \times 60 + 4 \times 3}{7/4 \times 200 + 4 \times 3} \rightarrow \theta = 0.6 \text{ [rad]}</math> </p>	<p><b>EMM</b></p> <p><b>Head-Joint</b></p> <p><i>Tensile strength determined by mortar</i></p> <p><i>FE in compression determined by masonry</i></p> <p><i>FE in tension and shear determined by mortar</i></p> <p><b>EMM</b></p> <p><b>Staircase</b></p> <p><i>Tensile strength based on masonry</i></p> <p><i>FE in tension based on brick failure</i></p>
<p><b>Concrete lintels:</b></p> $E = 31 \text{ Gpa}, \rho = 2400 \text{ kg/m}^3, \nu = 0.2$	

CALCULATION 3: Estimation of material parameters according Jafari, 2021

# **Appendix 1.3: Total Strain based Crack Model (TSCM) analysis results**

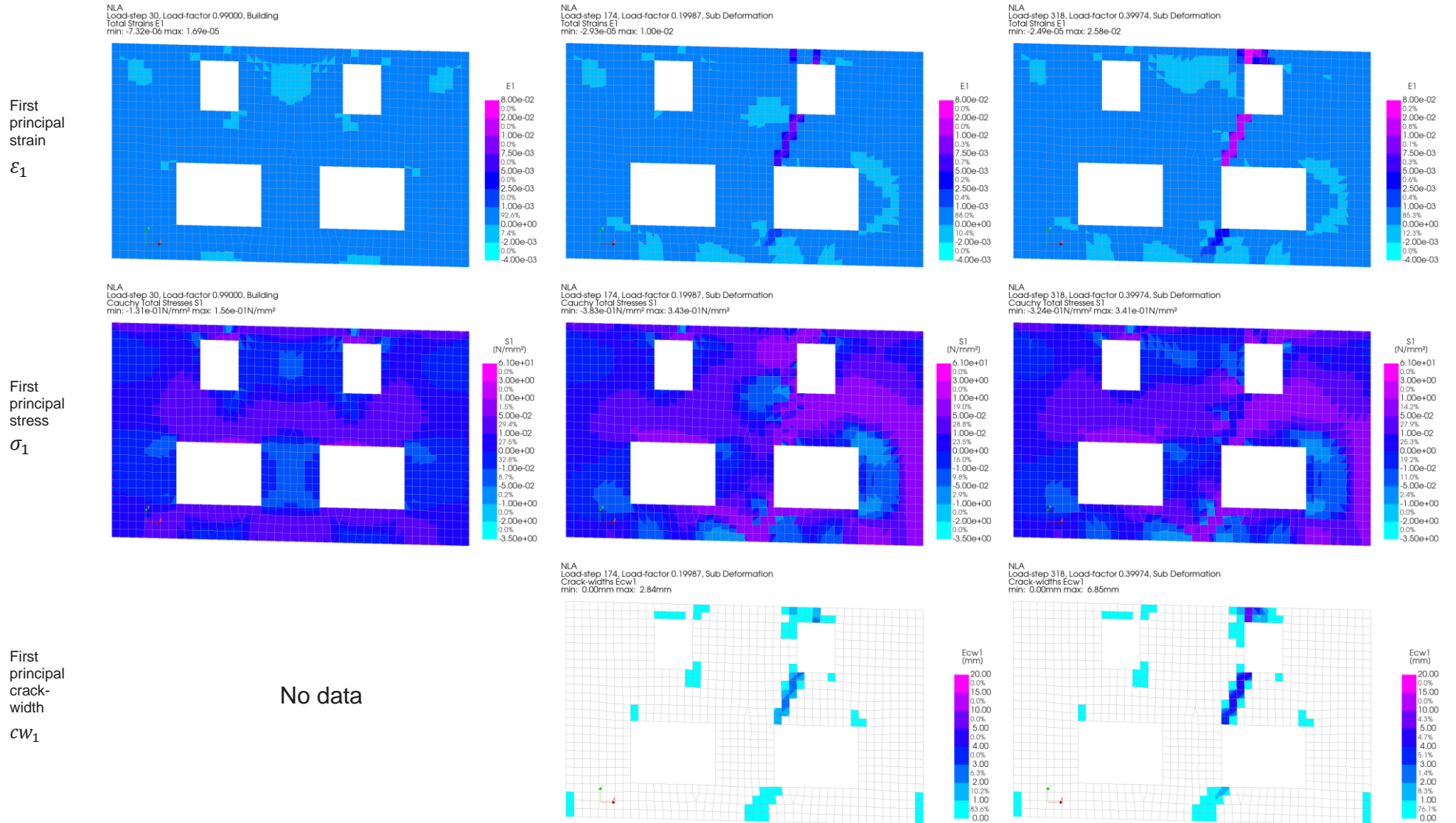
**Analysis Results**

**Model: W20 - TSCM – 0.2m**

**Output LS-30 LF-1: End of Building loads**

**LS-174 LF-0.2: Main crack formation occurs**

**LS-318 LF-0.4: Superior cracks coalesce**



Analysis Results

Model: W20 – TSCM – 0.2m

Output LS-462 LF-0.6: Cracks grow

LS-606 LF-0.8: Cracks continue to grow

LS-750 LF-1: Final damage state

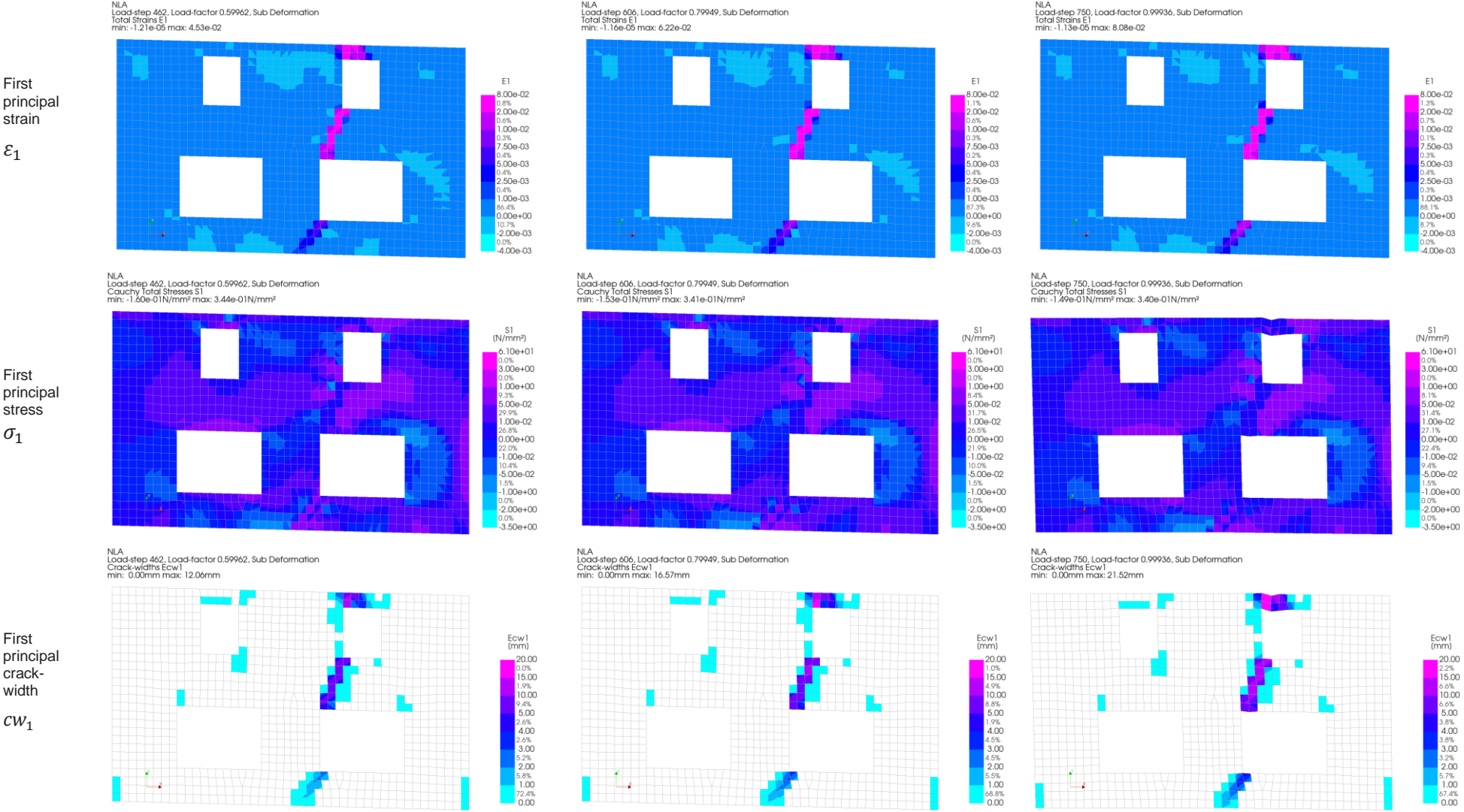


TABLE 46: Analysis results for W20 – TSCM – 0.2m

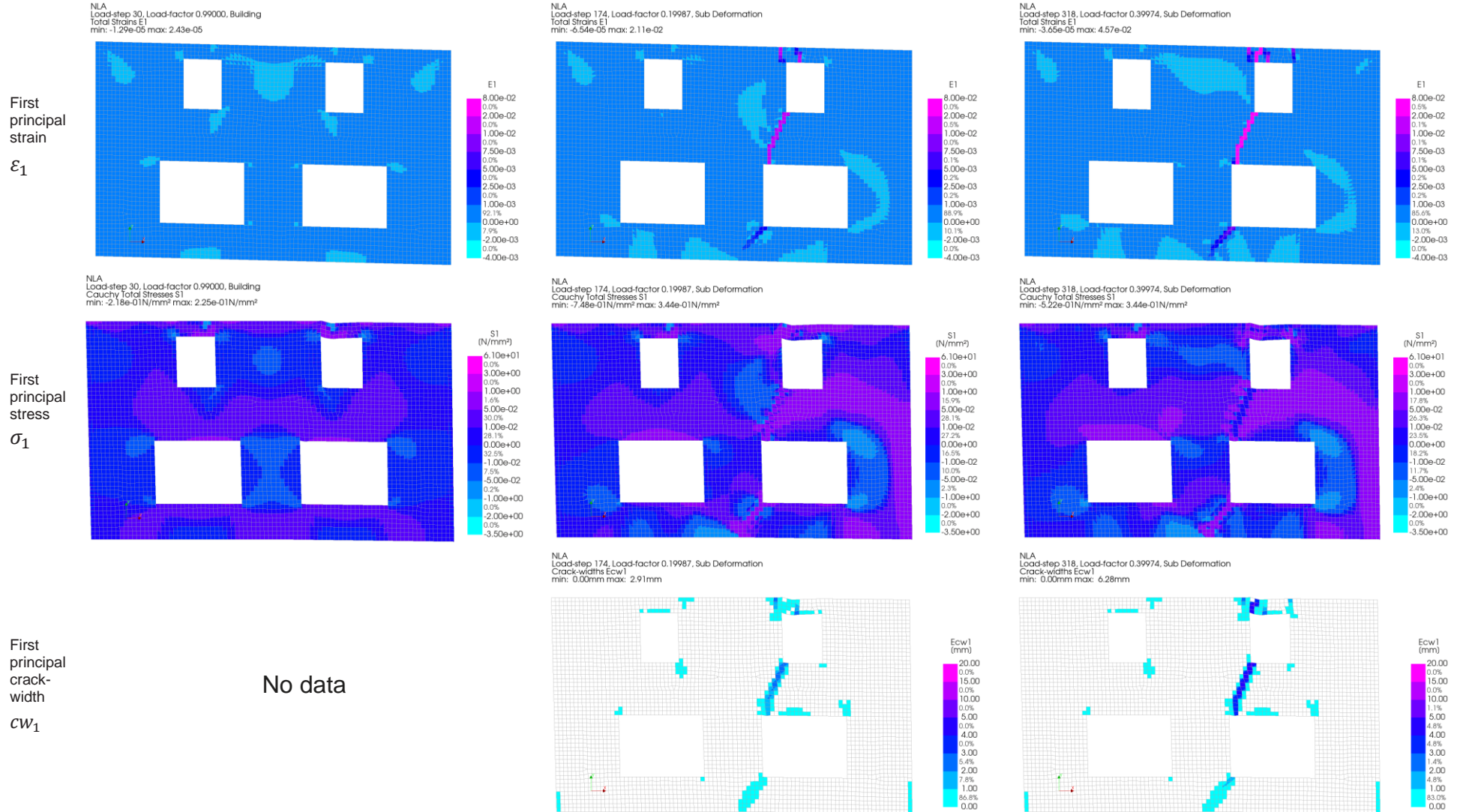
Analysis Results

Model: W2O - TSCM - 0.1m

Output LS-30 LF-1: End of Building loads

LS-174 LF-0.2: Main crack formation occurs

LS-318 LF-0.4: Damage progresses





Analysis Results

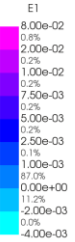
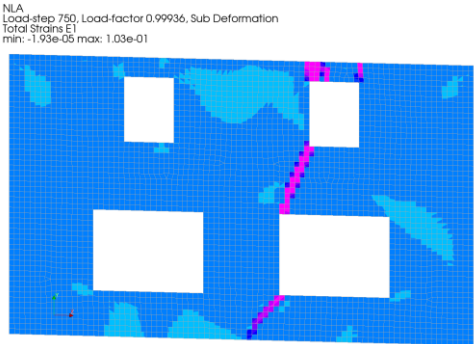
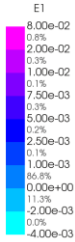
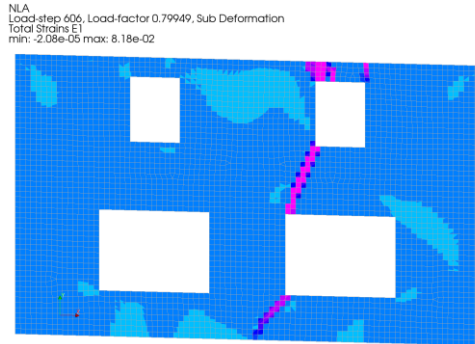
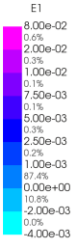
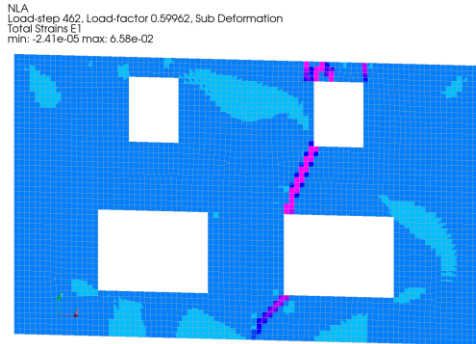
Model: W20 - TSCM - 0.1m

Output LS-462 LF-0.6: Cracks grow

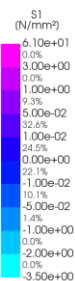
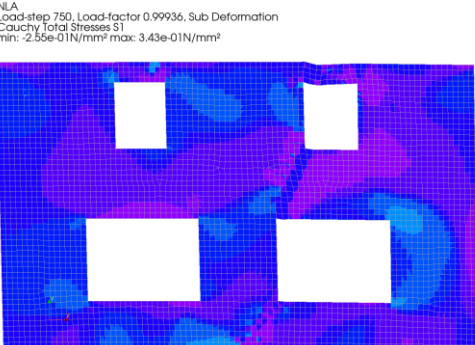
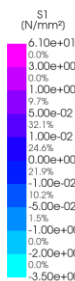
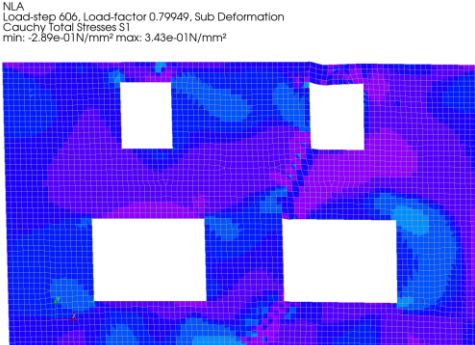
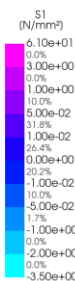
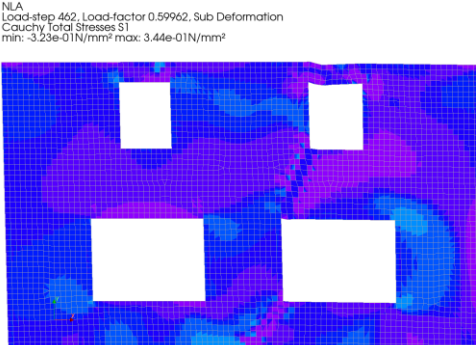
LS-606 LF-0.8: Top cracks coalesce

LS-750 LF-1: END

First principal strain  $\epsilon_1$



First principal stress  $\sigma_1$



First principal crack-width  $CW_1$

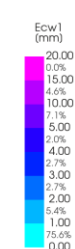
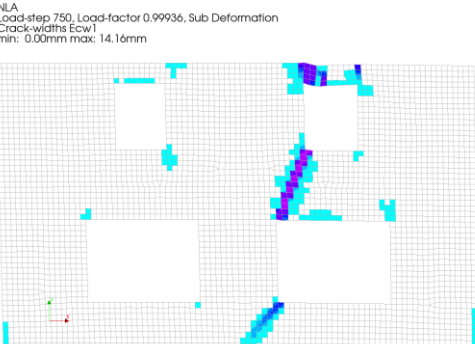
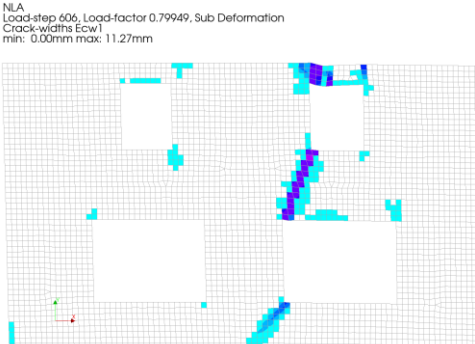
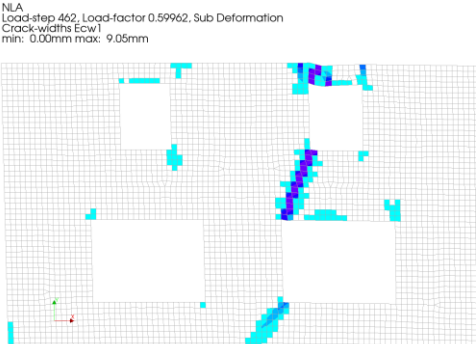


TABLE 47: Analysis results for W20 – TSCM – 0.1m

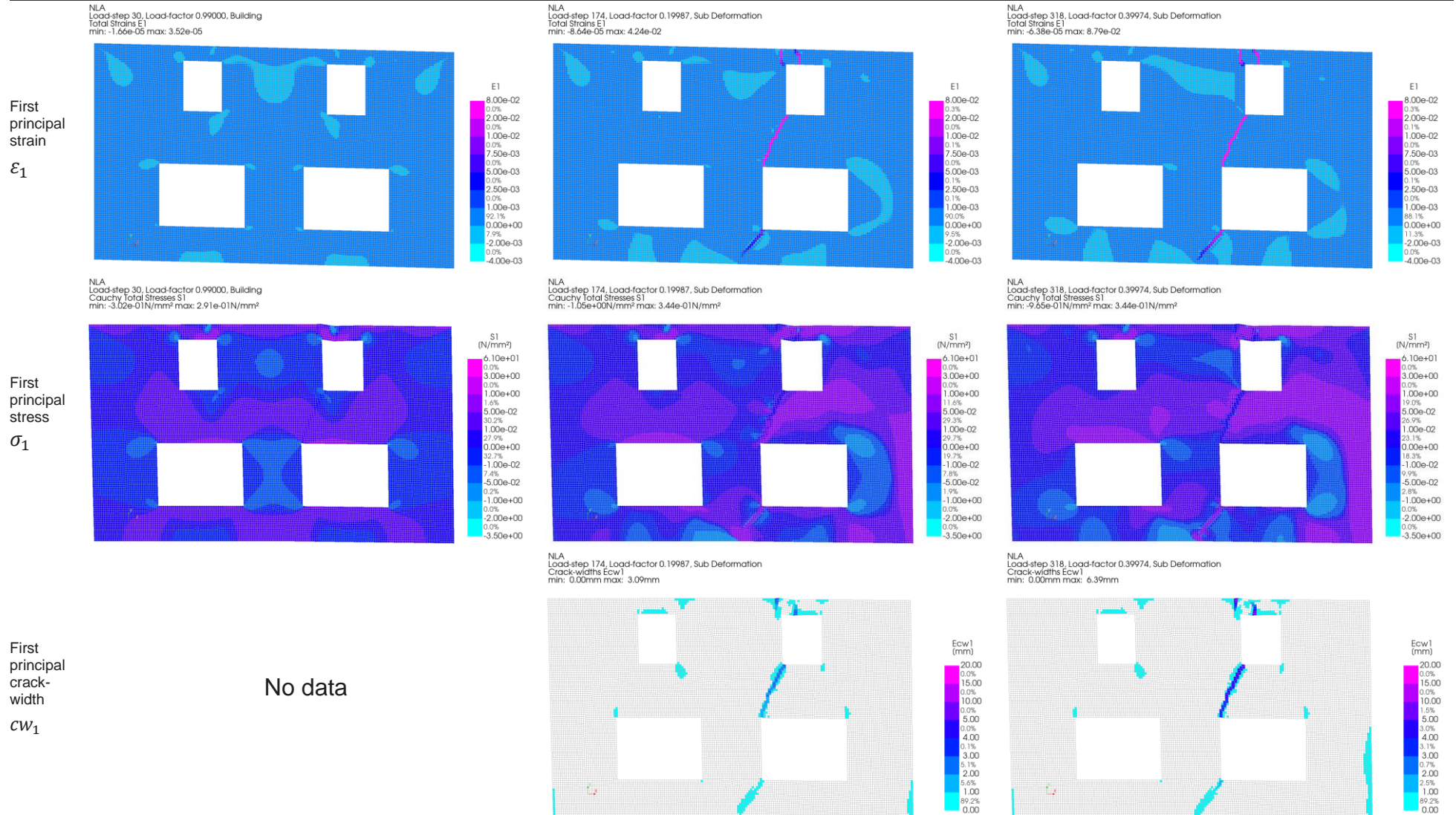
**Analysis Results**

**Model: W2O - TSCM - 0.05m**

**Output LS-30 LF-1: End of Building loads**

**LS-174 LF-0.2: Main crack formation occurs**

**LS-318 LF-0.4: Cracks coalesce**



Analysis Results

Model: W2O - TSCM - 0.05m

Output **LS-462 LF-0.6: Crack grows**

**LS-606 LF-0.8: Crack continues to grow**

**LS-750 LF-1: Final damage state**

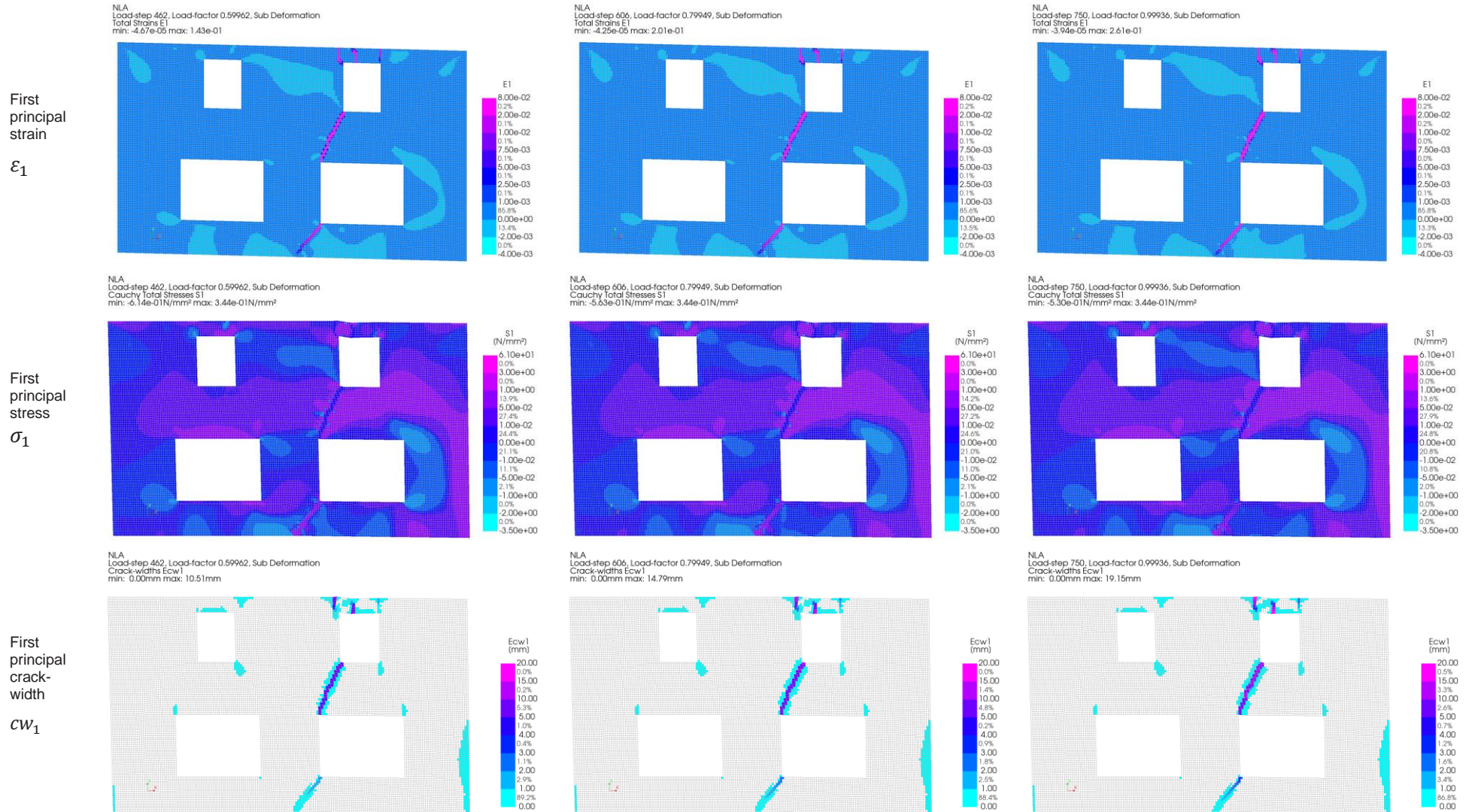


TABLE 48: Analysis results for W2O – TSCM – 0.05m

**Analysis Results**

**Model: W2I - TSCM - 0.2m**

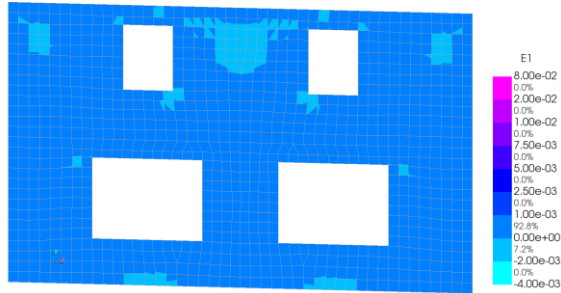
**Output LS-30 LF-1: End of Building loads**

**LS-174 LF-0.2: Main crack formation occurs**

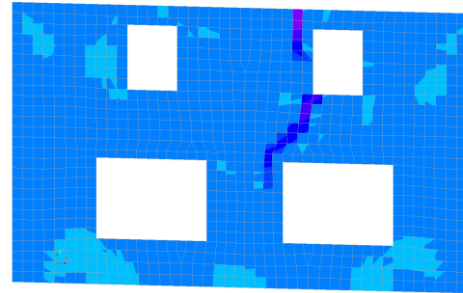
**LS-318 LF-0.4: Cracks grow**

First principal strain  
 $\epsilon_1$

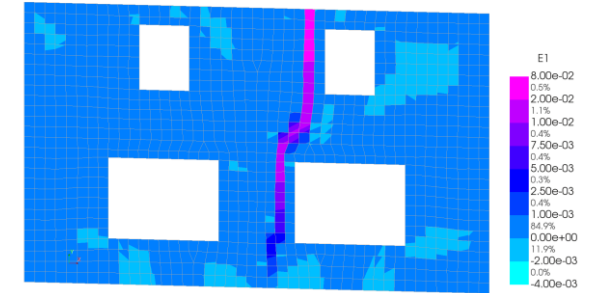
N/A  
Load-step 30, Load-factor 0.99000, Building  
Total Strains E1  
min: -9.49e-06 max: 9.17e-06



N/A  
Load-step 174, Load-factor 0.19987, Sub Deformation  
Total Strains E1  
min: -1.09e-04 max: 9.40e-03

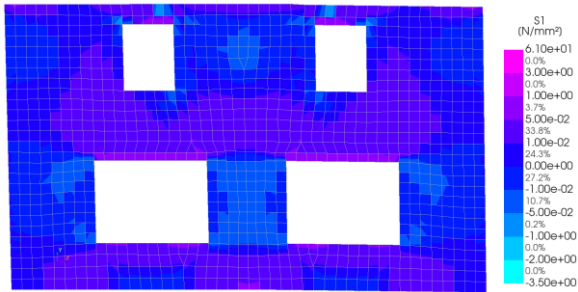


N/A  
Load-step 318, Load-factor 0.39974, Sub Deformation  
Total Strains E1  
min: -1.34e-05 max: 2.74e-02

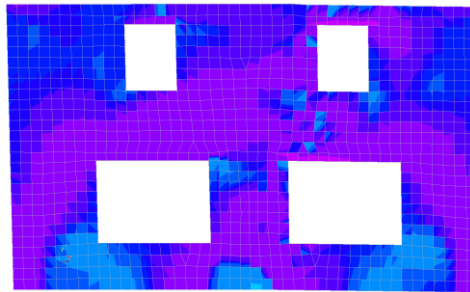


First principal stress  
 $\sigma_1$

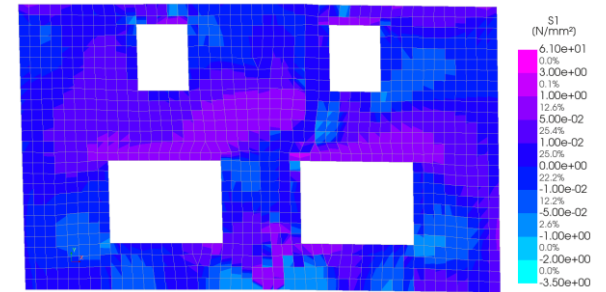
N/A  
Load-step 30, Load-factor 0.99000, Building  
Cauchy Total Stresses S1  
min: -1.25e-01N/mm² max: 2.54e-01N/mm²



N/A  
Load-step 174, Load-factor 0.19987, Sub Deformation  
Cauchy Total Stresses S1  
min: -1.32e+00N/mm² max: 1.69e+00N/mm²



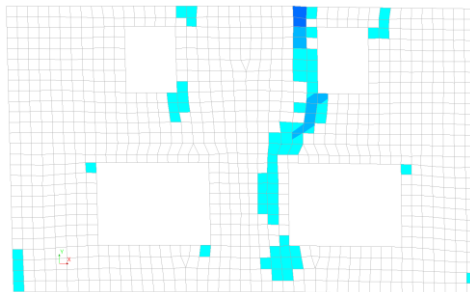
N/A  
Load-step 318, Load-factor 0.39974, Sub Deformation  
Cauchy Total Stresses S1  
min: -2.59e-01N/mm² max: 2.14e+00N/mm²



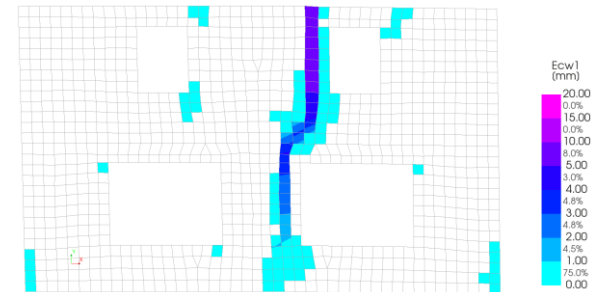
First principal crack-width  
 $cw_1$

No data

N/A  
Load-step 174, Load-factor 0.19987, Sub Deformation  
Crack-widths Ecw1  
min: 0.00mm max: 2.70mm



N/A  
Load-step 318, Load-factor 0.39974, Sub Deformation  
Crack-widths Ecw1  
min: 0.00mm max: 7.89mm



Analysis Results

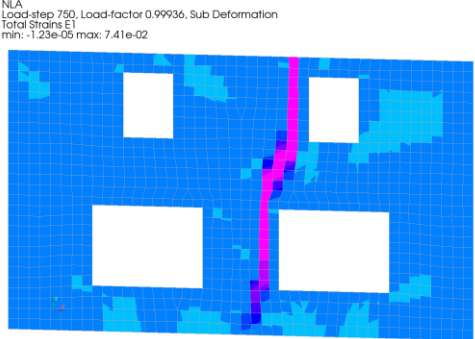
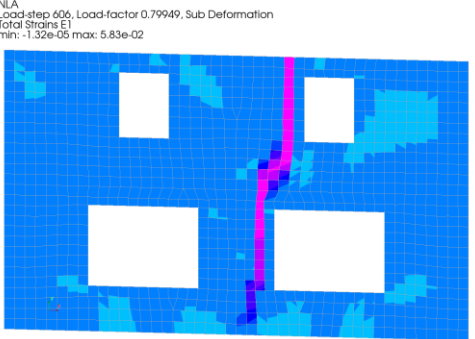
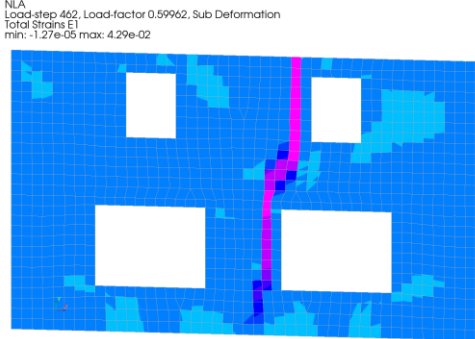
Model: W2I - TSCM - 0.2m

Output LS-462 LF-0.6: Crack coalesces

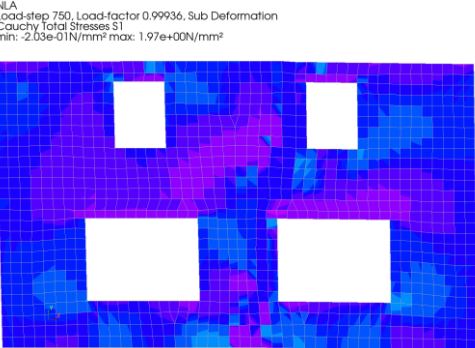
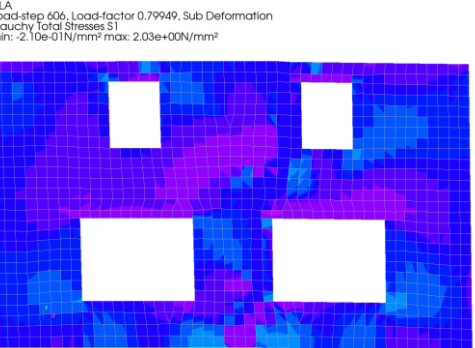
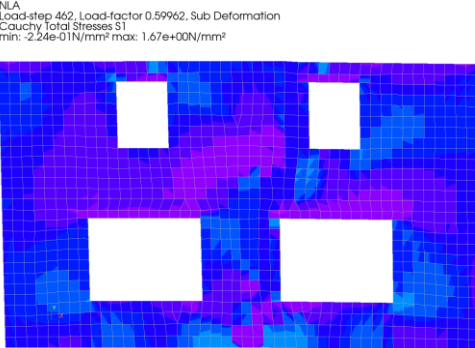
LS-606 LF-0.8: Crack continues to grow

LS-750 LF-1: Final damage state

First principal strain  $\epsilon_1$



First principal stress  $\sigma_1$



First principal crack-width  $CW_1$

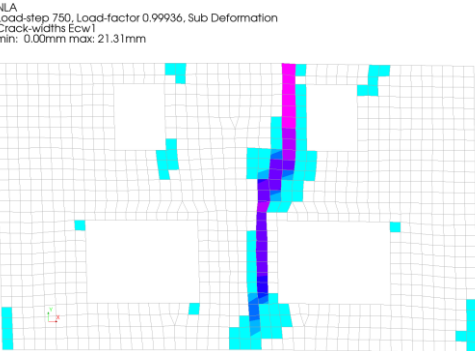
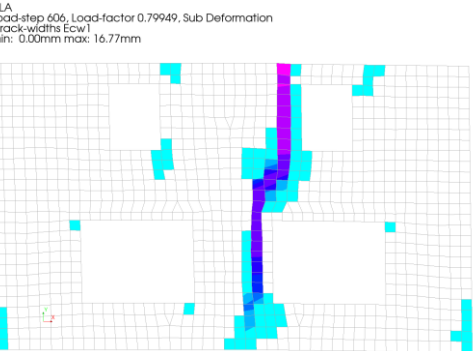
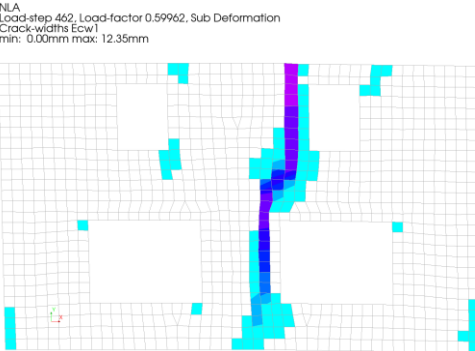


TABLE 49: Analysis results for W2I – TSCM – 0.2m

**Analysis Results**

**Model: W2I - TSCM - 0.1m**

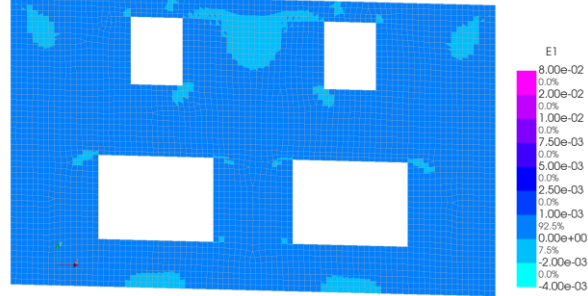
**Output LS-30 LF-1: End of Building loads**

**LS-174 LF-0.2: Main crack formation occurs**

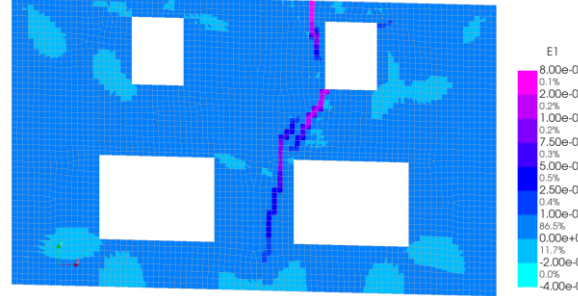
**LS-318 LF-0.4: Cracks grow**

First principal strain  
 $\epsilon_1$

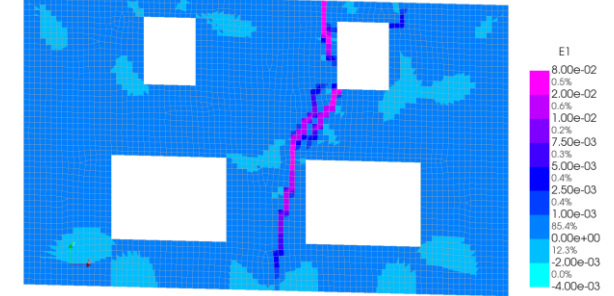
NLA  
Load-step 30, Load-factor 0.99000, Building  
Total Strains E1  
min: -1.10e-05 max: 1.77e-05



NLA  
Load-step 174, Load-factor 0.19987, Sub Deformation  
Total Strains E1  
min: -9.00e-05 max: 2.28e-02

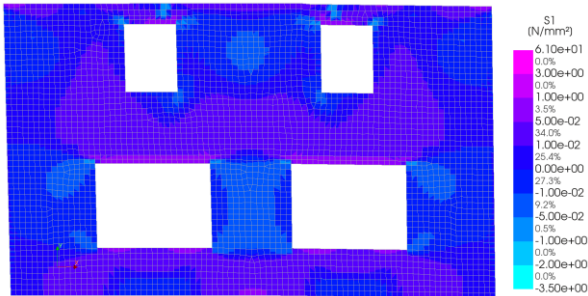


NLA  
Load-step 318, Load-factor 0.39974, Sub Deformation  
Total Strains E1  
min: -4.93e-05 max: 5.41e-02

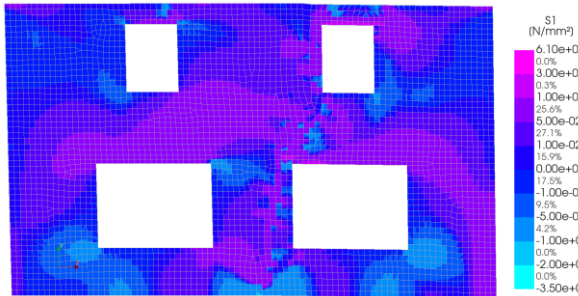


First principal stress  
 $\sigma_1$

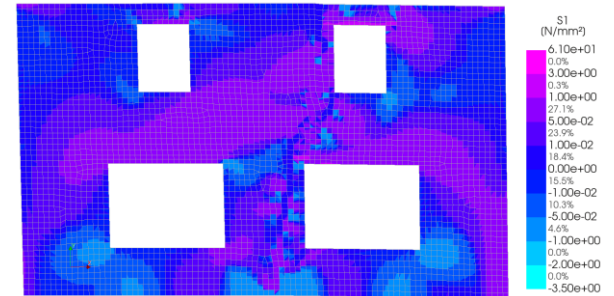
NLA  
Load-step 30, Load-factor 0.99000, Building  
Cauchy Total Stresses S1  
min: -1.90e-01N/mm² max: 3.71e-01N/mm²



NLA  
Load-step 174, Load-factor 0.19987, Sub Deformation  
Cauchy Total Stresses S1  
min: -1.20e+00N/mm² max: 3.22e+00N/mm²



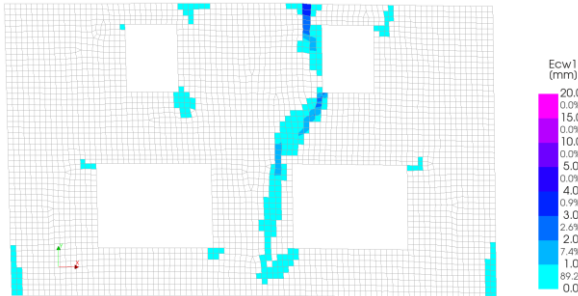
NLA  
Load-step 318, Load-factor 0.39974, Sub Deformation  
Cauchy Total Stresses S1  
min: -9.80e-01N/mm² max: 3.18e+00N/mm²



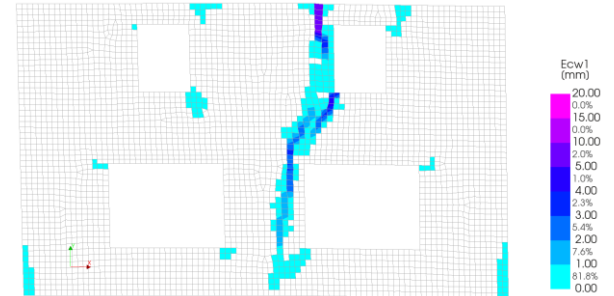
First principal crack-width  
 $CW_1$

No data

NLA  
Load-step 174, Load-factor 0.19987, Sub Deformation  
Crack-widths Ecw1  
min: 0.00mm max: 3.24mm



NLA  
Load-step 318, Load-factor 0.39974, Sub Deformation  
Crack-widths Ecw1  
min: 0.00mm max: 7.55mm



Analysis Results

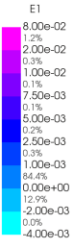
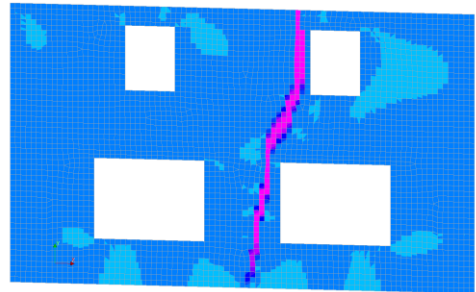
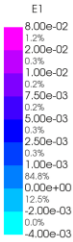
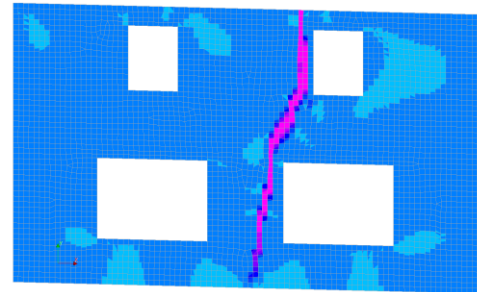
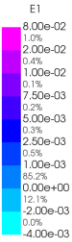
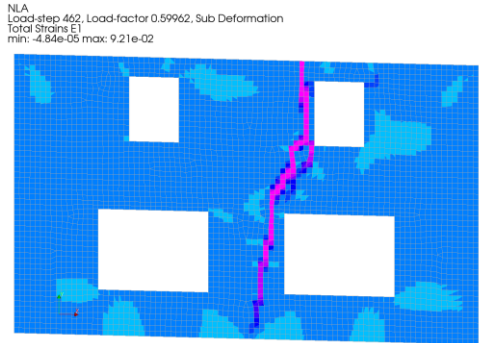
Model: W2I - TSCM - 0.1m

Output **LS-462 LF-0.6: Crack coalesces**

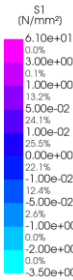
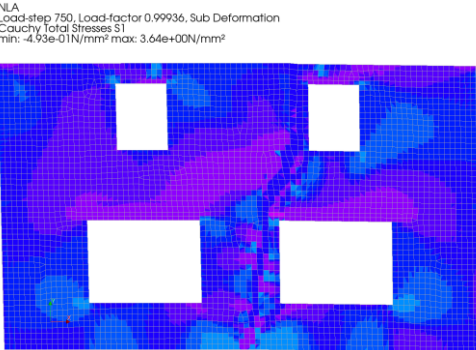
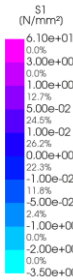
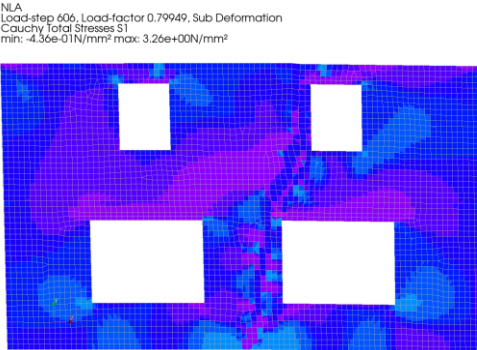
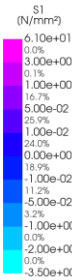
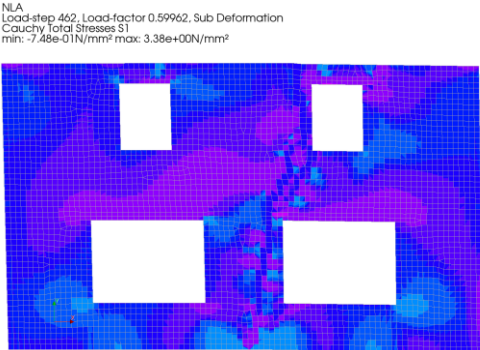
**LS-606 LF-0.8: Crack continues to grow**

**LS-750 LF-1: Final damage state**

First principal strain  
 $\epsilon_1$



First principal stress  
 $\sigma_1$



First principal crack-width  
 $CW_1$

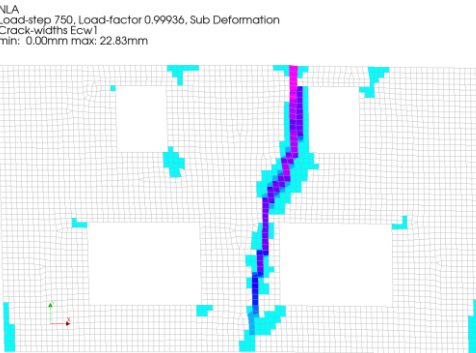
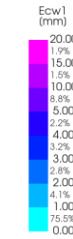
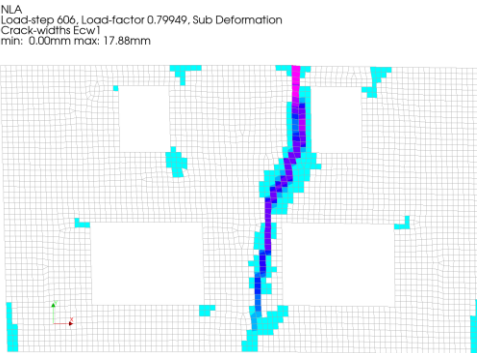
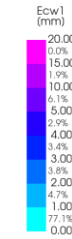
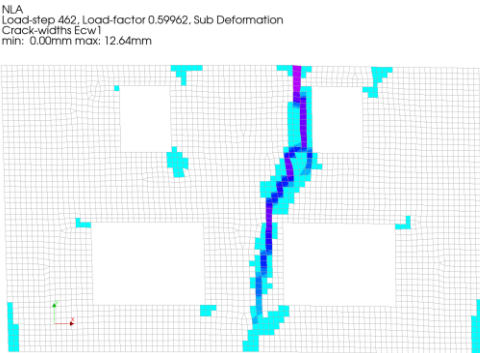


TABLE 50: Analysis results for W2I – TSCM – 0.1m

**Analysis Results**

**Model: W2I - TSCM - 0.05m**

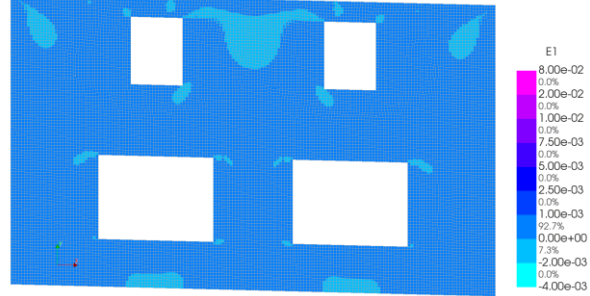
**Output LS-30 LF-1: End of Building loads**

**LS-174 LF-0.2: Main crack formation occurs**

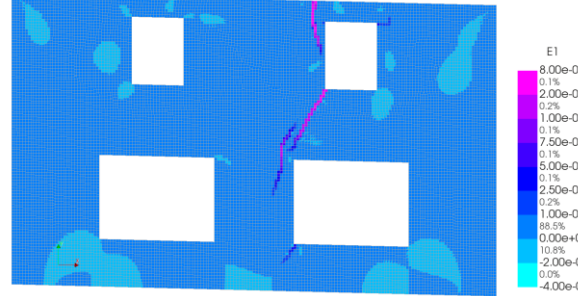
**LS-318 LF-0.4: Cracks grow**

First principal strain  
 $\epsilon_1$

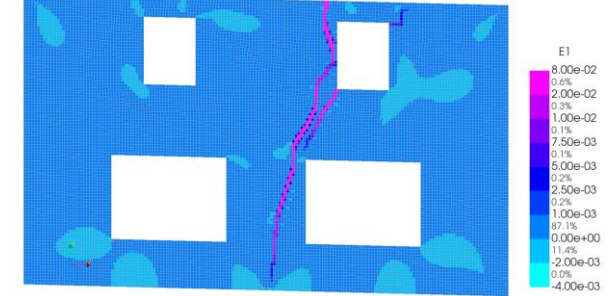
NLA  
Load-step 30, Load-factor 0.99000, Building  
Total Strains E1  
min: -1.33e-05 max: 3.53e-05



NLA  
Load-step 174, Load-factor 0.19987, Sub Deformation  
Total Strains E1  
min: -1.66e-04 max: 3.44e-02

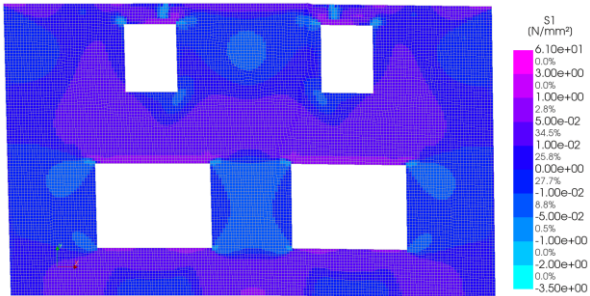


NLA  
Load-step 318, Load-factor 0.39974, Sub Deformation  
Total Strains E1  
min: -8.48e-05 max: 9.88e-02

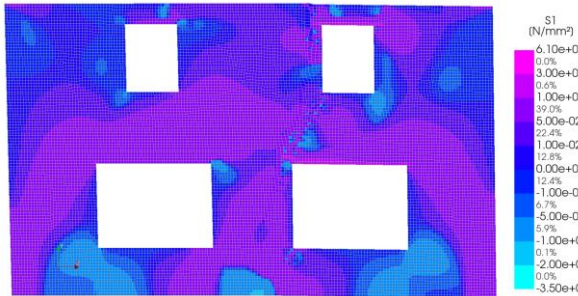


First principal stress  
 $\sigma_1$

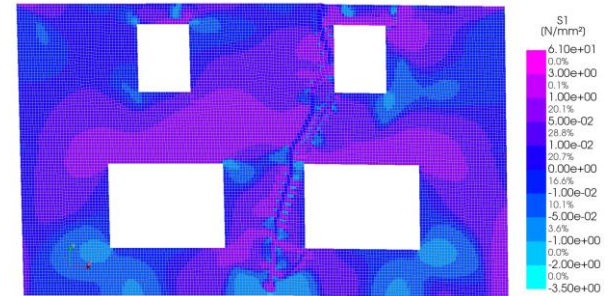
NLA  
Load-step 30, Load-factor 0.99000, Building  
Cauchy Total Stresses S1  
min: -2.68e-01N/mm² max: 4.27e-01N/mm²



NLA  
Load-step 174, Load-factor 0.19987, Sub Deformation  
Cauchy Total Stresses S1  
min: -2.11e+00N/mm² max: 4.26e+00N/mm²



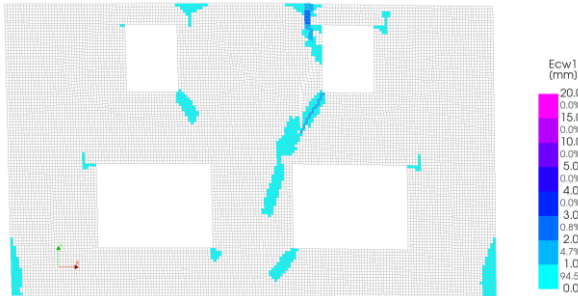
NLA  
Load-step 318, Load-factor 0.39974, Sub Deformation  
Cauchy Total Stresses S1  
min: -1.53e+00N/mm² max: 3.21e+00N/mm²



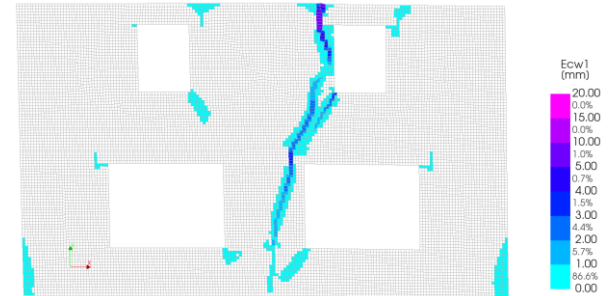
First principal crack-width  
 $CW_1$

No data

NLA  
Load-step 174, Load-factor 0.19987, Sub Deformation  
Crack-widths Ecw1  
min: 0.00mm max: 2.58mm



NLA  
Load-step 318, Load-factor 0.39974, Sub Deformation  
Crack-widths Ecw1  
min: 0.00mm max: 7.42mm





Analysis Results

Model: W2I - TSCM - 0.05m

Output **LS-462 LF-0.6: Crack coalesces**

**LS-606 LF-0.8: Crack continues to grow**

**LS-750 LF-1: Final damage state**

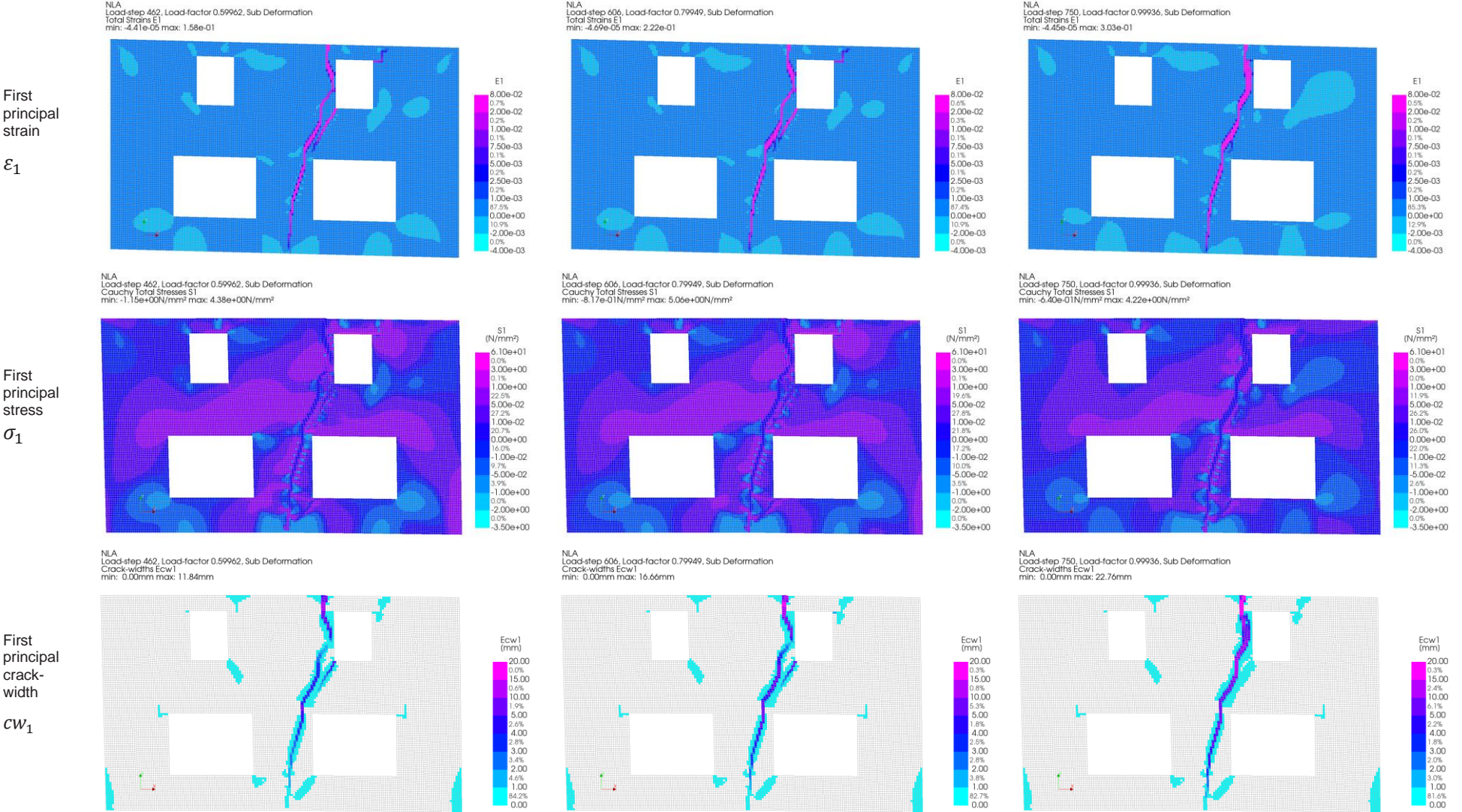


TABLE 51: Analysis results for W2I TSCM - 0.05m

# **Appendix 1.4: Engineering Masonry Model (EMM) analysis results**

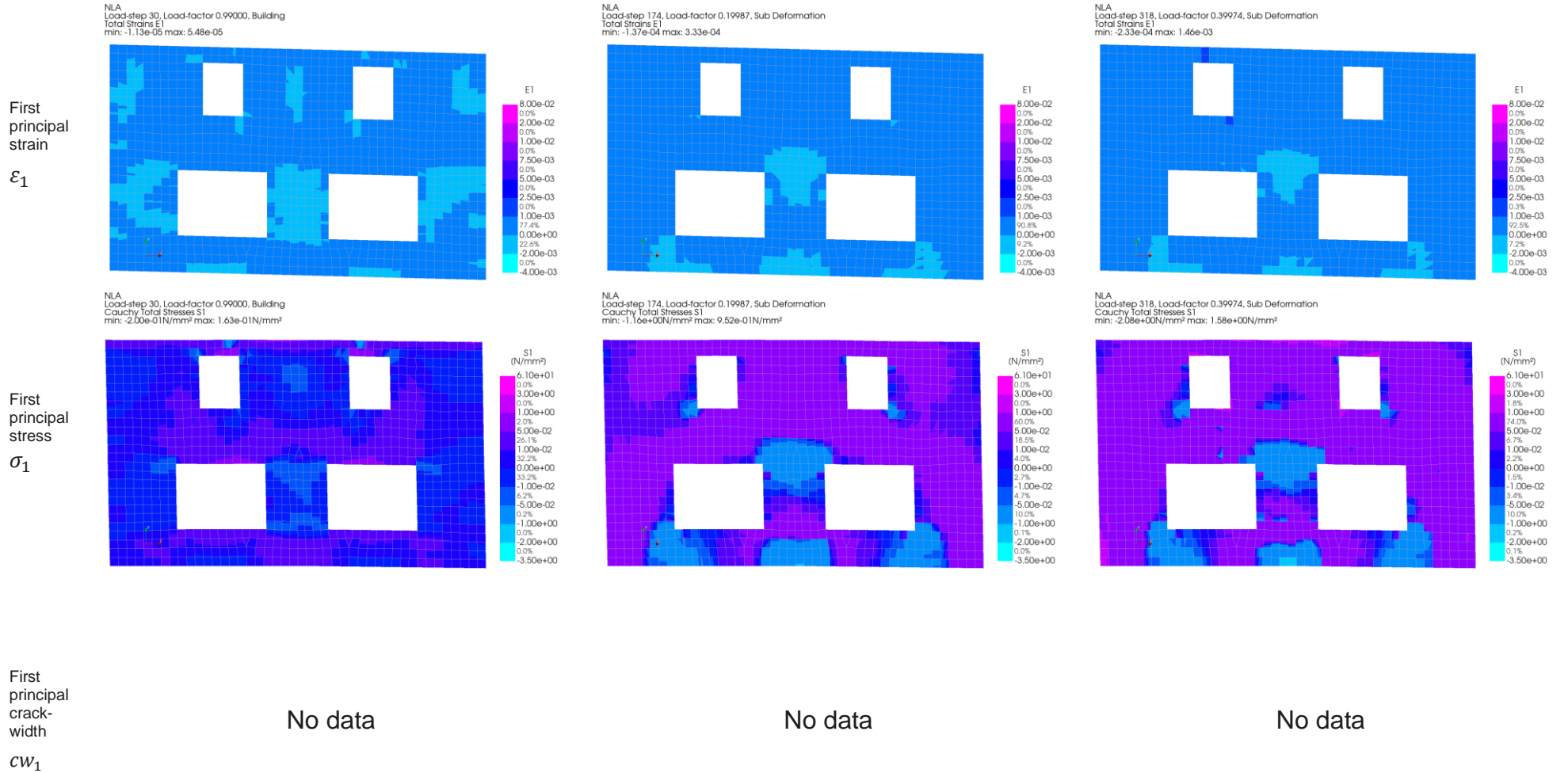
**Analysis Results**

**Model: W20 – EMM – HJ – 0.2m**

**Output LS-30 LF-1: End of Building loads**

**LS-174 LF-0.2: Displacements have been applied**

**LS-318 LF-0.4: Continued..**



Analysis Results

Model: W20 – EMM – HJ – 0.2m

Output LS-462 LF-0.6: First crack formations

LS-606 LF-0.8: Cracks grow

LS-750 LF-1: END

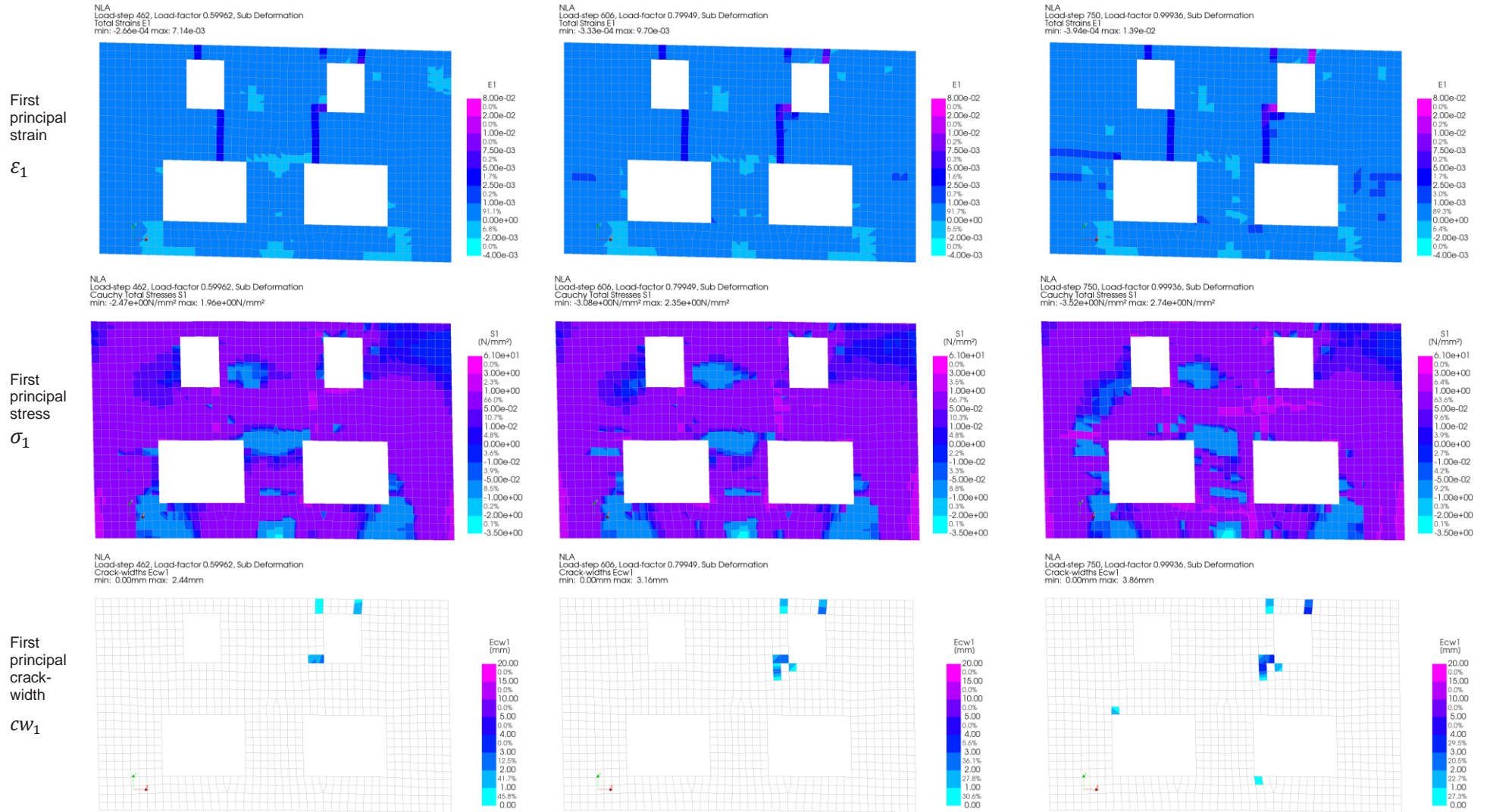


TABLE 52: Analysis results for W20 - EMHJ

Analysis Results

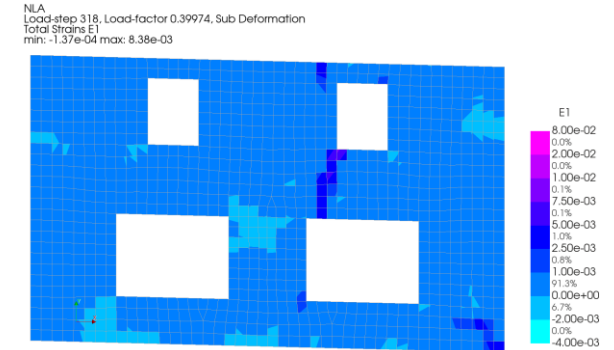
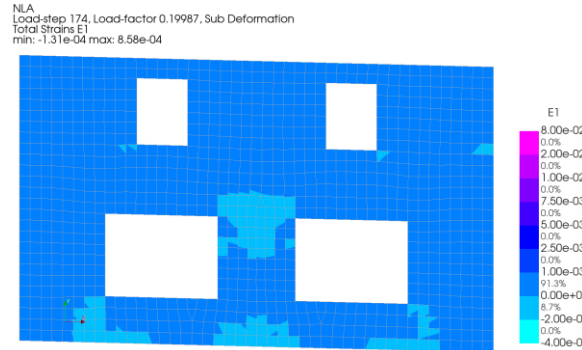
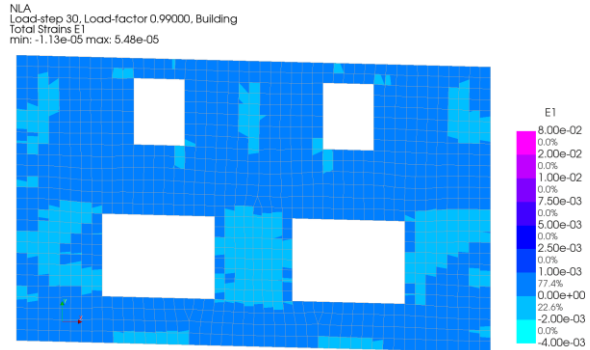
Model: W20 – EMM – S – 0.2m

Output LS-30 LF-1: End of Building loads

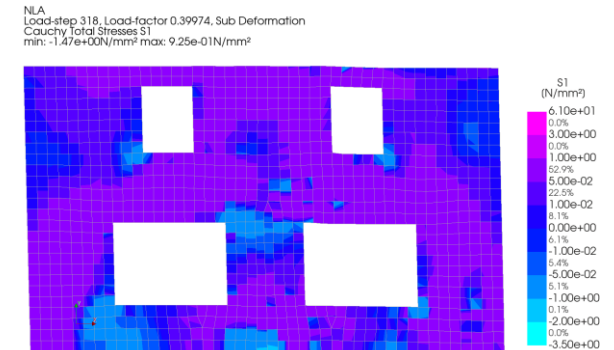
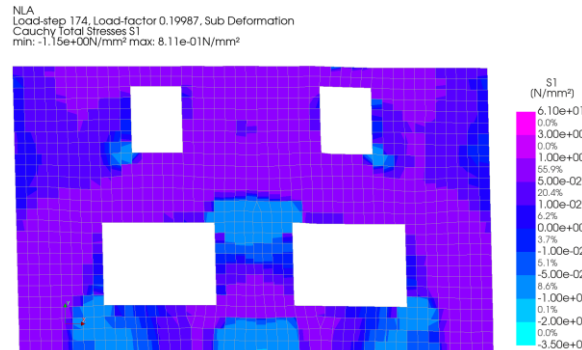
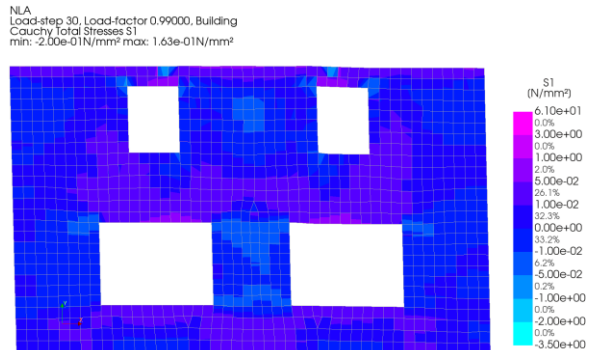
LS-174 LF-0.2: First crack formations

LS-318 LF-0.4: Main crack formation

First principal strain  $\epsilon_1$

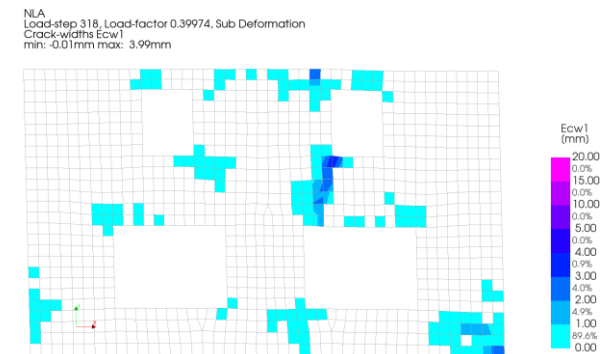
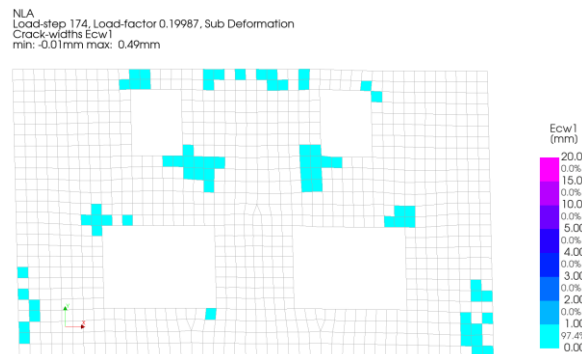


First principal stress  $\sigma_1$



First principal crack-width  $cw_1$

No data



**Analysis Results**

**Model: W20 – EMM – S – 0.2m**

**Output LS-462 LF-0.6: Cracks grow**

**LS-606 LF-0.8: Cracks grow**

**LS-750 LF-1: END**

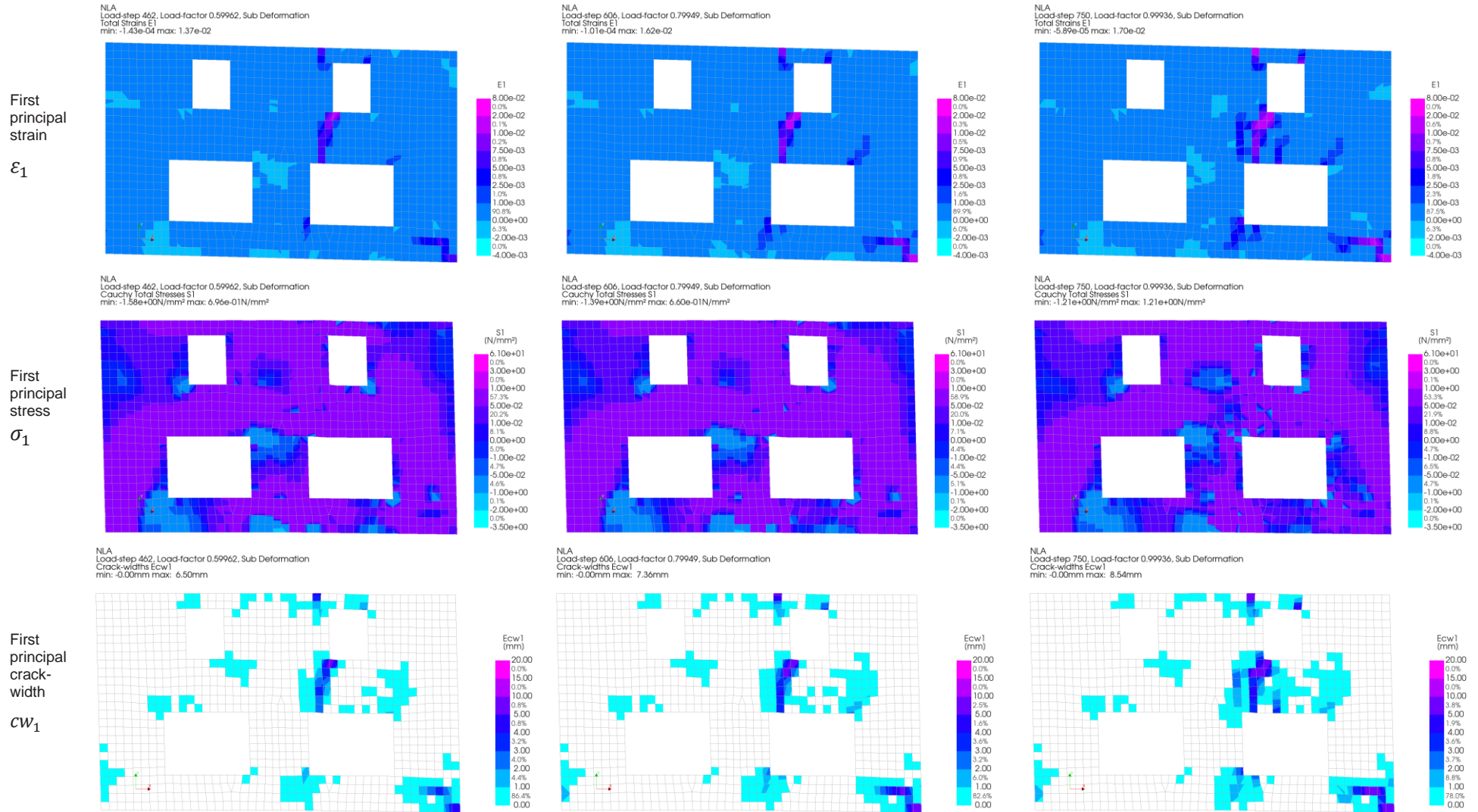


TABLE 53: Analysis results for W20 – EMMS – 0.2m

Analysis Results

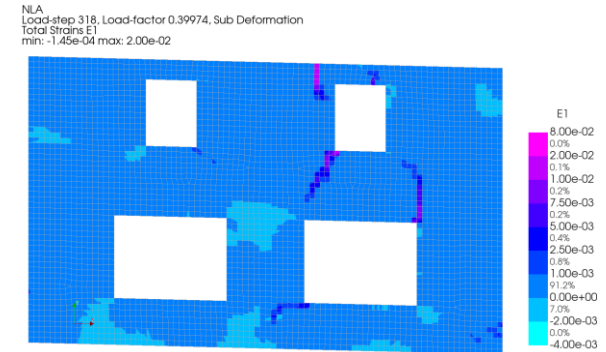
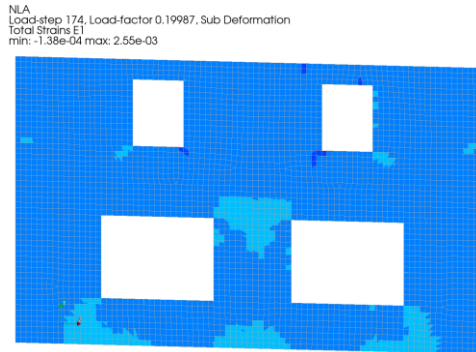
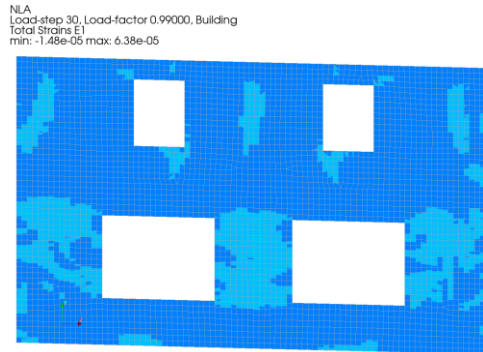
Model: W20 – EMM – S – 0.1m

Output LS-30 LF-1: End of Building loads

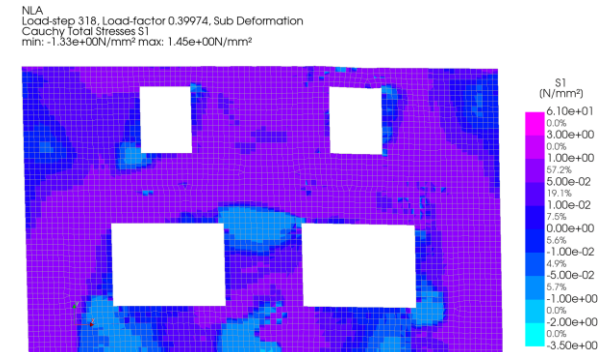
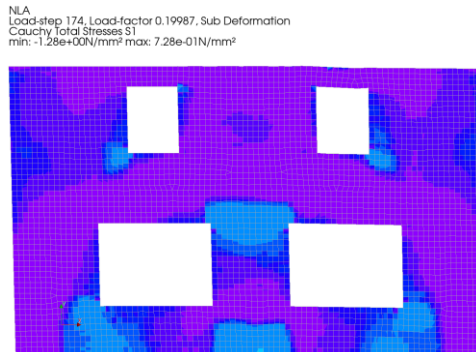
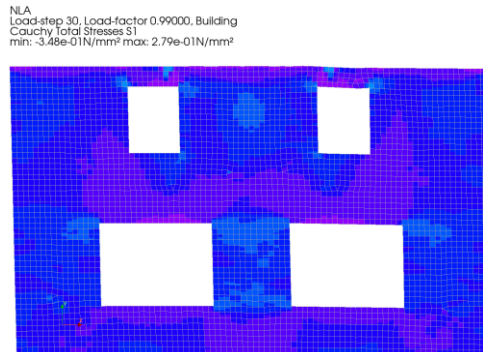
LS-174 LF-0.2: First crack formations

LS-318 LF-0.4: Main crack formation

First principal strain  $\epsilon_1$

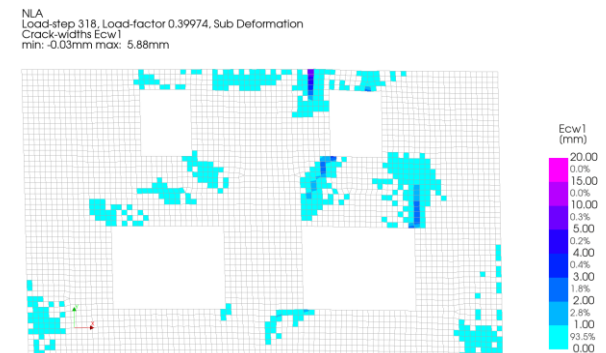
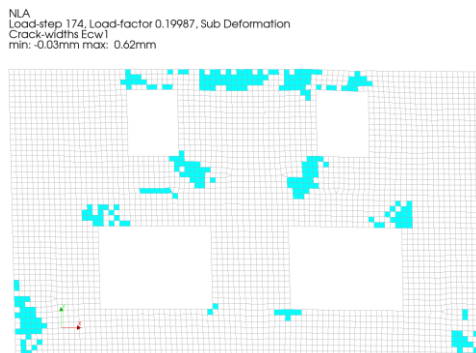


First principal stress  $\sigma_1$



First principal crack-width  $CW_1$

No data



Analysis Results

Model: W20 – EMM – S – 0.1m

Output LS-462 LF-0.6: Cracks grow

LS-606 LF-0.8: Cracks grow

LS-750 LF-1: END

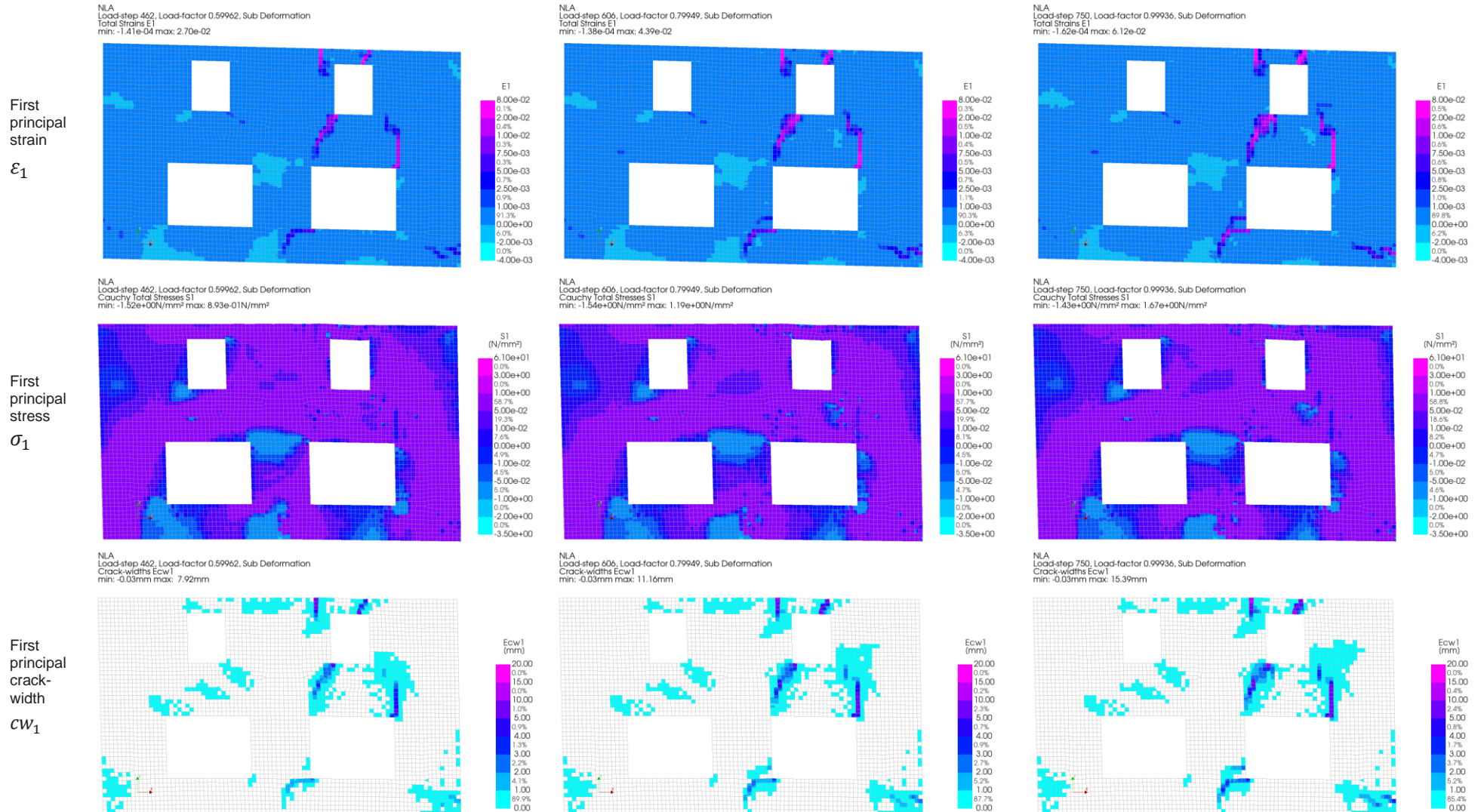


TABLE 54: Analysis results for W20 – EMMS – 0.1m



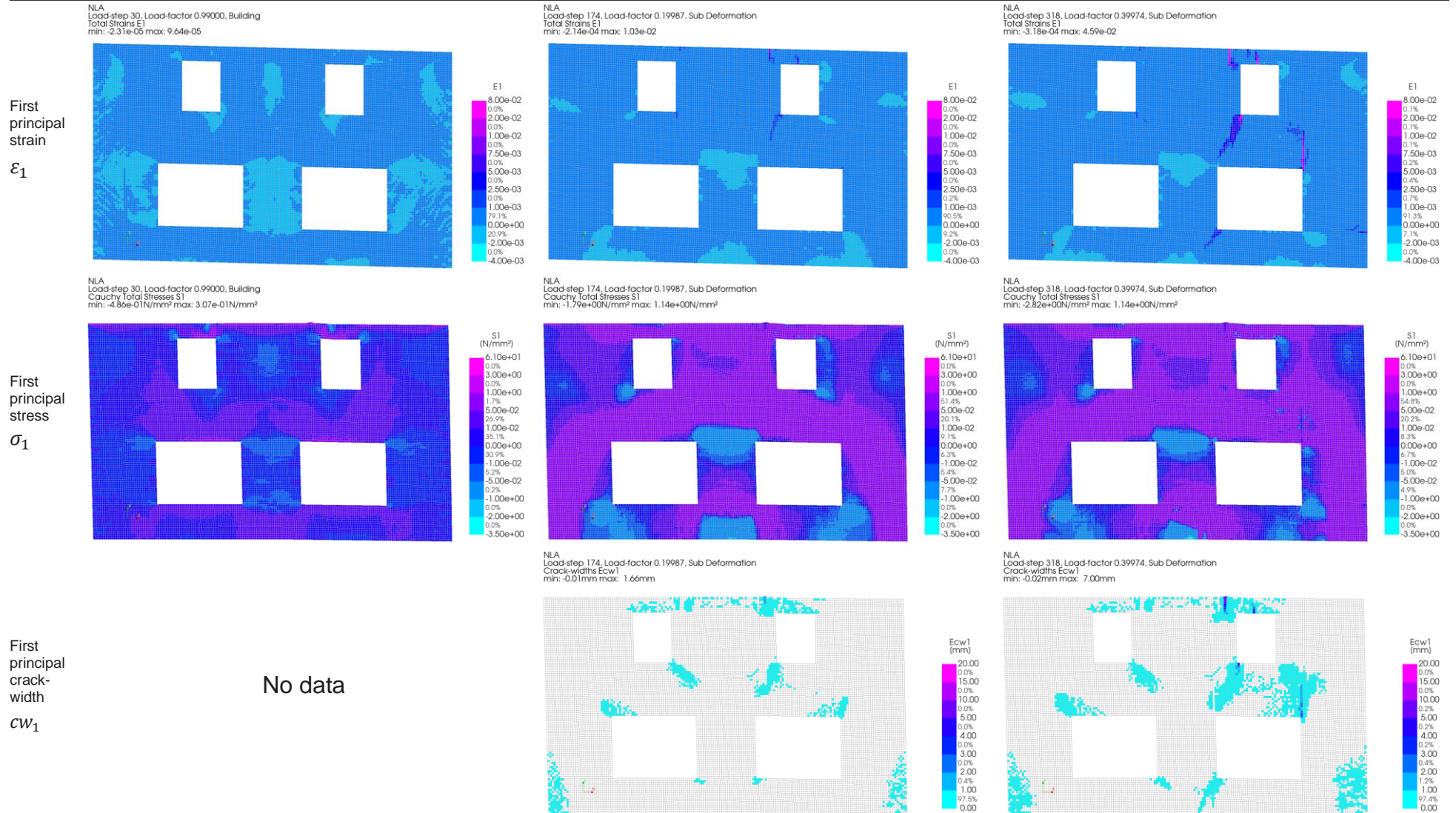
Analysis Results

Model: W20 – EMM – S – 0.05m

Output LS-30 LF-1: End of Building loads

LS-174 LF-0.2: First crack formations

LS-318 LF-0.4: Main crack formation



**Analysis Results**

**Model: W20 – EMM – S – 0.05m**

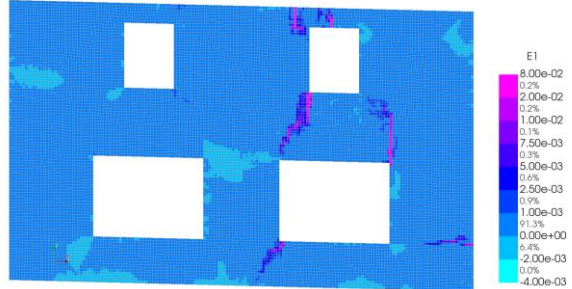
**Output LS-462 LF-0.6: Cracks grow**

**LS-606 LF-0.8: Cracks grow**

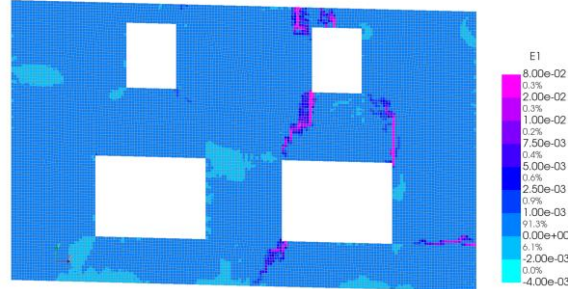
**LS-750 LF-1: END**

First principal strain  $\epsilon_1$

NLA  
Load-step 462, Load-factor 0.59962, Sub Deformation  
Total Strains E1  
min: -3.26e-04 max: 8.17e-02



NLA  
Load-step 606, Load-factor 0.79949, Sub Deformation  
Total Strains E1  
min: -3.37e-04 max: 1.16e-01

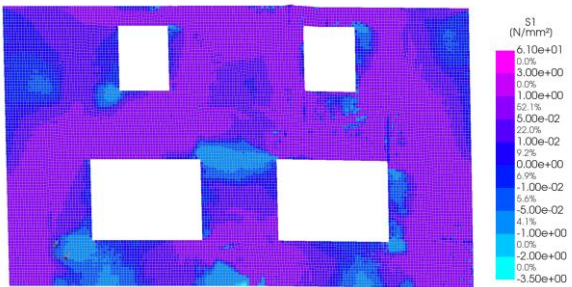


NLA  
Load-step 750, Load-factor 0.99936, Sub Deformation  
Total Strains E1  
min: -3.23e-04 max: 1.53e-01

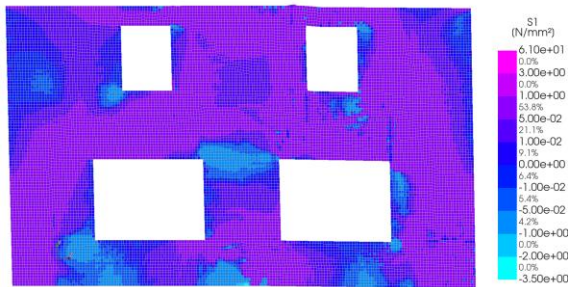


First principal stress  $\sigma_1$

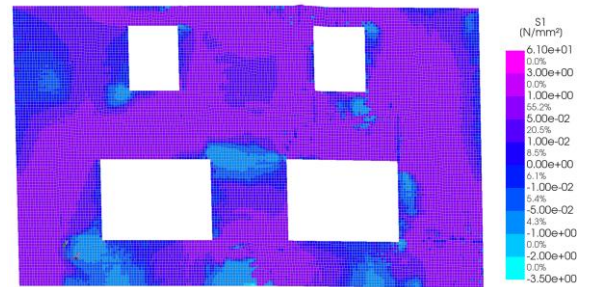
NLA  
Load-step 462, Load-factor 0.59962, Sub Deformation  
Cauchy Total Stresses S1  
min: -2.88e+00N/mm² max: 1.26e+00N/mm²



NLA  
Load-step 606, Load-factor 0.79949, Sub Deformation  
Cauchy Total Stresses S1  
min: -2.94e+00N/mm² max: 1.25e+00N/mm²

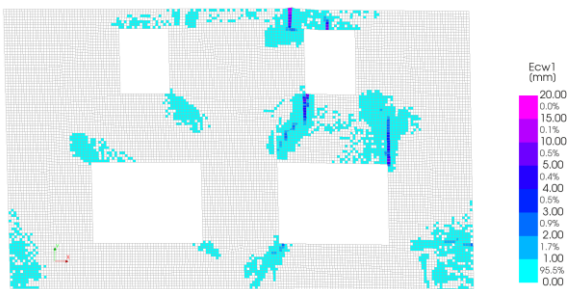


NLA  
Load-step 750, Load-factor 0.99936, Sub Deformation  
Cauchy Total Stresses S1  
min: -2.85e+00N/mm² max: 1.32e+00N/mm²

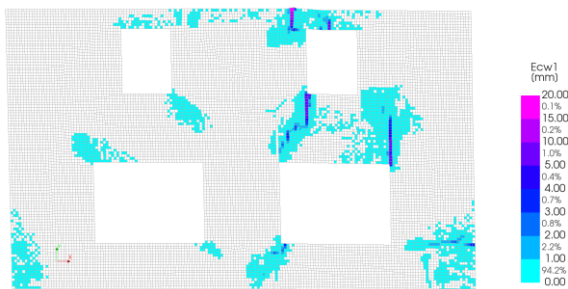


First principal crack-width  $cw_1$

NLA  
Load-step 462, Load-factor 0.59962, Sub Deformation  
Crack-widths Ecw1  
min: -0.01mm max: 12.52mm



NLA  
Load-step 606, Load-factor 0.79949, Sub Deformation  
Crack-widths Ecw1  
min: -0.02mm max: 16.85mm



NLA  
Load-step 750, Load-factor 0.99936, Sub Deformation  
Crack-widths Ecw1  
min: -0.01mm max: 21.02mm

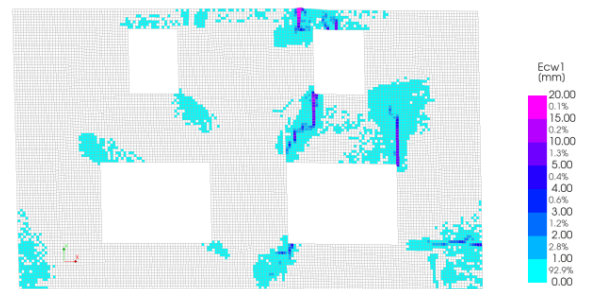


TABLE 55: Analysis results for W20 – EMMS – 0.05m

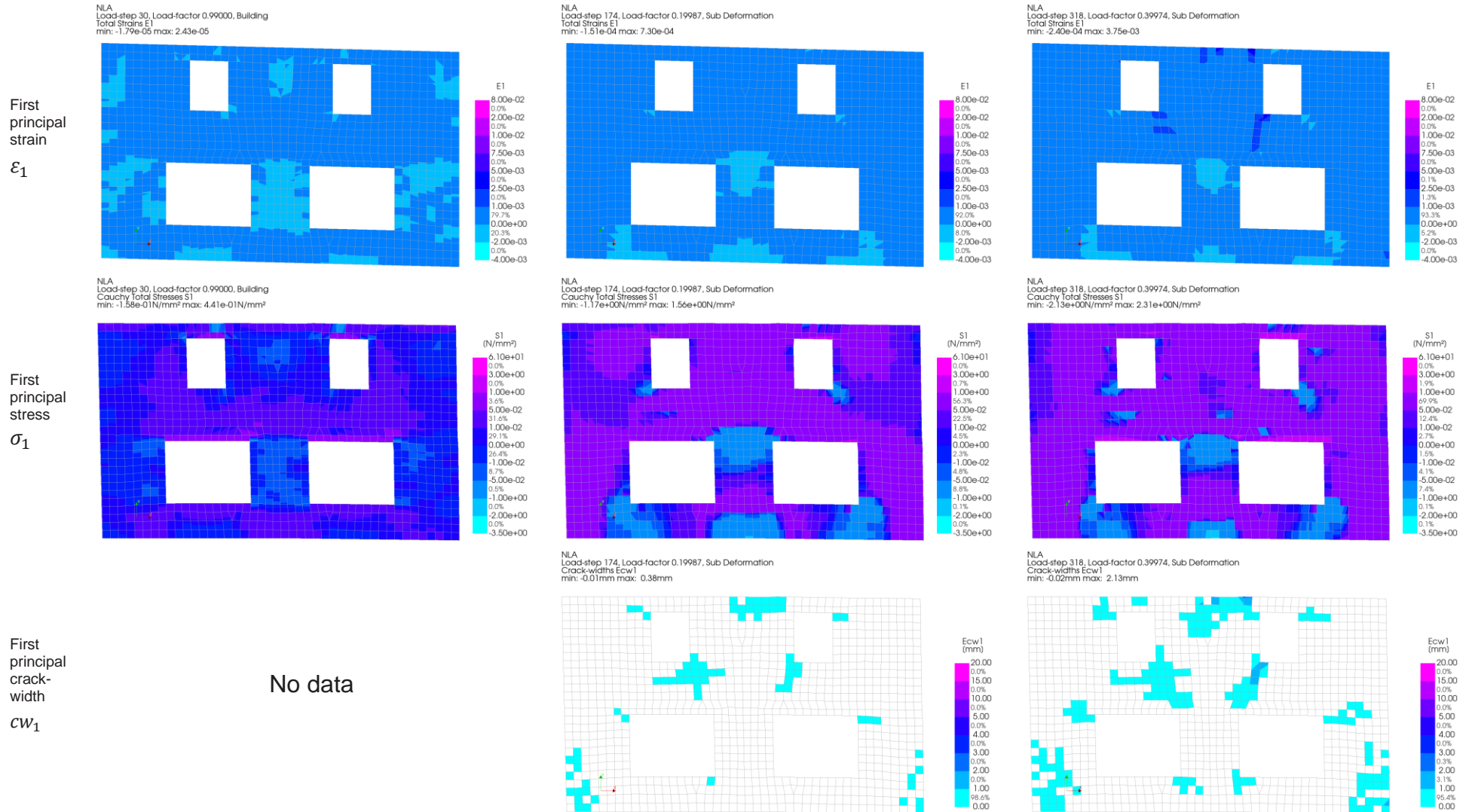
Analysis Results

Model: W2I – EMM – S – 0.2m

Output LS-30 LF-1: End of Building loads

LS-174 LF-0.2: First crack formations

LS-318 LF-0.4: Cracks grow



**Analysis Results**

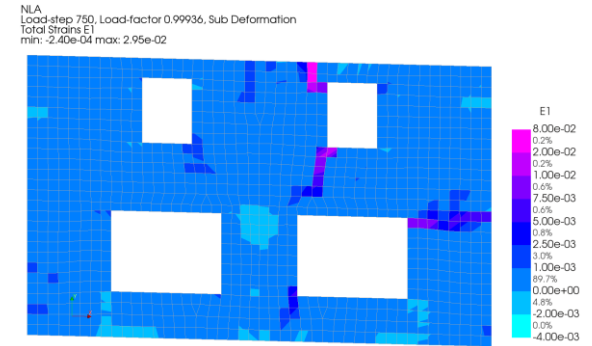
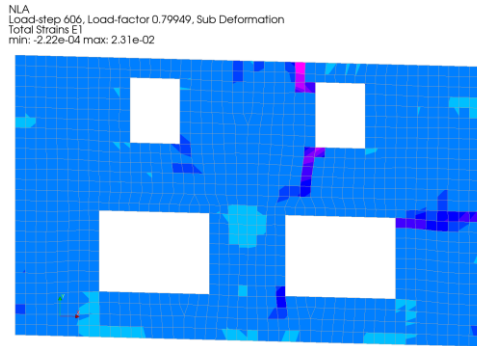
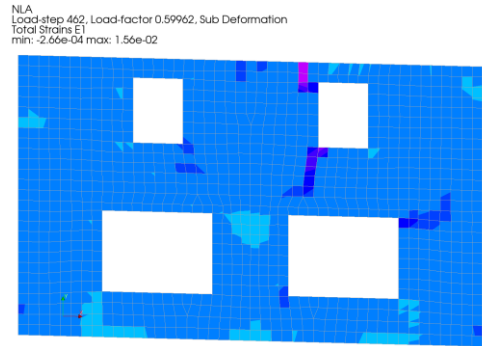
**Model: W2I – EMM – S – 0.2m**

**Output LS-462 LF-0.6: Main cracks formation**

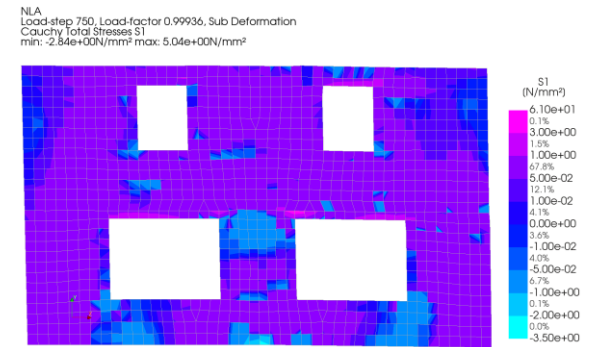
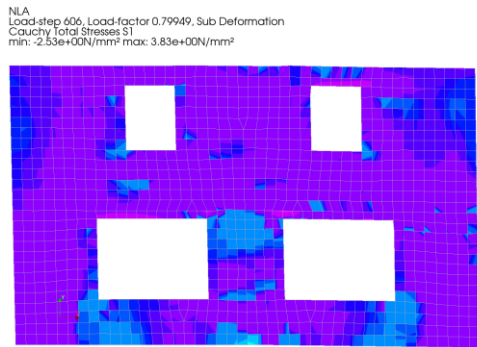
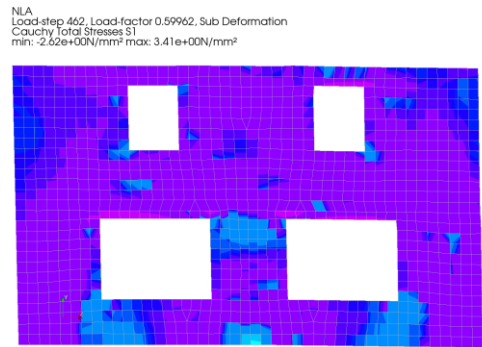
**LS-606 LF-0.8: Cracks grow**

**LS-750 LF-1: END**

First principal strain  
 $\epsilon_1$



First principal stress  
 $\sigma_1$



First principal crack-width  
 $CW_1$

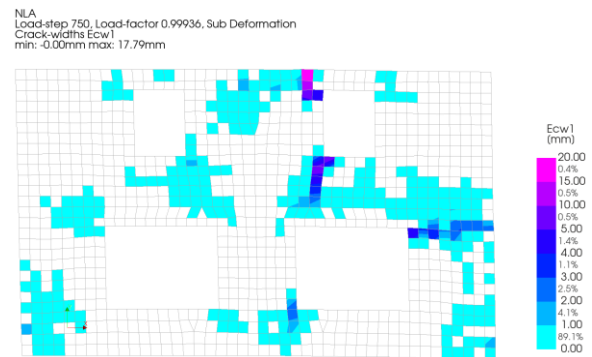
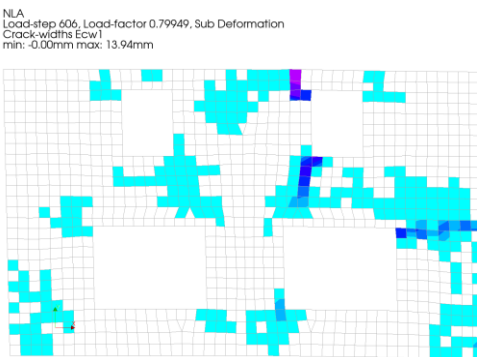
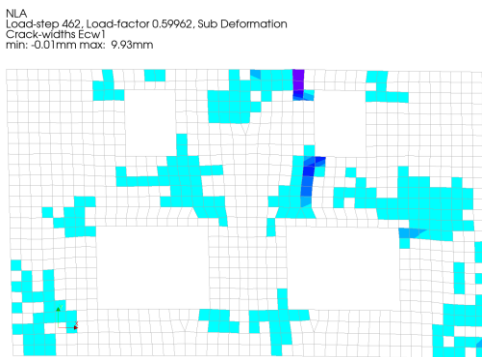


TABLE 56: Analysis results for W2I – EMM – 0.2m

Analysis Results

Model: W2I – EMM – S – 0.2m

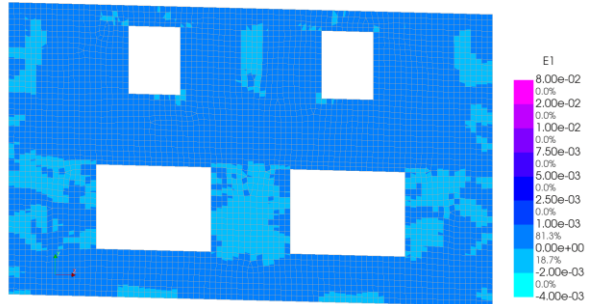
Output LS-30 LF-1: End of Building loads

LS-174 LF-0.2: First crack formations

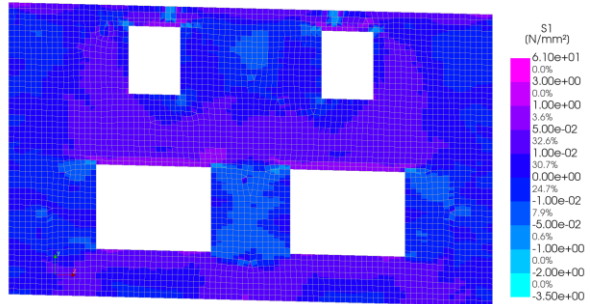
LS-318 LF-0.4: Cracks grow

First principal strain  $\epsilon_1$

NLA  
Load-step 30, Load-factor 0.99000, Building  
Total Strains E1  
min: -1.91e-05 max: 4.19e-05

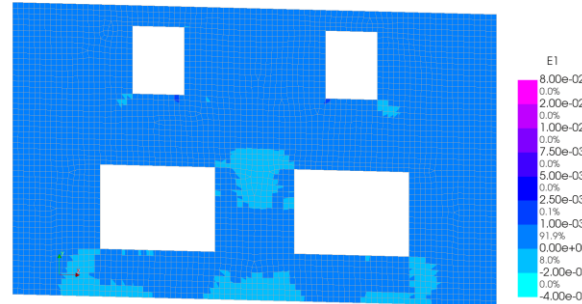


NLA  
Load-step 30, Load-factor 0.99000, Building  
Cauchy Total Stresses S1  
min: -2.34e-01N/mm² max: 6.62e-01N/mm²

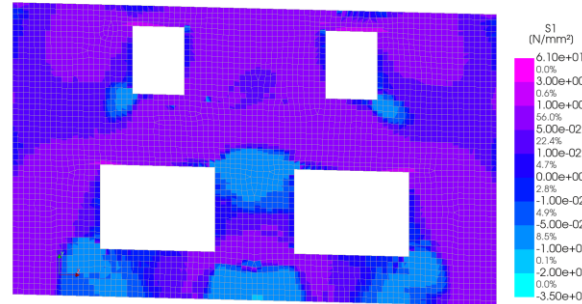


First principal stress  $\sigma_1$

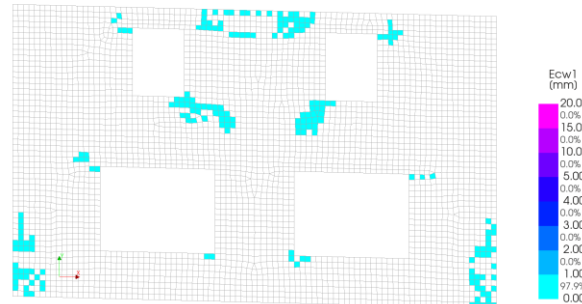
NLA  
Load-step 174, Load-factor 0.19987, Sub Deformation  
Total Strains E1  
min: -1.78e-04 max: 1.71e-03



NLA  
Load-step 174, Load-factor 0.19987, Sub Deformation  
Cauchy Total Stresses S1  
min: -1.40e+00N/mm² max: 1.81e+00N/mm²



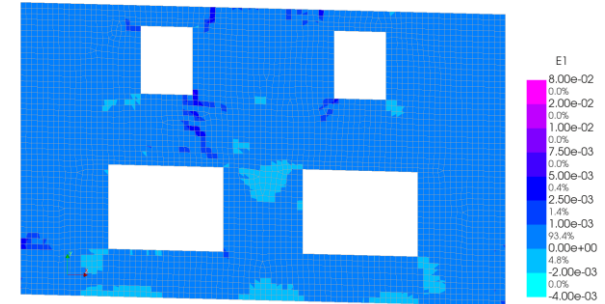
NLA  
Load-step 174, Load-factor 0.19987, Sub Deformation  
Crack-widths Ecw1  
min: -0.03mm max: 0.38mm



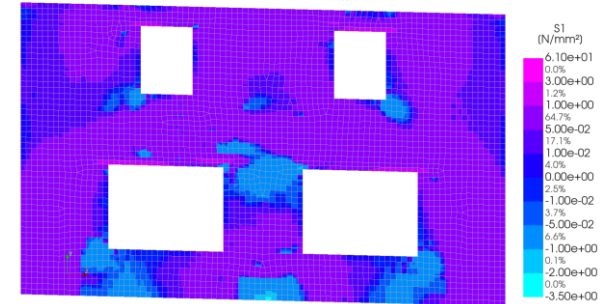
First principal crack-width  $cw_1$

No data

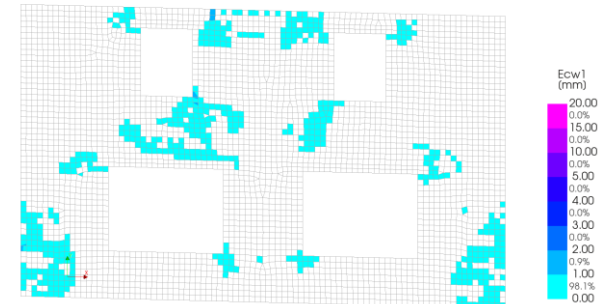
NLA  
Load-step 318, Load-factor 0.39974, Sub Deformation  
Total Strains E1  
min: -2.90e-04 max: 6.48e-03



NLA  
Load-step 318, Load-factor 0.39974, Sub Deformation  
Cauchy Total Stresses S1  
min: -2.53e+00N/mm² max: 3.43e+00N/mm²



NLA  
Load-step 318, Load-factor 0.39974, Sub Deformation  
Crack-widths Ecw1  
min: -0.08mm max: 1.46mm



**Analysis Results**

**Model: W2I – EMM – S – 0.1m**

**Output LS-462 LF-0.6: Cracks grow**

**LS-606 LF-0.8: Cracks grow**

**LS-750 LF-1: END**

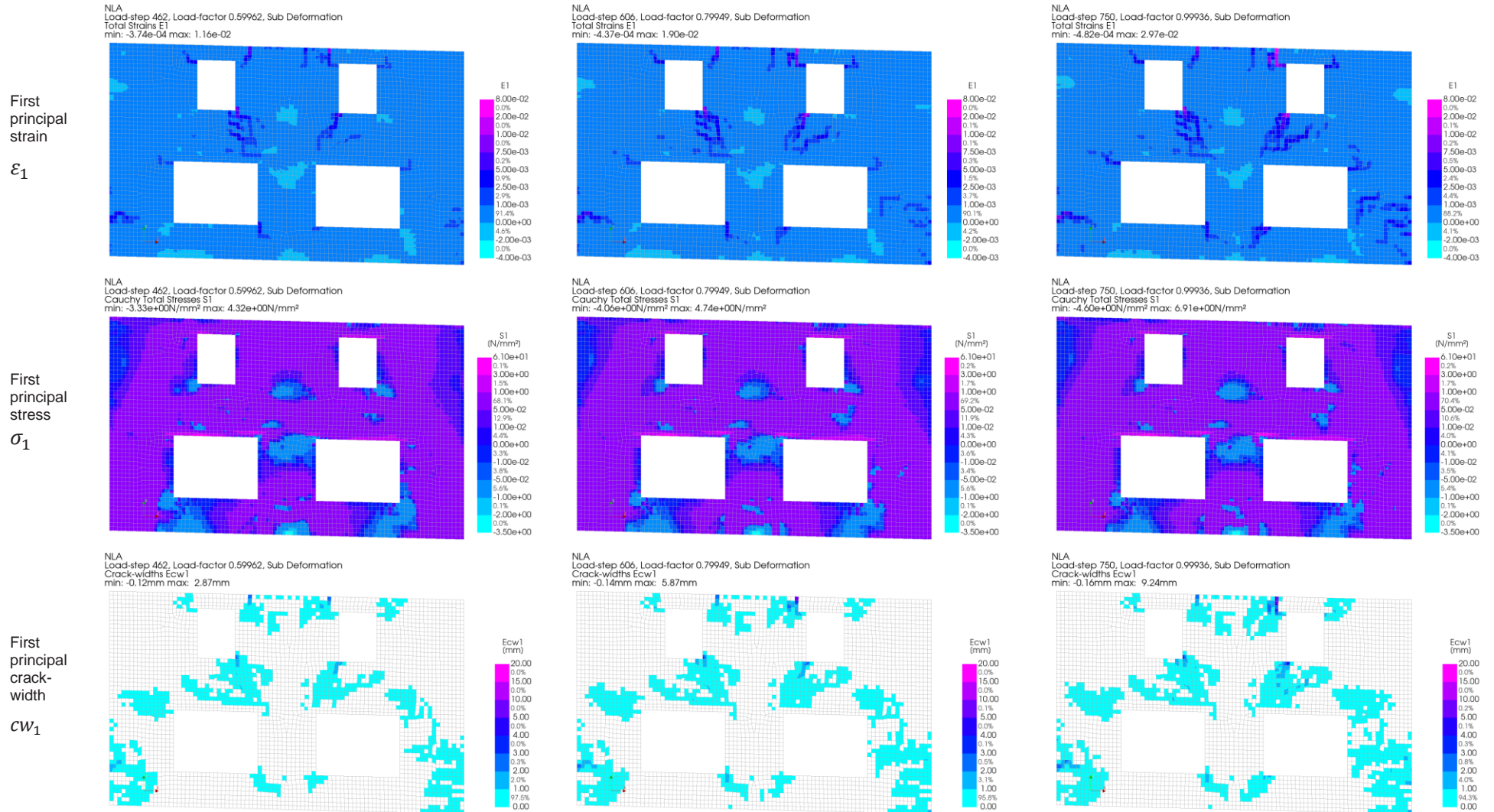


TABLE 57: Analysis results for W2I – EMMS – 0.1m

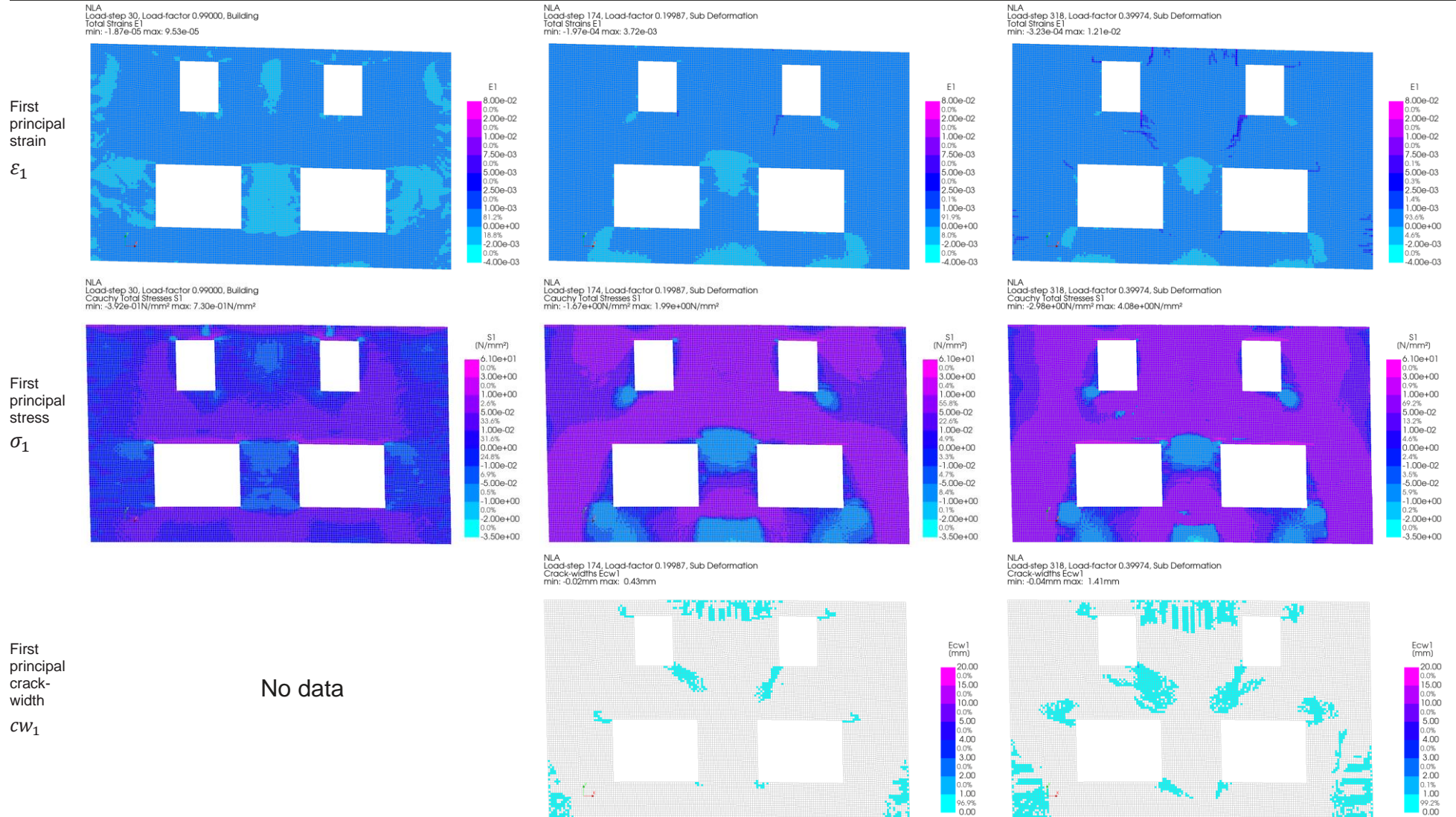
Analysis Results

Model: W2I – EMM – S – 0.05m

Output LS-30 LF-1: End of Building loads

LS-174 LF-0.2: First crack formations

LS-318 LF-0.4: Cracks grow



**Analysis Results**

**Model: W2I – EMM – S – 0.05m**

**Output LS-462 LF-0.6: Cracks grow**

**LS-606 LF-0.8: Cracks grow**

**LS-750 LF-1: END**

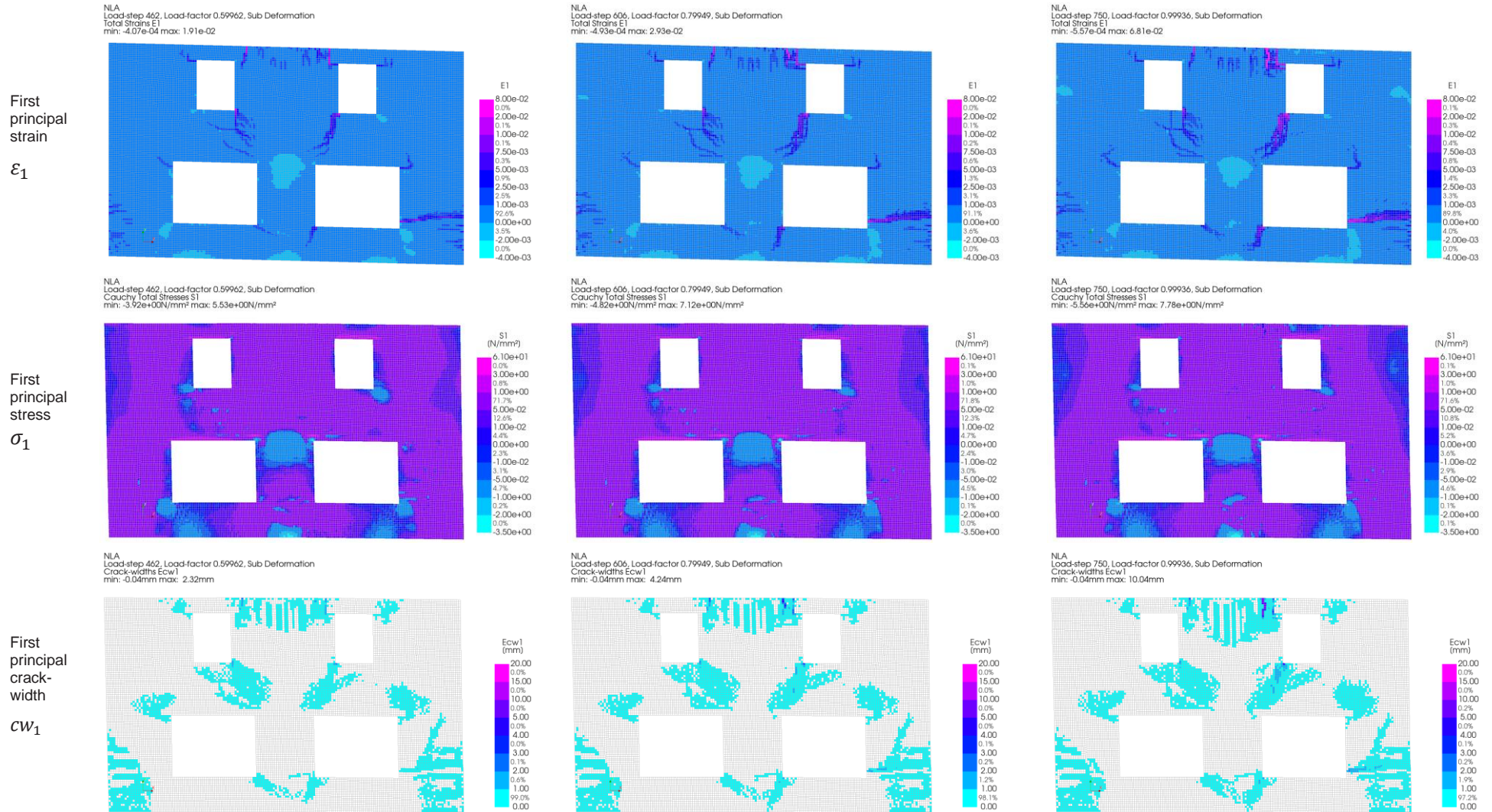


TABLE 58: Analysis results for W2I – EMMS – 0.05m



## Appendix 1.5: Influence on results by using different damage assessment indicators

A main component for the evaluation of models in this thesis has been the benchmarking of the models, the chosen damage assessment indicator has been Korswagen, et al., 2019 damage parameter ( $\Psi$ ). This parameter is usually computed based on the maximum crack width but in this case it has been computed through the mean crack-width. Other studies have made use of different measures to cross evaluate results with another popular indicator being the crack-widths.

Therefore, this appendix aims to firstly, highlight the influence the Damage parameter computation method change has had on the parameter values and secondly, it aims to compare the influence different damage assessment indicators may have when making model conclusions when making use of mean versus maximum crack-width formulations or making use of the damage parameter. Lastly, it will also aim to discuss further Damage Parameter characteristics observed when evaluating the models. For comparison the values for different Damage assessment indicators have been presented in TABLE 59, and between brackets their percentage deviation against their expected values is also provided. The RMSE scores and standard deviations against the case study are also presented on a per material model family basis.

<b>Model</b>		<b>Damage Parameter via Mean CW [<math>\Psi</math>]</b>	<b>Damage Parameter via Max CW [<math>\Psi</math>]</b>	<b>Mean max Crack Width [mm]</b>	<b>Max Crack Width [mm]</b>
TSCM	Outer 200mm	4.53 [+29%]	5.76 [+64%]	9.45 [+136%]	21.52 [+438%]
	Outer 100mm	4.31 [+23%]	5.37 [+53%]	8.56 [+114%]	14.16 [+254%]
	Outer 50mm	4.87 [+39%]	5.76 [+64%]	10.16 [+154%]	19.15 [+378%]
	Inner 200mm	3.93 [+31%]	5.0 [+66%]	9.56 [+218%]	21.31 [+610%]
	Inner 100mm	3.81 [+27%]	5.11 [+70%]	8.63 [+187%]	22.83 [+661%]
	Inner 50mm	4.09 [+36%]	5.64 [+88%]	7.87 [+162%]	22.76 [+658%]
		RMSE= 31% $\sigma=6\%$	RMSE= 68% $\sigma=11\%$	RMSE= 165% $\sigma=37\%$	RMSE= 523% $\sigma=168\%$
EMM	Outer 200mm	3.7 [+5%]	5.12 [+50%]	3.79 [-5%]	8.54 [+113%]
	Outer 100mm	4.47 [+27%]	6.04 [+72%]	6.51 [+62%]	15.39 [+284%]
	Outer 50mm	4.85 [+38%]	6.69 [+91%]	8.31 [+107%]	21.02 [+425%]
	Inner 200mm	4.09 [+36%]	5.0 [+66%]	10.18 [+239%]	17.79 [+493%]
	Inner 100mm	3.4 [+13%]	5.64 [+88%]	3.10 [+3%]	9.24 [+208%]
	Inner 50mm	4.06 [+35%]	5.53 [+84%]	5.66 [+88%]	10.04 [+234%]
		RMSE= 29% $\sigma=14\%$	RMSE= 76% $\sigma=17\%$	RMSE= 115% $\sigma=88\%$	RMSE= 320% $\sigma=141\%$

TABLE 59: Analysis benchmark scores according to different damage assessment indicators.

A color scale has been used to indicate from Green (1st - closest rank) to Red (12th - worst rank) has been used for all indicators.

The color scale shown in TABLE 59 illustrates the possible ambiguity that may arise when benchmarking models through different damage assessment indicators. As the relative accuracy index against the case study building changes quite strongly through all different indicators. Out of all results, in the authors view the mean crack-width index scores present the most accurate damage picture.

The colours also illustrate how crack-width specific benchmark disfavour TSCM models as these tend to produce wider cracks, whilst damage parameter benchmarks more heavily penalise EMM models as the greater number of cracks penalises their damage level. The RMSE scores through different damage assessment indicators show that the deviation is less through the Damage Parameter rather than the crack widths. Similarly the mean computations deviate less than the maximum computations.

Despite, the above rationale in the authors opinion the best damage assessment indicator is the baseline Damage Parameter ( $\Psi$ ) its formulation is the most balanced and versatile as it accounts for the main damage severity features. Nevertheless, throughout its use in the analyses in this study some characteristic were observed mainly concerning the relative influence crack lengths and the number of cracks have in its computation.

### Appendix 1.5.1: Max-Mean influence on the Damage parameter $\Psi$

Below the equations used and the original formulation for the Damage parameter is shown the influence of the change is that in the computation of the quadratic weighted crack average the mean crack-width has been used instead of the maximum crack -width.

<b>Parameter</b>	<b>Actual formulation</b>	<b>Used formulation</b>
Damage parameter ( $\Psi$ ) for single-wall		$\Psi = 2 \cdot n_c^{0.15} \cdot \widehat{c}_w^{0.3}$
Calculation of weighted crack width for a single wall	$\widehat{c}_w = \frac{\sum_{i=1}^{n_c} c_{w-max,i}^2 \cdot c_{L,i}}{\sum_{i=1}^{n_c} c_{w-max,i} \cdot c_{L,i}}$	$\widehat{c}_w = \frac{\sum_{i=1}^{n_c} c_{w-\mu,i}^2 \cdot c_{L,i}}{\sum_{i=1}^{n_c} c_{w-\mu,i} \cdot c_{L,i}}$

Equation 9: PSI formulation change used in the benchmarking of the FEA results.

The use of the mean crack-widths to compute the damage parameter ( $\Psi$ ) significantly reduces the parameter estimations, this has been approximated to be by  $-1.4 \Psi$ . This decision mostly influences the possibility to use the DL- $\Psi$  equivalence scale from Equation 1, as this scale expects  $\Psi$  to be computed via the maximum crack widths, and therefore doesn't allow DL evaluations. Nevertheless, when making use of the original  $\Psi$  formulation the obtained damage levels would have corresponded to significantly large DL 4's.

This DL estimation is not fully realistic because the  $\Psi$  parameter is intended to quantify lighter damage. As a result, the  $\Psi$  values obtained from these models may not accurately represent the crack patterns, especially when more significant structural damage is present. Additionally, using the original  $\Psi$  formulation would have further emphasized the conservative nature of FEA as an assessment method. While the conclusions drawn from the computations would remain the same, they would have been amplified.

Overall, the use of the mean crack width is not recommended as it less easily evaluates tapering in cracks. Nevertheless, it may produce more optimistic scores when results are being compared against harder to discern features from crack photographs that make the determination of maximum crack widths difficult.

# **Appendix 1.6: TSCM and EMM GP at the mean material properties**

**TSCM GP Mean and variance**

**At mean material parameters**

**Model Mean**

**Model Variance**

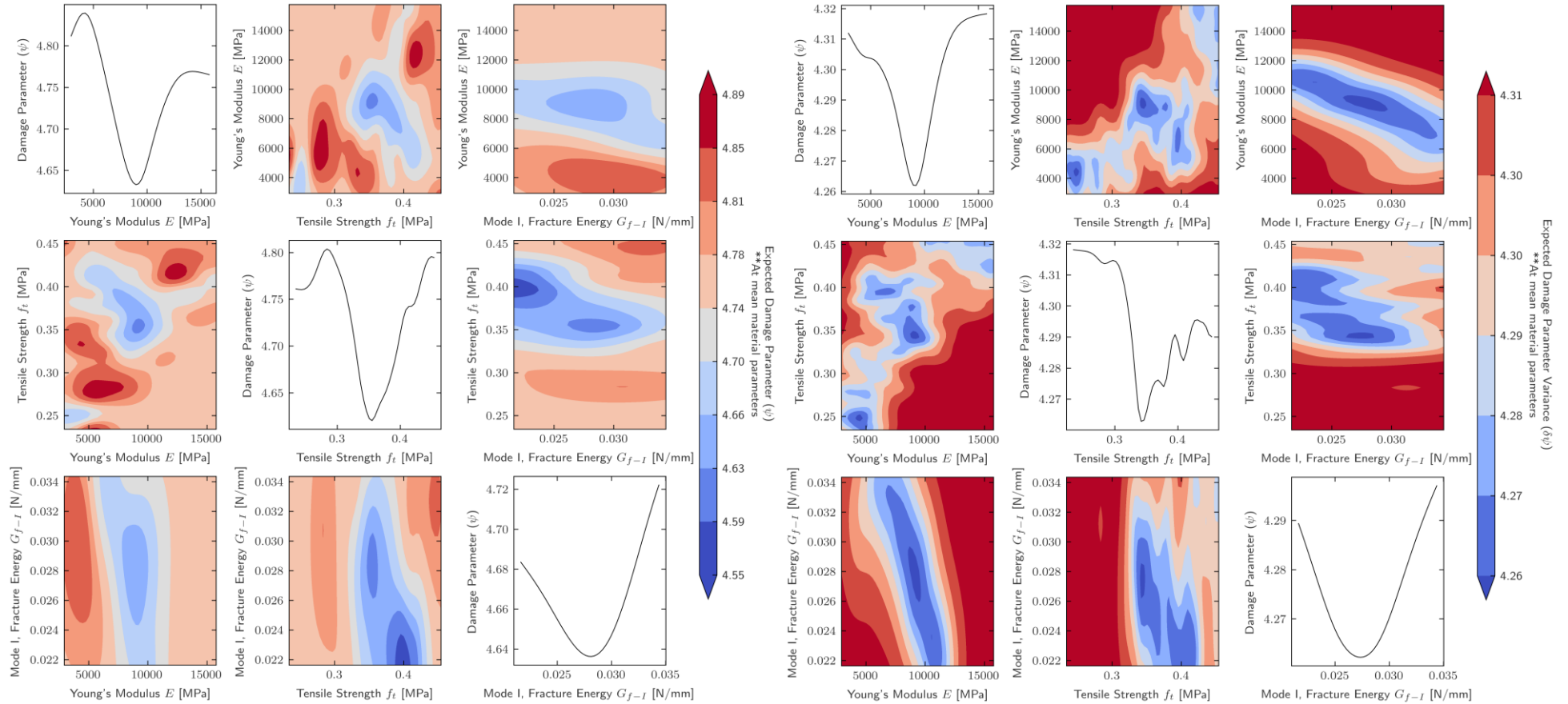


TABLE 60:  $\Psi$  Mean and variance for the TSCM results at mean material parameters.

EMM GP Mean and variance

At mean material parameters

Model Mean

Model Variance

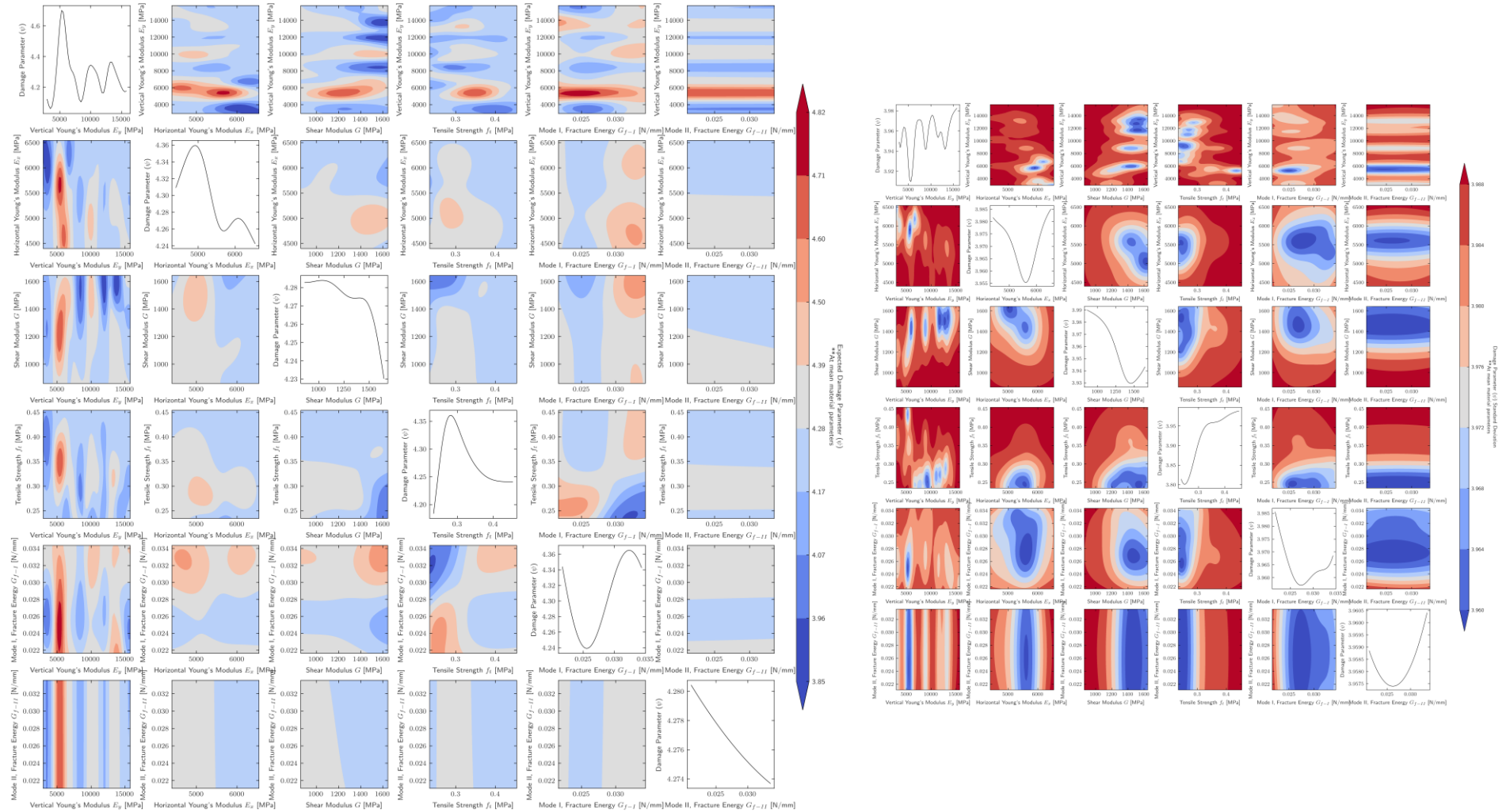


TABLE 61:  $\Psi$  Mean and variance for the EMM results at the mean model parameters.

# Appendix 2: Model analysis algorithms

---

This chapter provides a detailed breakdown of a key component used for the evaluation of the models presented in this thesis. The algorithm discussed is part of a codebase developed to support the Finite Element Analysis (FEA) of masonry buildings, referred to as the [Bricks](#) module.

The 'Bricks' module consists of two submodules: 'Bricks.Analytical,' which contains the code for the assessments presented in Section 4, and 'Bricks.FEA,' which houses the code used in Sections 5 and 6.

In this appendix, a central component of the 'Bricks.FEA' submodule, the crack detection algorithm, is explained in detail.

## Appendix 2.1: Crack detection algorithm

This appendix aims to illustrate the procedure that the developed crack detection algorithm has taken for the evaluation of all model results. The algorithm is split into two sections: a first section whose purpose is to process tabulated (.tb) output files generated by Diana FEA software package, and a second component whose purpose is the determination of the connectivity between cracked elements to identify crack clusters, and their principal component. This breakdown also aims to illustrate the limitations of the algorithm and the rationale for the decisions made in its processing and how they could influence results.

To demonstrate the algorithm model: W20 – TS – 200mm at its last load step will be used. The crack pattern (Figure 43) shows three cracks Crack 1 (Superior), Crack 5 (middle) and Crack 9 (bottom). These cracks have been approximated to have an average crack width of 11mm, 10mm, and 2.5mm respectively, whilst the crack lengths are approximately 900mm, 1100mm, and 900mm respectively.

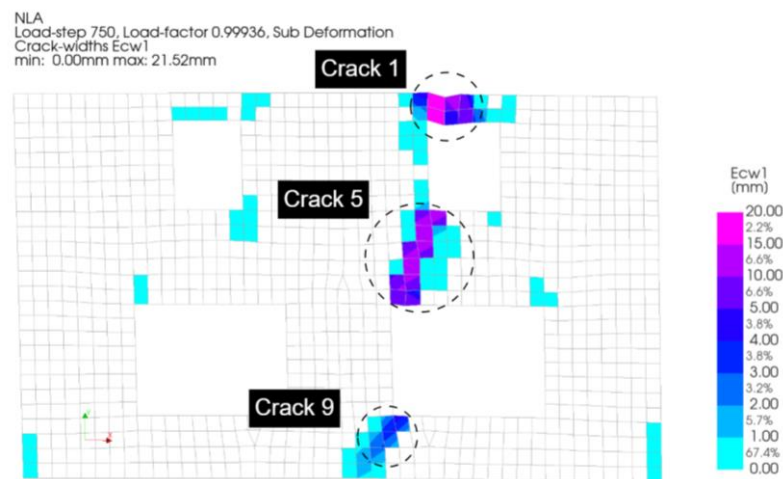


Figure 43: TSCM 200mm mesh results final crack pattern

Firstly, the analysis output tabulated file (.tb extension) is processed. A script for this was built which is called through the function “process\_tb(file\_path)”. For a successful use of this function, some changes to the tabulated output configuration need to be made in Diana’s analysis output configuration. The following crack detection algorithm was built expecting the coordinates of the nodes and integration points. This is necessary to determine the adjacency between elements in the mesh. Some other settings are also preferably changed, the maximum number of columns of the tabulated file should be increased to reduce the number of rows in the file making the final Data frame less heavy. An example of the best configuration is available in the [example model](#) in the repository.

Analysis type	Step nr.	Load factor	X0	Y0	Z0	Element	Integration Point	E1	E2	...	Node	TD1X	TD1y	TD1Z	FBX	FBy	FBZ	Ecw1	Ecw2	Ecw3	
0	NONLIN	1	0.0330	240.600006	5093.0	0.0	1.0	1.0	8.171000e-08	-4.547000e-08	...	NaN	NaN	NaN	NaN	NaN	NaN	NaN	NaN	NaN	NaN
1	NONLIN	1	0.0330	239.699997	5208.0	0.0	1.0	2.0	2.078000e-07	-2.086000e-08	...	NaN	NaN	NaN	NaN	NaN	NaN	NaN	NaN	NaN	NaN
2	NONLIN	1	0.0330	354.600006	5093.0	0.0	1.0	3.0	3.397000e-08	-1.912000e-08	...	NaN	NaN	NaN	NaN	NaN	NaN	NaN	NaN	NaN	NaN
3	NONLIN	1	0.0330	353.799988	5208.0	0.0	1.0	4.0	1.820000e-07	-1.611000e-08	...	NaN	NaN	NaN	NaN	NaN	NaN	NaN	NaN	NaN	NaN
4	NONLIN	1	0.0330	563.200012	1973.0	0.0	2.0	1.0	3.369000e-08	-3.383000e-07	...	NaN	NaN	NaN	NaN	NaN	NaN	NaN	NaN	NaN	NaN
...	...	...	...	...	...	...	...	...	...	...	...	...	...	...	...	...	...	...	...	...	...
3627745	NONLIN	750	0.9994	3331.000000	3218.0	NaN	NaN	NaN	NaN	NaN	1066.0	-16.969999	-17.080	0.0	NaN	NaN	NaN	NaN	NaN	NaN	NaN

Figure 44: Processed Data frame for W2O - TS - 200mm

The output for the model W2O – TS – 200mm is shown Figure 44, this Data Frame has around 3.6 million rows which shows how even for a small model and coarse mesh the produced Data Frames

are memory expensive. For this reason, the algorithm processes the file in chunks and the floating point accuracy was reduced to 32 to prevent MemoryErrors which were present in the model with a mesh size of 50x50mm. A shift to Sql tables may be necessary for more expensive models.

The above DF is passed into the “analyse\_tabulated” function (EXTRACT 8). This function parses the cracks for every load step and computes the damage parameter. For a specific load step the procedure is as follows, the rows from the DF for that step are indexed as well as the lines whose integration points produced crack-widths within one order of magnitude to the maximum crack width. This last step was implemented to improve the resilience of the algorithm to smeared cracks produced such as in EMM results and produce more realistic PSI values. As the number of cracks in EMM models could be 30 when realistically 4 cracks were relevant.

Once the specific step load and crack-width specific DF are indexed, this DF is passed onto the main crack detection logic (“analyse\_cracks” - EXTRACT 9). This function firstly detects the connected integration points (“find\_connected\_components” - EXTRACT 10) by extracting the coordinates for the relevant set of integration points over which the distance between them is calculated through the Scipy “distance\_matrix” function which returns the pairwise distance in a symmetric matrix. A distance threshold “d\_threshold” is determined by computing,  $\sqrt{2 * (\text{mesh\_size}/2)^2}$ , which has been approximated to correspond to the maximum possible distance between two adjacent or diagonal integration points in any mesh size. Which is then checked by evaluated and returns boolean statements when the distance between integration points is less than the threshold.

This matrix is then passed to the “connected\_components” SciPy function from which the shared components in the adjacency matrix return different number labels for different clusters. Lastly, the original DF is updated with the labels as updated passed onto the “calculate\_crack\_properties” function (EXTRACT 11). This function then validates cracks from the original clusters as those clusters which contain more than two elements or 3 integration points. If this condition is this cluster is validates as a crack and the maximum computed distances between integration points in the cluster are again evaluated whose maximum is determined to be the crack length and the average crack width is also determined. The results for this process on model W20 – TS – 200mm are shown in Figure 45 and the results for all models are presented in TABLE 62 and TABLE 63.

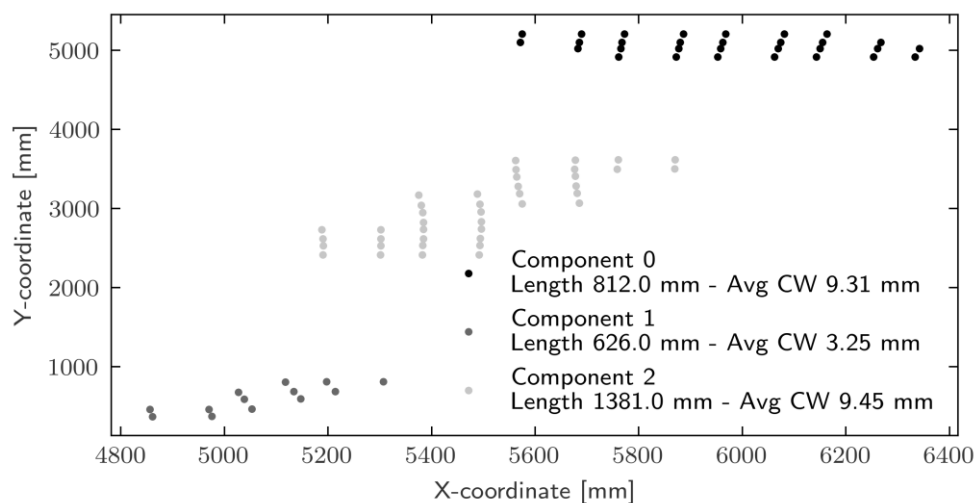


Figure 45: Identified integration point clusters for load step 750 of W20 – TS – 200mm



## Appendix 2.2: Initial benchmarking of the parameter identification algorithm

Before carrying out the calibration procedure the algorithm was first tested to make sure its implementation was suitable before making use of it for the lengthy calibration runs. It did so by making use of the BoTorch test function Branin. The Branin function is a 2-dimensional, continuous problem with three global minima. This makes it more of a challenge for conventional optimisation algorithms and quasi-random search methods as there is the possibility of getting stuck in different locations.

The developed algorithm was compared to Sobol, a quasi-random search algorithm that aims to maximise the discrepancy between points, a BoTorch built BOpt algorithm through a qEI variant for the acquisition function, and lastly the solver prepared for the optimisation of the FEM.

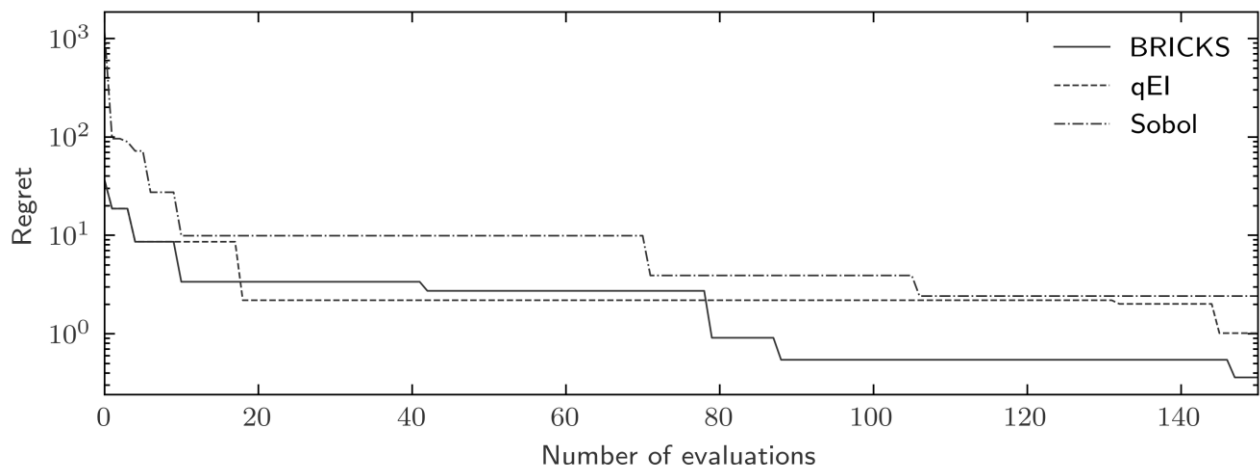


Figure 46: Best regret against number of objective function evaluations of different solvers against the Branin benchmark problem.

The results indicate that Bayesian optimization techniques performed well overall, with the Bricks algorithm achieving superior results, as shown by a near-zero regret value (logarithmic scale). Additionally, the thesis solver identified optimal solutions faster than the standard BoTorch BOpt algorithm. In contrast, the SOBOL quasi-random search algorithm, often used in surrogate models, exhibited moderate performance. Variations in quasi-random initialization influenced the speed and accuracy of the BOpt algorithms between different runs. On the whole, the only difference between runs was between the relative speed and performance of both BOpt algorithms.

## Appendix 2.3: Parameter identification results

The optimisation results from all model evaluations have not been presented as the results showed that the changes to the material parameters influenced the specific crack patterns characteristics but had less influence on the overall mechanism in the wall. Nevertheless these results are available in the following hyperlink “[BRICKS](#)” which contains the results (screenshots, GP’s and monitoring dataframe), model and algorithm used in the optimisation of the TSCM model. In case there is any interest in the procedure or results.

**Crack detection algorithm results**

Model	Final Cracks
W20 TS 200mm	{'Crack 0': {'length': 811.9390371203986, 'max_mean_width': 9.3145685, 'component': [5.0, 33.0, 164.0, 177.0, 178.0, 179.0, 279.0, 341.0, 435.0]}, 'Crack 1': {'length': 625.7389483088492, 'max_mean_width': 3.2482312, 'component': [9.0, 206.0, 263.0, 567.0, 612.0]}, 'Crack 2': {'length': 1381.015568340922, 'max_mean_width': 9.451726, 'component': [30.0, 35.0, 166.0, 203.0, 387.0, 523.0, 594.0, 684.0, 723.0, 867.0]}}
W20 TS 100mm	{'Crack 0': {'length': 539.656372148055, 'max_mean_width': 6.0574102, 'component': [64.0, 360.0, 361.0, 363.0, 364.0, 426.0, 489.0, 542.0, 647.0, 691.0, 835.0, 880.0, 1104.0, 1258.0, 1346.0]}, 'Crack 1': {'length': 646.2665698261844, 'max_mean_width': 2.7299232, 'component': [140.0, 557.0, 763.0, 1481.0, 1601.0, 2136.0, 2200.0, 2474.0, 2624.0]}, 'Crack 2': {'length': 1392.6237826491404, 'max_mean_width': 8.555794, 'component': [148.0, 249.0, 329.0, 382.0, 693.0, 787.0, 910.0, 991.0, 1002.0, 1039.0, 1374.0, 1454.0, 1500.0, 1647.0, 1741.0, 2409.0, 2510.0, 2665.0, 2754.0, 3048.0, 3101.0, 3256.0, 3285.0]}}
W20 TS 50mm	{'Crack 0': {'length': 1398.3204210766573, 'max_mean_width': 9.161433, 'component': [39.0, 522.0, 651.0, 1945.0, 2246.0, 2247.0, 2605.0, 3192.0, 4183.0, 4397.0, 4627.0, 4771.0, 4958.0, 5156.0, 5403.0, 6493.0, 6914.0, 7039.0, 7597.0, 7822.0, 7830.0, 8770.0, 8816.0, 9432.0, 9623.0, 9751.0, 10315.0, 10316.0, 10474.0, 10749.0, 11325.0, 11643.0, 11734.0, 12237.0, 12268.0, 12347.0, 12547.0, 12751.0, 13506.0]}, 'Crack 1': {'length': 355.1689738701848, 'max_mean_width': 9.068063, 'component': [128.0, 2332.0, 2948.0, 3033.0, 3193.0, 3838.0, 3943.0, 3944.0, 3984.0]}, 'Crack 2': {'length': 608.7653716666869, 'max_mean_width': 2.8110974, 'component': [423.0, 926.0, 1795.0, 2705.0, 3998.0, 5054.0, 5089.0, 6958.0, 7103.0, 7587.0, 8735.0, 9037.0, 9106.0, 9165.0, 9328.0, 9360.0, 9563.0, 11449.0]}, 'Crack 3': {'length': 304.39612349699854, 'max_mean_width': 10.156539, 'component': [712.0, 714.0, 1789.0, 1790.0, 2764.0, 2765.0, 3394.0]}, 'Crack 4': {'length': 111.31936040060597, 'max_mean_width': 2.6112, 'component': [1858.0, 2861.0, 3179.0]}}
W2I TS 200mm	{'Crack 0': {'length': 4698.534064245048, 'max_mean_width': 9.557363, 'component': [34.0, 35.0, 71.0, 88.0, 146.0, 184.0, 211.0, 248.0, 259.0, 276.0, 293.0, 318.0, 335.0, 336.0, 363.0, 364.0, 367.0, 420.0, 607.0, 609.0, 731.0, 736.0, 750.0, 751.0, 794.0, 815.0, 850.0, 877.0, 887.0, 904.0, 966.0]}}
W2I TS 100mm	{'Crack 0': {'length': 4592.605660211854, 'max_mean_width': 8.629594, 'component': [58.0, 59.0, 60.0, 123.0, 228.0, 258.0, 259.0, 280.0, 357.0, 362.0, 379.0, 424.0, 426.0, 590.0, 663.0, 669.0, 697.0, 704.0, 716.0, 727.0, 744.0, 745.0, 777.0, 787.0, 792.0, 821.0, 847.0, 946.0, 961.0, 984.0, 1006.0, 1036.0, 1041.0, 1053.0, 1055.0, 1151.0, 1176.0, 1217.0, 1339.0, 1358.0, 1359.0, 1369.0, 1536.0, 1562.0, 2227.0, 2235.0, 2277.0, 2344.0, 2345.0, 2498.0, 2729.0, 2740.0, 2859.0, 3040.0, 3239.0, 3271.0, 3275.0, 3301.0, 3313.0, 3323.0, 3368.0, 3411.0, 3432.0, 3474.0, 3509.0, 3569.0, 3647.0]}}
W2I TS 50mm	{'Crack 0': {'length': 4301.047895571497, 'max_mean_width': 7.866412, 'component': [32.0, 127.0, 129.0, 132.0, 259.0, 389.0, 444.0, 535.0, 538.0, 558.0, 584.0, 618.0, 731.0, 752.0, 843.0, 900.0, 954.0, 965.0, 995.0, 1096.0, 1123.0, 1145.0, 1268.0, 1270.0, 1271.0, 1295.0, 1328.0, 1331.0, 1401.0, 1440.0, 1477.0, 1486.0, 1502.0, 1503.0, 1527.0, 1607.0, 1685.0, 1721.0, 1745.0, 1771.0, 1848.0, 1871.0, 1886.0, 1934.0, 1945.0, 1960.0, 1966.0, 1972.0, 2032.0, 2037.0, 2040.0, 2044.0, 2071.0, 2074.0, 2197.0, 2203.0, 2245.0, 2255.0, 2261.0, 2397.0, 2406.0, 2469.0, 2501.0, 2618.0, 2638.0, 2653.0, 2666.0, 2726.0, 2751.0, 2825.0, 2864.0, 2881.0, 2933.0, 2956.0, 2980.0, 3161.0, 3403.0, 3499.0, 3509.0, 3514.0, 3524.0, 3598.0, 3651.0, 3789.0, 3915.0, 3916.0, 4133.0, 4155.0, 4368.0, 4878.0, 5126.0, 5445.0, 5510.0, 5644.0, 5679.0, 5874.0, 5934.0, 6044.0, 6128.0, 6293.0]}, 'Crack 1': {'length': 376.36973620374783, 'max_mean_width': 2.8682256, 'component': [13542.0, 14054.0, 14232.0, 14397.0, 14446.0, 14479.0, 14510.0, 14546.0, 14855.0]}}

TABLE 62: Crack detection algorithm results for TSCM models.

**Crack detection algorithm results**

Model	Final Cracks
Engineering Masonry Model (EMM)	W20 EMM 200mm {'Crack 0': {'length': 1460.8627587833157, 'max_mean_width': 3.2002664, 'component': [28.0, 35.0, 166.0, 185.0, 203.0, 212.0, 213.0, 387.0, 421.0, 485.0, 523.0, 594.0, 602.0, 637.0, 684.0, 692.0, 723.0, 724.0, 766.0, 815.0, 818.0, 867.0]}, 'Crack 2': {'length': 357.865896670806, 'max_mean_width': 1.4976667, 'component': [39.0, 361.0, 472.0]}, 'Crack 3': {'length': 1616.5473436662542, 'max_mean_width': 3.7936614, 'component': [64.0, 67.0, 221.0, 266.0, 308.0, 396.0, 467.0, 568.0, 569.0, 599.0, 664.0, 700.0]}, 'Crack 4': {'length': 587.272509147159, 'max_mean_width': 2.0976, 'component': [79.0, 350.0, 487.0, 588.0]}, 'Crack 5': {'length': 823.6025553696551, 'max_mean_width': 1.5079818, 'component': [80.0, 151.0, 206.0, 263.0, 415.0, 480.0, 567.0, 612.0]}, 'Crack 8': {'length': 528.2092388438506, 'max_mean_width': 3.536846, 'component': [209.0, 267.0, 277.0, 412.0]}}
	W20 EMM 100mm {'Crack 0': {'length': 392.3072775261759, 'max_mean_width': 6.382621, 'component': [13.0, 70.0, 356.0, 493.0, 697.0, 777.0, 907.0, 3752.0]}, 'Crack 1': {'length': 337.8059120903073, 'max_mean_width': 2.7229376, 'component': [111.0, 450.0, 932.0, 1702.0, 1919.0]}, 'Crack 2': {'length': 758.5644654910117, 'max_mean_width': 2.6904685, 'component': [137.0, 140.0, 763.0, 1672.0, 1690.0, 1878.0, 1957.0, 2417.0, 2897.0, 3235.0]}, 'Crack 3': {'length': 268.7824399026097, 'max_mean_width': 1.9483333, 'component': [139.0, 490.0, 946.0]}, 'Crack 4': {'length': 936.055553906925, 'max_mean_width': 6.5073185, 'component': [241.0, 438.0, 856.0, 1285.0, 1524.0, 2070.0, 2192.0, 2343.0, 2726.0, 3355.0, 3453.0, 3615.0]}, 'Crack 5': {'length': 1144.1420366370603, 'max_mean_width': 3.0148227, 'component': [329.0, 331.0, 382.0, 485.0, 964.0, 991.0, 1002.0, 1071.0, 1073.0, 1374.0, 1387.0, 1500.0, 1514.0, 1647.0, 1741.0, 1785.0, 1920.0, 2116.0, 2182.0, 2408.0, 2409.0, 2571.0, 2665.0, 2674.0, 3090.0, 3101.0, 3205.0, 3206.0, 3241.0, 3285.0]}, 'Crack 6': {'length': 486.6343596582551, 'max_mean_width': 6.1619277, 'component': [362.0, 432.0, 852.0, 1240.0, 1456.0, 1740.0, 2294.0, 2499.0]}, 'Crack 7': {'length': 154.8709139896837, 'max_mean_width': 2.0775714, 'component': [504.0, 1010.0, 1617.0]}, 'Crack 9': {'length': 353.696197321939, 'max_mean_width': 2.832875, 'component': [1434.0, 2457.0, 2711.0, 3026.0]}}
	W20 EMM 50mm {'Crack 0': {'length': 421.6313555702422, 'max_mean_width': 8.312302, 'component': [19.0, 883.0, 1462.0, 1538.0, 1665.0, 2166.0, 2392.0, 2872.0, 4058.0, 4494.0, 5440.0, 5470.0, 5529.0, 6624.0, 6748.0, 7026.0]}, 'Crack 1': {'length': 180.31484357229823, 'max_mean_width': 4.010375, 'component': [239.0, 1669.0, 3918.0, 4197.0]}, 'Crack 3': {'length': 924.6253295254246, 'max_mean_width': 6.249, 'component': [502.0, 512.0, 1030.0, 1972.0, 4298.0, 4615.0, 4814.0, 6517.0, 6573.0, 7262.0, 8117.0, 9351.0, 10409.0, 10876.0, 11912.0, 12189.0, 12517.0, 13478.0, 13731.0, 13814.0, 13960.0]}, 'Crack 4': {'length': 679.4622874008535, 'max_mean_width': 6.9316525, 'component': [651.0, 751.0, 821.0, 1945.0, 3192.0, 3475.0, 4337.0, 4397.0, 5175.0, 6707.0, 7276.0, 8431.0, 9171.0, 9320.0, 9521.0, 10188.0, 10754.0, 11061.0, 12050.0, 12683.0]}, 'Crack 5': {'length': 160.22796260328596, 'max_mean_width': 7.066143, 'component': [710.0, 1096.0, 1987.0, 2903.0]}, 'Crack 6': {'length': 103.84603988597736, 'max_mean_width': 2.9008, 'component': [925.0, 1524.0, 3182.0]}, 'Crack 12': {'length': 331.50180647368256, 'max_mean_width': 2.9134285, 'component': [4879.0, 4925.0, 6334.0, 6561.0, 6929.0, 8094.0, 9687.0, 10591.0, 11101.0]}, 'Crack 13': {'length': 104.09232157624984, 'max_mean_width': 2.7778888, 'component': [5054.0, 5089.0, 6781.0]}, 'Crack 17': {'length': 201.9504889818294, 'max_mean_width': 4.1300554, 'component': [6914.0, 7830.0, 9751.0, 10316.0, 10474.0]}}
	W21 EMM 200mm {'Crack 0': {'length': 570.6110759527894, 'max_mean_width': 10.180626, 'component': [34.0, 35.0, 154.0, 248.0]}, 'Crack 1': {'length': 836.588309743807, 'max_mean_width': 4.1469526, 'component': [65.0, 66.0, 145.0, 226.0, 227.0, 354.0]}, 'Crack 2': {'length': 1524.49663823834, 'max_mean_width': 2.9414, 'component': [613.0, 646.0, 692.0, 699.0, 701.0, 703.0, 758.0, 876.0, 910.0, 920.0]}}
	W21 EMM 100mm {'Crack 0': {'length': 514.9485411184306, 'max_mean_width': 3.097338, 'component': [16.0, 60.0, 218.0, 258.0, 259.0, 362.0, 363.0, 379.0, 542.0, 629.0, 731.0, 787.0, 901.0]}, 'Crack 1': {'length': 118.79393923933998, 'max_mean_width': 1.01896, 'component': [74.0, 76.0, 491.0]}, 'Crack 2': {'length': 477.4232922679831, 'max_mean_width': 1.617908, 'component': [120.0, 121.0, 304.0, 484.0, 558.0, 618.0, 714.0, 717.0, 960.0, 963.0, 1058.0, 1292.0]}, 'Crack 3': {'length': 259.0829982843336, 'max_mean_width': 1.9239093, 'component': [191.0, 202.0, 699.0]}, 'Crack 5': {'length': 313.29219588109754, 'max_mean_width': 1.6706218, 'component': [273.0, 275.0, 329.0, 340.0, 404.0, 458.0, 673.0]}, 'Crack 25': {'length': 581.583574844206, 'max_mean_width': 1.7237966, 'component': [2181.0, 2362.0, 2430.0, 2734.0, 2829.0, 3183.0, 3273.0, 3290.0, 3436.0]}, 'Crack 29': {'length': 260.55713854410067, 'max_mean_width': 1.1837636, 'component': [2388.0, 2850.0, 2891.0, 3065.0]}, 'Crack 31': {'length': 142.8355697996826, 'max_mean_width': 1.147543, 'component': [2651.0, 2716.0, 3017.0]}}
W21 EMM 50mm {'Crack 0': {'length': 167.83622970026465, 'max_mean_width': 1.8229284, 'component': [111.0, 402.0, 1520.0, 1553.0]}, 'elements': [111.0, 402.0, 1520.0, 1553.0]}, 'Crack 1': {'length': 502.47885527651806, 'max_mean_width': 5.655685, 'component': [130.0, 764.0, 879.0, 983.0, 1322.0, 1774.0, 2511.0, 2578.0, 2801.0, 3240.0, 3588.0, 3739.0, 3798.0, 4530.0]}, 'Crack 2': {'length': 238.8723508487326, 'max_mean_width': 2.0478635, 'component': [132.0, 442.0, 444.0, 558.0, 618.0, 900.0]}, 'Crack 3': {'length': 524.4091913763526, 'max_mean_width': 1.4312897, 'component': [246.0, 249.0, 252.0, 466.0, 470.0, 1626.0, 1691.0, 1777.0, 1790.0, 2011.0, 2391.0, 2402.0, 2630.0, 2691.0, 2957.0, 2971.0, 3333.0, 3355.0, 3498.0, 3935.0, 3944.0, 4210.0, 4280.0, 4816.0, 5043.0, 5069.0, 5110.0, 5139.0, 5317.0, 5427.0, 5428.0, 5879.0]}, 'Crack 8': {'length': 113.03096920755833, 'max_mean_width': 1.6968889, 'component': [843.0, 954.0, 1745.0]}, 'Crack 10': {'length': 153.57408635573907, 'max_mean_width': 1.2991428, 'component': [1307.0, 2330.0, 3693.0, 3703.0]}, 'Crack 11': {'length': 132.4424403278647, 'max_mean_width': 1.068875, 'component': [1502.0, 1848.0, 2666.0]}, 'Crack 17': {'length': 490.51095808350703, 'max_mean_width': 1.4157704, 'component': [9506.0, 9713.0, 10105.0, 10111.0, 10816.0, 10932.0, 10979.0, 11018.0, 11235.0, 11424.0, 11610.0, 12300.0, 12803.0, 12873.0, 13359.0, 13561.0, 13580.0]}, 'Crack 21': {'length': 196.4001018329675, 'max_mean_width': 1.1908, 'component': [14770.0, 14808.0, 14930.0, 14947.0, 14967.0, 15003.0]}}	

TABLE 63: Crack detection algorithm results for EMM models.

```

import pandas as pd

def analyse_tabulated(df, analysis_info):
    """
    Analyses tabulated data based on the given analysis information.

    Args:
        df (pandas.DataFrame): The tabulated data to be analysed.
        analysis_info (dict): Information about the analysis to be performed.

    Returns:
        dict: A dictionary containing the analysis results for each analysis type.

    """
    data = {}
    for analysis in analysis_info:
        vals = []

        ..... Other analysis types .....

        if 'Damage' in analysis:
            if analysis_info[analysis].get('parameters'):
                mesh_size = analysis_info[analysis]['parameters']['mesh']

                temp = []
                for step in df['Step nr.'].unique():
                    max_cw = df[df['Step nr.'] == step]['Ecw1'].max()
                    df_filtered = df[(df['Step nr.'] == step) &
                                     (df['Ecw1'] >= max_cw/10) &
                                     (pd.notna(df['Element']))][['Element', 'Integration Point', 'X0',
                                                                  'Y0', 'Ecw1']]

                    crack_dict = analyse_cracks(df_filtered, mesh_size)
                    psi = compute_damage_parameter(crack_dict)
                    temp.append({'step': step, 'psi': psi})
                vals = pd.DataFrame(temp)
            else:
                for crack_set in analysis_info[analysis]['parameters']['cracks']:
                    c_w = compute_damage_parameter_manual(df, crack_set)
                    vals.append(c_w)

        data[analysis] = vals
    return data

```

---

*EXTRACT 8: Tabulated analysis main function “analyse\_tabulated”*

```
import numpy as np
import pandas as pd
from scipy.spatial import distance_matrix
from scipy.sparse import csr_matrix
from scipy.sparse.csgraph import connected_components

def analyse_cracks(df_filtered: pd.DataFrame, mesh_size: float) -> Dict[str, Dict]:
    """
    Main function to analyse cracks in the data.

    Args:
        df (pd.DataFrame): Original dataframe containing the crack data.
        mesh_size (float): The mesh size used for calculating the distance threshold.

    Returns:
        Dict[str, Dict]: Dictionary containing the crack properties.
    """
    points = df_filtered[['X0', 'Y0']].values
    dist_matrix = distance_matrix(points, points)

    d_threshold = np.sqrt(2 * (mesh_size / 2)**2)
    # Max diagonal distance between int points in quadratic mesh
    n_components, labels = find_connected_components(dist_matrix, d_threshold)

    df_filtered['Component'] = labels
    cracks = calculate_crack_properties(df_filtered, n_components, d_threshold)

    return cracks
```

---

*EXTRACT 9: Crack detection main "analyse\_cracks"*

```
def find_connected_components(dist_matrix: np.ndarray, d_threshold: float):  
    """  
    Find connected components in a distance matrix based on a distance threshold.  
  
    Args:  
        dist_matrix (np.ndarray): A 2D array representing the distance matrix.  
        d_threshold (float): The distance threshold to determine connectivity.  
  
    Returns:  
        Tuple[int, np.ndarray]: A tuple containing:  
            - n_components (int): The number of connected components found.  
            - labels (np.ndarray): Array each element represents the component label of the nodes.  
    """  
    connectivity = dist_matrix <= d_threshold  
    connectivity_sparse = csr_matrix(connectivity)  
    n_components, labels = connected_components(csgraph=connectivity_sparse,  
                                              directed=False, return_labels=True)  
    return n_components, labels
```

---

*EXTRACT 10: Principal crack component detection function "find\_connected\_components"*

```

def calculate_crack_properties(df_filtered: pd.DataFrame, n_components: int,
                             d_threshold: float):
    """
    Calculate properties of cracks from filtered DataFrame.
    Args:
        df_filtered (pd.DataFrame): Filtered DataFrame.
        n_components (int): Number of components to analyse.
        d_threshold (float): Distance threshold between adjacent Int points.
    Returns:
        Dict[str, Dict]: Dictionary containing crack properties for each component.
    """
    cracks = {}

    for component in range(n_components):
        component_data = df_filtered[df_filtered['Component'] == component]
        component_points = component_data[['X0', 'Y0']].values
        component_elements = component_data['Element'].unique()

        if len(component_points) > 1:
            component_dist_matrix = distance_matrix(component_points,
                                                    component_points)

            crack_length = np.max(component_dist_matrix)
            components = component_elements.tolist()
            max_mean_crack_width = component_data['Ecw1'].mean()
            if len(components) > 2 and crack_length > 3 * d_threshold:
                # Crack Length should go through a minimum of 3 IntPoints
                cracks[f'Crack {component}'] = {
                    'length': crack_length,
                    'max_mean_width': max_mean_crack_width,
                    'component': components,
                }
    return cracks

```

---

*EXTRACT 11: Crack property processing function “calculate\_crack\_properties”*

# Bibliography

---



- Ajitkumar, K., 2022. Integrating machine learning and computational physics to assess crack pattern similarity in masonry buildings, s.l.: s.n.
- Albers, B., 2012. 2D Numerical Analysis of Settlement Damage to buildings, s.l.: s.n.
- Alessandrini, C., Garutti, M., Mallardo, V. & Milani, G., 2015. Crack patterns induced by foundation settlement integrated analysis on a renaissance masonry place in italy. *International Journal of architectural heritage: Conservation, Analysis and resotration*, Volume 9, pp. 111-129.
- Ament, S. et al., 2023. Unexpected Improvements to Expected Improvement. s.l., NeurIPS.
- Asteris, P. et al., 2015. Numerical modeling of historic masonry structures. In: *Handbook of research on seismic assessment and rehabilitation of historic structures*. Hershey: IGI global, pp. 213-256.
- Atamturktur, S., Hemez, F. & Unal, C., 2010. Calibration under uncertainty for finite element models of masonry monuments, s.l.: Los Alamos National Laboratory.
- Bagheri-Gavkosh, M. et al., 2021. Land subsidence: A global challenge. *Science of the Total environment*, Volume 778.
- Baird, S. G., 2024. Traditional DoE vs. Bayesian Optimization. [Online] Available at: <https://github.com/sparks-baird/self-driving-lab-demo/blob/main/notebooks/escience/1.0-traditional-doe-vs-bayesian.ipynb> [Accessed 26 8 2024].
- Balandat, M. et al., 2020. BoTorch: A Framework for Efficient Monte-Carlo Bayesian optimization. Vancouver, NEURIPS.
- Bapir, B., Abrahamczyk, L., Wichtmann, T. & Prada-Sarmiento, L. F., 2023. Soil-structure interaction: A state-of-the-art review of modeling techniques and studies on seismic response of building structures. *Frontiers in Built Environment*.
- Bartoli, G. et al., 2017. Bayesian model updating of historic masonry towers through dynamic experimental data. s.l., *Procedia Engineering*.
- Bejarano-Urrego, L., Verstryngge, E., Giardina, G. & Van Balen, K., 2018. Crack growth in masonry: Numerical analysis and sensitivity study for discrete and smeared crack modelling. *Engineering stuctures*, Volume 165, pp. 471-485.
- Berry, W., 1992. Section News. *Fourth international symposium on land subsidence*, 73(19), p. 213.
- Blanken, M. C., 1976. Housing and Urban planning. In: G. Beyer, ed. "Force of order and methods ..." *An american view into the dutch directed society*. The Hague: Martinus Nijhoff, p. 184.
- Boscardin, D. M. & Cording, J. E., 1989. Building response to excavation-induced settlement. *Journal of geotechnical engineering*, 115(1), pp. 1-139.
- Burland, J. B., Broms, B. B. & Mello, V. F., 1977. Behaviour of foundations and structures. Tokyo, *International conference on soil mechanics and foundation engineering*.
- Burland, J. B. & Wroth, C. P., 1974. Settlement of buildings and associated damage. *British Geotechnical Society*, pp. 611-654.
- CEN, 2022. Eurocode 7: Geotechnical design - Part 1: Gernal rules, s.l.: NEN.
- Chancery group, n.d. Chancery group. [Online]

Available at: <https://www.chancerygroup.ie/cracking-in-buildings/>  
[Accessed 26 09 2024].

Charles, J. A. & Skinner, H. D., 2004. Settlement and tilt of low-rise buildings. *Gotechnical Engineering*, Volume 157, pp. 65-75.

Chen, X. et al., 2021. Simulating the failure of masonry walls subjected to support settlement with the combine finite-discrete element method. *Journal of building engineering*, 43(102558).

Chiozzi, A., Milani, G. & Tralli, A., 2017. A genetic algorithm NURBS-based new approach for fast kinematic limit analysis of masonry vaults. *Computers and structures*, Volume 183, pp. 187-204.

CUR, 1996. Building on soft soils design and construction of earthstructures both on and into highly compressible subsoils of low bearing capacity. Rotterdam: Balkema.

D'Altri, A. M. et al., 2020. Modeling Strategies for the Computational Analysis of Unreinforced Masonry Structures: Review and classification. *Archives of Computational Mehtods in Engineering*, Volume 27, pp. 1153-1185.

Dan, V., 2017. Empirical and Non-empirical methods, Berlin: Free University of Berlin.

de Vent, A. E., Rots, J. G. & van Hees, R. P. J., 2013. Interpreting structural damage in Masonry: Diagnostic Tool and Approach. *Restoration of Buildings and Monuments*, pp. 291-308.

de Vent, I., 2011. Prototype of a diagnostic decision support tool for Structural damage in masonry,. Delft: s.n.

de Vent, I., 2011. Structural Damage in Masonry. s.l.:Wöhrmann Print Service Zutphen.

de Vos-Effting, S. et al., 2017. Een verkenning van de milieu-impact van circulair bouwen in de woning-en utiliteitsbouw, Utrecht: TNO.

DeJong, M., 2016. Settlement effects on masonry structures. *Structural analysis of Historical constructions*, pp. 449-456.

Deniz Dalgic, K. et al., 2023. Masonry buildings subjected to settlements: Half-scale testing, detailed measurements, and insights into behaviour. *Engineering Structures*.

Desai, C. S., Zaman, M. M., Lightner, J. G. & Siriwardane, H. J., 1984. Thin-layer element for interfaces and joints. *International Journal for numerical ana anlytical methods in geomechanics*, pp. 19-43.

Dhadse, G. D., Ramtekkar, G. & Bhatt, G., 2021. Influence due to interface in finite element modeling of soil-structure interaction system: a study considering modified interface element. *Research on engineering structures & materials*.

Dhadse, G. D., Ramtekkar, G. D. & Bhatt, G., 2020. Finite element modelling of soil structure interaction system with interface: A review. *Archives of computational methods in engineering*.

DIANA FEA BV, 2024. Theory manual. [Online]

Available at: <https://manuals.dianafea.com/d108/en/1219784-1219784-theory-108.html>  
[Accessed 18 05 2024].

Dinar, A. et al., 2021. We lose ground: Global assessment of land subsidence impact extent. *Science of the total environment*, Volume 786, p. 147415.

Erkens, G. & Stouthamer, E., 2020. The 6M approach to land subsidence. s.l., Copernicus Publications.

- Erturk Atmaca, E. et al., 2023. Numerical simulation of Sever Damage to a Historical Masonry Building by Soil Settlement. Buildings.
- Escudero, C., 2014. Numerical calculation model for the global analysis of concrete structures with masonry walls, Barcelona: UPC.
- Fernandes, F. M., Lourenço, P. B. & Castro, F., 2009. Materials technologies and practice in historic heritage structures. In: M. Bosternaru Dan, R. Prikryl & A. Torok, eds. Ancient Clay Bricks: Manufacture and properties. Dordrecht: Springer Dordrecht, pp. 29-48.
- Frazier, P. I., 2018. A tutorial on Bayesian optimization. s.l., s.n.
- Gagliardo, R., 2021. Performance - Based damage assessment of masonry structures subjected to settlement using rigid block models, Napoli: University of Naples.
- Ghiassi, B., Vermelfoort, A. T. & Lourenço, P. B., 2019. Chapter 7 - Masonry mechanical properties. In: Numerical Modeling of Masonry and Historical structures. s.l.:Woodhead Publishing, pp. 239-261.
- Giambanco, G., Rizzo, S. & Spallino, R., 2001. Numerical analysis of masonry structures via interface models. Computer method in applied mechanics and engineering, Volume 190, pp. 6493-6511.
- Giardina, G., 2013. Modelling of Settlement Induced Building Damage. Delft: Ipskamp Drukkers.
- Giardina, G., Hendricks, M. A. & Rots, J., 2009. Assessment of the settlement vulnerability of masonry buildings. Leuven, s.n.
- Giardina, G., Hendriks, M. A. & Rots, J. G., 2008. Numerical Analyses of tunnel-induced settlement damage to a masonry wall. Stuttgart, s.n., pp. 11-13.
- Giardina, G. et al., 2013. Numerical analysis of a masonry façade subject to tunnelling-induced settlements. Engineering Structures, pp. 234-247.
- Grant, D. N. et al., 2021. Explicit modelling of collapse for Dutch unreinforced masonry building typology fragility functions. Bulletin of earthquake engineering, Volume 19, pp. 6497-6519.
- Huijgen, M., Remmelts, G. & Roholl, J., 2020. Land subsidence due to gas extraction does not cause any damage, s.l.: BottomBroad.
- Jafari, S., 2021. Material characterisation of existing masonry. Delft: s.n.
- Jafari, S., Rots, J. G. & Esposito, R., 2022. A correlation study to support material characterisation of typical Dutch masonry structures.. Journal of Building Engineering, 45(103540), pp. 1-14.
- Jafari, S., Rots, J. G., Esposito, R. & Messali, F., 2017. Characterizing the material properties of dutch unreinforced masonry.. Procedia Engineering, Volume 193, pp. 250-257.
- KCAF, 2022. KCAF. [Online]  
Available at: <https://www.kcaf.nl/wat-doet-het-kcaf/kennisbank/>
- KCAF, 2022. KCAF. [Online]  
Available at: <https://www.kcaf.nl/wat-doet-het-kcaf/>  
[Accessed 22 11 2023].
- Kibriya, G., Botzheim, J., Orosz, Á. O. & Bagi, K., 2024. Automatic calibration of a discrete element model of a masonry arch by swarm intelligence methods.. Computers and structures, Volume 299.
- Kok, S., Korff, M. & Costa, A. L., 2020. Systematic assessment of damage to buildings due to

- groundwater lowering-induced subsidence: methodology for large scale application in the Netherlands. s.l., Copernicus publications, pp. 577-585.
- Kok, S., Van der Putten, S. & Kraus, J., 2021. Towards a knowledge agenda for foundation problems, s.l.: Deltares.
- Kok, S., Van der Putten, S. & Kraus, J., 2021. Naar een kennisagenda funderingsproblematiek, s.l.: Deltares.
- Kooi, H. et al., 1998. Geological causes of recent (-100 yr) vertical land movement in the Netherlands. *Tectonophysics*, Volume 299, pp. 297-316.
- Korff, M., 2009. Deformations and damage to buildings adjacent to deep excavations in soft soils, Delft: Deltares.
- Korswagen, P. A., Longo, M., Meulman, E. & Rots, G. J., 2019. Crack Initiation and propagation in unreinforced masonry specimens subjected to repeated in-plane loading during light damage. *Bulletin of Earthquake engineering*, Volume 17, pp. 4651-4687.
- Korswagen, P. A., Longo, M. & Rots, J. G., 2021. Experimental and computational study into the onset of light damage of Dutch masonry structures. *Heron*, 66(1), pp. 91-114.
- Korswagen, P., Longo, M., Meulman, E. & van Hoogdalem, C. A., 2017. Damage sensitivity of Groningen masonry structures - Experimental and computational studies, Delft: Delft University of Technology.
- Koster, K., Stafleu, J. & Stouthamer, E., 2018. Differential subsidence in the urbanised coastal-deltaic plain of the Netherlands. *Netherlands Journal of Geosciences*, 97(4), pp. 215-227.
- Krauth, K., Bonilla, E. V., Cutajar, K. & Filippone, M., 2017. AutoGP: Exploring the Capabilities and Limitations of Gaussian Process Models. s.l., s.n.
- Lagomarsino, S., Penna, A., Galasco, A. & Cattari, S., 2013. Trmuri program: An equivalent frame model for the nonlinear seismic analysis of masonry buildings. *Engineering structures*, Volume 56, pp. 1787-1799.
- Lemos, J. V., 2019. Discrete Element Modeling of the Seismic behaviour of Masonry construction. *Buildings*, 10(3390).
- Lisane, E. V., 2019. The equivalent shear masonry model, s.l.: s.n.
- Liu, P., Huang, S., Song, M. & Yang, W., 2021. Bayesian model updating of a twin-tower masonry structure through subset simulation optimization using ambient vibration data.. *Journal of Civil Structural Health Monitoring*, 11(1), pp. 129-148.
- Lourenço, P. B., 2014. Masonry Structures, Overview. *Encyclopedia of Earthquake Engineering*, pp. 1-9.
- Lourenço, P. J. B. B., 1996. Computational strategies for masonry structures. 1 ed. Den Haag: Delft University Press.
- Marto, A. et al., 2015. Surface settlement Induced by tunneling in Greenfield condition through physical modelling. *Jurnal Teknologi*, 76(2), p. 8.
- Masia, M. J., Kleeman, P. W. & Melchers, R. E., 2004. Modeling Soil/Structure Interaction for Masonry Structures. *Journal of Structural engineering*, 140(4), pp. 641-649.

- Muntendam-Bos, A. G., Roest, J. P. A. & De Waal, J. A., 2015. Production induced subsidence and seismicity in the Groningen gas field.. Proceedings of IAHS, pp. 129-139.
- NEN, 2016. Sepcification for ancillary components for masonry - Part 2: Lintels, Delft: NEN.
- NEN, 2020. NPR 9998 Assessment of structural safety of buildings in case of erection, reconstruction and disapproval - induced earthquakes - Basis of design,actions and resistances, s.l.: NPR.
- Netzel, H., 2003. Review of the limiting tensile strain method for predicting settlement induced building damag. 1 ed. s.l.:Taylor & Francis group.
- Netzel, H., 2009. Building response due to ground movement, Delft: IOS Press.
- Ozer, I. E. & Geurts, C. W., 2021. Literature Review: Effects of subsidence on buildings, Delft: TNO.
- Palmisano, F. & Elia, A., 2015. Shape optimization of strut-and-tie models in masonry buildings subjected to landslide-induced settlements. Engineering structures, Volume 84, pp. 223-232.
- Prosperi, A. et al., 2023. Empirical fragility and ROC curves for masonry buildings subjected to settlements. Journal of Building Engineering.
- Prosperi, A. et al., 2023. Accurate and Efficient 2D Modelling of Historical Masonry Buildings subjected to settlements in comparinson to 3D approaches. Kyoto, s.n., pp. 232-244.
- Prosperi, A. et al., 2024. 2D and 3D modelling strategies to reproduce the response of historical masonry buildings subjected to settlements. International journal of architectural heritage, p. 1'17.
- Prosperi, A. et al., 2023. Sensitivity modelling with objective damge assessment of unreinforced masonry façades undergoing different subsidence settlement patterns.. Engineering Structures.
- Ramancha, M. K. et al., 2022. Bayesian model updating with finite element vs surrogate models: Application to a miter gate structural system. Engineering structures, Volume 272.
- Rastbood, B. A., Shahriar, K., Khoshravan Azar, A. & Rastbood, A., 2006. Prediction of ground settlement by Peck-Fujita and Numerical methods. International society for soil mechanics and geotechnical engineering, pp. 295-298.
- Ritter, S., Giardina, G., Franza, A. & DeJong, M. J., 2020. Building Deformation Cause by tunneling: Centrifuge Modeling. Journal of Geotechnical and Geoenvironmental Engineering, 146(5).
- Rots, J., 1988. Computational modeling of concrete fracture. Delft, s.n.
- Rots, J., 2000. Computational modelling of cracking and settlement damage in masonry structures. Madrid, s.n.
- Rots, J. G., Korswagen Eguren, P. & Longo , M., 2021. Computational modelling checks of masonry building damage de to deep subsidence, Delft: TUDelft.
- Sangirardi, M., Malena, M. & de Felice , G., 2020. Settlement Induced crack pattern prediction through the jointed masonry model. s.l., Springer, Cham.
- SBR, 1998. Over het bepalen en bewaken van de kwaliteit van gebouwen. Stichting Bouwresearch Rotterdam. s.l.:s.n.
- Schlaich, J., Schaefer, K. & Jennewein, M., 1987. Toward a consistent design of structural concrete. PCI Journal, pp. 74-150.
- Seung-Seop, J. & Hyung-Jo, J., 2016. Sequential surrogate modeling for efficient finite element model

updating. *Computers and structures*, Volume 168, pp. 30-45.

Sidney, L. M., 1992. *Masonry and stone construction*, s.l.: s.n.

Skempton, A. H. & MacDonald, D. H., 1956. *The allowable settlement of buildings*. s.l., ICE, pp. 727-768.

Son, M. & Cording, E. J., 2007. Evaluation of building stiffness for building response analysis to excavation-induced ground movements. *Journal of geotechnical and geoenvironmental engineering*, Volume 133, pp. 995-1002.

Southamer, E. et al., 2020. *Dutch national scientific research program on land subsidence: Living on soft soils - subsidence and societ.* s.l., Copernicus Publications.

Theodossopoulos, D. & Sinha, B., 2013. A review of analytical methods in the current design process and assessment of performance of masonry structures. *Construction and Building Materials*, Volume 41, pp. 990-1001.

Tzamtzis, A. & Asteris, P., 2003. *Finite element analysis of masonry structures: Part 1 - Review of previous work*. Clemson, The masonry society.

van Alphen, J., Haasnoot, M. & Diermanse, F., 2022. *Uncertain Accelerated Sea-Level Rise, Potential Consequences, and Adaptive Strategies in the Netherlands*. *Water*, 14(1527).

van der Meulen, M. J., Maljers, D., van Gessel, S. F. & Gruijters, S. L., 2007. Clay resources in the Netherlands. *Netherlands journal of geosciences*, 86(2), pp. 117-130.

van Gils, M., Stouthamer, E. & Groothuijse, F., 2020. *Towards a legal strategy fitting today's challenge of reducing impacts of subsidence in the Netherlands*. s.l., Copernicus publications, pp. 825-529.

Viladkar, M. N., Godbole, P. N. & Noorzaeei, J., 1994. Modelling of interface for soil-structure interaction studies.. *Computers & Structures*, pp. 765-779.

Vindhyashree, Rahamath, A., Kumar, P. & Kumar, P., 2015. Numerical simulation of masonry prism test using ANSYS and ABAQUS. *International journal of engineering research & technology*, pp. 1019-1027.

Xu, H. et al., 2018. A unified model for the seismic analysis of brick masonry structures. *Construction and Building Materials*, Volume 184, pp. 733-751.